Dark Matter and Gravitational Lensing as Teaching Tools for Physics and Astronomy

Dissertation zur Erlangung des akademischen Grades
doctor rerum naturalium (Dr. rer. nat.)

vorgelegt dem Rat der Physikalisch-Astronomischen Fakultät
der Friedrich-Schiller-Universität Jena

von Silvia Simionato
geboren am 28.03.1979 in Mirano (Venedig), Italien

Gutachter
1. Prof. Dr. Karl-Heinz Lotze, Friedrich-Schiller-Universität Jena
2. Prof. Dr. Oliver Schwarz, Universität Siegen
3. Prof. Dr. Matthias Bartelmann, Universität Heidelberg

Tag der Disputation: 12.04.2022

Abstract

We know from literature and direct experience that applying the notions of physics, mathematics and astronomy to real and interesting astrophysical problems fascinates and particularly stimulates many students. Even more if they are given the opportunity to work actively on the chosen problem through experimental activities. Moreover, this approach is also known to stimulate a more effective and lasting acquisition of knowledge related to the topic under investigation.

In this work, which is primarily aimed at teachers of physics, mathematics and astronomy, it is illustrated how two important topics of cosmology can be introduced as valuable teaching aids: the dark matter problem and gravitational lensing. These complex and articulated topics lend themselves very well to appropriate elementarisation and the use of simplified models. This process has made them suitable for introduction into the classroom in the form of exercises and/or extracurricular projects for students in their final years of secondary school or first years of university.

In the first part of this thesis, the concepts of radial and rotational velocity, together with those of spider diagram and rotation curve, are introduced and applied to the solar system and a spiral galaxy. The inclusion of the spider diagram in this educational context is, as far as we know, innovative. The analysis of the dynamics of these astronomical systems provides important information on their mass and its distribution. And the profound differences between these two systems are also highlighted. All this is discussed while working with real data and using the dynamic mathematical software Geogebra. Finally, thanks to this analysis and the mass-luminosity ratio of the spiral galaxy, we can estimate the amount of non-visible mass that apparently influences the motion of all matter in this galaxy. This provides evidence for the possible existence of dark matter.

In the second part of this thesis, which is also the main part, we explore how a concentration of mass can act like a lens, deflecting the path of light rays. We thus discuss the phenomenon of strong gravitational lensing, which can produce optical illusions observable in the universe. This effect is investigated for several examples of mass distributions acting as lenses. By examining the geometry of the gravitational lens system, some important relationships that exist between the various elements of the system are deduced, such as size, distances and alignment of the components. Using this information and thanks to the software Geogebra, visualisations and interactive simulations of the images resulting from the gravitational lensing effect are created. Finally, the form to be given to lenses made of glass, so that they can recreate the same effects produced by gravitational lenses, is studied. This leads to the illustration of the five models of plexiglass lenses we have designed and produced. These add an experimental part to the teaching of this subject, as they reproduce the gravitational lens effect directly in the classroom, allowing this phenomenon to be observed, understood in depth and discussed. In addition, two of these models, Kuzmin disk and Plummer sphere, are explored and realised in this framework for the first time.

Zusammenfassung

Wir wissen aus der Literatur und aus direkter Erfahrung, dass die Anwendung von Begriffen der Physik, Mathematik und Astronomie auf reale und interessante astrophysikalische Probleme viele Schülerinnen und Schüler fasziniert und besonders motiviert. Dies gilt umso mehr, wenn sie die Möglichkeit haben, auch experimentell an dem gewählten Problem zu arbeiten. Außerdem ist bekannt, dass dieser Ansatz einen effektiveren und nachhaltigeren Wissenserwerb in Bezug auf das untersuchte Thema fördert.

In dieser Arbeit, die sich in erster Linie an Physik-, Mathematik- und Astronomielehrer richtet, wird aufgezeigt, wie zwei wichtige Themen der Kosmologie als wertvolle Unterrichtsmittel eingeführt werden können: das Problem der dunklen Materie und der Gravitationslinseneffekt. Diese komplexen Themen eignen sich sehr gut für eine angemessene Elementarisierung und die Verwendung von vereinfachten Modellen. Dieser Prozess hat sie für die Einführung in den Unterricht in Form von Übungen und/oder außerschulischen Projekten für Schülerinnen und Schüler in den letzten Jahren der Sekundarstufe oder Studentinnen und Studenten in den ersten Jahren der Universität geeignet gemacht.

Im ersten Teil dieser Dissertation werden die Konzepte der Radial- und Rotationsgeschwindigkeit zusammen mit denen des "Spinnen"-Diagramms (spider diagram) und der Rotationskurve eingeführt und auf das Sonnensystem und eine Spiralgalaxie angewendet. Die Einbeziehung des Spinnendiagramms in diesen Bildungskontext erfolgt nach unserer Kenntnis hier zum ersten Mal. Die Analyse der Dynamik dieser beiden astronomischen Systeme liefert wichtige Informationen über ihre Masse und deren Verteilung. Außerdem werden die tiefgreifenden Unterschiede zwischen diesen beiden Systemen hervorgehoben. All dies wird diskutiert, während man mit realen Daten arbeitet und die dynamische mathematische Software Geogebra verwendet. Dank dieser Analyse und des Masse-Leuchtkraft-Verhältnisses der Spiralgalaxie können wir schließlich die Menge der nicht sichtbaren Masse abschätzen, die scheinbar die Bewegung alle Materie dieser Galaxie beeinflusst. Dies ist ein Hinweis auf die mögliche Existenz von dunkler Materie.

Im zweiten Teil dieser Doktorarbeit, der gleichzeitig der Hauptteil ist, untersuchen wir, wie eine Massenkonzentration wie eine Linse wirken kann, die Lichtstrahlen ablenkt. Wir diskutieren also das Phänomen des starken Gravitationslinseneffekts, der im Universum beobachtbare optische Illusionen erzeugen kann. Dieser Effekt wird für mehrere Beispiele von Massenverteilungen analysiert, die wie Linsen wirken. Durch die Untersuchung der Geometrie des Gravitationslinsensystems werden einige wichtige Beziehungen zwischen den verschiedenen Elementen des Systems abgeleitet, wie Größe, Abstände und Ausrichtung der Komponenten. Anhand dieser Informationen und dank der Software Geogebra werden Visualisierungen und interaktive Simulationen der Bilder erstellt, die durch den Gravitationslinseneffekt entstehen. Schließlich wird studiert, welche Form gläserne Linsen haben müssen, damit sie die gleichen Effekte erzeugen können wie Gravitationslinsen. Dies führt zu fünf Modellen von Plexiglaslinsen, die wir entworfen und hergestellt haben. Sie ergänzen den Unterricht zu diesem Thema um einen experimentellen Teil, da sie den Effekt der Gravitationslinsen direkt im Klassenzimmer nachbilden und es ermöglichen, dieses Phänomen zu beobachten, zu verstehen und zu diskutieren. Darüber hinaus werden zwei dieser Modelle, die Kuzmin-Scheibe und die Plummer-Kugel, in diesem Rahmen zum ersten Mal erforscht und realisiert.

Contents

Chapter 1

Introduction

Astronomy and physics have been my passion for many years now, as well as finding the most effective, suitable and stimulating way to teach and disseminate these subjects. Over the years, I have learnt about the interesting benefits for students that this brings. Besides fascinating and motivating many of them, these themes lend themselves effectively to promoting the development of skills and competences that are important not only in education, but also in life [49][43][40][99]. In this respect, astronomy is also regarded as one of the most suited subjects to achieve this goal. Not only because it is particularly well equipped for inquiry-based learning and ideal for interdisciplinary teaching, but also because it is extremely appealing to all levels of education [41]. These are the basic motivations that led to the formulation and development of this project at the research group in physics and astronomy teaching at the Friedrich-Schiller University (Jena) and ultimately to this thesis. The aim is to bring innovation by introducing topics of modern astrophysics into the teaching of physics, mathematics[1] and astronomy. The use of supportive teaching tools, which facilitate learning and stimulate students to a greater extent, are also promoted. It is also important for us to actively involve the students in the learning process so that they achieve more long-lasting knowledge, but above all learn to use their minds and develop a way of thinking.

Basically, the idea is to introduce, when teaching physics, mathematics and astronomy, examples based on known real problems that engage scientists. In this way it is possible to motivate and inspire students [113] as well as increase their level of interest and ability in scientific subjects [84]. Moreover, in this context, cosmology is considered particularly appropriate because it offers a number of interesting and useful applications of physical and mathematical concepts [113].

Another purpose of this work is to introduce a hands-on part in the developed teaching activities, i.e. we want to give an experimental note. The intention is to give students, after an appropriate theoretical basis, the possibility to carry out this part autonomously. They are therefore able to apply their knowledge, analyse, experiment, understand and discuss the results and thus build up their own knowledge.

Alongside these aspects, it is also important to introduce modern tools that make the teaching-learning process more efficient [87]. For example, we have noticed that students are sometimes overcome by boredom if the level of technological stimulation does not correspond to what they are used to on a daily basis. Students are constantly immersed in technology, which is now an integral part of our lives, so we believe it is useful to introduce resources from an area that is familiar to them.

---

[1]Mathematics is the language of the laws of physics and astronomy, so it must be included. That is why it is always included in this thesis when discussing the teaching of physics and astronomy, even in cases where it is not explicitly mentioned.

In the light of these guidelines and after extensive literature research, it was clear that our main target audience was teachers. Actually, the educational materials and tools produced are intended for a final use with students in the last years of secondary school and the first years of university, including teacher students. However, it is important to involve above all those who must then transmit this knowledge and actually guide and involve the students. Ultimately, educating those who are responsible for educating students is the best way to reach as many students as possible. Inspired teachers can inspire students and transfer knowledge more effectively and promote the development of important skills [14].

It is precisely the teachers (in-service and future) that we are addressing first and foremost, meaning that this text as well as the created material is specifically written and produced for them. Essentially, the level held in this thesis takes into account an already solid background in physics and mathematics and the topics presented, already elementarised, can be understood without great effort. For those who want to teach and introduce these topics in the classroom there is however one more step to take, which is to adapt the content to the level of the students for whom it is intended. This extra step is left to teachers, but we are always willing to work together (and happy to do so) to find the most convenient and useful solution, should it be requested.

The teaching methodology to be adopted, on the other hand, is not examined in depth, as we are convinced that we cannot identify with and limit ourselves to a single definition. However, a special consideration for what stimulates the minds of students should be always present, for example the so-called Socratic method or debate (a form of enquiry and discussion, based on asking and answering questions to stimulate critical thinking and the development of ideas [20][36][69]), regardless of which way we teach.

In addition, although we leave it up to the teacher to choose the teaching method he/she finds most suitable, we think that direct lessons are necessary when dealing with new topics to give students a background to work with. Then they can start to think independently, develop their own ideas and solve problems by applying what they have learned. Practically, we recommend a combined use of teacher- and student-centred approaches.

The teacher has a very special role in all this. In fact the teacher is the source of knowledge and is also the guide of the investigation and learning processes. That is, the teacher can transfer knowledge and help with skills and also guides and supervises the reasoning process and helps students to develop new capabilities. Making hypotheses, refuting, experimenting and so on are all part of this process. In this perspective, a clarifying thought is that of the Swiss developmental psychologist Piaget, who states [52] that learning is characterised by the movement of know-how towards knowledge, which occurs through reflexive abstraction, i.e. a process that leads the individual to construct theories to justify results. Teaching is instead guiding, encouraging, relating. Therefore, it is much more than informing since learning is an individual process that takes place internally.

An important part of our work is the choice of topics. The school curricula that relate to our target audience, especially for Italy and Germany, but not only,[2] were obviously explored. It is perfectly clear that cosmology is not part of the physics curriculum in secondary school, and even at university level it is a separate course. However, as mentioned, our aim is to apply the knowledge that is part of the school curriculum to topics taken from cosmology, possibly also known from the media. Whether this is done by introducing specific exercises in the lessons or by carrying out an entire extra-curricular school project on the subject, the goal is to stimulate the interest of more students. We also like the idea of dispelling the myth of many that science is boring.

Basically, before selecting the topics to be covered in this thesis, we formulated a questionnaire for

---

[2]For Italy and Germany we have direct experience, but in the literature there is much material on other countries.

teachers for understanding their ideas, needs and preferences about possible teaching materials to be produced and to get an indication of what most attracts their students. We managed to collect 50 questionnaires with a total of 123 suggestions on topics to be developed in student projects or to be introduced in lessons. From the results of our questionnaire on preferred themes,[3] which we see summarised in the graph in fig. 1.1, the most sought-after trends are clear. These include the use of experiments, astonishing phenomena, the introduction of unsolved problems, the use of real data and the practice of computer skills, i.e. the guidelines we then adopted for our projects. As can be seen from the graph, some of the suggested topics are very general, more of an indication of how to develop the project. For example use of experiments, combining theory and practice, historical or interdisciplinary themes. However, they are important indications of
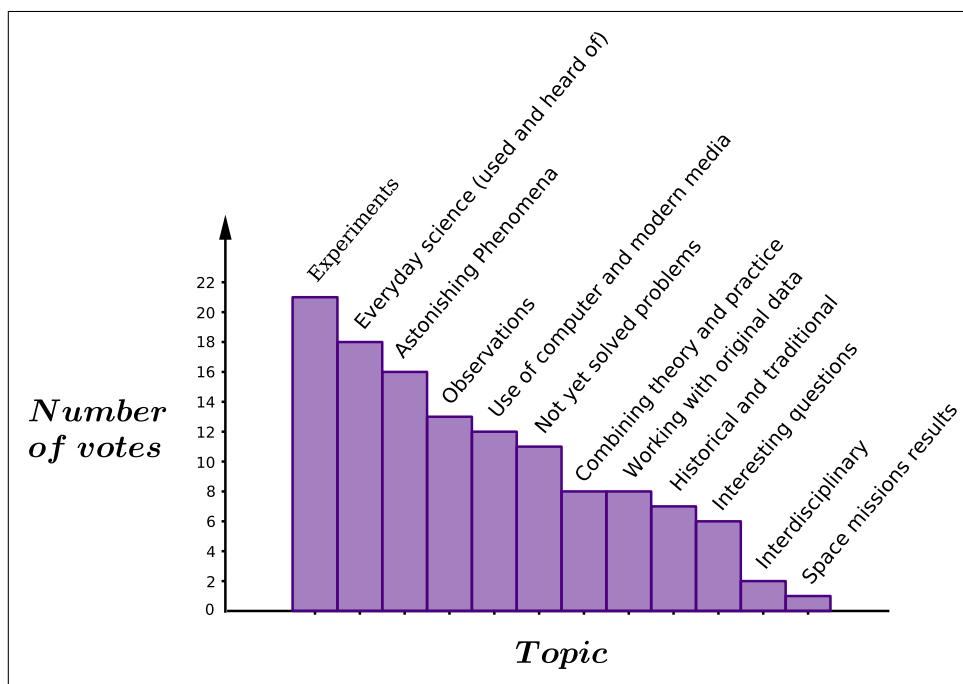

Figure 1.1: Trends, in descending order of popularity, for topics that are most appealing to teachers and their students. The pool is 50 teachers of physics and/or mathematics and/or astronomy (40 from secondary school and 10 future teachers).

teachers' and students' needs.

Furthermore, it is normal that students are more attracted to the information they receive in everyday life (another result of the questionnaire), but do not fully understand it due to a lack of knowledge. For example, there are often reports on television, in newspapers or online about topics such as dark matter, black holes, extrasolar planets, gravitational lensing and gravitational waves. These are all profoundly complex topics, but the students' curiosity and interest are stimulated. Thus, these subjects are well suited to our purpose. This is provided that it is possible to deal with them through a simplified approach and an effective elementarisation, in order to make them accessible in a clear and comprehensible way first to teachers and then to students.

Another important aspect is the use of the software Geogebra in our activities and exercises. This is done with the scope of training and developing computer skills and maintaining the appropriate level of technology, but always with the intention of simplifying and clarifying the topics covered. Geogebra is an open-source dynamic mathematics software for all levels of

---

[3]Some of the results have also been confirmed recently by other doctoral projects in the field of physics and astronomy education: use of original data in [112] and surprising phenomena, use of computers and unsolved problems in [46].

education that brings together geometry, algebra, spreadsheets, graphics, statistics and calculus. It is also the winner of many awards in the education sector.[4] Geogebra, besides being known by many teachers and students, has great potential in teaching and learning STEM subjects (Science, Technology, Engineering and Mathematics) and also supports their innovation [78]. Not only is it simple and intuitive to use even for beginners, but it also comes with a rich manual, examples and useful tutorials.

In our research group it has been used for some time, as can be seen from [112], and its use is suggested to all future teachers, involving them in specific activities and raising awareness of the advantages it brings. Amongst these, it has been proven that it increases student participation and motivation, as well as interest in the content covered, stimulates knowledge building, exercises interpretation and graphic presentation of the concepts dealt with, facilitating learning [78][106][52]. In our specific case and considering our educational purposes, it is valuable for students to learn how to visualise data sets graphically. Indeed, this process not only teaches them which data are meaningful for the exercise they have to perform and how they are related, but also gives them the opportunity to become familiar with reading, analysing and extracting information from graphs. Various specific computer programmes can be used for this purpose, but they are not always easy to use. This is another reason why we decided to use Geogebra, which is perfectly suited to support work with the chosen themes. Of course it is also possible to draw graphs manually (some 'old school' people still do it and it is a real art), this is fascinating. However, it is also extremely time-consuming. Therefore, sometimes it is not really possible to produce hand-drawn graphs, especially in the classroom, with large amounts of data and the need to achieve high accuracy or to exploit interactivity. Not to mention the fact that it is almost always attractive for students to work with computers.

At the end of this process of choosing the subjects and the means to be included, two main topics that meet all the above criteria were isolated and they are also well suited to the development of an experimental part: the dark matter problem and gravitational lensing.

In addition to the necessary elementarisation of these themes, one of our priorities is to introduce new and original aspects for both developed projects. Innovations on which we are now shedding light and which we are going to list by briefly explaining the approach adopted.

Basically, in the case of the first topic, evidence of the hypothetical presence of non-visible matter, the so-called dark matter, is searched by considering the rotation curves of spiral galaxies. In this context, the concept of the spider diagram is introduced, which is new to the field of education. The spider diagram is a graphical display of constant radial velocity contours of the galaxy under consideration and obtained through observations. As we shall see, it not only introduces several important topics in physics, but also allows us to analyse and work with the corresponding original data, also providing the rotation curve (or vice versa). This is an interesting approach that enables students to use Geogebra in the processing and visualisation of original data and to manipulate them in order to obtain realistic results, despite being simplified. For educational purposes and to fully understand this new concept, it is initially applied to the solar system, an application never before encountered in the literature.

The second subject, namely the gravitational lensing effect in its strong form, covers the main part of this PhD project. Indeed, it has proved to be very fitting to and fruitful in the production of new teaching material. In the educational sector, the basic idea is not new, but we provide an original contribution by first of all deepening and exploring new models. Indeed, this process has led to a widening of the range of models available as gravitational lenses. Furthermore, the development of this new analysis inspired the creation of new and innovative teaching tools. In essence, to understand and explore this wonderful phenomenon we start from the geometry of

---

[4]Definition taken from https://www.geogebra.org/about. Recent awards received include "Archimedes 2016: MNU Award in category Mathematics", MNU – Verband zur Förderung des MINT-Unterrichts.

the system and use mainly a graphical and experimental approach. To this end, we have devised, designed and produced teaching tools which, alongside the theory, allow us to supplement the explanation with a very useful practical part. In this respect, we are able to explore and discuss in depth five different simplified models of gravitational lenses, two of which (the Plummer sphere and the Kuzmin disk) are being addressed and developed in this context for the first time. Also innovative is the fact that, for these five models, Geogebra allows students to produce real simulations of effects resulting from the gravitational lensing phenomenon in the presence of point-like and extended sources. Moreover, collaborating with our faculty's laboratory, we could build five different plexiglass lenses (included the totally new ones) that can reproduce live the effects representative of the chosen gravitational lens.

These lenses in particular have interested and impressed many teachers, students and colleagues, and have always received very positive feedback. They proved so popular that LIGO's Exploration Center at LIGO Hanford Observatory (Washington), with whom we hope to collaborate, requested a set for their education and public outreach department.

The work performed with this project presented many challenges and involved many teachers, teacher students and students, These are mainly from Italy and Germany, but on several occasions also from other countries. The collaboration is extremely important because, in order to create valid teaching support material, the contents and results has to be tested and revised several times. All the feedback collected in this phase is valuable. This process helps to improve the feasibility and simplicity of teaching and its effectiveness. Also the enthusiasm expressed by the students as well as the final learning evaluations are taken into account.

The methodology adopted is inspired by the scientific method. In fact, the definition of the problem to be treated considering the basic knowledge is the first step. Obviously followed by a study of the literature and the consideration of related topics, elaborating the theoretical framework of the project. Once the educational activity is created taking into account the needs of our target audience, before disseminating it, we proceed with the frontal and formative evaluation. In practice, the high quality of the resource, assessed in the field, is checked in order to allow its improvement through revision phases. Finally, after several positive results from all points of view, more general conclusions can be drawn on the success of the research project.

Another important and fundamental aspect was working in collaboration with the university laboratory to produce the plexiglass lenses. This was a new type of workmanship for them to explore. So together we started with trials and refinements and finally succeeded in producing our own set of gravitational lens effect simulators.[5]

This entire process of revising and improving the material and building the lenses took a lot of time and patience, but it also brought a lot of satisfaction and we can say that it was absolutely worth it. In fact, the final results, the teaching materials and the educational tools produced have proved to be an absolutely valuable teaching aid and are appreciated by teachers and students alike. Obviously, it is not possible to go into detail and present all the phases and aspects of this work, which we have carried out with great passion, in 100 pages, which is our limit for the main body of doctoral theses. That is why we prefer to concentrate on introducing and providing with this thesis the educational material in its final form and thus be of help and support to the teaching world.

As already mentioned, topics are elementarised at an early stage and presented in a simplified version cut out for teachers. However, they have to be differentiated and adapted to the level of the target group. For this reason, when presenting at conferences, workshops and teacher trainings, also further simplified material is used, which is very close to what could be used in the classroom directly with the students. An example can be seen in appendix G. We also encourage

---

[5]Sincere thanks to Bernhard Klumbies, Martin Huber and Thomas Köhler for their invaluable collaboration and help in creating our lenses.

teachers to produce their own geometric files with Geogebra, in order to understand concepts and mechanisms more deeply. However, our ready-made files, which are collected on the CD attached to this thesis, are always provided.

Finally, a few words on the structure of this thesis. It is divided into two parts in accordance with the two developed themes: the Dark Matter Problem (chapter 2) and Gravitational Lensing (chapter 3). Practically, contextualising these two topics, the concept of movement under the influence of gravity, first for matter and then for light, can be thought as the main narrative thread of this thesis.

For each of these two chapters, developed as student projects, we begin by presenting the motivations and objectives of the project (sections 2.1 and 3.1) and then providing the basic knowledge of the subject (sections 2.2 and 3.2). The background knowledge is the necessary information and explanations on the topic under consideration, which are essential to carry out the project. However, a deeper preparation is always recommended, although not necessary to use this material, for those who want to teach these subjects.

We continue by developing the core of the project in both chapters, a process that is approached in stages, slowly increasing the difficulty of the required tasks. In this sections not only the results of the scientific work are discussed, but also a number of educational suggestions on how best to use and present the material effectively. And so it is that in section 2.3 the acquired knowledge on rotation curves and spider diagrams are applied to the Solar System first, understanding the basic principles more thoroughly. Then the same approach is applied to spiral galaxies in general, thus generalising the problem and making it applicable to any galaxy we choose to analyse. At the end a concrete example is presented, that of the spiral galaxy NGC3198. In section 3.3 the theme of visualising the effects generated by the phenomenon of gravitational lensing is instead developed. After having introduced the concept of the deflection angle from General Relativity, we see how it is possible to solve graphically and interactively, with the help of Geogebra, the lensing equation for each discussed model. Then computer simulations are created, which make it possible to observe and study the images that are produced by gravitational lensing. In addition, it is offered the possibility of discovering what shape the special plexiglass lenses must have in order to reproduce the same effects observed with the simulations. And finally, gravitational lens effects can be created in the classroom with the lenses that we have designed and produced. At this point it is possible to use these lenses, experiment, test different sources and, why not, play with them, so that the phenomenon is understood as clearly and completely as possible. Practical examples of how to use the lenses are illustrated and discussed. In conclusion both chapters have a short section (sections 2.4 and 3.4) that comments on the results obtained with each project and gathers final considerations on their success.

Finally, in the last chapter (chapter 4) the main points touched upon in the thesis are summarised and general conclusions on the performed work are drawn.

Chapter 2

The Dark Matter Problem

With this project students learn how to calculate the mass of spiral galaxies starting from their dynamics, therefore using radial and rotation velocity. The goal is to show evidence of the hypothetical presence of non-visible matter, the so-called dark matter, while practising and applying many physics and mathematical concepts typical of the last years of secondary school and first years of the undergraduate studies.

2.1 Motivation and Purpose

The dark matter problem is still an unresolved and fascinating issue of modern physics and cosmology. This problem has its origin explicitly in the 1930s, even though there were some ideas already at the end of the nineteenth century, but it started to be prominent only in the 1970s [19]. This hypothetical exotic matter, transparent to any electromagnetic radiation and interacting only gravitationally with the visible matter, is still at the moment not directly detectable. Most of the evidence of its existence, if at all (despite the large acceptance of this theory, the debate is still lively [8][59][21]), comes from the gravitational effects that dark matter has on the motion of matter inside galaxies [89] and clusters of galaxies [119] and on the phenomenon of gravitational lensing [81]. Although in these last decades many projects and experiments are trying to identify (directly and indirectly) the famous dark matter, its nature and distribution remains a mystery [9][7]. Entering into the details of these search programmes and their methodologies is rather complicated. However, simply considering and relying on the first evidence of the "missing matter" issue gives a clear idea of the dark matter problem.

The simplest choice falls on treating the rotation curves of spiral galaxies with the final purpose of calculating their mass. Doing a step forward, we can introduce along with the rotation curves also the diagram of constant radial velocities, the so-called spider diagram. The problem of dark matter, as well as the rotation curves and spider diagrams, are quite complicated to deal with, however, it is fortunately possible to analyse them through a simplified approach. Apart from its intrinsic fascination, the reasons for the choice to address this subject lie in the fact that, in its simplified approach, many subjects treated in physics and mathematics of the last two years of secondary school (k11 and k12) are involved [108][38]. It is also suitable for an undergraduate level thanks to a more advanced implementation concerning mathematical development. Moreover, we should also not forget that this is a current and appealing theme and the fact that the dark matter problem is still an ongoing conundrum renders everything more mysterious and exciting. Finally, all this makes the topic a useful educational tool in physics, mathematics and astronomy teaching with examples from cosmology, which engage and attract many students.

In performing this project, using simplified models, students will retrace the steps that led to the hypothesis that around spiral galaxies a halo of non-visible matter is present. It is an interesting process that will allow students to (hopefully) draw the same conclusions and the achieved results

are comparable with those published in the literature. In addition, thanks to the computer programme Geogebra, students will learn how to visually plot and analyse rotation curves and spider diagrams. It is in fact known that students struggle to interpret graphs of kinematic quantities [71]. However, using simplified representations (which lose the detailed information from real data and the relation with their uncertainties and errors), we enable students to focus their attention on the critical concepts we are trying to teach. Consequently, in this way we stimulate students to reason about how the information given by a graph relates to aspects of the real physical universe [113].

Finally, applying all these concepts to the Solar System first and to stars and gas in spiral galaxies then, students will indeed learn how to extrapolate important information from data and plots and isolate the fundamental elements in order to be able to understand the dark matter problem.

2.2 Background Knowledge

The topics covered, despite their basic form, are sufficient to understand the subject and to carry out this project. However, scattered throughout the text are many references that allow, should anyone wish to do so, for further study of the subject. This in-depth study is not necessary to complete this project, but especially for those who wish to teach these themes, we highly recommend it.

2.2.1 The Dark Matter Problem

The information in this section is elaborated mainly from [94], [59] and [88].

An interesting result arises studying spiral galaxies and galaxies clusters, in particular their dynamics: the presence in the universe of invisible matter. In fact, these objects seem to be composed not only of stars, gas and dust (between around 10% and 20%), but also of a huge amount of hidden matter, the so-called dark matter. This matter reveals its presence only through gravitational effects and its dominance over visible matter is constantly consolidated thanks to the technological advancement of instruments used in radio, optical and X-ray observations. Although there are many theories and possible candidates, what dark matter really is remains a mystery and the unambiguous evidence for its existence is called the *dark matter problem*. To find a solution to the dark matter problem is of central importance not only for astrophysics, but also for fundamental and particle physics. In fact, among various possible candidates, the common idea today is that dark matter consists of a new kind of elementary particle.

During the 1920s the scientific community started to be aware of the existence of our and other galaxies in the universe. Considering a galaxy a compact, gravitationally bound system of stars is a scenario that opens many horizons in studying the motion of these celestial objects. Indeed, at the beginning of the 1930s, Lindblad [60] and Oort [79] compared observations with predictions from Newtonian mechanics of the Milky Way's rotation. This led to the result that, given the visible amount of matter, our galaxy is rotating too fast. Therefore, there seemed to be two to three times more mass than what we can observe. However, the first actual doubts about the coincidence between the distribution of luminous matter and the real distribution of mass in the universe arose in 1933 with Zwicky [119]. According to his theory, the amount of visible mass in some galaxy clusters is not enough for preventing them from falling apart, due to the high velocity of the individual galaxies. Once again we are facing the hypothesis of missing matter and this dark matter, whose name was invented by Zwicky, accounts now for 90% of the total mass of the cluster. Nowadays, thanks to modern observations in X-ray, it is actually possible to include also the big amount of hot gas (more than the mass of stars) between the galaxies in the cluster.

Nevertheless, the total mass exceeds that of the visible mass by a factor of five. Finally, it was after 1970 that the problem of missing matter in the universe started to be largely considered. In fact, in 1970 Rubin and Ford [89] reached the same result of hypothesising significantly hidden matter, this time analysing the rotation curve of the Andromeda galaxy (M31). And after that also for many other spiral galaxies the presence of a halo of dark matter was confirmed (there is also around elliptical galaxies, but estimating its presence is far more complicated) which extends well beyond the visible edge of the galaxy and accounts for between 80% and 90% of the total mass.

Besides its detection, the real challenge is to understand what the dark matter consists of. We only know that it is a kind of matter that does not emit or absorb light and interact with the visible mass only through gravity. Therefore, from an astrophysical perspective and starting with ordinary baryonic matter, the prime candidates were MAssive Compact Halo Objects (MACHOs), such as white dwarfs, brown dwarfs, rogue planets, black holes and similar objects. In the 1990s, projects like MACHO, OGLE and others searched for these objects, but the result was that MACHOs account only for a small fraction of the missing matter, therefore not enough to be the famous dark matter. Then, from a particle physics perspective, it was the turn of non-baryonic matter as candidate. The subatomic particles we are searching are electrically neutral, stable, have mass and possibly interact only weakly (weak nuclear force). Neutrinos could be good candidates, but they would constitute hot dark matter and according to simulations the large-scale structure of the universe would be very different from ours. Indeed, studies about our large-scale structure are strongly in favour of cold dark matter, namely heavy slow particles with smaller mean free path than neutrinos. Since the physical nature of these particles is unknown, they are called Weakly Interacting Massive Particles (WIMPs).
Now, if WIMPs exist, there are three methods for detecting them: direct, indirect or creating them. Several projects are trying to detect WIMPs directly. Such detectors are deep in the underground, shielded from cosmic rays, and use many different modern technologies (for instance solid state, bubble chambers, scintillator and others) that should interact with WIMPs. The indirect approach instead considers also the possibility of the existence of dark matter antiparticles. When these encounter the dark matter particles, they should annihilate making them visible (gamma rays or electron-positron pairs). Unfortunately, both these ways have disagreements between various experiments. Therefore, the best option left is to create the dark matter particles in large particle accelerators, but for the moment this is not the case.

Among all this evidence and methods, the simplest approach for students to understand this topic is through the analysis of rotation curves of spiral galaxies. It is important to underline the fact that the chain of reasoning is conceptually complex for students because they need to understand the physics behind expected and observed rotation curves and the related implications. However, studies in physics education reveal that accompanying explicit lecture-based instruction with research-validated activities makes the way of teaching this chain of reasoning very efficient. In particular, this method helps students to built knowledge by themselves, a process which always gives the best result [113]. This project is therefore based on this approach and method, it will moreover be performed under appropriate simplifications and approximations and with the interesting and new implementation of the spider diagram.

2.2.2 Newton's Shell Theorem

The real distribution of mass of a typical spiral galaxy is quite complex, however if we consider a strongly simplified model, understanding this object and its properties becomes more simple and accessible [94]. Therefore, for educational purposes we always use simplifying approximations and we treat the galaxy as a spherically symmetric gravitating object. This is not what we normally see on the celestial sphere, namely the visible, luminous mass, but this approximation is not totally far from reality if we consider that galaxies are surrounded by a nearly spherical galactic halo which

consists of globular clusters, old stars and gas (Fig. 2.1) [94]. This halo should not be confused
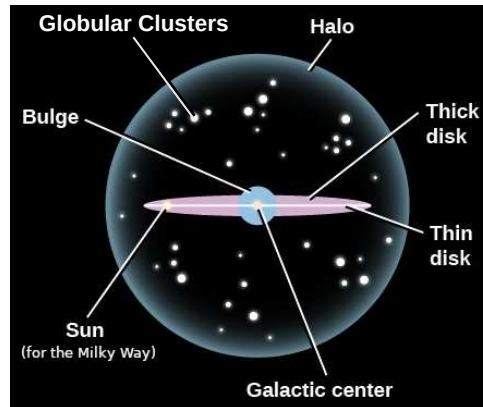

Figure 2.1: Structure of a spiral galaxy. The surface brightness of the galaxy (the measure of brightness per area on the sky expressed in mag/arcsec^2) is higher in the bulge, then comes the disk. The galactic halo instead has a very low surface brightness due to the very small presence of stars. Credit: `courses.lumenlearning.com/astronomy`.

with the dark matter halo component, which is an extra component and much more extended, but at the actual state of the art we have no clue of it yet. Therefore, this approximation allows the very useful Newton's shell theorem to be applied for this analysis [50]. Although it is not considered very relevant in schools today, this theorem is of great importance for understanding gravitation and electrostatics [61]. Moreover, it can be used alone as an exercise in the context of Newtonian gravitation.

In the prepositions 70 and 71 of his Principia (1687), Newton gave proof of the fact that an external body of mass m is attracted by a spherically symmetric distribution of mass M as if all the mass M were concentrated at the distribution's centre C. Moreover, if it happens that there is
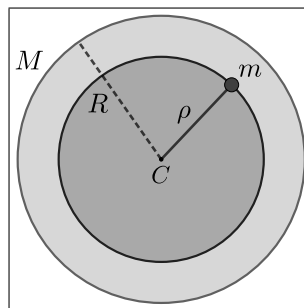
Figure 2.2: Representation of a point-mass m situated inside a spherical distribution of mass M. According to Newton's shell theorem, only the mass of the sphere with radius $R \leq \rho$ acts gravitationally on the point-mass.

a shell of mass at a distance greater than that of the position of the body m with respect to this centre, as illustrated in fig. 2.2, this external mass does not act gravitationally on m.
In the literature we can find many different approaches to this theorem. They are mainly based on the geometry of the system, but the execution can involve different aspects and properties. Now we only present the method that we consider the easiest and in appendix A another common approach of slightly increased difficulty is introduced. Furthermore, in order to really understand this theorem, it is necessary to divide the analysis in small parts and introduce new elements step by step.

2.2.2.1 Gravitational Potential Energy Analysis

This is one of those cases in which an energy analysis is simpler than others [54][10], nevertheless it is common experience among teachers that students continues to prefer other methods, for example the forces analysis [70][93] (see appendix A). The reason for this probably lies in the fact that the concept of force is intuitively simpler and more verifiable in everyday experiences. Nonetheless, we start with the simplest approach, then it will be the teacher's task to direct the student's attention to the preferred method.

Following a step-by-step reasoning, the discussion starts considering a spherically symmetric hollow shell of total mass M and a test point-like body of mass m. The point-mass m can be positioned outside or inside the shell giving us the possibility of studying the implications of its position. We imagine now that the hollow shell M is divided into many rings of very small angular thickness $\Delta\theta_i$ (not to be confused with the height of the ring). Our first goal is to calculate the gravitational potential energy of the system composed of one such a ring, the ith ring (the one in green in fig. 2.3), and the point-mass m at a distance ρ away from the centre of the sphere of radius R.[1] In fig. 2.3 we see the point-mass m positioned outside the spherical shell, however the same reasoning is applied when it is inside. To calculate the gravitational potential energy, we
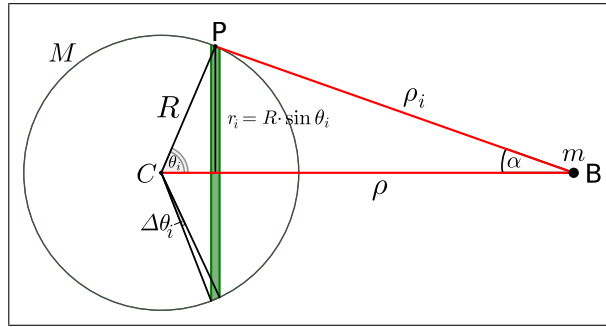
Figure 2.3: 2D-representation of the system composed of a spherically symmetric hollow shell of total mass M and a test point-like body of mass m distant ρ from the centre C of the sphere and ρ_i from the ith ring (shown in green).

consider the mass of the ith ring, $M_i = \Sigma \cdot 2\pi r_i \cdot R\,\Delta\theta_i$ with Σ its constant surface mass density ($[\Sigma] = \frac{\text{kg}}{\text{m}^2}$), and the mass m of the point-mass according to

$$U_i = -G\,\frac{M_i \cdot m}{\rho_i} = -G\,\frac{\Sigma \cdot 2\pi R^2 \cdot \sin\theta_i\,\Delta\theta_i \cdot m}{\rho_i}\;, \tag{2.1}$$

where $R \cdot \sin\theta_i$ is expression of the radius r_i and G is, as usual, Newton's gravitational constant.[2] The next steps aim at simplifying eq. (2.1). This is achieved by eliminating the index i as much as possible and introducing the distance ρ, which remains constant. In fact, applying now the law of cosines[3] to the triangle $\triangle CBP$ (Fig. 2.3) and considering the ring's thickness, so that we have $\rho_i \pm \frac{1}{2}\Delta\rho_i$ and $\theta_i \pm \frac{1}{2}\Delta\theta_i$, after few simple steps we obtain

$$\rho_i\,\Delta\rho_i = 2\rho R \cdot \sin\theta_i \cdot \sin\left(\frac{1}{2}\Delta\theta_i\right)\;. \tag{2.2}$$

At this point, using the small angle approximation (since $\Delta\theta_i$ is very small) and introducing the result in eq. (2.1) we get

$$U_i = -G\,\frac{\Sigma \cdot 2\pi R \cdot m}{\rho}\,\Delta\rho_i\;. \tag{2.3}$$

---

[1]Note also that this method is a good introduction to infinitesimal calculus.

[2]Gravitational constant $G = 6.674 \cdot 10^{-11}\,\frac{\text{m}^3}{\text{kg}\cdot\text{s}^2}$.

[3]$\rho_i{}^2 = \rho^2 + R^2 - 2\rho R \cdot \cos\theta_i$, this is a generalisation of the Pythagorean theorem, for a detailed explanation see [3] or search in any trigonometry textbook.

For the total gravitational potential energy of the entire spherical shell, it is necessary to sum[4] the contributions of all rings $U = \sum_i U_i$. Thus, the solution to this problem focuses on solving the summation $\sum_i \Delta\rho_i$. Precisely at this point, the ease of this summation gives us the main reason to choose energy analysis as the simplest approach, besides the fact that we don't need to consider angles, which we should have done in the case of vector algebra for force components. In particular, solving this summation means to understand which of all the distances between m and the various rings are the longest and the shortest, respectively in the two cases with the point-mass outside and inside the spherical shell. The situation is shown in fig. 2.4. Since $\Delta\rho_i$
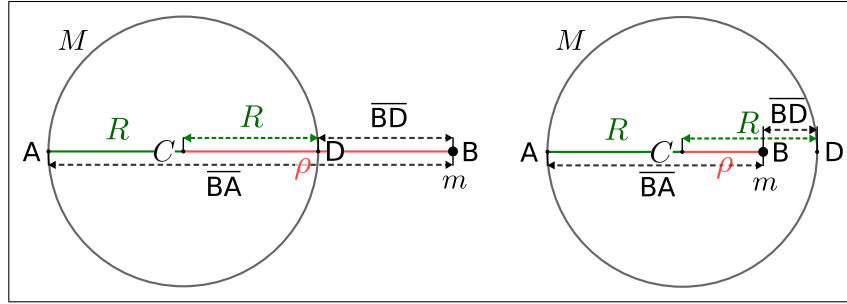
Figure 2.4: Representation of how ρ_i varies, in relation to ρ and R, in its minimum $\rho_{i,\min} = \overline{BD}$ and maximum $\rho_{i,\max} = \overline{BA}$ distance from the sphere's rings. On the left m is in position B outside the sphere, on the right inside the sphere.

is the difference between two consecutive ρ_i, adding up this difference for all ρ_i (namely $\sum_i \Delta\rho_i$), pairs of them cancel each other out leaving finally only the difference between the maximum and the minimum ρ_i. Therefore, for the two cases we have:

- $\sum_i \Delta\rho_i = \rho_{i,\max} - \rho_{i,\min} = (\rho + R) - (\rho - R) = 2R$ with $\rho \geq R$

- $\sum_i \Delta\rho_i = \rho_{i,\max} - \rho_{i,\min} = (\rho + R) - (R - \rho) = 2\rho$ with $\rho < R$.

Specifically, since the mass of the entire shell is $M = \Sigma \cdot 4\pi R^2$, the potential energy of a point-mass in the gravitational field of this hollow sphere is given by

$$U(\rho) = \begin{cases} -G \, \frac{M \cdot m}{\rho} & \text{if } \rho \geq R \\[2ex] -G \, \frac{M \cdot m}{R} = \text{const} & \text{if } \rho < R \, . \end{cases}$$

(2.4)

Interestingly, the potential energy depends only on the distance ρ for $\rho \geq R$, exactly as if all the mass of the sphere were concentrated at its centre. On the contrary, for $\rho < R$ the potential energy is constant, i.e. independent from the position and no force acts on the point-mass inside. Notably, for the special case $\rho = R$ both solution are actually equal and simultaneously valid.

Let's do another step considering the sphere M full of mass and not empty anymore. The next procedure consists in dividing the sphere in n shells of radius R_α (α goes from 1 to n) one inside the other, like a spherical matryoshka doll. In addition, the surface mass density Σ, constant in every single shell, is not necessarily the same for all of them. Basically, this approach derives from the Cavalieri method [34], which is considered an introduction to integral calculus. Now, if m is positioned outside the sphere M, namely for $\rho \geq R$, we sum the contribution to the potential energy of each of the n shells of mass M_α. Therefore, in the upper eq. (2.4) the term

---

[4]The symbol of summation $\sum_i$ should not to be confused with the surface mass density Σ.

$M_{\text{tot}} = \sum_{\alpha=1}^{n} M_\alpha$ should appear instead of simply M. This is nothing more than the total mass of the full sphere and the potential energy results once more dependent exclusively on the distance ρ as if all the mass of the sphere were concentrated at its centre.

However, if m is positioned inside the sphere M, with $\rho < R$, we consider the layer outside m as a hollow sphere whose mass is given by the sum of the masses of the shells forming it. Therefore, for this part the potential energy, as we know, is constant (lower eq. (2.4)). Instead, considering the inner shells, the situation corresponds to the case just seen where m is external to a sphere full of mass and so the same conclusions apply. This in fact brings us back to the basic idea that only the mass inside the radius ρ acts gravitationally on the point-mass under consideration.

For an approach suitable for more advanced or undergraduate students see appendix B.

2.2.3   Projections on the Sky Plane and Radial Velocity

In this section, the key point is how much we can actually rely on what our eyes see of a spiral galaxy. Regarding this, the geometry of projections plays an important role when speaking of observations of extended objects in the universe. In fact, because of the large distances involved, 3-dimensional objects appear as 2-dimensional parallelly[5] projected images on the plane tangential to the celestial sphere, named sky plane. Everything that is observed or measured in the sky is seen on this plane. Therefore, it is necessary to take this aspect into account together with all the consequences, for example when measuring velocities. Luckily, there are clear and known geometrical rules to understand these effects. In particular, the projection on the sky plane of a spherical mass distribution is a disk, as in the case of planets, stars, galaxy bulges and so on. On the other hand, when we consider the projection of mass distributed on a disk, such as the disk of a spiral galaxy (assuming it is axially symmetrical), the final result depends on the inclination angle i of the disk with respect to the plane of the sky. In fact, we will see a disk if $i = 0°$, therefore observed face-on, an ellipse, the more eccentric the more the galaxy is inclined, if $i > 0°$, arriving at the extreme case of a galaxy seen edge-on ($i = 90°$) of which we see only the edge. A summary of these configurations is shown in fig. 2.5.
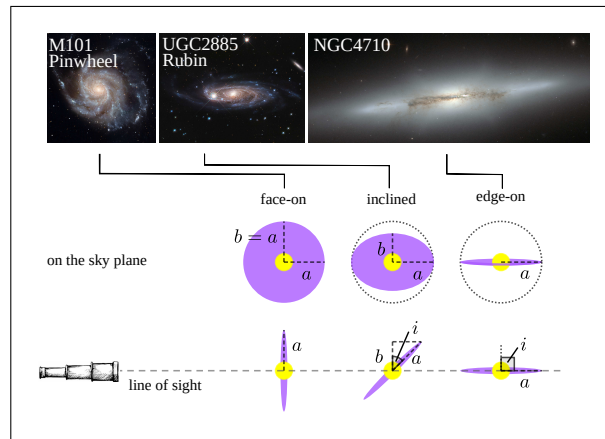
Figure 2.5: Different orientations of a spiral galaxy respect to the sky plane ($i = 0°$, 45°, 90°). The observer sees the galaxy images projected on this plane. Pictures' credit: ESA/NASA/STScI.

Since the galactic halo has a too low surface brightness to be observed in distant galaxies, our attention when analysing and measuring the motion of stars and gas in spiral galaxies lies in the disk. Therefore, the first concept to convey is that a disk or a circle, randomly inclined at an angle i with respect to the sky plane, is seen as an ellipse whose semi-major axis is equal to the unchanged radius of the circle $a = r$. Figure 2.6 illustrates this idea. This diagram is very

---

[5]Given the large distances involved, we can consider the projection not only parallel, but in particular orthogonal.

useful in explaining this effect because, since it is produced with Geogebra in 3-dimensions, it is possible to rotate it and look at the situation from literally every angle. Nevertheless, only this image is sufficient to illustrate the problem. Essentially, the circle in green of radius r on the
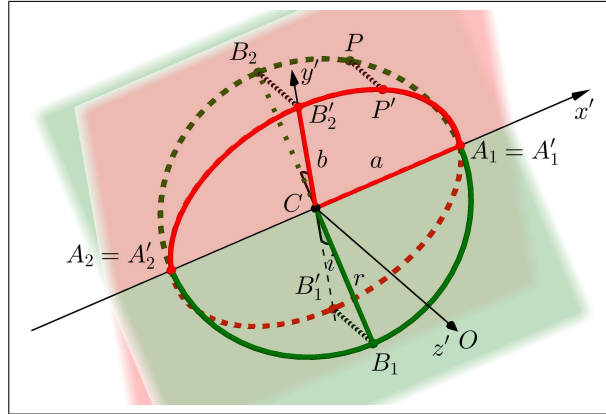

Figure 2.6: A spiral galaxy, schematically represented by the circle on the galaxy plane (both in green), inclined of an angle i with respect to the sky plane and its projections on this, represented by the ellipse (both in red).

galaxy plane represents a spiral galaxy disk whose stars and gas lie on the same plane and rotate circularly around the centre C. Far along the z'-axis the observer in O sees the sky plane, since it is perpendicular to the line of sight, and the ellipse in red with semi-major axis a and semi-minor axis b. Thanks to the large distance between observer and galaxy, it is moreover possible to consider in good approximation the lines $\overline{CO}$, $\overline{B_1 B_1' O}$, $\overline{B_2 B_2' O}$ and $\overline{PP'O}$ parallel to the line of sight. Thus, from the figure it is easy to infer that

$$r \cdot \cos i = a \cdot \cos i = b . \tag{2.5}$$

At this point, observing the two graphs in fig. 2.7, separate representations of the galaxy and sky planes, we can see that on the galaxy plane the position of the point P on the circle of radius r can be expressed through its polar coordinates $x = r \cos \theta$ and $y = r \sin \theta$. On the sky plane, instead, the position of its projection P' is described by $x' = r' \cos \theta'$ and $y' = r' \sin \theta'$. Given
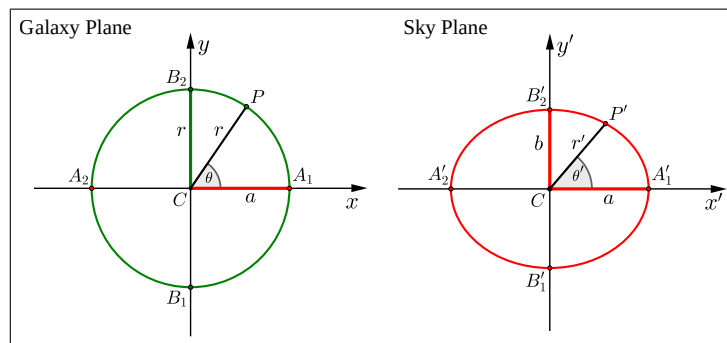
Figure 2.7: Diagrams showing the situation from figure 2.6 separately in the galaxy plane and in the sky plane.

that with parallel projections all lines parallel to the plane of projection remain unchanged, like for instance the semi-major axis a, we deduce that in our configuration this is true for all the x-coordinates, thus $x = x'$. For the y-coordinates, being not parallel to the plane of projection, this is not valid, so generalising eq. (2.5) we obtain $y' = y \cos i$. Expressing these properties in

polar coordinates we get

$$r' \cdot \cos \theta' = r \cdot \cos \theta \tag{2.6}$$
$$r' \cdot \sin \theta' = r \cdot \sin \theta \cdot \cos i \ . \tag{2.7}$$

In other words, if we want to project the circle described by $x^2 + y^2 = r^2$ according to the parallel projection rules, we end up with

$$x'^2 + \frac{y'^2}{\cos^2 i} = r^2 \ , \tag{2.8}$$

which is obviously an ellipse.

In order to be able to convert measurements between sky plane and galaxy plane[6] we need to finally take the ratio of equations (2.7) and (2.6) which leads to

$$\tan \theta' = \tan \theta \cdot \cos i \ . \tag{2.9}$$

In the next part the orbital velocity is taken into account and the effect that the parallel projection has on its measurement is analysed. Thus, keeping in mind now fig. 2.6, it is possible to imagine that the point P is rotating anticlockwise around the circle centre C with a certain orbital velocity v, constant in modulus. Since the distance galaxy-observer is very large, what can be measured, i.e. the radial velocity v_r, is actually the component of the rotation velocity parallel to the line of sight. The component perpendicular to this is instead the tangential velocity v_t. This means that the observer in O measures the variation of the position of P with time (towards or away from him/her) along the z'-axis. In particular, such measurements are performed mainly on stars and gas in the galaxy with spectroscopic methods [94], involving the spectrum detected from these objects.

We start discussing now two special cases with help from fig. 2.8. Actually, in the original diagram file, it is possible to move the point P on the circle and observe how the components of the rotation velocity vary with time, making it a successful tool for explaining this topic with the use of a visualisation. Firstly, we direct our attention to when the inclination angle is $i = 0°$, namely when the spiral galaxy is seen face-on. In this situation we cannot detect any radial velocity because the motion of P never has a component parallel to the line of sight. Looking at fig.
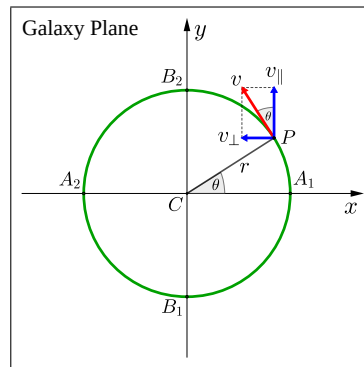
Figure 2.8: Diagram showing the orbital velocity vector v and its components $v_\parallel$ and $v_\perp$ for the point P rotating on the circle of centre C and radius r.

2.8, in fact, the line of sight for this case is the z-axis, which comes out from the page. If the

---

[6]It is important to remember that all what is on the sky plane is measurable, but the inclination angle and what is on the galaxy plane can be only calculated. Moreover, from an educational point of view, expressing r in terms of measurable quantities is always a good exercise for understanding how these quantities are related. Thus, thanks to equations (2.6), (2.9) and the trigonometric identity $\cos \theta = (1 + \tan^2 \theta)^{-\frac{1}{2}}$ we obtain $r = r' \sqrt{\cos^2 \theta' + \frac{\sin^2 \theta'}{\cos^2 i}}$.

galaxy is instead seen edge-on with $i = 90°$, we can decompose the rotation velocity v into its components, one parallel to the y-axis (now the line of sight), $v_\parallel$, which represents the measurable radial velocity, and the other perpendicular to it, $v_\perp$. From fig. 2.8, it is then easy for this specific case to define the radial velocity as

$$v_r = v_\parallel = v \cdot \cos\theta \ . \tag{2.10}$$

This equation describes the radial velocity of P for each of its positions on the circle. In fact, it is clear that in B_1 and B_2 the entire rotation velocity is perpendicular to the y-axis, $v = v_\perp$, and in A_1 and A_2, on the contrary, the entire rotation velocity is parallel to the y-axis, $v = v_\parallel$. However, when the angle of inclination i is not one of these extreme cases, the situation is slightly more complicated.

Basically, in these other configurations it is necessary to consider how the inclination affects our measurements. This means that we don't measure the total component of the rotation velocity parallel to the y-axis, $v_\parallel$, but its projection along the line of sight, as shown in fig. 2.9. The radial
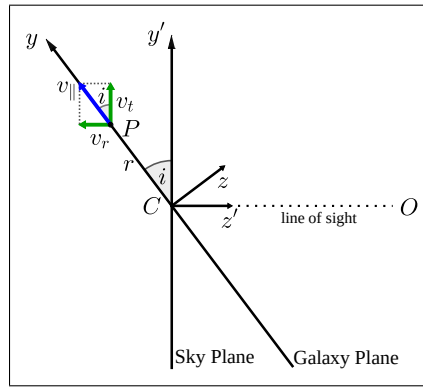
Figure 2.9: Side view of the galaxy plane tilted at an angle i with respect to the plane of the sky. The line of sight is here the z'-axis. Highlighted are the rotation velocity component parallel to the y-axis, $v_\parallel$ (blue), and for this latter its radial, v_r, and tangential, v_t, components (green).

velocity is therefore expressed by its general form

$$v_r = v_\parallel \cdot \sin i = v \cdot \cos\theta \cdot \sin i \ , \tag{2.11}$$

which describes any possible situation, including the already-seen extreme cases.[7]

2.2.4 Rotation Curve

A rotation curve is the graphical visualisation of the orbital or rotational velocity $v(r)$ of objects in a gravitationally bound rotating system as function of the distances r from the system's centre or axis of rotation.

This is the case for instance of planetary systems and spiral galaxies. For the Solar System it is possible to measure the orbital velocity of planets, for galaxies stars and gas are instead used as tracers. Before starting to discuss these systems, it is important to say that we always use circular orbits in our simplified models. In fact, we have already seen that this is a good approximation as far as spiral galaxies are concerned. But it is also a good approximation for the Solar System, in fact the eccentricity of its planets' orbits is so small that we can consider them practically circular. Moreover, in order to keep our model as simple as possible and to fit measurements taken on the disk of spiral galaxies, all orbits are considered lying on the same plane. At this point, for

---

[7]As we did for r, we can now express v in terms of measurable quantities obtaining $v = v_r \frac{\sqrt{\cos^2 i + \tan^2 \theta'}}{\cos i \cdot \sin i}$.

drawing the rotation curve of these systems, we derive the equation expressing the rotation velocity of their components with respect to the radius of the various orbits r. In particular, equalling the centripetal force of circular motion, $F_c = mv^2(r)/r$, to the Newtonian gravitational force $F_g = GmM(r)/r^2$, which in the universe keeps rotating objects on their orbits, we get for the rotational velocity

$$v(r) = \sqrt{\frac{GM(r)}{r}} \ . \tag{2.12}$$

Of course Newton's shell theorem applies, therefore only the mass inside the radius of the rotating object we observe acts gravitationally on it. The quantity of mass inside this radius depends on how the mass is distributed inside the system and this defines also the shape of the curve. In this regard, in fact, if we consider a spherical solid body of radius R_B, total mass M_B and constant mass density σ_B, which, according to observations, is a good approximation for the bulge of a spiral galaxy, we can calculate the mass at any intermediate radius r from $\frac{M(r)}{r^3} = \frac{M_B}{R_B^3}$. Now, from this equation and eq. (2.12) we easily see that the rotation velocity is expressed by

$$v(r) = \sqrt{\frac{GM_B}{R_B^3} \cdot r^2} \ . \tag{2.13}$$

This represents a wheel-like rotation in which the velocity grows linearly with the radius $v(r) \sim r$, as shown in fig. 2.10. Analysing instead a different system in which most of the matter M_B is
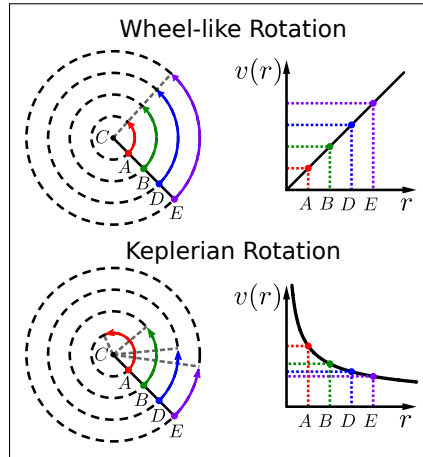
Figure 2.10: Diagrams representing different cases of orbital velocity. Above: Solid-body-like rotation, where $v(r)$ linearly increases with the distance r. Below: Planet-like circular motion, where $v(r)$ decreases as $r^{-1/2}$.

concentrated in its centre, we can say that outside the central area the mass remains constant $M(r) = M_B = $ const. We can therefore calculate right away the orbital velocity to be

$$v(r) = \sqrt{\frac{GM_B}{r}} \ . \tag{2.14}$$

This describes nothing more than the Keplerian planet-like or differential orbital motion (Fig.2.10), where the bigger the orbit is the slower the objects rotate, in fact $v(r) \sim r^{-1/2}$. Regardless of whether it is the Solar System or a spiral galaxy, this behaviour is exactly what we expect from the rotation curve. In fact, as we know, the Solar System has 99.8% of the mass concentrated in the Sun. However, the same can be said for a spiral galaxy if we consider the appearance of the distribution of the visible, luminous mass, which is mostly concentrated in the central bulge. Contrary to our expectations, though, this is not what is detected by observations of spiral galaxies' rotation curves,
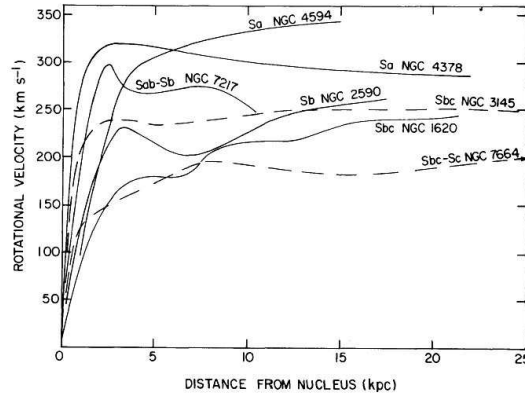
Figure 2.11: Examples of rotation curves of spiral galaxies. Credit: [90].

as it is clear form the examples in fig. 2.11. Basically, from measurements on spiral galaxies for $r \geq R_B$, namely outside the bulge, the rotation velocity remains approximately constant and equal to $v(r) = \sqrt{\frac{GM_B}{R_B}} = v_B$, thus the rotation curve is flat. These measurements are performed till very far away from the luminous, visible border of galaxies and even from the galactic halo edge, but the rotation curves continue to appear flat. It is believed, according to results from simulations, that eventually at a radius 10 times bigger than the galaxies' visible radius, we could encounter the so called keplerian decline [117]. However, we are not yet able to see so far away from the galaxies' centre because our spectroscopic measurements are mainly connected with observations of the 21cm emission of HI, which gives us an inferior limit for the radius of the dark halo of $30\,h^{-1}\,\mathrm{kpc}$ [94].[8]

What is really interesting about the behaviour of the spiral galaxies rotation curve is the meaning of this curve which remains flat till very large radii. As we will see in detail in section 2.3.3, this phenomenon could mean that there is much more mass in this region than we can actually see. Essentially, it is a huge halo of dark matter of still undetermined outer edge, which acts only gravitationally on the visible mass. Additionally, in this system the mass cannot be considered mainly concentrated in its centre anymore and we have to review our assumptions. Of course this is not the only hypothesis approached to solve the discrepancy between the expected rotation curve with Keplerian decline, suggested by the observed distribution of mass, and the actual detected flat rotation curve. Other ways to explain it are explored, for example considering the Newton's laws of motion and gravity in need of a modification. However, at least for the moment, the existence of a type of matter which is invisible remains the most accepted theory [59].

2.2.5   Spider Diagram

A spider diagram is a representation of the velocity field of gravitationally bound rotating systems. Specifically, it is the graphical visualisation of contours of constant radial velocity v_r of the observed object. Its name *spider diagram* comes from the fact that this kind of diagrams resembles the shape of a spider.

The radial velocities plotted in this graph are measured on the galaxy disk thanks to the Doppler effect using spectroscopy and of course considering the eventual inclination of the disk [94]. The luminous tracers are mainly stars and HI gas and especially this last, as we saw in the previous section, permits to analyse the velocity field at larger radii than the stellar disk. There are methods which enable to look even further, using for instance the motion of satellite galaxies, but to analyse their motion is much more complicated and the associated uncertainties are bigger [94]. Therefore, for our educational purpose, treating such difficult approaches has no sense and we

---

[8]h is the scaled Hubble constant defined as $H_0 = h \cdot 100\,\mathrm{km\,s^{-1}\,Mpc^{-1}}$. Note that $1\,\mathrm{pc} = 3.09 \cdot 10^{16}\,\mathrm{m}$.

limit our analysis to measurements of HI gas. At this point, we need to consider that the velocity we measure can consist not only of pure rotation, but also of other kinds of motion. In this regard, we add an extra term in the radial velocity equation, the so-called systemic velocity, v_{sys}. Consequently, eq. (2.11) is actually more complete if expressed by

$$v_r = v_{sys} + v(r) \cdot \cos\theta \cdot \sin i . \tag{2.15}$$

Basically, the systemic velocity includes the recessional velocity, v_{rec}, due to the expansion of the universe (Hubble flow) and eventually some peculiar velocities, v_{pec}, produced by other gravitationally bound galaxies. It is moreover important to remember that the measured radial velocity obeys the rules of parallel projection seen in section 2.2.3. Thus, only the velocity's components parallel to the line of sight can be measured. Ultimately, the starting point of our project could consist of measurements of the radial velocity field of a galaxy and its visualisation through a spider diagram. This, together with the geometry of the system and eq. (2.15), permits to calculate the orbital velocity and draw the corresponding rotation curve.

An example of a spider diagram is shown in fig. 2.12 for the galaxy NGC5033. As we can see from
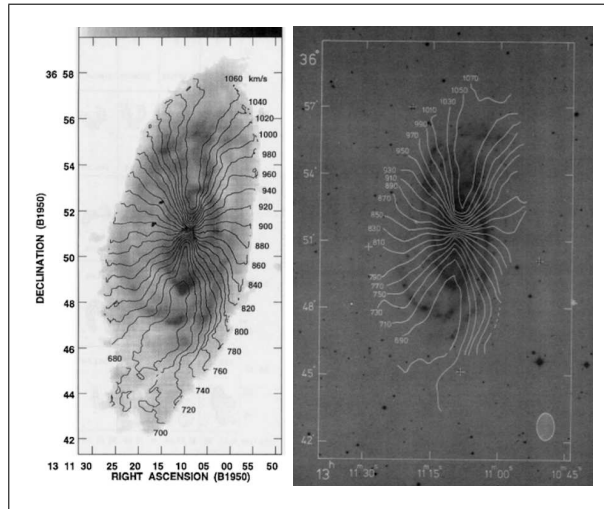
Figure 2.12: Spider diagram of the galaxy NGC5033 superimposed on the distribution of HI (Left – Credit: [107]) and on a black-white image of the galaxy (Right – Credit: [11]).

this figure, when working with galaxies it could be particularly useful to superimpose the plot on an image of the galaxy's distribution of HI or of the observed object. In fact, this enables us to better understand where the iso-velocity lines are and how they are connected with other galaxy's components. Now, if we look carefully at the spider diagram, we can distinguish three different concentric regions:

- the central part, which corresponds to the bulge area, is defined by almost-straight lines. The central line lies along the ellipse's minor axis and the corresponding radial velocity expresses the pure systemic velocity, v_{sys}, with respect to the observer.

- The next region, which corresponds to the region with constant rotation velocity $v(r) = v_B = $ const, has lines distributed radially away from the center. As expected from eq. (2.10), the more the angle θ decreases, i.e. the further away from the minor axis we go, the higher the modulus of measured radial velocity is until it reaches its maximum value along the major axis of the ellipse. In fact, along this axis we have the greatest deviations of the radial velocity from the systemic velocity.

- There is another region that can be encountered. In this part, the lines, starting from the extreme on the major axis, close on themselves. This is the case if it happens that the

rotation velocity declines. Nevertheless, as we already know, the true Keplerian decline at the edge of the galaxy's dark matter halo has not yet been found by measurement.

Now that all the key elements for understanding these topics are presented, we can get to the heart of the issue. In fact, we will retrace the path that leads to the hypothesis of the existence of dark matter in the universe.

2.3   Inferring the Presence of a Dark Matter Halo in Spiral Galaxies

This part of the project is performed step by step starting with the exploration of the notions discussed so far, firstly in the framework of the Solar System, then applying them theoretically to a spiral galaxy and finally to the example of the spiral galaxy NGC3198.

Every separated step can be used in class as exercise to practise specific topics of physics and mathematics applied to a real problem. For instance, among others, plane trigonometry, the Cavalieri approach to integration, forces, Kepler's laws of motion, Newton's laws of motion and gravitation, orbital motion, together with notions of kinematics and dynamics. All together instead, these steps create a student project that, through increasing degrees of difficulty, guides them through the discovery of the evidence that led to the hypothesis of the existence of dark matter. In this way, after a proper introduction, the process of conceptual building is valuably stimulated and enhanced [113]. The project is based on complex cosmology and astrophysics principles and examples, but in this simplified approach it uses and applies important basic concepts. It also addresses an ongoing problem, something that fascinates students and may inspire them to be part of the future generation of physicists engaged in solving it.

2.3.1   The Solar System's Rotation Curve

This type of discussion involves the dynamical analysis of the gravitationally bound rotating system we have chosen to study. The most appropriate and easy candidate to start with is the Solar System whose Sun has mass $M_\odot = 1.99 \cdot 10^{30}$ kg. In this respect, it is possible to set the exercise in two different ways according to what we want to achieve:

- The first approach uses the real data[9] on the mass of the Solar System planets in table 2.1, combined with the radius of the various orbits, to derive the orbital velocities and draw the corresponding rotation curve.

- The second approach starts with the rotation curve of the Solar System, from which the orbital velocities of its planets are derived. These, together with data on the radii of the various orbits, provide important information on the amount and distribution of mass, which will rightly be concentrated in the Sun.

Both of these methods require applying the relations of Newtonian dynamics that we have seen in section 2.2.4, including the notions of Newton's shell theorem from section 2.2.2. However, since this is actually the same approach carried out in the second case in reverse, we only show the first one here.

Considering eq. (2.12),[10] it is easy to see that it describes the relation between velocities, distances from the centre of the system and mass inside each orbit. Therefore, introducing the

---

[9]The data for the Solar System used in this project are available at `https://solarsystem.nasa.gov/solar-system/our-solar-system/overview/` and `https://nssdc.gsfc.nasa.gov/planetary/planetfact.html`.

[10]Interestingly, if the orbital period P is introduced, this equation is nothing more than Kepler's third law of motion for circular orbits, $P^2 = \frac{4\pi^2}{GM_\odot} \, r^3$.

	MERCURY	VENUS	EARTH	MARS	JUPITER	SATURN	URANUS	NEPTUNE	PLUTO
Mass (10^{24}kg)	0.33	4.87	5.97	0.64	1898.19	568.34	86.81	102.41	0.01
Distance from Sun (10^6km)	57.91	108.21	149.60	227.92	778.57	1433.53	2872.46	4495.06	5906.38
Orbital Velocity (km/s)	47.36	35.02	29.78	24.07	13.06	9.68	6.80	5.43	4.67
Orbital Period (days)	88.00	224.70	365.20	687.00	4331.00	10747.00	30589.00	59800.00	90560.00
Orbital Eccentricity	0.205	0.007	0.017	0.094	0.049	0.057	0.046	0.011	0.244

Table 2.1: Data for the Solar System planets including Pluto.

data about the radii of the orbits and the related enclosed mass in this equation, we derive the orbital velocity for each planet and consequently the corresponding rotation curve. The results are shown in table 2.2, calculated with the mass of the Sun alone in the first row, $v_1(r)$, and including the planets' mass gradually within the various orbits in the second, $v_2(r)$. This is

	MERCURY	VENUS	EARTH	MARS	JUPITER	SATURN	URANUS	NEPTUNE	PLUTO
Orbital Velocity $v_1(r)$ (km/s)	47.87	35.02	29.78	24.13	13.06	9.62	6.80	5.43	4.74
Orbital Velocity $v_2(r)$ (km/s)	47.87	35.02	29.78	24.13	13.06	9.63	6.80	5.44	4.74

Table 2.2: In the first two rows the orbital velocity for each planet of the Solar System is shown. $v_1(r)$ is calculated with the mass of the Sun only and $v_2(r)$ gradually including also the planets within the various orbits.

to show that the mass of the various planets is negligible compared to that of the Sun, which represents basically the totality of the mass of the Solar System. The results, without including any kind of uncertainties are comparable with the values in table 2.1. Then, representing the obtained velocities as points in a plot $v_1(r)$ vs. r with Geogebra, easily with the command "FitPow", we draw the regression curve of the points in the form of a power law function, which in this case is (provided by Geogebra)

$$v_1(r) = K \cdot r^{-\frac{1}{2}} \tag{2.16}$$

where $K = 36.43 \cdot 10^4 \text{ km}^{\frac{3}{2}}/\text{s}$. We have just obtained the rotation curve in fig. 2.13. It is also
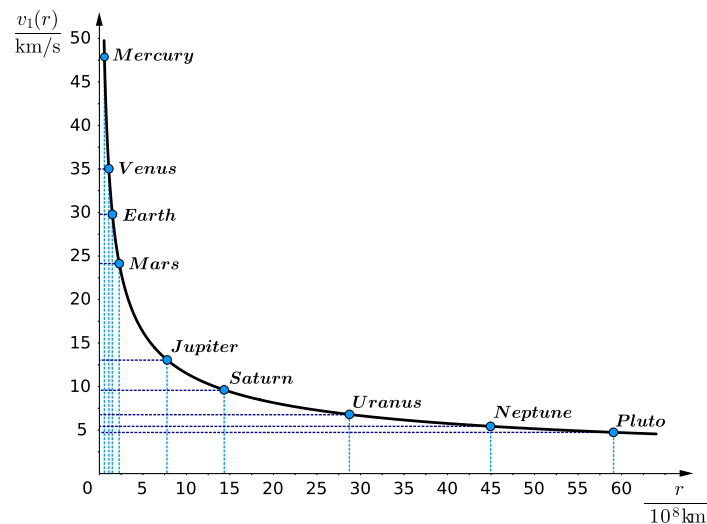
Figure 2.13: The rotation curve of the Solar System as from the data in tables 2.1 and 2.2.

possible to draw this simple graph by hand, but in this project (and in general) we are clearly in favour of and warmly encourage the use of easy-to-use software. Software that has proved to be a very good educational tool and that also manages to involve the students more.

2.3.2 The Solar System's Spider Diagram

The concept of spider diagrams is new in the panorama of physics and astronomy teaching at secondary school level, but it allows basic physics topics to be approached in a more practical way and above all by applying them to a real problem. The aim is to engage students more closely with astronomical topics and at the same time promote longer-term learning and the development of new skills.

In order to better understand this concept, i.e. the graphical visualisation of contours of constant radial velocity v_r, before seeing it applied to galaxies, we analyse and draw it for the Solar System. It is now necessary to imagine an observer outside the Solar System without forgetting that in our simplified system the planets have circular orbits which lie on the same plane. This hypothetical observer has the possibility of moving easily around and inside the solar system, therefore he/she can measure the radial velocity of every planet from different points of view, namely different angles of inclination for the system, and draw the corresponding spider diagrams.

First of all, for drawing the spider diagram the question that needs an answer is: where does the radial velocity remain constant in this system? The answer for the Solar System comes from equations (2.15) and (2.16). This last equation is the numerical solution for the rotation curve of the Solar System calculated from eq. (2.14) and shown in fig. 2.13.[11] Now, establishing for simplicity that for the Solar System $v_{\mathrm{sys}} = 0$ and introducing eq. (2.16) in eq. (2.15) we obtain

$$v_r = K \cdot r^{-\frac{1}{2}} \, \cos\theta \, \sin i \,. \tag{2.17}$$

Basically, switching now eq. (2.17) to Cartesian coordinates ($x = r \cdot \cos\theta$, $y = r \cdot \sin\theta$) and, in order to answer the above question, setting $v_r \overset{!}{=}$ const, after few steps we have

$$y^2 = K^{4/3} \, \frac{x^{4/3}}{(v_r / \sin i)^{4/3}} - x^2 \,. \tag{2.18}$$

For each measured value of radial velocity v_r, this equation describes where this remains constant throughout the entire observed system. This represents in general the contours of constant radial velocity of the Solar System. Important to notice here is that, from eq. (2.11), the term $(v_r / \sin i)$ is the same as $(v(r) \cdot \cos\theta)$, namely the component of the orbital velocity parallel to the y-axis, $v_\parallel$, in the system plane, as in fig. 2.8. This would be in fact the radial velocity measured by our observer positioned in the Solar System plane far away along the y-axis ($i = 90°$, edge-on). This is indeed the radial velocity that on the x-axis ($\theta = 0$), at the extreme point of the orbital radius of each planet, corresponds to the pure orbital velocity $v_r = v(r)$. Clearly, observing from this orientation the observer will never draw a spider diagram, but it is possible to use this information and the data obtained to better understand the velocity field on the system plane. In fact, although unrealistic, since in any case we will never obtain the radial velocity of a rotating system observed face-on, we can thus draw the spider diagram in the system plane. This is done for educational purposes only, however, this visualisation is important for two reasons:

- this is the starting point for drawing the spider diagram of the system seen from every other angle of inclination i,

- superimposing it to a schematic representation of the Solar System seen face-on, we have a general overview of the situation and of which radial velocities our hypothetical observer measures from his/her point of view.

Practically, all this means that with this procedure we define first the lines of constant radial velocity as the lines of constant $v_\parallel$ drawn on the system plane (Fig. 2.14). Then, we need to use

---

[11]Note that the orbital radius is measured in $[r] = 10^8$ km.

again the theory of projections to be able to draw the diagram back on the observed sky plane, inclined of a generic angle i with respect to the system plane.

Teachers and students can directly use the provided diagram of fig. 2.14 from the Geogebra file or draw it easily by themselves using the values for the radial velocity corresponding to the pure orbital velocities for each planet from table 2.2.

To better understand the concept of a constant radial velocity contour we can observe fig. 2.15. This is a detail of fig. 2.14(a) in which, for five planets, the orbital velocities, $v(r)$, and radial

(a) External Planets   (b) Internal Planets
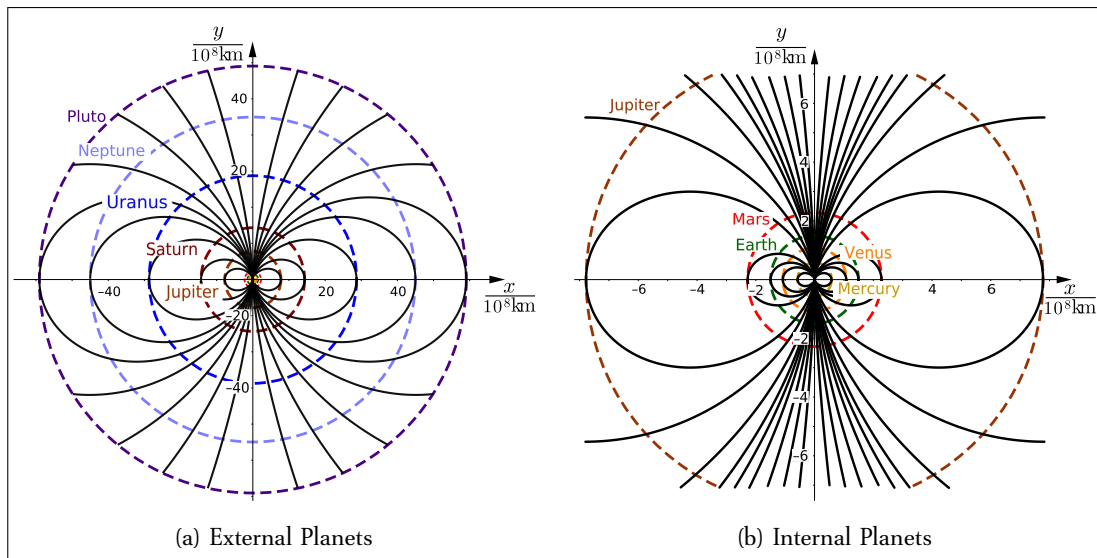
Figure 2.14: Spider diagram for the Solar System in the system plane. It is drawn for the values of the radial velocities measured by the hypothetical observer along the y-axis and then superimposed to the planets' orbits. (a) shows the entire Solar System and (b) is an enlargement of the centre of diagram (a) showing the most internal planets.

velocities, $v_r = v_\parallel$, are introduced as a vector together with the corresponding numerical value. This shows that v_r remains indeed constant along the chosen contour. In fact, starting from the $v(r)$ of each planet, the corresponding v_r is calculated at different points along Pluto's iso-velocity line. This is another simple exercise that helps students understand how the components of vectors change and can be applied to other elements of the graph. But even without involving
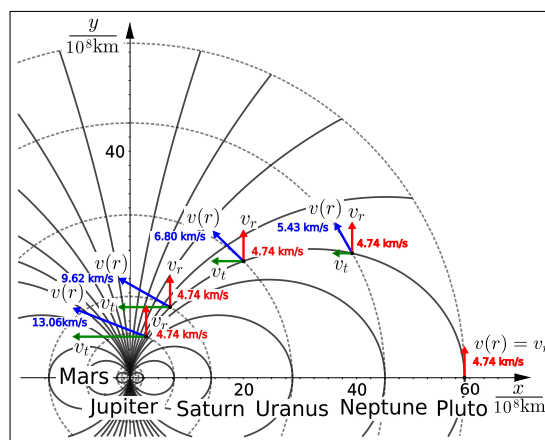
Figure 2.15: Detail from figure 2.14(a) which shows the orbital velocity vectors (blue) for 5 planets and their components. The components in red represent the radial velocities and they are constant along the chosen black line. The components in green are the tangential velocities.

students in these calculations, this visualisation is in itself an excellent teaching tool. In fact, it is

useful just to show the diagram of the original file because by moving the vectors representing the orbital velocity along the orbits, we observe in real time how the radial and tangential velocities vary and can thus compare them.

Now we discover how it is possible for our hypothetical observer to draw the spider diagram of the Solar System when observed under an inclination angle between 0° and 90°. This procedure can be performed for any intermediate angle, we show it here for $i = 60°$. From eq. (2.17), we know that the measured radial velocity v_r in the case of $i = 60°$ is given by

$$v_r = K \cdot r^{-\frac{1}{2}} \, \cos\theta \cdot \frac{\sqrt{3}}{2} \, . \tag{2.19}$$

Now changing to Cartesian coordinates, namely using eq. (2.18), we have

$$y^2 = K^{4/3} \frac{x^{4/3}}{\left(\frac{2}{\sqrt{3}} v_r\right)^{4/3}} - x^2 \, . \tag{2.20}$$

As we can easily predict at this point, the term $v_r / \sin i = \frac{2}{\sqrt{3}} v_r$ in eq. (2.20) restores the measured value for v_r to $v_\parallel = v(r) \cdot \cos\theta$ on the system plane, so we obtain again the spider diagram of fig. 2.14. We can now project on the sky plane the circular orbits of the planets and the lines of constant radial velocity we have just obtained. This is easily done knowing that with parallel projections $x = x'$ and $y = y' / \cos i$. The orbits are therefore now described by eq. (2.8) and the spider diagram by

$$\frac{y'^2}{\cos^2 i} = K^{4/3} \frac{x'^{4/3}}{\left(\frac{2}{\sqrt{3}} v_r\right)^{4/3}} - x'^2 \, . \tag{2.21}$$

The resulting spider diagram is shown in fig. 2.16. In this way we modify the one in fig. 2.14 and in the Geogebra file, using a cursor with values between 0° and 90° for the inclination angle i, we are able to represent all possible spider diagrams, including the one in the system plane.
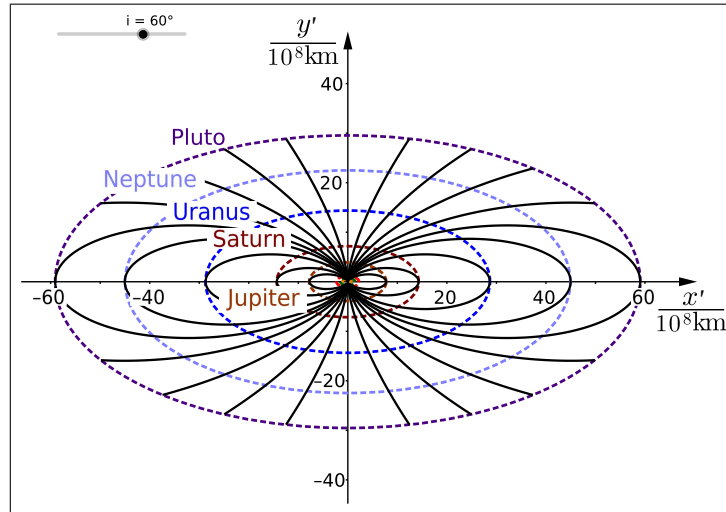
Figure 2.16: Spider diagram for the Solar System as seen in the sky plane inclined of $i = 60°$ (see slider above on the left) with respect to the system plane.

Alternatively, it is possible to reconstruct the exercise in reverse, i.e. as it is normally done in science. This means that starting from a spider diagram like the one in fig. 2.16, we obtain the radial velocities, v_r, measured by the hypothetical observer and we can thus calculate the orbital velocity, $v(r)$, of each planet and draw the rotation curve of the Solar System. We will soon see this kind of exercise in section 2.3.5, applying this procedure to the galaxy NGC3198.

2.3.3   The Rotation Curve of a Spiral Galaxy

This section focuses on the theory of the rotation curve in relation to spiral galaxies. The outcomes of this process can be used as exercises to deepen and broaden student knowledge, to apply and practise basic concepts of physics and mathematics and stimulate the process of concept building. So far we've encountered no evidence of dark matter. This happens because for detecting gravitational effects of dark matter on the dynamics of a rotating system, we need a much bigger quantity of matter. Therefore, we are going now to analyse a bigger system: the spiral galaxy. The results obtained with the work done about the Solar System can serve as comparison for a system without (or negligible) presence of dark matter. In fact, the discrepancy that the students have to analyse and understand, together with the consequences this brings, comes from comparing the expected Keplerian rotation curve, like the one for the Solar System, with the flat one detected for these galaxies. In order to do this and explain how this discrepancy could be interpreted as evidence of dark matter, students must use the dynamics they already learned and be prepared for the idea that probably we cannot trust our eyes alone. Practically, this means that the luminous mass we see is perhaps not an expression of the real mass distribution of this system. So it may be that this system doesn't have most of its mass concentrated in the centre, as we believe when we observe it. This is the information students have to infer while proving that there is evidence here to hypothesize the existence of dark matter.

Let us remember once again that we use simplified models for our analysis and in our simplified model of a rotation curve, we have sharp separation between different sections of the curve and perfectly straight lines or regular functions, as can be seen from fig. 2.17. Naturally, in reality this is not the case. In fact, the galaxy has a complex structure, therefore the transition between sections is smooth (as in fig. 2.11) and the sections themselves reflect the mass distribution gradient of the galaxy, i.e. the lines do not drastically change from one to another and are not so regular [59]. Observing fig. 2.17, there are here three distinct areas: the bulge in red with $r \leq R_\mathrm{B}$
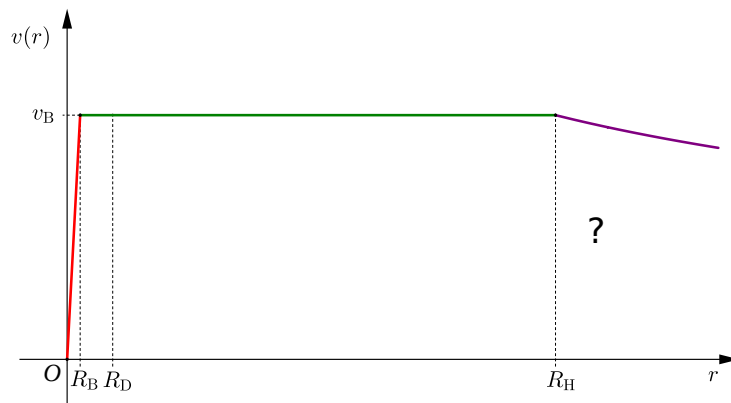
Figure 2.17: Model of a spiral galaxy rotation curve. R_B is the bulge radius, R_D is the visible disk radius and R_H is the halo radius which includes galactic and dark halo. The position of the various radii reflect typical proportions of a spiral galaxy as from the literature [94] [117] [6].

and velocity $v_\mathrm{B}(r)$, the halo in green with $R_\mathrm{B} \leq r \leq R_\mathrm{H}$ and velocity $v_\mathrm{H}(r)$ and eventually the Keplerian decline in purple with $r \geq R_\mathrm{H}$ and velocity $v_\mathrm{K}(r)$. Let's see more in detail the characteristics of the bulge and halo areas and what is the important information that we can extract from this plot. For the hypothetical Keplerian decline, we refer to the work done with the Solar System, as it would fall in the same case, but for a detailed explanation see appendix C.
Also in this case the reasoning we are going to see now can be done in reverse, ending up with the rotation curve as a result. However, we find more efficient, in terms of education, to analyse the curve first, infer the important information from it and understand the related consequences for

the analysed system. Moreover, this approach is very close to the true story of how the hypothesis of the existence of dark matter arose and to retrace the steps of important scientific discoveries is always educationally very interesting.

2.3.3.1   The Bulge

Since in the bulge section we are dealing with a wheel-like rotation described by eq. (2.13), we already know that we are facing the rotation of a solid body with constant mass density. In order to prove that we are really facing this kind of body and understand what such velocity behaviour implies for its mass and mass distribution, the easiest approach we can use comes from the Cavalieri method we saw in section 2.2.2. We apply the procedure to this section of the rotation curve even though it would not really be necessary, because the properties of this type of rotation have already been explored. However, for didactic reasons and to better understand the technique, we start with this well-known case and then proceed with the halo.

Analysing the rotation curve for $r \leq R_B$, the only available information is that the rotation velocity $v_B(r)$ is proportional to the radius r. Consequently, we can set

$$v_B(r)^2 = G\frac{M_B(r)}{r} \overset{!}{=} b \cdot r^2 \tag{2.22}$$

and b is a constant. We make then the assumption that the mass density profile should be in the power-law form $\sigma_B(r) = a \cdot r^k$, where a and k are also constants. Such an assumption comes as result of observations in particular of our galaxy and of the Solar System [94], therefore we suppose that a power law can fit also the mass density of every other spiral galaxy. Now the bulge can be approximated with a sphere full of mass and we can apply our analysis at any intermediate generic radius r till the border of the bulge where $r = R_B$. Thus, applying the Cavalieri approach, we divide the sphere in n very thin concentric shells of constant mass density. Figure 2.18 illustrates the case and definitely we see that $n = \frac{r}{\Delta r}$. For each shell we can define its radius and mass in terms of the maximum radius r we choose for the considered sphere as

$$r_\alpha = r - \frac{1}{2}(2\alpha - 1)\Delta r = r\left(1 - \frac{2\alpha - 1}{2n}\right) \tag{2.23}$$

$$M_\alpha = \sigma_B(r_\alpha) \cdot 4\pi r_\alpha^2 \cdot \Delta r = \sigma_B(r_\alpha) \cdot 4\pi r_\alpha^2 \frac{r}{n} \ . \tag{2.24}$$

In order to obtain the mass of the entire sphere, it is necessary to introduce eq. (2.23) and the
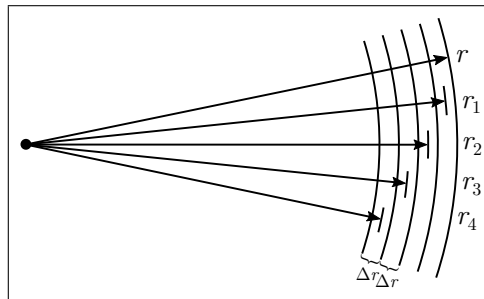
Figure 2.18: Schematic representation of the Cavalieri approach applied to a full-of-mass sphere of radius r. The radii r_α reach the middle point of each shell of thickness Δr.

mass density $\sigma_B(r_\alpha)$ in eq. (2.24) and then sum the contribution of all shells obtaining

$$M_B(r) = \sum_{\alpha=1}^{n} M_\alpha = 4\pi a \cdot r^{(k+3)} \sum_{\alpha=1}^{n} \frac{1}{n}\left(1 - \frac{2\alpha - 1}{2n}\right)^{(k+2)} \ . \tag{2.25}$$

With $r = R_{\mathrm{B}}$ the mass of the entire bulge is calculated. At this point we match eq. (2.25) and the mass $M_{\mathrm{B}}(r)$ expressed from eq. (2.22) obtaining

$$M_{\mathrm{B}}(r) = r^3 \cdot \frac{b}{G} = r^{(k+3)} \cdot 4\pi a \sum_{\alpha=1}^{n} \frac{1}{n} \left(1 - \frac{2\alpha - 1}{2n} \right)^{(k+2)} . \tag{2.26}$$

Here we achieve an important result: in fact, observing the exponents of r it is evident that $k = 0$ and all other terms can be traced back to constants. This confirms, as expected, that the mass density is constant $\sigma_{\mathrm{B}}(r) = a = \sigma_{\mathrm{B}}$. Therefore, for deriving the mass of the bulge at a radius r, we need to consider this first result and solve eq. (2.25). This involves a few basic summations, as it is evident from

$$\begin{aligned}
M_{\mathrm{B}}(r) &= r^3 \cdot 4\pi\sigma_{\mathrm{B}} \cdot \frac{1}{n} \sum_{\alpha=1}^{n} \left(1 + \frac{1}{2n} - \frac{\alpha}{n} \right)^2 \\
&= r^3 \cdot 4\pi\sigma_{\mathrm{B}} \cdot \frac{1}{n} \left(\left(1 + \frac{1}{2n} \right)^2 \boxed{\sum_{\alpha=1}^{n} 1} - \frac{2}{n} \left(1 + \frac{1}{2n} \right) \boxed{\sum_{\alpha=1}^{n} \alpha} + \frac{1}{n^2} \boxed{\sum_{\alpha=1}^{n} \alpha^2} \right) \\
&= r^3 \cdot 4\pi\sigma_{\mathrm{B}} \cdot \frac{1}{n} \left(\left(1 + \frac{1}{2n} \right)^2 \boxed{n} - \frac{2}{n} \left(1 + \frac{1}{2n} \right) \boxed{\frac{1}{2}n(n+1)} + \frac{1}{n^2} \boxed{\frac{1}{6}n(n+1)(2n+1)} \right) \\
&= r^3 \cdot 4\pi\sigma_{\mathrm{B}} \frac{1}{3} \left(1 - \frac{1}{4n^2} \right) .
\end{aligned} \tag{2.27}$$

The three highlighted summations have a certain importance in mathematics and are found in all lists of mathematical series, an example of which is [39]. In particular, the first summation defines the n-sum of the number 1, the second is known as the Gauss sum of the first n positive integers, who first realised it, and finally the third is the sum of the first n squares, usually used for the proof by induction. As we can see, in this case the dark matter problem, albeit in this simplified approach, provides an opportunity to engage our students in putting this knowledge into practice by applying it to a concrete example, promoting longer lasting learning.

Now, if we take the limit of eq. (2.27) for $n \to \infty$ ($\Delta r \to 0$), which means doing a step more towards the continuum and approaching the idea of integration, we derive the usual formula for the mass of a homogeneous sphere of radius r

$$M_{\mathrm{B}}(r) = \frac{4}{3} \pi\sigma_{\mathrm{B}} \cdot r^3 . \tag{2.28}$$

For an approach suitable for more advanced or undergraduate students see appendix B.

In conclusion, comparing and combining together the results for equations (2.28) and (2.22) estimated at a generic radius $r < R_{\mathrm{B}}$ and at the bulge edge $r = R_{\mathrm{B}}$, we are able to express important quantities in terms of the total mass $M_{\mathrm{B}}(R_{\mathrm{B}})$ and radius R_{B}. Hence, we get

$$v_{\mathrm{B}}(r) = \frac{v_{\mathrm{B}}(R_{\mathrm{B}})}{R_{\mathrm{B}}} r \tag{2.29}$$

$$M_{\mathrm{B}}(r) = \frac{M_{\mathrm{B}}(R_{\mathrm{B}})}{R_{\mathrm{B}}^3} r^3 \tag{2.30}$$

$$\sigma_{\mathrm{B}} = \frac{3}{4\pi} \frac{M_{\mathrm{B}}(R_{\mathrm{B}})}{R_{\mathrm{B}}^3} . \tag{2.31}$$

In summary, we can say that the bulge of a spiral galaxy behaves like a rotating solid body. As a matter of fact, we have constant mass density σ_{B}, velocity $v(r)_{\mathrm{B}}$ that grows proportionally with r and mass $M_{\mathrm{B}}(r)$ with r^3.

2.3.3.2 The Halo

We follow now exactly the same reasoning for the rotation curve of the halo. We would have expected here a decline as for the Solar System, but in this case the rotation curve tells us that the velocity remains constant from the border of the bulge till very large radii. Because of this unexpected behaviour, we need to extrapolate for this part any information useful to explain what can cause this discrepancy between expectations and observations. Therefore, the information we can deduce from the rotation curve is

$$v_{\mathrm{H}}(r)^2 = G\frac{M_{\mathrm{G}}(r)}{r} = G\frac{M_{\mathrm{B}}(R_{\mathrm{B}})}{R_{\mathrm{B}}} = v_{\mathrm{B}}(R_{\mathrm{B}})^2 = v_{\mathrm{H}}(R_{\mathrm{B}})^2 = \mathrm{const} \,, \tag{2.32}$$

where $M_{\mathrm{G}}(r)$ represents the mass of the galaxy, which includes the contributions from bulge and halo, till the maximum radius $r \leq R_{\mathrm{H}}$. This is assuming that this limit exists, a hypothesis not yet proven, but for our exercise we consider it valid. As we did for Newton's shell theorem and on the same assumptions, we approximate the galaxy with a full-of-mass sphere [50][94]. Assuming again that the mass density profile is in the form of a power law, $\sigma_{\mathrm{H}}(r) = d \cdot r^k$, with d and k constant, we apply the Cavalieri method exactly as for the bulge. Equations (2.23), (2.24) and (2.25) are still valid, but used with $\sigma_{\mathrm{H}}(r_\alpha)$ instead. Considering eq. (2.32), the total mass of the galaxy for a radius in the halo region is determined by

$$M_{\mathrm{G}}(r) = \frac{M_{\mathrm{B}}(R_{\mathrm{B}})}{R_{\mathrm{B}}} \, r = M_{\mathrm{B}}(R_{\mathrm{B}}) + M_{\mathrm{H}}(r) \tag{2.33}$$

and we need to isolate the halo section for deducing the related information. This means that from the mass of a sphere of radius r, with $R_{\mathrm{B}} \leq r \leq R_{\mathrm{H}}$, we have to subtract the mass of a sphere of radius R_{B}. The latter, in calculating $M_{\mathrm{G}}(r)$ then, will be replaced by the results obtained for the bulge. Equation (2.25) under these new conditions and for $R_{\mathrm{B}} \leq r \leq R_{\mathrm{H}}$ becomes

$$M_{\mathrm{H}}(r) = \left(r^{(k+3)} - R_{\mathrm{B}}^{(k+3)}\right) \cdot 4\pi d \sum_{\alpha=1}^{n} \frac{1}{n}\left(1 - \frac{2\alpha - 1}{2n}\right)^{(k+2)} . \tag{2.34}$$

Equalling now eq. (2.34) and the mass $M_{\mathrm{H}}(r)$ expressed from eq. (2.33), in the same way as we did for the bulge, we deduce from the exponents of r that in this section $k = -2$ and the mass density is then $\sigma_{\mathrm{H}}(r) = d \cdot r^{-2}$. Thus, for calculating the mass of the halo alone from eq. (2.34), we get

$$M_{\mathrm{H}}(r) = (r - R_{\mathrm{B}}) \cdot 4\pi d \cdot \frac{1}{n}\boxed{\sum_{\alpha=1}^{n} 1}$$
$$= (r - R_{\mathrm{B}}) \cdot 4\pi d \,. \tag{2.35}$$

Although the reasoning is a little more complex here, the calculation is simpler than in the bulge section. In fact we again encounter the easy n-sum of the number 1 and do not need to calculate the limit because n is no longer present in the equation at this point.
For an approach suitable for more advanced or undergraduate students see appendix B.

Finally, it is possible to compare and combine together the results for equations (2.32), (2.33) and (2.35) estimated at a generic radius, $R_{\mathrm{B}} < r < R_{\mathrm{H}}$, and at the halo edges, $r = R_{\mathrm{B}}$ and $r = R_{\mathrm{H}}$. In this way we are able to express important quantities in terms of the total mass of the bulge $M_{\mathrm{B}}(R_{\mathrm{B}})$ and radius R_{B}, parameters that we can measure. It is also possible to express them in other terms, such as the total mass of the halo alone, $M_{\mathrm{H}}(R_{\mathrm{H}})$, or the total mass of the galaxy (bulge + halo), $M_{\mathrm{G}}(R_{\mathrm{H}})$, and the radius R_{H}. Interesting relations between the various components

of the galaxy are indeed highlighted, obtaining

$$v_H(r) = v_B(R_B) = v_H(R_B) = v_H(R_H) \tag{2.36}$$

$$M_H(r) = M_B(R_B)\left(\frac{r - R_B}{R_B}\right) = M_H(R_H)\left(\frac{r - R_B}{R_H - R_B}\right) = M_G(R_H)\left(\frac{r - R_B}{R_H}\right) \tag{2.37}$$

$$M_G(r) = \frac{M_B(R_B)}{R_B}\, r = \frac{M_H(R_H)}{R_H - R_B}\, r = \frac{M_G(R_H)}{R_H}\, r \; . \tag{2.38}$$

One last step is here missing. Since the mass density profile is not constant in this part of the galaxy, we want to determine the value of the constant d in relation to σ_B. Basically, from the combination of equations (2.32), (2.33) and (2.35), together with eq. (2.31), we end up with $d = \frac{1}{3}\sigma_B R_B^2$, which gives

$$\sigma_H(r) = d \cdot r^{-2} = \frac{1}{3}\sigma_B \left(\frac{R_B}{r}\right)^2 = \frac{v_B(R_B)^2}{4\pi G}\frac{1}{r^2} \; . \tag{2.39}$$

Summarising, we can say that the halo of a spiral galaxy behaves not only differently from the core, but also differently from the assumptions. In fact, we would have expected a Keplerian decline in velocity, typical of a system with almost all the mass concentrated in its center, the bulge. We have here instead a mass density $\sigma_H(r)$ that declines proportionally to r^{-2}, velocity $v_H(r)$ that remains constant and mass $M_G(r)$ that grows directly proportional to r. Moreover, all this extends well beyond the visible limit of the galaxy disk, R_D.

To understand the meaning of these results we now plot the radial profile of mass and mass density with Geogebra, i.e. we plot the equations (2.30) and (2.38) in the former and (2.31) and (2.39) in the latter. At this stage, in order to visualize the trend of these physical quantities, it is sufficient to use random values for the various constants included, while in section 2.3.5 we will see a real example. The resulting graphs are in fig. 2.19.

(a) Mass Profile (b) Mass Density Profile
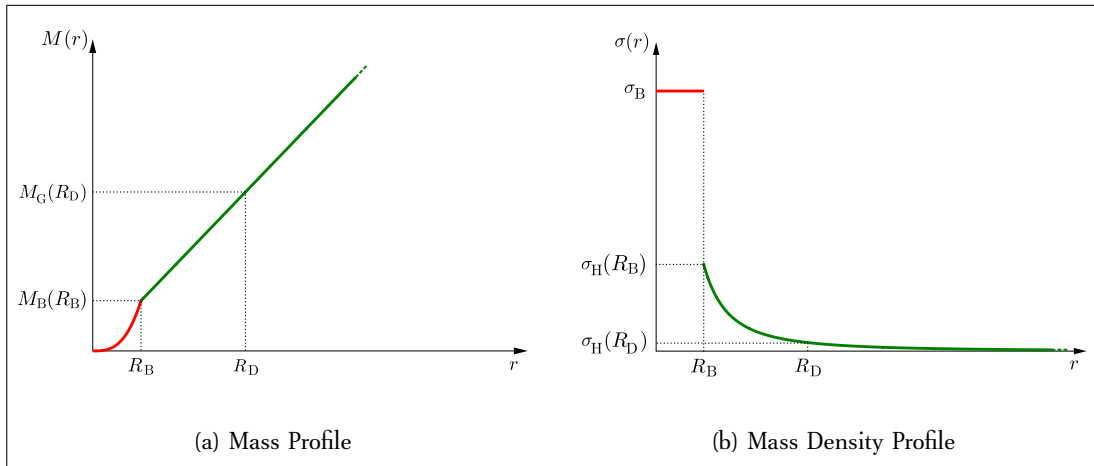
Figure 2.19: Mass and mass density radial profile for a spiral galaxy, deduced from the rotation curve in fig. 2.17. The functions in red correspond to the bulge of radius R_B and the ones in green to the halo. The radius of the halo, R_H, is not visible here as we do not know if it exists and if so, not even its size. The only certain information is that it extends much further than the visible radius of the galaxy disk, R_D.

The conclusion we can draw from looking at these diagrams in relation to the light curve in fig. 2.17 is that there must be much more matter than we actually see. In fact, what we record is the gravitational interaction of this matter with the visible mass of the galaxy. We expected a drastic

decrease of the mass in the halo, according to the visual distribution of stars and gas, but instead we have a continuous increase. Given that there is no direct confirmation of the presence of this hidden mass, the theory of exotic dark matter completely transparent to all electromagnetic radiation has thus been formulated. For precisely these reasons, the rotation curves of spiral galaxies are considered to be one of the strongest pieces of evidence for the existence of dark matter.

2.3.4 The Spider Diagram of a Spiral Galaxy

The theory of the spider diagram of spiral galaxies is introduced here and, as for the solar system, represents an innovative topic in the field of physics and astronomy education. Moreover, it lends itself very well to the teaching of mathematics and physics with examples from astronomy.

We already explored how this diagram appears for the Solar System, but applying it to spiral galaxies, we have new elements to take into account. In addition, it is important to understand how these elements are related to the rotation curve. The purpose of this section is to represent, and draw with Geogebra, the constant radial velocity contours corresponding to the rotation curve in fig. 2.17. The analysis is again divided into bulge and halo areas. For the Keplerian decline instead we refer again to the work on the Solar System and appendix C.

Moreover, in this case we have to consider that due to the huge distances involved in the observation of spiral galaxies, even if the bulge was perfectly spherical, it would be very difficult to distinguish its shape as it is small compared to the size of the galaxy disk and embedded in it. Therefore, for simplicity we consider all the visible mass of the galaxy, bulge included, distributed on a disk.

We already know from section 2.2.5 that the connection between radial velocity and rotational velocity is expressed by eq. (2.15). Thus, this is our starting point and from here we develop our analysis.

2.3.4.1 The Bulge

According to the definition of a spider diagram, in this region, characterized by $r \leq R_{\mathrm{B}}$ and a rotational velocity $v_{\mathrm{B}}(r)$, expressed by eq. (2.29), we set the pure radial velocity due to rotation, $(v_r - v_{\mathrm{sys}})$, constant and eq. (2.15) becomes

$$v_r - v_{\mathrm{sys}} = v(r) \cdot \cos\theta \cdot \sin i = \frac{v_{\mathrm{B}}(R_{\mathrm{B}})}{R_{\mathrm{B}}} \, r \cdot \cos\theta \cdot \sin i \overset{!}{=} B \, . \tag{2.40}$$

Here B is a constant that can adopt different values. $\frac{v_{\mathrm{B}}(R_{\mathrm{B}})}{R_{\mathrm{B}}}$ is also a constant and $\sin i$ as well, since the inclination angle i in our model remains the same for the entire galaxy. Grouping now the constants together we derive

$$r \cdot \cos\theta = \frac{B \cdot R_{\mathrm{B}}}{\sin i \cdot v_{\mathrm{B}}(R_{\mathrm{B}})} \, . \tag{2.41}$$

Remembering that in Cartesian coordinates $r \cdot \cos\theta = x$, we find out that the radial velocity remains constant for every constant x, namely for all vertical lines parallel to the y-axis as in fig. 2.20. Specifically, these lines are limited inside an ellipse positioned at the centre of the galaxy, which is the projection on the sky plane of the disk representing the bulge on the galaxy plane. As we did before in section 2.3.2, the projection in the sky plane is achieved setting $x' = x$ and $y' = y\cos i$ for the spider diagram lines and the circles representing different areas.[12] As we already know, the semi-major axis of the ellipse corresponds to the actual radius of the bulge.

---

[12]Also in this diagram for $i = 0°$ we are on the galaxy plane.
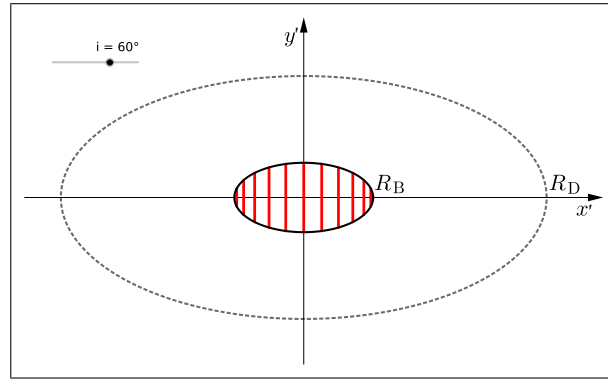
Figure 2.20: Spider diagram of the spiral galaxy bulge with its typical vertical lines. The galaxy is inclined of $i = 60°$. R_B is the bulge radius and R_D is the radius of the visible, luminous disk.

2.3.4.2 The Halo

We draw now the spider diagram for the halo region where we have $R_B \leq r \leq R_H$ and the velocity is constant, $v_B(R_B) = v_H(R_H)$. From the definition of the spider diagram and eq. (2.15) we derive

$$v_r - v_{\text{sys}} = v(r) \cdot \cos\theta \cdot \sin i = v_B(R_B) \cdot \cos\theta \cdot \sin i \stackrel{!}{=} B . \tag{2.42}$$

Grouping again all constants and defining them all under the letter A, we obtain then

$$\cos\theta = \frac{B}{\sin i \cdot v_B(R_B)} = A . \tag{2.43}$$

We express then this result in Cartesian coordinates and obtain after a few steps

$$\cos\theta = \frac{x}{r} = \frac{x}{\sqrt{x^2 + y^2}} = A . \tag{2.44}$$

As it was already perceivable from eq. (2.43), the result is in this case a radial-lines bundle through the centre expressed by the equation

$$y = \pm(A^{-2} - 1)^{1/2} \, x . \tag{2.45}$$

This is shown in fig. 2.21 for a spiral galaxy inclined by $i = 60°$. This figure is actually a completion of fig. 2.20, to which the halo part is added. Again, the lines are restricted inside an
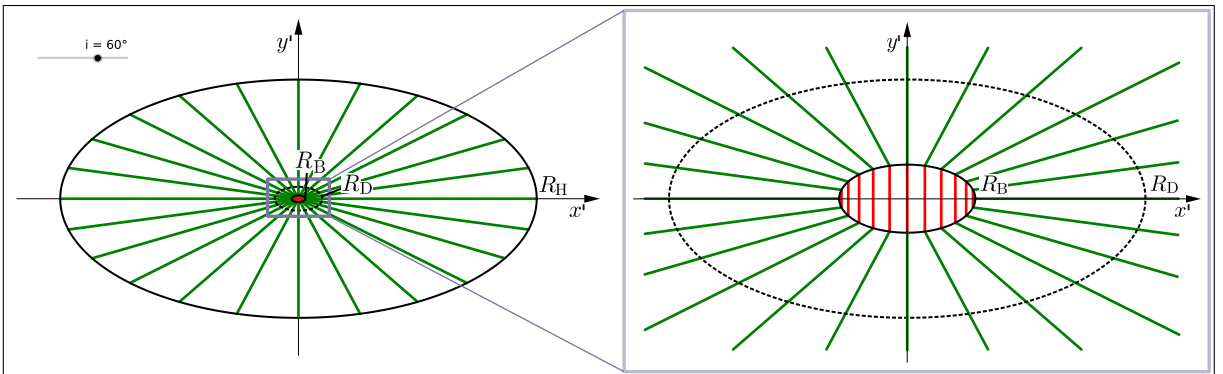
Figure 2.21: Spider diagram of the spiral galaxy bulge and halo with both types of lines. Besides the bulge lines in red, we can see in green the lines of the halo. R_H is the radius of the hypothetical edge of the halo. In the right box an enlargement of the visible disk part.

ellipse representing the projection of the halo onto the sky plane in the usual way, considering the

halo finite in size.

A useful task, not only for understanding, but also for drawing the spider diagram, is to identify free and not-free parameters and among all of them which are in common between the two equations. In fact, according to the definition of A in eq. (2.43), we can express eq. (2.41) as

$$x = r \cdot \cos\theta = A \cdot R_{\mathrm{B}} \, . \tag{2.46}$$

We notice that free parameters are the radius r from the centre of the galaxy at which we choose to analyse the system and the angle θ between this radius and the x-axis. The constant A is the same in both cases and for the bulge we have its radius R_{B} as an extra constant. The various radii defining the different sections are the same used for the rotation curve of a spiral galaxy.

When a spiral galaxy is observed and its radial velocities are measured, on the basis of what we have just seen, the corresponding spider diagram can be drawn. Then doing the process presented here in reverse order, the rotation curve is extrapolated and analysed for important information that it can provide us with, as we have seen in the previous section. Among other information, the most interesting is that the dynamics of these galaxies seems to suggest the presence of much more matter than we can actually see. According to simulation and motion of stars through the galaxy disk, it seems that this large amount of unseen gravitating matter, the so-called dark matter, is distributed in a huge almost spherical halo around the galaxy [94][15]. This is exactly the type of exercise that we are going to do in the next section, applying this method to a real example, the spiral galaxy NGC3198.

2.3.5   The Spiral Galaxy NGC3198

Considering spiral galaxies, we have seen so far the practical application to a real astronomical problem of basic concepts of mathematics and physics, albeit treated at a theoretical level, i.e. without real data. As interesting and stimulating as it may be, using a specific astronomical object with real data always provides the most engaging alternative and ultimately gives a deeper understanding of the subject discussed. In fact, for this reason, it is often advisable in didactic research in physics and astronomy to support the theory with exercises applied to real examples [49][84][113].

Therefore, we apply now this method to the spiral galaxy NGC3198 (Fig. 2.22), a barred spiral galaxy in the constellation Ursa Major, in order to calculate its amount of mass and see if there actually is hidden matter. It is possible to choose any galaxy for which a spider diagram or at
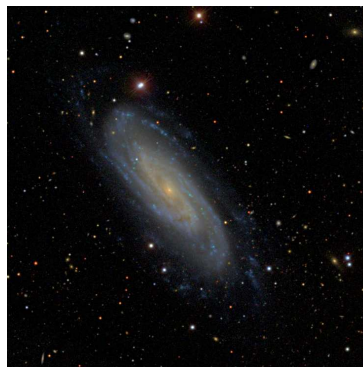
Figure 2.22: The galaxy NGC3198 in optical passband from the NASA/IPAC Extragalactic Database. Credit: ned.ipac.caltech.edu.

least a rotation curve is of public domain.[13] Our choice for this galaxy lies in several factors:

---

[13]It is not so easy to find spider diagrams on-line, for a non-complete list of them see [11] and [114].

- it is in fact an excellent representative for studying the flat rotation curve up to large radii and has a good orientation ($i = 71°$),

- it has been extensively observed and studied, so there are many articles about it in the literature,

- it is one of the few galaxies for which the spider diagram is available,

- it has observations of Cepheid variable stars, therefore, it is suitable for another interesting student project on autonomously determining the distance of nearby galaxies with real data [101] and this gives the chance to understand how elaborate the distance determination problem in cosmology is.

In fact, the idea of connecting various projects using the same celestial objects gives continuity and self-consistency to our work and stimulate students to achieve always new conclusions. Moreover, this enables students to perform independently many tasks and achieve multiple results, building in this way new interconnected knowledge at every step.

For this galaxy, as mentioned, there is a lot of data and information in the literature,[14] although not always in agreement with each other, and at least three spider diagrams [6][11][114]. Nevertheless, we base our analysis on the spider diagram from [6] because this is very clear and not superimposed to any pictures of the galaxy NGC3198, as shown in fig. 2.23. In addition, table 2.3,[15] is a short collection of data about the galaxy, chosen among the many obtainable from the mentioned literature and on-line on `https://ned.ipac.caltech.edu/cgi-bin/objsearch?objname=NGC+3198`.

The first thing to be noticed is that the spider diagram in fig. 2.23 is not really shaped like the one we already studied. This is because a real galaxy is a complex object and we instead use

	Redshift z	Mean Dist. r	Dist. Modulus (m − M)	Bulge Radius R_B	Disk Radius $R_D = a$	Inclination i	Abs. Mag. M_V	Luminosity L_V
NGC3198	0.0022	12.8 Mpc	30.49	4 kpc	14 kpc	71°	-19.8	$7.3 \cdot 10^9 \, L_{V\odot}$

Table 2.3: Spiral galaxy NGC3198 data. The subscript V for absolute magnitude and luminosity stand for visual V (wavelength range 480-650 nm) passband.

a simplified model. For achieving a more realistic diagram, we should analyse more complex functions representing specific distribution of mass for the galaxy. However, for our purpose of making this project a useful teaching tool, it is not essential to consider the real nature of a galaxy in all details, on the contrary it would keep our attention away from the important concepts and outcomes. For the same reason, we do not even consider the presence of any distortions, warps and uncertainties. Our focus is only the pure problem of finding evidence of the existence of dark matter and we need to keep it as simple as possible.

At this point, since measurements of galaxy dimensions are taken as angular sizes (in arcminutes – ′ and arcseconds – ″), we need to work out how much $1' = 60''$ is in kpc, i.e. how big is the length we see as $1'$ from our distance. In fig. 2.24, we notice that the semi-major (a) and semi-minor (b) axes correspond respectively to the angles α and β. If we now consider the triangle $\triangle COA'_2$ and the fact that $a \ll \overline{CO}$, we can apply the small angle approximation and calculate

$$a = \overline{CO} \cdot \tan \alpha \cong \overline{CO} \cdot \widehat{\alpha} = \overline{CO} \, \frac{2\pi \cdot \alpha}{360 \cdot 60'}. \tag{2.47}$$

---

[14]Non-complete list of publications:[6][11][12][114][53][33][13][110][67][55][18] etc.

[15]The mean distance is the mean values among the many measurements performed with various methods, taken from the NASA/IPAC Extragalactic Database – NED `https://ned.ipac.caltech.edu/`.
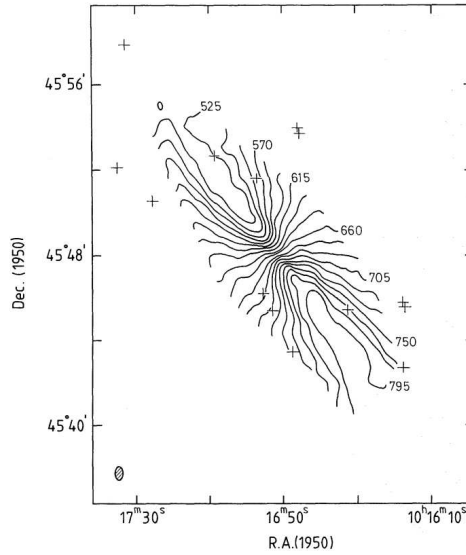
Figure 2.23: Spider diagram for the galaxy NGC3198 from [6].
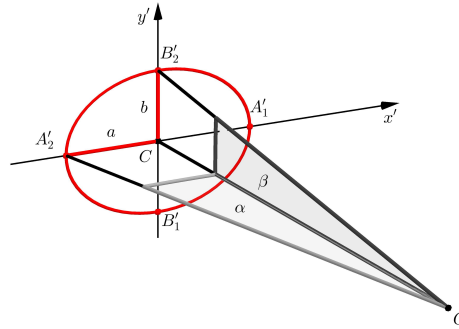
Figure 2.24: Lengths on the sky plane for a spiral galaxy. The semi-major axis a seen under the angle α and the minor, b, under the angle β. O is the observer.

Knowing that $\overline{CO} = 12.8$ Mpc and for example setting $\alpha = 1'$, we get $a = 3.72$ kpc. For galaxies at different distances, this conversion factor will be another one. This rule can be applied to convert any angular measurement of this galaxy into a linear length and vice-versa, depending on the available information. In this specific case, however, using neither an image of the galaxy nor angular measurements, but knowing from the literature that $R_B \simeq 4$ kpc and $R_D \simeq 14$ kpc, we can convert these values into angular measures. Indeed, due to eq. (2.47) we get $R_B \cong 1'.07$ and $R_D \cong 3'.76$.

It is possible to start the project using a scaled printed copy of the provided diagram as in fig. 2.25 or the corresponding Geogebra file. In fact, we have imported the spider diagram taken from [6] into Geogebra and drawn on it few helpful elements. As we can see from fig. 2.25, first we introduce the axes x' and y' passing through the centre of the galaxy, with the y'-axis parallel as much as possible to the central vertical line of the diagram with 660 written next to it. Using the data at our disposal we now need to draw ellipses corresponding to the areas of the bulge and the visible disk. Thus, by measuring the length in cm of the arrow in green on the left side, we derive how many cm correspond to $4'$. With this information, we calculate the length in cm of the semi-major axes, R_B and R_D. In addition, knowing from section 2.2.3 that all lengths parallel to the y-axis in the galaxy plane are seen in the sky plane as $y' = y \cos i$, we calculate the value of the semi-minor axes. Now having the length of the axes, we can draw the respective ellipses which are in red (bulge) and blue (visible disk) in the figure. Besides, there are in the literature different definitions of the visible radius of a galaxy, while measurements arrive actually at $12'$
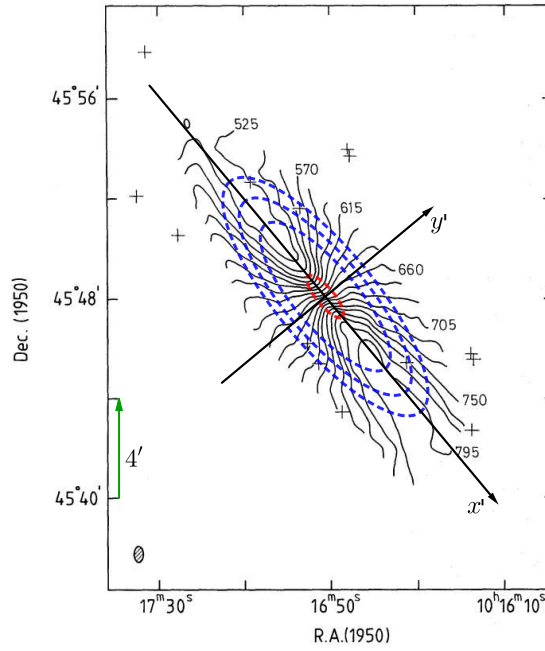
Figure 2.25: Spider diagram for the galaxy NGC3198 from [6] elaborated with Geogebra. The coordinate system axes are introduced together with the ellipses for the bulge (red) and three different sizes for the visible radius (blue). The arrow in green is representative of $4'$.

from the centre (almost 50 kpc). In particular, the innermost ellipse in blue corresponds to the visible radius of 14 kpc. The intermediate ellipse corresponds to the de Vaucouleurs visible radius ($5'$) and the last one to the Holmberg radius ($5.95'$) [110].[16] It is a free choice which radius to use as the visible border of the galaxy disk. In this project we decided to work with the visible radius of 14 kpc.

The next step consists of verifying the components of the systemic velocity of this spiral galaxy. As we know from section 2.2.5, this includes the recessional velocity v_{rec}, eventually some peculiar velocities v_{pec} and it is expressed by $v_{\text{sys}} = v_{\text{rec}} + v_{\text{pec}}$. In our spider diagram v_{sys} is given by the value of the central line and it is $v_{\text{sys}} = 660$ km/s $= c \cdot z$.[17] Since the redshift z in this case is small, we can consider this galaxy to be in our cosmic neighbourhood and thanks to the Hubble law, we can calculate the recessional velocity as $v_{\text{rec}} = H_0 \cdot r = 896$ km/s, where H_0 is the Hubble constant[18] and r the distance galaxy-observer ($\overline{CO}$ in fig. 2.24),[19]. This leads us to

$$v_{\text{pec}} = (660 - 896) \text{ km/s} = -236 \text{ km/s} .$$

As we can see from this rough estimate, most probably this galaxy has a small peculiar velocity directed towards the Sun. However, we do not have any official confirmation of this motion.

Analysing the spider diagram in fig. 2.25, we notice that the iso-velocity contours are separated by equal steps of 15 km/s and of course they are not regular, straight and perfectly symmetric. This, together with the fact that some estimates should be done by eye inspection, can lead to less accuracy, but the principles of measurement are more important for our educational goals and in the end the results are almost always comparable with the literature. Now, for extrapolating the

---

[16]The de Vaucouleurs radius is reached when the surface brightness in band V attains the value of $25 \frac{\text{mag}}{\text{arcsec}^2}$, the Holmberg radius is reached when the surface brightness in band B attains the value of $26.5 \frac{\text{mag}}{\text{arcsec}^2}$.

[17]z is the measured redshift for this galaxy, for a definition of redshift see [100]. Speed of light $c = 2.99 \cdot 10^8$ m/s.

[18]We adopt the value $H_0 = 70 \frac{\text{km}}{\text{Mpc} \cdot \text{s}}$ for the Hubble constant.

[19]Of course this result is dependent on which values we adopt for H_0 and the distance r, therefore it can lead in other cases to a very different estimate.

rotation curve corresponding to this spider diagram we only need to focus our attention on the first quadrant of the coordinate system because, for simplicity, we consider the system symmetric in any case. Moreover, for this analysis we use only the lines where the velocity is indicated, but students can work with others or all of them.

The very first thing to do with the radial velocity values from the spider diagram is calculating the radial velocity due to rotation alone,[20] from now on called simply v_r, for each of them and its value when re-projected back on the galaxy plane by virtue of $v_r / \sin i = v(r) \cos \theta = v_\parallel$. In the first three lines of table 2.4 the values we derived are shown.

Let us consider now the bulge section, as we already know, here all vertical lines of constant radial velocity tell us that we are facing a rotating solid body. The difference now is that in our simplified

Measured v_r (including v_{sys})	660 km/s	705 km/s	750 km/s	795 km/s
$v_r - v_{sys}$ (from now only v_r)	0 km/s	45 km/s	90 km/s	135 km/s
$v_r / \sin i = v(r) \cdot \cos \theta$	0 km/s	47.60 km/s	95.19 km/s	142.79 km/s
Observed Angle θ' – Halo	90°	44.5°	22°	5.5°
Re-projected Angle θ – Halo	90°	71.67°	51.14°	16.48°
Rotation Velocity $v_H(r)$ – Halo	0 km/s	151.34 km/s	151.71 km/s	148.90 km/s

Table 2.4: Results for the rotation velocities of the spiral galaxy NGC3198, whose inclination angle is $i = 71°$ (table 2.3). θ and θ' are defined as in fig. 2.7.

model all vertical lines are included in the bulge area and here some do not fall inside it. We don't need to worry about this, it is just an indication of the smooth change in velocity when moving from one area to another. So, we analyse the lines within the bulge zone and, to overcome the problem, we finally adjust the maximum velocity[21] with the same value obtained from the halo analysis at the distance R_B from the centre. At this point, we obtain the corresponding rotation velocity for each vertical line considered using eq. (2.15). In particular, considering eq. (2.11), we infer that along the x'-axis, where $\theta' = \theta = 0$, the rotation velocity corresponds exactly to $v_r / \sin i$. The last element we need is the distance r from the centre of the system of each line considered and we easily measure it from the diagram in fig. 2.25.

And again eq. (2.15) allows us to calculate the rotation velocity in the halo area, but now we have to take into account the angle θ as well. Therefore, moving now our interest on the halo part, we have to extract from the diagram of fig. 2.25 the approximate measure of the angle θ' between the x'-axis and the considered contours. Since the contours are not straight lines, this operation is slightly difficult, but by eye inspection we try to approximate the contours with radial lines from the centre to the ellipse in blue, as shown in fig. 2.26. At this point, thanks to eq. (2.9), we calculate the corresponding angle θ in the galaxy plane and with this finally the rotation velocity. The values we find reliable and all these results are collected in table 2.4. It is interesting to notice that, as expected, all values are distributed around a mean value, which in our simplified model remains constant. The mean value of the rotation velocities of the halo is $v_H(r) = 150.54$ km/s ≈ 150 km/s.

Next, we put all information together in order to draw the rotation curve of the galaxy NGC3198 and, as anticipated before, we set the maximum rotation velocity of $v_B(R_B) = v_H(R_B) = 150$ km/s. The resulting rotation curve is shown in fig. 2.27. Summarising the results for every section we get

$$v_B(r) = \frac{v_B(R_B)}{R_B} \, r = 37.50 \left(\frac{r}{\text{kpc}} \right) \text{ km/s} \qquad (\text{with} \quad v_B(R_B) = 150 \text{ km/s}) \qquad (2.48)$$

$$v_H(r) = v_B(R_B) = v_H(R_H) = 150 \text{ km/s} \,. \qquad (2.49)$$

---

[20]$(v_r - v_{\text{sys}})$

[21]In our simplified model the maximum velocity should be reached at the border of the bulge (4 kpc).
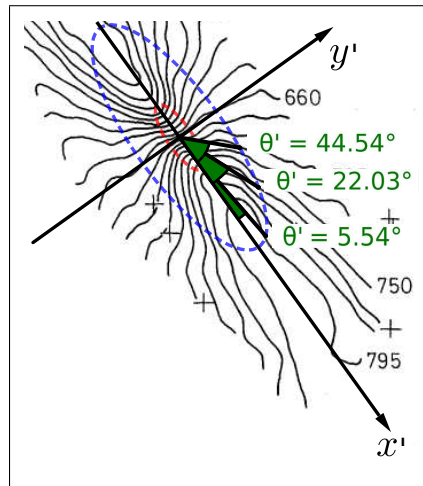
Figure 2.26: Example of fitting by eye inspection the angles θ' for three iso-velocity contours on the spider diagram for the galaxy NGC3198 from [6].
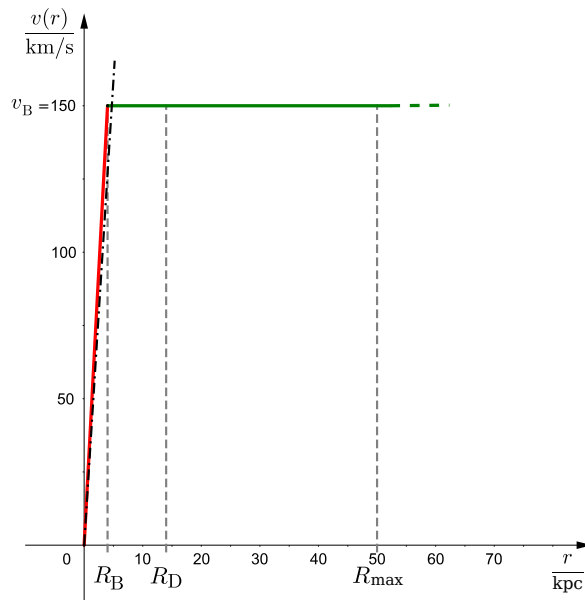
Figure 2.27: Rotation curve of NGC3198 deduced from the spider diagram in fig. 2.25. The dash-dot black line corresponds to the bulge rotation velocity profile calculated from the spider diagram (where the maximum velocity is actually reached outside the bulge edge). The red line instead represents the velocity profile corrected for $v_B(R_B) = 150$ km/s. As we can see, the difference between the two lines is negligibly small. $R_{max} = 50$ kpc is the maximum measurement available.

In order to have an idea about how in reality the spider diagram in its actual complex structure is translated into a rotation curve, in fig. 2.28 we can see the rotation curve from real data for NGC3198.

It is also possible to create our own spider diagram from the rotation curve in fig. 2.27 using the data we have, the equations (2.46) for the bulge, (2.45) for the halo and setting $y' = y \cos i$ to project everything on the sky plane. The resulting simplified spider diagram is an approximation of the real one and is shown in fig. 2.29. From experience, we can say that if we introduce the difference between the real and simplified spider diagram in advance, and use the simplified spider diagram with the procedure just described, the students perform the exercise with less difficulty. Another possibility is to start the exercise directly from the rotation curve in its simplified version (which will be very similar to fig. 2.27) and continue as we are going to see now, thus simplifying
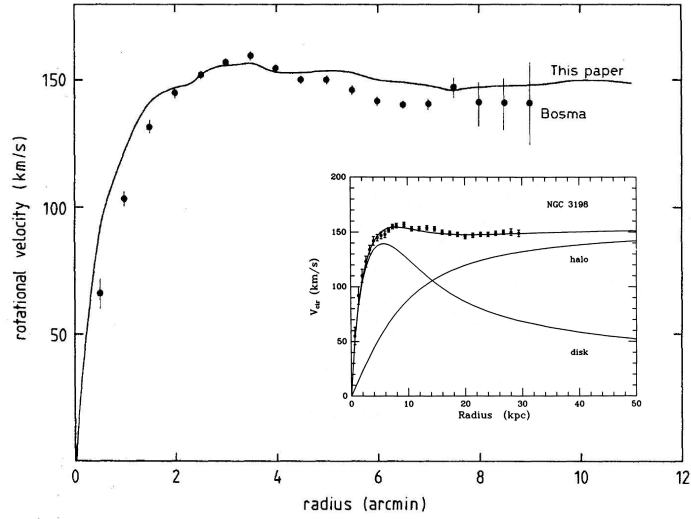
Figure 2.28: The real rotation curve for the galaxy NGC3198 from [6]. In the small plot the rotation curve from [110] with also the curves expected from the different components: disk and dark matter halo.

the practice even more.
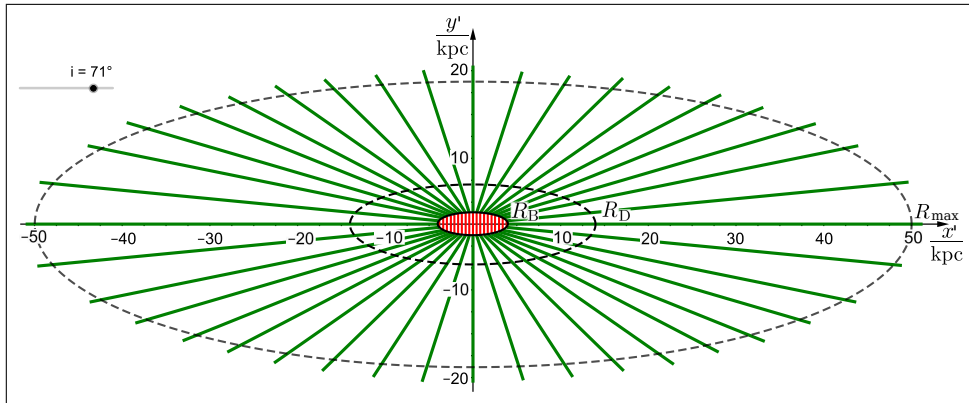
Figure 2.29: Spider diagram for the galaxy NGC3198 calculated from the simplified rotation curve in fig. 2.27. The diagram reaches the distance corresponding to the maximum measurement available at around $R_{\text{max}} = 50$ kpc.

The next analysis regards the mass density and mass profiles for the chosen galaxy. Thus, we calculate the mass density for the bulge and the halo from equations (2.31) and (2.39)

$$\sigma_{\text{B}} = \frac{3}{4\pi G} \frac{v_{\text{B}}(R_{\text{B}})^2}{R_{\text{B}}^2} = 1.55 \cdot 10^{38} \frac{\text{kg}}{\text{kpc}^3} = 0.78 \cdot 10^8 \frac{M_\odot}{\text{kpc}^3} \tag{2.50}$$

$$\sigma_{\text{H}} = \frac{v_{\text{B}}(R_{\text{B}})^2}{4\pi G} \frac{1}{r^2} = 8.28 \cdot 10^{38} \left(\frac{\text{kpc}}{r}\right)^2 \frac{\text{kg}}{\text{kpc}^3} = 4.16 \cdot 10^8 \left(\frac{\text{kpc}}{r}\right)^2 \frac{M_\odot}{\text{kpc}^3} \ . \tag{2.51}$$

For the mass profile, applying equations (2.30) and (2.38) we have

$$M_{\text{B}}(r) = \frac{v_{\text{B}}(R_{\text{B}})^2}{G \, R_{\text{B}}^2} \cdot r^3 = 6.50 \cdot 10^{38} \left(\frac{r}{\text{kpc}}\right)^3 \text{kg} = 3.27 \cdot 10^8 \left(\frac{r}{\text{kpc}}\right)^3 M_\odot \tag{2.52}$$

$$M_{\text{G}}(r) = \frac{v_{\text{B}}(R_{\text{B}})^2}{G} \, r = 104.03 \cdot 10^{38} \left(\frac{r}{\text{kpc}}\right) \text{kg} = 52.28 \cdot 10^8 \left(\frac{r}{\text{kpc}}\right) M_\odot \ . \tag{2.53}$$

Results calculated from these equations for radii of special interest are collected in table 2.5 and the mass and density profiles are shown in fig. 2.30.

Analysing the results obtained so far and the graphs produced, we obtain important information. Basically, from the dynamics of the galaxy we deduce that its mass increases steadily with the
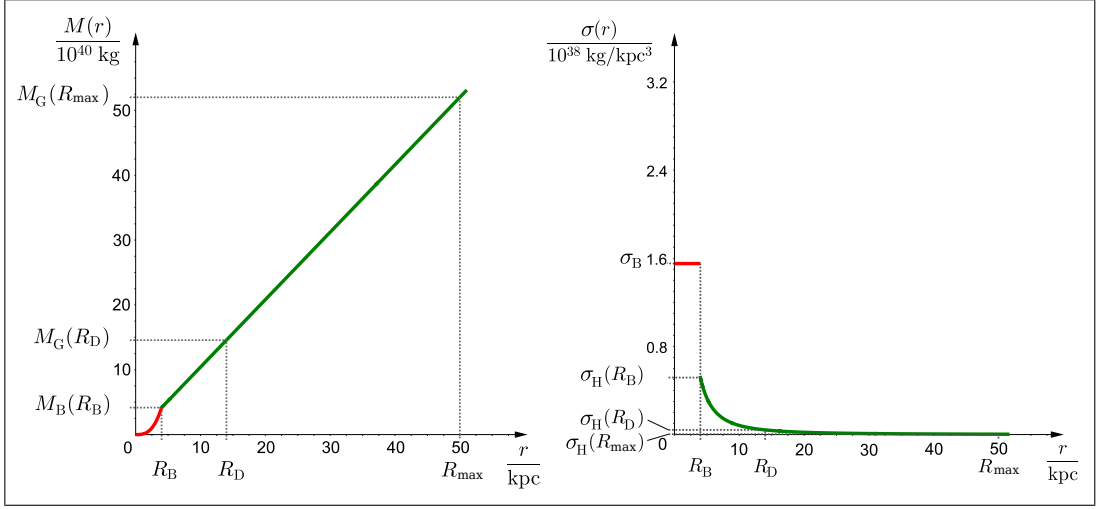
Figure 2.30: Mass and mass density profiles for the galaxy NGC3198 drawn till $R_{\max} = 50$ kpc.

radius well beyond its visible limit and it is not yet known if and where this behaviour changes. Therefore, it becomes evident that the galaxy is composed of much more mass than we can actually see, which is considered to be well-founded evidence of missing matter and therefore the basis for the hypothesis of the existence of dark matter.

Our last analysis aims to give a rough estimate of the amount of visible and dark matter for NGC3198, we will now follow a simple reasoning that will lead us to this information. For a more

NGC3198	$\sigma_{\mathrm{H}}(r)$ in kg/kpc^3	$\sigma_{\mathrm{H}}(r)$ in $M_\odot$/kpc^3	$M_{\mathrm{G}}(r)$ in kg	$M_{\mathrm{G}}(r)$ in $M_\odot$
R_{B}	$5.18 \cdot 10^{37}$	$2.60 \cdot 10^7$	$4.16 \cdot 10^{40}$	$2.09 \cdot 10^{10}$
R_{D}	$4.23 \cdot 10^{36}$	$2.12 \cdot 10^6$	$14.56 \cdot 10^{40}$	$7.32 \cdot 10^{10}$
$R_{\max}$	$3.31 \cdot 10^{35}$	$1.66 \cdot 10^5$	$52.02 \cdot 10^{40}$	$2.61 \cdot 10^{11}$

Table 2.5: Results for mass density and mass at different radii of the spiral galaxy NGC3198. $R_{\max} = 50$ kpc is the maximum radius reached for measurements.

detailed, complete and rigorous discussion and a comparison of the results with those found in the literature, see appendix D instead.

The mass-to-luminosity ratio $\frac{M}{L}$ (see appendix D), an indicator of how efficient a certain amount of visible luminous mass is in producing photons, comes to our aid in this task. In fact, since the luminosity of the celestial object we observe is given by its entire visible mass, for radii larger than the visible limit of the galaxy, fixed as R_{D}, this value obviously remains constant.

From the literature we know that for spiral galaxies the average $\frac{M}{L}$ ratio in solar units, considering their visible mass, is $\frac{M_{\mathrm{vis}}}{L} = 3\frac{M_\odot}{L_\odot}$ [94].[22] Now we calculate the same ratio by entering the total mass of the galaxy, obtained from eq. (2.53) (whose results are collected in table 2.5), and the luminosity of NGC3198 in the visual band, L_{V}, from table 2.3. We concentrate on analysing the situation at the distance of the visible radius, R_{D}, and the maximum radius reached by the observations, $R_{\max}$, obtaining $\frac{M_{\mathrm{G}}(R_{\mathrm{D}})}{L} = 10\frac{M_\odot}{L_\odot}$ and $\frac{M_{\mathrm{G}}(R_{\max})}{L} = 35.8\frac{M_\odot}{L_\odot}$. At this point we can easily achieve the results for $\frac{M_{\mathrm{vis}}}{M_{\mathrm{G}}(r)}$, $\frac{M_{\mathrm{dark}}}{M_{\mathrm{G}}(r)}$ and consequently $\frac{M_{\mathrm{dark}}}{M_{\mathrm{vis}}}$ which are collected in table 2.6. Particularly

---

[22]The luminosity of the Sun is $L\odot = 3.9 \cdot 10^{26}$ W.

NGC3198	$M_{\mathrm{vis}}/M_{\mathrm{G}}(r)$	$M_{\mathrm{dark}}(r)/M_{\mathrm{G}}(r)$	$M_{\mathrm{dark}}(r)/M_{\mathrm{vis}}$
R_{D}	0.30	0.70	2.33
R_{max}	0.08	0.92	11.50

Table 2.6: Results for the ratio between the amounts of total, visible and dark matter at different radii of the spiral galaxy NGC3198.

evident from table 2.6 is the presence of a large amount of matter that is not directly visible in the galaxy halo, the famous dark matter that is only detected by the gravitational effects it exerts on the matter we see. Therefore, in conclusion, we can describe this part of the galaxy NGC3198 as consisting of the visible disk and the dark matter halo.

2.4 Conclusions

In conclusion, we can declare ourselves satisfied with the outcomes of this project because we have been able to successfully retrace the process and principles of measurement that led to one of the first clues to assume the existence of dark matter. Moreover, we provide various theoretical exercises even without the final numerical case. These can be directly used and introduced in physics and mathematics lessons as an application to a real example from astronomy of the notions that students learn in class. This not only permits to practice the taught concepts, but also serves as a stimulus to engage and fascinate students. In fact, it has been shown [49][75][84] that teaching with help of practical and real examples, which actively involve students to experience scientific concepts, enhances their level of interest and their ability with regard to science subjects. This is due to their role as active learners and not just passive listeners, often called student-centred learning. Additionally, not only learning outcomes (physics, mathematics, astronomy and computational competencies) are positively influenced, but also the development of important skills such as problem solving, creative and critical thinking, researching, questioning, decision making and adaptability [99][49].

From direct experience and feedback from teachers who have used the project material, this project has proved to be feasible and can be implemented in the final years of secondary school and at a college level. This is especially true for the real example of the spiral galaxy NGC3198. In fact, after a few hours of introductory teaching of the background knowledge, it represents a valuable experience for the students who demonstrated to be involved with great interest in the topic and eventually showed a deeper understanding of the subject. The students' interest was driven mainly by the idea of understanding what the exotic dark-matter is and, secondly, because it is an unresolved conundrum. Furthermore, the application to the solar system in the first instance was very much appreciated by teachers, as it represents a simpler and clarifying example before moving on to the case of spiral galaxies.

Finally, we can say that this student project is a valid teaching tool to support physics, mathematics and also astronomy lectures with interesting and simple exercises that, with adequate guidance from the teacher, stimulates students' inquiry-based learning. As a whole, the project involves the story of how dark matter was hypothesised and brings students, thanks to suitable simplifications and approximations, on the same path that Vera Rubin and other scientists followed in the 1970s and then came to this hypothesis. All this is passing through important concepts such as Newton's shell theorem, Cavalieri's approach to integration, the theory of parallel projections, orbital and rotational velocity and radial velocity, the rotation curve and the innovative aspect of the introduction of the spider diagram concept.

Chapter 3

Gravitational Lensing

With this project students learn about the phenomenon of light deflection and in particular the strong gravitational lens effect in weak gravitational fields. Starting from the geometry of the system, step by step, they will understand how different models of mass distribution, which act as lenses in the universe, influence the images resulting from the gravitational lensing process. All this once again exercises the mathematical and physical knowledge of the last years of secondary school and the first years of university.

3.1 Motivation and Purpose

Light deflection, in particular the gravitational lens effect in its strong form, is an interesting and fascinating subject of astrophysics. The idea of this phenomenon already occupied the minds of great physicists of the 18th century. However, its correct formulation was presented by Einstein in his General Relativity. Nevertheless, the real interest in gravitational lensing actually began in the 1960s and received a major boost after the first detection of a gravitational lensing system in 1979 [96].

The reasons that have led us to deal with this topic are many. First of all, it is a captivating modern subject that we often hear about and that can inspire and motivate students. It is also stimulating that this phenomenon leads us to think that what we see in the universe with our own eyes does not necessarily reflect the real situation. Although it is conceptually articulated and complex, it is fortunately possible to approach this topic through a simplified method and analysis, involving different concepts of physics and mathematics typical of the last years of secondary school and first years of the undergraduate studies. All this makes gravitational lensing an excellent educational tool for teaching physics, mathematics and astronomy using examples from cosmology.

The basic idea is the visualisation of light on curved paths under the influence of gravity. In fact, by combining optics and general relativity, it is possible to design plexiglass lenses in order to reproduce the images of any source, whose light is deflected by different types of celestial objects. The work with these lenses is moreover supported by interactive simulations performed with the software Geogebra and the help of astonishing images from the best telescopes. An added value that this project has, together with the teaching tools that have been specifically designed during its development, is to enable students to combine an experimental part with a topic that is frequently treated in a purely theoretical way. Furthermore, it has the power to bring to a more accessible level a phenomenon that is normally considered out of reach and abstract, especially when treated in the educational context.

Therefore, by adopting mainly a graphical and experimental approach, we aim to highlight how this allows us to achieve the same results as those obtained analytically and in addition provides a powerful visualisation of the phenomenon we are exploring and investigating. In this way we actively involve students and free them from being mere passive listeners, promoting longer

lasting learning and the development of important skills. As we know from the previous chapter, these include problem solving, critical and creative thinking, application of the scientific method, adaptability and many more [99].

3.2   Background Knowledge

As we always do in our student projects, we now provide some essential background information for the execution of the project itself. These concepts are expressed in a basic form, but sufficient to understand the topics we deal with and will then be applied and deepened through specific examples. If teachers or students are interested in learning more about them, there are various references in the text. Obviously a deeper knowledge of the covered subjects always brings advantages and we recommend it, especially if the aim is to teach these topics, but it is not necessary for the implementation of this project.

3.2.1   Deflection of Light and The Gravitational Lens Effect

When light coming from one or more distant sources passes by a mass distribution positioned between the source and the observer, the light path is bent by the gravitational potential of the mass distribution, from now on called lens. This effect is known as gravitational lensing and the amount of bending was predicted by Albert Einstein's General Theory of Relativity.
Why do we call this effect *gravitational lens effect*? The name comes from the analogy with "real" lenses we know from optics. In fact, just as lenses deflect light rays due to their refractive power, in the universe a massive object, thanks to its gravitational attraction, deflects the rays of light that pass near it in a straight line [65].

The idea arose, however, well before Einstein and obviously starting from totally different conceptual assumptions, namely assuming that light consists of material particles, using Newtonian gravity and the Sun as lens. In fact, already Newton hypothesised this effect in his book Opticks (1704) [77]. Afterwards, Henry Cavendish, in an unpublished note (1783/84) [109][66],[1] and Johann Georg von Soldner, in a published work from 1801 [102], predicted the amount of the bending of light which was only half of the real value [17][65][95]. The amount of bending is expressed by an angle, namely the angular change of the rectilinear trajectory of the ray, that in the case of Cavendish and Soldner we call Newtonian deflection angle[2]

$$\delta_{\mathrm{N}} = 2\,\frac{GM}{R\,c^2} = \frac{R_{\mathrm{S}}}{R}\;, \tag{3.1}$$

where G is Newton's gravitational constant, M the mass of the deflecting body (lens), R the radius of the lens and obviously the smallest possible distance of the light ray from its centre, c the velocity of light and R_{S} the Schwarzschild radius[3] of the lens. This result (and all the following) is valid only if $\frac{GM}{Rc^2} \ll 1$, which is the case of weak gravitational fields,[4] where the value of the gravitational potential is $|\Phi| = |\frac{GM}{R}| \ll c^2$, and true for all the cases we are going to analyse [65][76][94][115]. Actually, in his first attempt also Einstein obtained one half of the correct value. This was in 1911 using the equivalence principle and assuming that the spatial metric is Euclidean. Then in 1915, elaborating and completing his General Theory of Relativity, he corrected this result

---

[1]It is thought that this note may have been written in 1783/84, inspired by a letter from Reverend John Michell (1724-1793) dated 26 May 1783 [118]. However, there are some authors who argue that it was written no earlier than 1804 because of the watermarks on the piece of paper [51].

[2]The Newtonian deflection angle is derived in books of classical mechanics or see also [17][65].

[3]In General Relativity, the Schwarzschild radius is the smallest radius of a celestial object of a given mass for which a light ray can escape.

[4]Not to be confused with weak gravitational lens effect.

and for the first time the real amount of light bending was known [76]. The correct value is in fact twice his previous estimate, because the curvature of space has to be taken into account. In addition, General Relativity allows another interesting interpretation that leads to the same correct result and makes the analogy with geometric optics clear. Basically, the space in which the light propagates can be considered locally flat and the lensing effect the result of a weak perturbation due to the Newtonian gravitational potential of the lens, expressed by an effective refractive index $n(r) = 1 + \frac{R_S}{r} = 1 - 2\frac{\Phi}{c^2}$ dependent on the distance r from the lens itself (as if the space were hypothetically pervaded by a medium with this characteristic). At this point, applying Fermat's principle,[5] it is possible to derive the deflection angle [65][73][76][95]. This approach is very similar to the idea of the "fata morgana" (mirage) phenomenon on Earth caused by the temperature and density gradient of the lower atmosphere [65][85]. Ultimately, the correct deflection angle[6] is expressed by

$$\delta = 4\,\frac{GM}{b\,c^2} = 2\,\frac{R_S}{b}\,, \tag{3.2}$$

where b represents the distance of the light ray from the lens centre which is called impact parameter. This gives an estimate for the deflection of a light ray passing at the solar limb ($b = R_\odot$) of $\delta = 2\delta_N = 1.75''$. Einstein's prediction about the deflection of light was proven during the solar eclipse of 29 May 1919 and this was also the first observation of the gravitational lens effect which made Einstein and his theory famous in the entire world [17][65][95].

Einstein was also the first to consider the fact that other stars besides the Sun could act as gravitational lenses and deflect light of distant sources from its original path. But he gave no hope to such observations for basically two reasons. In fact, he considered the necessary alignments between the stars and the observer highly unlikely and, moreover, the order of magnitude of such effects was too small to be actually observed with the instruments of that time [24]. In this respect, it was the astronomer Fritz Zwicky who, in 1937, suggested to consider galaxies, called at that time nebulae, instead of stars. Basically, these newly (from 1923) defined extragalactic objects had two advantages in the theoretical framework of gravitational lensing: they are much more massive than single stars and they are extended, therefore the necessary alignment is not so improbable anymore [120]. However, the real interest in gravitational lensing began in the early 1960s with independent research by S. Refsdal, S. Liebes and Yu. G. Klimov and the contemporary discovery of quasars [96].

Nevertheless, it still took more than a decade before the first gravitational lens system was observed in 1979. Indeed, Walsh, Carswell and Weymann discovered the first gravitational lensing, the quasar QSO 0957+561A,B, nowadays known as the Twin Quasar [96]. Hence a long history of observations and discoveries began.

The optical illusions of gravitational lensing in the universe can be created by different celestial objects. In fact, not only stars, but also quasars, galaxies and clusters of galaxies are involved in the process as sources and lenses. Basically, it is possible to distinguish three types of gravitational lensing [17][65]:

- **Strong** lensing, with resolved multiple images of distant sources. Among the various images are arcs as well as Einstein rings and crosses. In this case quasars, galaxies or clusters of galaxies are counted among the typical light sources, while the lenses responsible for this effect are galaxies or clusters of galaxies. Moreover, a high degree of source-lens-observer alignment is required for this type of effect to occur. The strong gravitational lensing permits to explore the distribution of matter within the lenses, including luminous and dark matter, and to determine cosmological parameters, like for instance the Hubble constant.

---

[5]"The light path between two points is the one that takes the least time" is a common formulation of Fermat's principle which is correct in most cases.

[6]The Einsteinian deflection angle is derived in many books on gravitational lensing, for example [17][73][76].

- **Weak** lensing, with alteration of shape and orientation of the sources, but without the production of multiple images. For detecting this effect, statistical analysis of many sources is required, in fact on a single object it cannot be inferred. In this case galaxy clusters are the lenses that distort background galaxies giving rise to cosmic shear that describes how the large-scale structure affects the shape of galaxies. Thanks to this effect it is possible to explore the mass concentration of celestial objects involved and also the large scale structure of the universe between observer and source.

- **Micro** lensing, with multiple images that cannot be resolved. It is possible to infer this effect from measuring the total brightness amplification of all the lensed images produced when source, lens and observer are in relative motion. Typical sources are stars and typical lenses are other stars, (exo)planets and other faint objects. An example is given by stars in the Large Magellanic Cloud as sources and MACHOs[7] in the Milky Way's halo as lenses. Of course the alignment source-lens-observer plays here a fundamental role and since it is a rare event, many stars have to be regularly monitored. This effect is used in searching for extrasolar planets and was also used for determining if MACHOs are components of dark matter.

In this project we take into consideration only the strong gravitational lensing in weak fields. This is because in nature it offers stunning images able to fascinate students and raise their motivation in understanding such a phenomenon and also because it better suits our educational goals, especially when it comes to the analogy and combination with classical optics. Once more, with this work, we have the opportunity to introduce research-validated activities to enhance the knowledge-building process of students [113]. In addition, by engaging students with in-class demonstrations, their interest increases and they can better appreciate this topic. Without underestimating the fact that with the introduction of other already-covered subjects, such as optics, the learning process is facilitated [47].
We aim for approaching gravitational lensing in the simplest way possible, in order to give the chance to our students to understand the key mechanism and the consequences of this process. The theme is theoretically quite complex, but it is possible, thanks to simplified models and appropriate approximations, to give students an insight into the subject. The simplest models for gravitational lenses are axially symmetric[8] [94], therefore we restrict our reasoning to such lenses. Furthermore, in our simplified models the expressions involved in describing this gravitational lens effect can be derived and discussed even in upper high school.

3.2.2 The Gravitational Lensing Geometry and The Deflection Angle

At this point we have a basic idea of how gravitational lensing works (fig. 3.1), however, before analysing this theme more deeply, we need to understand the geometry of the lens system and clarify some concepts, approximations and simplifications used as the basis of this project. Moreover, considering our target audience, we do not follow the more general approach based on General Relativity (see for example [4] or [5]), but limit ourselves to a more elementary one.
First of all, for simplicity and to reach our educational goals without distracting the attention of our students with intricate calculations, as said, all models of gravitational lenses we consider are axially symmetric. This fact brings the advantage that we can replace vectors by appropriate scalar quantities because in this case light deflection is independent of the azimuthal angle [17]. Thanks to the lens symmetry, additionally, the light rays from the source can be considered as confined

---

[7]MAssive Compact Halo Objects, e.g. brown dwarfs, Jupiter-like planets and other stellar remnants.

[8]The axisymmetric lens is when its mass distribution has spherical or cylindrical symmetry in three dimensions, corresponding to circular symmetry in two dimensions [17].
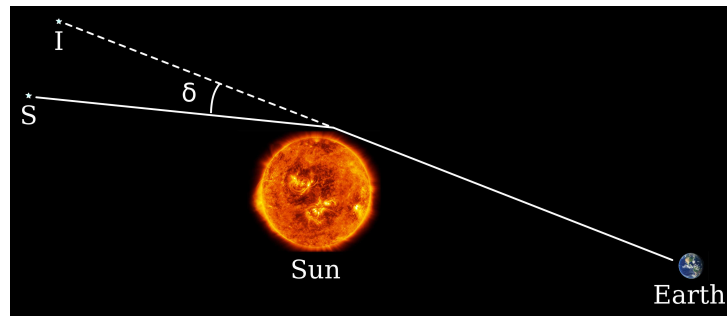
Figure 3.1: Representation of the gravitational lens effect (not to scale and exaggerated) of the system consisting of a distant star, the Sun and the Earth. We can see the indicated deflection angle δ, the actual position of the star S and its apparent position I as seen from Earth. Credit: (Sun) NASA/SDO/Seán Doran – (Earth) NASA Earth Observatory images by Robert Simmon.

in the plane defined by source, lens and observer. This plane cannot be defined in case of their perfect alignment [95], an important detail for this special case that we will recall later. Thanks to this simplification, many of the most important lensing concepts can be derived without problems. Focusing our attention now on the geometry of the gravitational lens system, whose general, schematic representation[9] produced with the software Geogebra is in fig. 3.2, we define the line connecting observer and lens $\overline{OL}$ and its extension as the "optical axis" of the system. The optical axis is perpendicular to the source and lens plane which are respectively at the source and lens distance from the observer [94]. Basically, in absence of the lens L, the observer O would directly
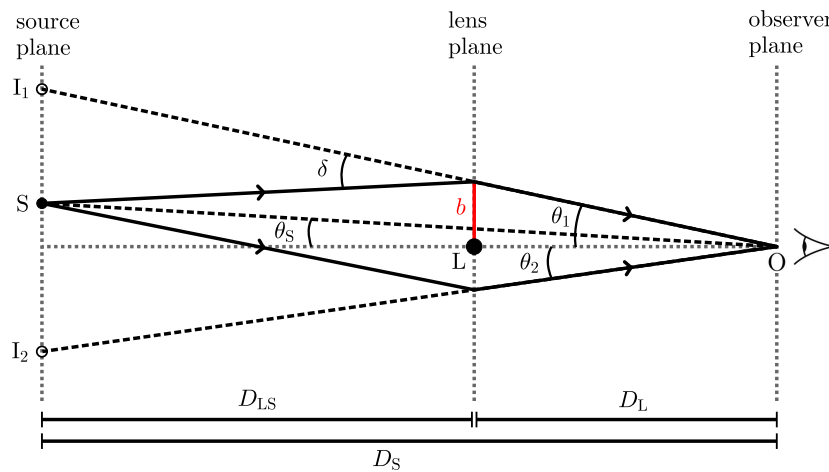
Figure 3.2: Geometry of the general situation of the gravitational lens effect (in this diagram the angles are intentionally highly exaggerated). The line starting from the observer O and passing through the lens L (that we call "optical axis" [95]) is the starting point for defining the angles that correspond to the position of the source, θ_S, and the position of the images, θ_1 and θ_2. It is to be noticed that the image I_1 appears on the same side as the source with respect to the optical axis and the second image I_2 on the opposite side (and so it will always be in what follows). The angular separation of the images is $\Delta\theta = |\theta_1| + |\theta_2|$, δ is the angle of deflection and b the impact parameter in the lens plane.

look at the source S in its true position. But the presence of L deflects the light from S by the angle δ, so that O cannot look directly at S anymore and sees instead two images,[10] I_1 and I_2, of

---

[9]Also in this case, when teaching, explanatory diagrams are important to understand the topic and they can be used as printed copy or as file.

[10]Although only one image is also possible, in general, multiple images are produced, even more than two.

the source in different positions. As we can infer from the figure, what we are able to measure are the angular distances with respect to the lens of the various elements of the system, normally expressed in arcseconds[11] ($''$). Thus, θ is in general defined as the angular separation of an image and θ_S that of the source in its actual position, both with respect to the lens. It is in this way that for instance the image I_1 is characterised by the angular distance θ_1 from the lens and this type of notation will henceforth be maintained and used interchangeably. In addition, unless stated otherwise, we always consider $\theta_S \geq 0$ and in the same way any distance on the same side. Then D_L is the distance of the lens and D_S of the source from the observer, D_{LS} is instead the distance of the source from the lens. These distances are normally very large, hence cosmologically important, and in cosmology the concept of distance is not unique and can be quite complex. In the context of gravitational lensing we actually use angular-diameter distances which require a cosmological model and in general $D_{LS} \neq (D_S - D_L)$ [17][95]. Only when we consider redshifts $z \ll 1$, like in the Local Group, we recover the additivity of distances ($D_{LS} = (D_S - D_L)$) [94]. This brings us to the next simplifications. In fact, since the distances involved between source, lens and observer are much larger than the spatial extent of the lens, we can apply two more approximations:

- the small angle approximation,

- the thin lens approximation.

As we already know, the strong lensing effect that we consider occurs in the weak gravitational field regime and $\Phi \sim -1/r$. This means that in our models the distance b, which describes the position of the light ray with respect to the lens centre, is always much larger than the Schwarzschild radius R_S of the lens, consequently the deflection angle is small, $\delta \ll 1$. This is true also if we choose b shorter than the actual border of the lens, for example when a ray passes through the transparent parts of a galaxy. In this case, according to Newton's shell theorem treated in section 2.2.2, R_S does not include the entire mass of the lens, but only the fraction of mass enclosed inside b. Again, thanks to Newton's shell theorem, the mass of the celestial object (or part of it) acting as deflector can be considered concentrated at its centre and in this way we draw it in our graphs and simulations.

Specifically, in the cases of gravitational lensing that we are going to study, the angles involved are always small. And this is true for all observed lensing effects in the universe, the angular separation between images is in fact always below $30''$ [95]. This fact allows us to use the first approximation, which brings the advantage that it is possible to interchangeably replace lines by arcs, as well as surface elements of the celestial sphere by corresponding tangential planes. In the second approximation, we can assume that all the lens mass is confined in a plane, the lens plane. If the lens is a galaxy, but even if it is a cluster of galaxies, this condition is fulfilled to very good extent if we remember that the size of a galaxy is typically $\sim 100\,\text{kpc}$ while the distances of lens and source are typically of the order of Gpc [94], which is about three orders of magnitude larger than the diameter of a typical galaxy cluster [76]. This also means that we can consider the gravitational lensing to occur at a point close to the lens instead of being a continuous process and therefore the light path is approximated by two consecutive straight lines (the asymptotes of the the real ray trajectory [95]). Thanks to these approximations, we can consider to a good extent the distance b from the lens centre as the impact parameter in the lens plane and it can be read off from fig. 3.2 that $b \approx \theta D_L$.

At this point we express the deflection angle δ, namely the amount of bending of the light path which was predicted by Einstein's General Relativity, in a more general form, suitable for all possible mass distributions describing the lens and different impact parameters:

$$\delta(\theta) = \frac{4G}{c^2} \frac{M(|\theta|)}{\theta D_L} \; . \tag{3.3}$$

---

[11]An arcsecond is $1/3600$ of an angular degree.

The modulus is here included because θ is not always a positive quantity because we describe also images that form on the other side of the optical axis of the lens system. In particular if $\theta > 0$, then $\delta > 0$ and, vice-versa, if $\theta < 0$, then $\delta < 0$ [17]. It is interesting to note that in eq. (3.3) the ratio $M(|\theta|)/\theta D_L$ expresses the strong dependence of the angle of deflection on the mass of the lens and on the impact parameter. In fact, $M(|\theta|)$, according to Newton's shell theorem, is the mass within the impact parameter $b \approx \theta D_L$, the only mass that acts gravitationally on the light ray, bending it [94]. From now on this equation is used in this project when working with the deflection angle δ.

3.2.3 The Lens Equation

The fact that the observer does not see the original source due to gravitational lensing, but rather images of it in different positions on the sky is now established. These images are deformed in various ways and deformations include, among other effects, also multiple images of the same source, arcs and rings. In this regard, we have to consider the fact that size and shape of the source, different mass distributions for the lens and the relative positions of source, lens and observer affect number, position, size and shape of the resulting images. All this and the geometry of the lens system is taken into account by the lens equation

$$\theta - \theta_S - \delta\,\frac{D_{LS}}{D_S} = 0\,,\tag{3.4}$$

whose solution gives us the information about the resulting images. To derive the lens equation is quite simple and a nice exercise. In fact, considering fig. 3.3, which without loss of generality
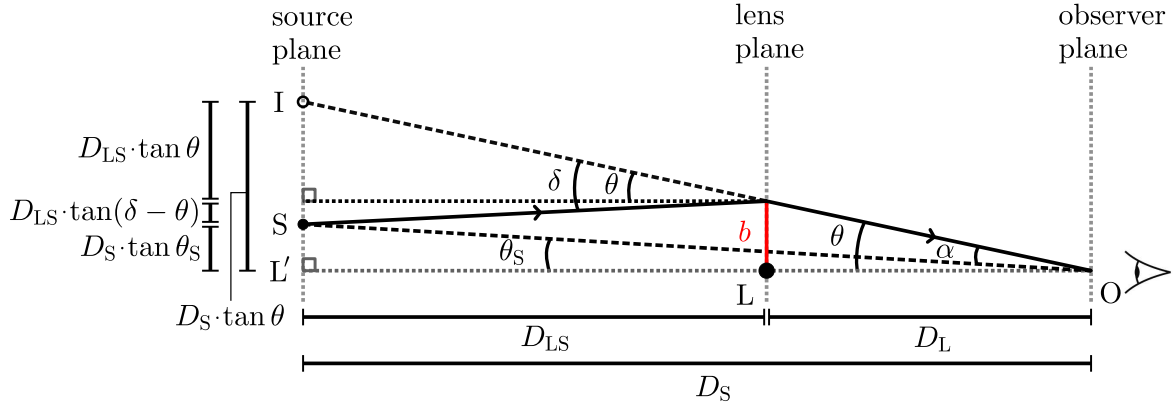
Figure 3.3: Detail from fig. 3.2 regarding only one side of the optical axis and thus one produced image I. Taking into account the approximations explained in section 3.2.2, the distance $\overline{L'I}$ is first defined as a whole distance and then also as the sum of the smaller distances that constitute it. As we saw in the previous section, under the same approximations we define the impact parameter $(b = D_L \cdot \tan\theta \approx \theta D_L)$.

focuses only on one of the produced images and includes $\theta_S \geq 0$, we deduce that

$$D_S \cdot \tan\theta = D_S \cdot \tan\theta_S + D_{LS} \cdot \tan(\delta - \theta) + D_{LS} \cdot \tan\theta\tag{3.5}$$

and

$$\theta = \theta_S + \alpha\,.\tag{3.6}$$

If we now apply the small angle approximation to eq. (3.5) and rearrange the terms more conveniently, we get exactly eq. (3.4). In addition, according to eq. (3.6), eq. (3.4) defines also

$\alpha(\theta) = (D_{\mathrm{LS}}/D_{\mathrm{S}}) \, \delta(\theta)$, sometimes called the reduced deflection angle [17]. Introducing now the deflection angle δ from eq. 3.3) in eq. (3.4), we obtain the lens equation

$$\theta - \theta_{\mathrm{S}} - \frac{4G}{c^2} \frac{M(|\theta|)}{\theta} \frac{D_{\mathrm{LS}}}{D_{\mathrm{L}} D_{\mathrm{S}}} = 0 \; . \tag{3.7}$$

At this point it is indeed possible to study many different mass distributions $M(|\theta|)$ for the lens and observe the corresponding outcomes, obtaining clear information about what the observer sees. In particular, since we are adopting the thin lens approximation, when we solve the lens equation for a specific deflecting object, $M(|\theta|)$ represents the projection on the lens plane of the chosen mass distribution (see appendix F). Moreover, at first glance eq. (3.7) looks like a simple quadratic equation, but we have to be careful because, once a function for the mass distribution is introduced, it could totally change the situation and turn the equation into a much more complicated one. We will later explore few cases in section 3.3.1.1. Basically, thanks to the lens equation, we are able to describe every possible configuration for the lens system and deduce important information on the images resulting from the gravitational lensing process.

A special case is represented by the perfect alignment of observer, lens and source which occurs when $\theta_{\mathrm{S}} = 0$. As we know, in this situation there is no plane defined by source, lens and observer. Therefore, due to full symmetry, in most cases the image of the source is seen as a ring around the lens, the so-called Einstein ring. This ring remains constant for each individual configuration and its radius is expressed from eq. (3.7) by

$$\theta_{\mathrm{E}} = \frac{4G}{c^2} \frac{M(|\theta_{\mathrm{E}}|)}{\theta_{\mathrm{E}}} \frac{D_{\mathrm{LS}}}{D_{\mathrm{L}} D_{\mathrm{S}}} \qquad \text{or} \qquad \theta_{\mathrm{E}}{}^2 = \frac{4GM(|\theta_{\mathrm{E}}|)}{c^2} \frac{D_{\mathrm{LS}}}{D_{\mathrm{L}} D_{\mathrm{S}}} \; . \tag{3.8}$$

Specifically, we observe also in this case the dependence on the lens mass enclosed inside the ring and the distances involved. This leads to the fact that in case of detection of an Einstein ring, knowing all other elements, we are able to calculate exactly this mass. In addition, since the Einstein ring radius is constant for a specific considered configuration, if the ring exists, we can express the lens equation (eq. (3.7)) in terms of its radius θ_{E} as

$$\theta - \theta_{\mathrm{S}} - \frac{M(|\theta|)}{M(|\theta_{\mathrm{E}}|)} \frac{\theta_{\mathrm{E}}{}^2}{\theta} = 0 \; . \tag{3.9}$$

The solutions of the lens equation tell us how many images are produced as well as their position with respect to the lens centre on both sides of the optical axis. It can be applied also to extended sources, as we will discuss later in section 3.3.1.2, describing in addition the distorted shape of the images.

3.2.4 Magnification

The images created by gravitational lensing are not only in different positions with respect to the original source, but also their shape and brightness are affected by this process. This happens because light rays are normally deflected by different amounts depending on their distance from the lens centre in the lens plane (expressed by the impact parameter b) and the considered model for the lens. This phenomenon is known as differential deflection [94]. This gives rise to a pure geometrical effect called magnification which involves the solid angles subtended by the images, $d\Omega_{\mathrm{I}} = dA_{\mathrm{I}}/D_{\mathrm{S}}^2$, at the position of the observer, magnifying or demagnifying them in comparison with the solid angle subtended by the source, $d\Omega_{\mathrm{S}} = dA_{\mathrm{S}}/D_{\mathrm{S}}^2$ [94]. Consequently, as seen from the observer, in the source plane the area that the source would span in absence of the lens, dA_{S}, and the area actually spanned by the lensed image, dA_{I}, as well as their shapes, are in general different. This is schematically shown in fig. 3.4 and the discussion is as always confined to our simplified model and the explained approximations.

In particular, the gravitational lensing does not involve emission or absorption of radiation, therefore the number of photons is conserved and the surface brightness ($[\mathrm{d}I] = \frac{\mathrm{W}}{\mathrm{m}^2 \cdot \mathrm{sr}}$) remains constant [95]. However, the flux density ($[\mathrm{d}F] = \frac{\mathrm{W}}{\mathrm{m}^2}$), given by the product of surface brightness and solid angle, changes due to the (de-)magnification of the solid angle and the resulting image appears brighter (or dimmer) [95]. At this point, the simplest way to derive the magnification,
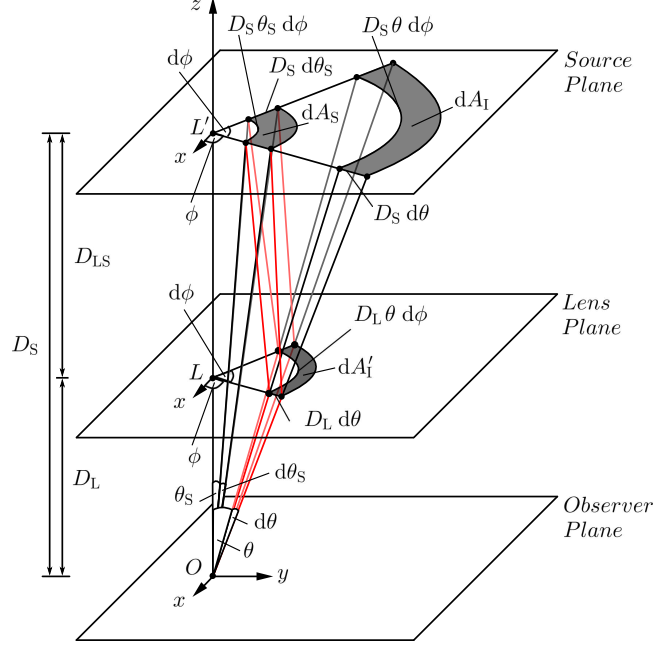
Figure 3.4: Geometry of magnification.

namely this change in flux density or spanned area or solid angle, is described by

$$\mu = \frac{\mathrm{d}F_\mathrm{I}}{\mathrm{d}F_\mathrm{S}} = \frac{\mathrm{d}\Omega_\mathrm{I}}{\mathrm{d}\Omega_\mathrm{S}} = \frac{\mathrm{d}A_\mathrm{I}}{\mathrm{d}A_\mathrm{S}} \ . \tag{3.10}$$

In fact, if we consider an infinitesimal source, as illustrated in fig. 3.4 (remember that all approximations hold), the corresponding spanned area,[12] $\mathrm{d}A_\mathrm{S}$, is given by multiplying the arc lengths corresponding to the radial and tangential dimensions of the source area. The result is

$$\mathrm{d}A_\mathrm{S} = D_\mathrm{S}{}^2 \cdot \theta_\mathrm{S} \, \mathrm{d}\phi_\mathrm{S} \, \mathrm{d}\theta_\mathrm{S} \ . \tag{3.11}$$

In the same way the area spanned by the image is

$$\mathrm{d}A_\mathrm{I} = D_\mathrm{S}{}^2 \cdot \theta \, \mathrm{d}\phi_\mathrm{I} \, \mathrm{d}\theta \ . \tag{3.12}$$

Since our models are axially symmetric, it is true that $\mathrm{d}\phi_\mathrm{S} = \mathrm{d}\phi_\mathrm{I} = \mathrm{d}\phi$ (the deflection is purely radial) [17], hence the magnification is expressed by

$$\mu(\theta) = \frac{\mathrm{d}A_\mathrm{I}}{\mathrm{d}A_\mathrm{S}} = \frac{\theta}{\theta_\mathrm{S}} \frac{\mathrm{d}\theta}{\mathrm{d}\theta_\mathrm{S}} \ . \tag{3.13}$$

We can identify in the first factor $\mu_\mathrm{t} = \frac{\theta}{\theta_\mathrm{S}}$ the tangential magnification and in the second $\mu_\mathrm{r} = \frac{\mathrm{d}\theta}{\mathrm{d}\theta_\mathrm{S}}$ the radial magnification, obtaining $\mu = \mu_\mathrm{t} \cdot \mu_\mathrm{r}$ [17].
By definition, for the real source $\mu = 1$, namely it is not magnified. In this perspective, an

---

[12]This result comes from the surface element of a sphere with radius R, $\mathrm{d}A = R^2 \cdot \sin\theta \, \mathrm{d}\phi \, \mathrm{d}\theta$, applying also the approximation $\sin\theta \approx \theta$.

image with $|\mu| > 1$ is brighter than the source and with $|\mu| < 1$ dimmer. The sign of μ instead determines the orientation of the image with respect to the source. This is called image parity and we can see an example of this effect in fig. 3.5. Basically, and this is valid for every θ_S, for images on the source side with respect to the lens with $\mu > 0$, the parity is positive and they are oriented like the source. On the other side of the lens, if $\mu < 0$, the parity is negative and the images are upside-down with respect to the source, flipped around the horizontal axis. However, if on this side $\mu > 0$, the parity is positive and this means that we have a double-flip on both the horizontal and vertical axis [22], as we will see later exploring various models. It is moreover

Figure 3.5: Example of parity for images from a lensed source. Left: Original un-lensed source (disk of 6 cm diameter). Right: Images produced when the source is seen through a plexiglass lens that reproduces the lensing effects of a point mass lens. Thanks to the different colours, we can observe that the image on the right (same side as the source) is oriented exactly as the source, thus it has positive parity. The image on the left instead is upside-down, inverted about the horizontal axis, hence the parity is negative. (Picture taken with our own equipment, see section 3.3.2.3)

interesting to note from eq. (3.13) that when $\theta_S \to 0$ then $\mu \to \infty$, this is the case of perfect alignment source-lens-observer. With this configuration we normally expect a ring, therefore a high brightness, but still finite. In fact, this result is not real, images cannot be infinitely bright, and real sources, however small, always have a finite extent [95].

Finally, since the magnification can be calculated for each image of the source, the sum of the absolute values of the individual magnifications $\mu_{\text{tot}} = \sum |\mu_I|$ gives the total magnification, which is purely an expression of the change in brightness of the source due to lensing [17].

It is clear that this topic involves a basic knowledge of infinitesimal calculus and the concept of solid angle, thus it is considered for a slightly more advanced audience. However, according to [108] and [38], we expect students at the end of secondary school to have such basic knowledge, at least as far as infinitesimal calculus is concerned. Instead, speaking of solid angle, it is possible to find nice explanations at the level of knowledge of secondary-school students in textbooks or on-line, for instance [2][56][116].

This reasoning can also easily be generalised when considering extended sources with homogeneous surface brightness. In that case for the magnification we get $\mu = \frac{F_I}{F_S} = \frac{\Omega_I}{\Omega_S} = \frac{A_I}{A_S}$. Conversely, if the surface brightness is not homogeneous, the calculations are too complex and bring us out of our educational purposes, thus we do not treat this case. Nevertheless, if interested in learning more about this subject, see [17], [95] and [96].

3.2.5 General Relativity Meets Optics

We have already mentioned the analogy between gravitational lensing and "real" lenses in optics and we now want to explore this aspect. The goal is to effectively combine General Relativity and optics in order to understand the properties of the lensing effect in the framework of the optical properties of a weak gravitational field characterized by the law of light deflection [92].

If we imagine that in the universe instead of a mass distribution there is a huge lens made of glass of refraction index n that deflects light rays exactly as the mass distribution would, it is

possible to study the characteristics of this hypothetical glass lens. Obviously the glass lens must have a special shape that depends on the mass distribution we want to represent. So how can we understand which profile the glass lens must have in order to represent and simulate the effects of a mass distribution of our choice? It is precisely for answering this question that we need to combine what we know from General Relativity and optics [85]. This procedure is not so complex as it seems, especially in our simplified approach. In fact, from experience, it is feasible to perform it with students of the last years of secondary school, especially if they are particularly interested in the subject.

Referring to fig. 3.6, we apply now this method and see how to extrapolate the general profile for the glass lens. First of all, one side of our glass lens is taken to be flat for simplicity, perpendicular
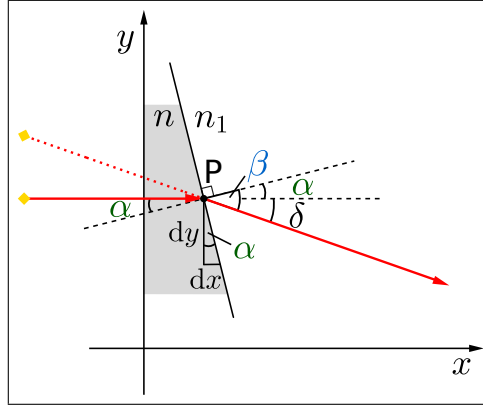
Figure 3.6: Deflection in P of a light ray travelling through two media with different index of refraction $n > n_1$ ($n_1 = 1$ is air) according to Snell's law and introduction of the deflection angle δ.

to the incoming-from-infinity light rays[13] and lies on the y-axis of the coordinate system we have introduced in fig. 3.6, the origin of which is in the center of the lens just on the flat side. We must therefore deduce the shape for the other side. Secondly, our lens models are, as always, axially symmetric and consequently the glass lens will be rotationally symmetric, hence it is enough to calculate the profile in two dimensions and then rotating it around a central axis in order to get the entire lens. Indeed, this simplifies our work considerably. The inclined black line in fig. 3.6 represents the tangent line to the surface of the glass lens in the point P. If we can understand how the tangent line changes for all points of the lens, it is possible to find the corresponding function which describes the shape of the lens. Basically, what we need is the deflection angle δ from General Relativity and Snell's law from optics. Let's introduce these concepts analysing fig. 3.6. We know that, when passing near a massive object, at a distance $b = y_P$, the path of a light ray from a distant source is deflected. This path is represented by the red arrows in the diagram. The amount of deflection at any point of the lens, as we know, is represented by the deflection angle δ, expressed by eq. (3.3). If we now apply Snell's law[14] to this configuration and make use of the trigonometric angle sum and difference identities,[15] we obtain

$$n = \frac{\sin(\alpha + \delta)}{\sin \alpha} = \cos \delta + \cot \alpha \sin \delta \ . \tag{3.14}$$

From eq. (3.14), inserting eq. (3.3) for the angle δ, and from the diagram, we see that

$$\frac{\mathrm{d}y}{\mathrm{d}x} = -\cot \alpha = -\frac{n - \cos \delta}{\sin \delta} \approx -\frac{n - 1}{\delta} = -\frac{(n-1) \, c^2}{4 \, G \, M(|y|)} \cdot y \ , \tag{3.15}$$

---

[13]Since the distances involved are very large, when the light rays reach the lens plane they are practically perpendicular to it and parallel to each other, like if they were coming from infinity.

[14]From fig. 3.6 Snell's law is $n \cdot \sin \alpha = n_1 \cdot \sin \beta$.

[15]$\sin(\alpha \pm \beta) = \sin \alpha \cos \beta \pm \sin \beta \cos \alpha$

where the deflection angle and the mass are expressed as functions of the y coordinate of point P and the small angle approximation is certainly used. At this point, substituting in the place of $M(|y|)$ the chosen mass distribution (the mass enclosed inside y and projected onto the lens plane) and solving this differential equation, the profile of the corresponding glass lens is obtained. Indeed, for mass distributions not too complicated, this differential equation is easily solved separating the variables and integrating and offers a nice mathematics practice applied to a real example, as we will later see in section 3.3.2.

We are aware that solving differential equations for secondary school students is not common practice. However, according to our direct experience and as written in [108] and [38], as long as elementary functions are concerned it should be taught and above all it is totally feasible.[16] Therefore, we think it is stimulating to involve even younger students in this type of reasoning and exercise. So that they can, stimulated also by curiosity, discover the shape of simple glass lenses that simulate the effects of gravitational lensing. Thanks to this connection between General Relativity and optics, a subject such as gravitational lensing, which can be abstract to most people, can be brought back to a more everyday level.

3.3 Exploring and Visualising Gravitational Lensing

Everything we have seen so far derives from the theory of light deflection and the real gravitational lens effect that we observe in the universe, obviously restricted to our simplified models and with all the approximations of the case. Nevertheless, under the same conditions, it is totally applicable also to the effect resulting from computer simulations of gravitational lensing produced with Geogebra or when the effect is reproduced using special plexiglass lenses. These alternatives give us the possibility to approach the topic from a different point of view and to apply the just-explored notions, which is in fact the focus of this new section and of the following ones. In addition, an example of activity which makes use of these educational tools, tested several times also with students at the end of secondary school, is presented in appendix G.

The basic idea is to be able to visualize the light on curved paths and analyse the characteristics of this process. As for the teaching aspect, the inspiration for the development of such teaching tools came from the work of scientists such as the Norwegian astrophysicist Refsdal, who tried to reproduce what the gravitational lens effect should look like, combining different knowledge, techniques and tools. Indeed, gravitational lensing, as we know, comes from a theoretical prediction made by Einstein decades before it could actually be detected. These are the reasons why it is a topic that is very often addressed from a purely theoretical point of view and it is obviously not possible to experiment with this kind of lensing. The question we want to answer from a teaching point of view is therefore how we can reproduce this effect on a small scale so that we can study it more closely and perhaps deal with it by adding an experimental note to the theoretical explanation. This is a way to attract students' attention and involve them in an active understanding of these concepts and not just as passive listeners. An approach that, as we know from the previous chapter, stimulates and promotes a deeper and more lasting acquisition of knowledge, as well as interest in scientific topics and the development and strengthening of important skills.

Our primary interest falls on galaxies as gravitational lenses. This is because galaxies offer a variety of shapes and internal morphologies and these objects can also be used to trace the distribution of dark matter.[17] This last aspect in particular comes from the fact that gravitational lensing is independent of the nature and state of the deflecting matter, therefore equally sensitive

---

[16]We do not expect students to solve differential equations, but by giving them the solution they are able to insert it into the differential equation and prove its correctness.

[17]Thus providing a second independent method for estimating the possible amount of dark matter, comparable with the results obtained with the rotation curves in Chapter 2.

to dark and visible matter [94]. The idea is that a galaxy, being made of stars, has "transparent" space between them, therefore it makes sense to choose an impact parameter inside the galaxy and study the result of the lens equation at different radii, always keeping in mind Newton's shell theorem (section 2.2.2).

As in the students project on dark matter, the content of this chapter can be divided and used to practice specific physics and mathematics topics through individual exercises applied to a real problem. This includes, among others, geometric optics and the concept of refraction, as well as the solution of equations of various degrees, geometry and differential calculus.[18] However, when considered in a single piece, this work represents a student project on the discovery of this effect due to gravity and on the understanding and visualization of this phenomenon bringing it back to a more accessible dimension. And now we are going to explore these teaching tools for visualising the gravitational lensing effect: computer simulations with Geogebra and special plexiglass lenses.

3.3.1 Computer Simulations of Gravitational Lensing Using Geogebra

Wanting to be able to visualise the gravitational lens effect, one tool that can accomplish this task is the use of computer simulations. In this regard we wanted to use the familiar Geogebra software for the educational and practical reasons we already know. The goal is to create such simulations for different lens models whose mass distribution is representative of galaxies. In this perspective, eight mass distributions were chosen and analysed as gravitational lenses: Point mass lens, Plummer sphere lens, Uniform disk lens, Singular isothermal sphere (SIS) lens, Kuzmin disk lens, SIS with a core lens, Spiral galaxy lens, Navarro-Frenk-White (NFW) lens.

Among these models we have focused mainly on the first five because, as we will see later, from an accurate comparison the other three give results very similar to one or another lens, thus we have chosen to deepen the easiest with regard to the equations involved. Furthermore, at the beginning the source is considered to be point-like for simplicity, however we will see later cases of extended sources and thus rise to a slightly higher degree of difficulty.

We would also like to point out that the use of such simulations in the classroom offers a very high degree of interactivity and provides many insights that are usually deduced by other approaches, e.g. the ray-tracing diagram method [85]. And in addition to the use of our files, after having understood the concepts that we will now see, it is also possible for anyone with a basic knowledge of Geogebra software to reproduce such simulations or create new ones. The students themselves appreciate the use of such educational means at first hand, which among the various benefits (we will discover them during the next sections) include the consolidation of computer skills. However, it is always possible to use frames from such simulations for teaching purposes, perhaps enlarged and printed clearly visible or as static illustrations, as we for obvious reasons use for the examples given in this thesis.

3.3.1.1 Graphical Solution of the Lens Equation and Image Magnification

We all know that using natural curiosity to stimulate the students' interest in these and other incredible phenomena helps the learning process. Allowing indeed in this way the development of deeper and longer term knowledge that can be then applied to more and more complex examples. And so, stimulated by curiosity, while teaching the concept of light deflection some useful questions that may for example arise are: *How many images of a distant source could we see if its light, during the journey, passes near a black hole or a galaxy? Where would we see these images? How bright would they be?* As said in sections 3.2.3 and 3.2.4, the answers arrive solving the lens and the magnification equations. This is the reason for investigating these equations and

---

[18]As stated in [108] and [38], secondary school students (K12) are able to perform differential and integral calculus applied to elementary functions, such as the exponential function.

for this reason we are going to study now these several examples of gravitational lenses. For these examples we have chosen that they contain inside the Einstein radius the same amount of mass, so that, when present, the size of the Einstein ring is always the same.

First of all, let us consider the Einstein ring defined by eq. (3.8) and lens equation eq. (3.7) for each lens model of our interest. Once it has been proven that the ring exists, let us insert the Einstein ring radius θ_E in eq. (3.7), together with the chosen mass distribution and then we solve it. In particular, the usefulness of the graphical solution of this equation, performed with Geogebra, is emphasised. This is because it actually provides a simulation of gravitational lensing that permits us to visually study the effect for different positions of the source, as seen in projection, with respect to the system's optical axis. Since in the case of point-like sources we obtain point-like images, in order to obtain information about their brightness, we calculate then the magnification of the observed images, thanks to eq. (3.13). In this respect we will see once again that Geogebra will be a valuable aid.

Having various examples available, it is not only possible to explore and discover different cases of gravitational lenses and related optical illusions, but also choose the levels of difficulty, especially in the mathematical part, that we want our students to face during this process. In this regard, the simplest models to deal with, among those chosen, are point mass, SIS and uniform disk, while for the others a more advanced mathematical background is required. However, we support the idea that, thanks to the use of Geogebra software, a considerable simplification of the resolution takes place, which allows even less advanced students to understand even the most mathematically complicated cases through visualisation. Let's investigate our lens models.

Point Mass Lens   This case represents the lensing effects produced by gravitational lenses as black holes (at such a distance from them in the lens plane that we remain in the weak gravitational field regime),[19] massive compact objects and even stars. In our view, this model represents galaxies as lenses when viewed from far away so that within the impact parameter b the total mass of the galaxy is contained. In this case we can consider them as points and are therefore able, around them, to study the effects on light from background sources. The main characteristic of this lens is that its mass is independent of the distance from its centre, expressed by the angle θ, it is totally concentrated in this precise central point (zero-dimension) and the mass density is represented by a Dirac delta function, i.e. this is a point mass.

Firstly, we introduce $M(|\theta|) = M(|\theta_\mathrm{E}|) = M_\mathrm{tot}$ in equations (3.8), obtaining

$$\theta_\mathrm{E}{}^2 = \frac{4G\,M_\mathrm{tot}}{c^2}\,\frac{D_\mathrm{LS}}{D_\mathrm{L}D_\mathrm{S}} = 2\,R_\mathrm{S}\,\frac{D_\mathrm{LS}}{D_\mathrm{L}D_\mathrm{S}}\;. \tag{3.16}$$

The same is done with eq. (3.7), expressing then the result in terms of the Einstein ring radius θ_E (or in alternative using directly eq. (3.9)). The resulting form of the lens equation for this lens model is

$$\theta - \theta_\mathrm{S} = \frac{\theta_\mathrm{E}{}^2}{\theta}\;. \tag{3.17}$$

Solving eq. (3.17), number and position of produced images from a background point-like source are obtained.

As we see, this equation is still a quadratic equation and easy to work with, but as said before this won't be always the case. Since for a point mass lens it is so easy, we start solving this quadratic equation analytically and discussing its outcomes. This is actually an easy maths

---

[19]In the strong gravitational field regime, as far as light deflection is concerned, absolutely extreme and very fascinating effects originate [26]. As motivating as it may be, the equations involved and the treatment of this case are highly complex and much more difficult to understand and therefore not suited to the level of our audience and the educational objectives we want to achieve.

practice for our students which involves one of the most-mentioned equations at school. The solution of eq. (3.17) is in fact given by

$$\theta_{1,2} = \frac{\theta_S \pm \sqrt{\theta_S^2 + 4 \cdot \theta_E^2}}{2} , \tag{3.18}$$

which defines the distance of the two images from the lens centre $\theta_L = 0$. We underline the fact that for these solutions it is always true that $\theta_1 > 0$ and $\theta_2 < 0$, in particular it is easily proven that $|\theta_1| \geq \theta_E$ and $|\theta_2| \leq \theta_E$. This means that we have an image on the right side of the lens and its distance from it is equal to or greater than the Einstein radius. And we have a second image on the left side of the lens with a distance from it equal to or less than the Einstein radius. Thanks to Vieta's theorem,[20] using the solutions (3.18), we can also deduce two special characteristics of this system, namely $|\theta_1| \cdot |\theta_2| = \theta_E^2$ and $|\theta_1| - |\theta_2| = \theta_S$. From the latter we obtain the distance to the lens of the real source.

The angular distance of the images from the lens, as well as their angular separation and its middle point are quantities directly measurable. However, when it is possible to understand their dependencies and relationships with other involved quantities, this provides extra useful information. In fact, calculating now the images' angular separation $\Delta\theta$, given by

$$\Delta\theta = |\theta_1| + |\theta_2| = \theta_1 - \theta_2 = \sqrt{\theta_S^2 + 4\theta_E^2} , \tag{3.19}$$

eq. (3.18) becomes

$$\theta_{1,2} = \frac{1}{2} \left(\theta_S \pm \Delta\theta \right) . \tag{3.20}$$

Also from this results, it is actually possible to infer the true position of the source even if we do not see it. The next step consists in calculating the angular distance from the lens of the middle point $\bar{\theta}$ of the images separation. In fact, starting from the position of one image, for simplicity we choose θ_1, we see that

$$\bar{\theta} = \theta_1 - \frac{\Delta\theta}{2} = \frac{1}{2}\theta_S . \tag{3.21}$$

It is clear that for this lens model this point is always halfway between lens and source.

Let's now consider few special cases, whose results from equations (3.18) (or (3.20)), (3.19) and (3.21) are collected in table 3.1.

The first case, defined by $\theta_S = 0$, represents the perfect source-lens-observer alignment. The

	$\boldsymbol{\theta_S = 0}$	$\boldsymbol{\theta_S = \theta_E}$	$\boldsymbol{\theta_S \gg \theta_E}$
$\boldsymbol{\theta_{1,2}}$	$\pm\theta_E$	$\frac{1\pm\sqrt{5}}{2}\theta_E$	$\approx \frac{1}{2}\left(\theta_S \pm \theta_S\right)$
$\boldsymbol{\Delta\theta}$	$2\,\theta_E$	$\sqrt{5}\,\theta_E$	$\approx \theta_S$
$\boldsymbol{\bar{\theta}}$	0	$\frac{1}{2}\theta_E$	$\approx \frac{1}{2}\theta_S$

Table 3.1: Results from equations (3.18) (or (3.20)), (3.19) and (3.21) in the cases of interest. θ_E refers to the Einstein radius.

related solutions mean that the two images form at the same distance of value $|\theta_E|$ from the lens centre and we know that for reasons of full symmetry the observer actually sees a ring of radius θ_E. The angular separation corresponds in fact to the ring diameter and the centre of the diameter is correctly the position of the lens.

---

[20]Vièta's theorem gives formulas that relate the roots and the coefficients of a polynomial of degree n, but for positive roots only [111]. The general form of Vièta's theorem was established by A. Girard [35].

The next case of interest for this lens model is when $\theta_S = \theta_E$. Considering this configuration, the images are clearly positioned at well defined and fixed distances, fractions of the Einstein radius θ_E. In fact, I_1 is outside the Einstein ring, on the same side of the source, and at an angular distance from the lens of $|\theta_1| = 1.62\,|\theta_E|$. I_2 is instead inside the Einstein ring, on the other side with respect to the lens, and at an angular distance of $|\theta_2| = 0.62\,|\theta_E|$. Note that, as expected, if the angular distances are multiplied it gives θ_E^2, confirming in this way the first special feature we saw. Also for this configuration the angular separation of the images is also a specific fraction of θ_E and its midpoint is now positioned at the distance of half Einstein radius from the lens centre. The last treated case is $\theta_S \gg \theta_E$. Basically, in all our equations now θ_E is negligible as compared to θ_S. These results tell us that the image on the source side is at practically the same real position as the source and the other is approximately at the origin, where the lens is located. We can deduce that the observer basically sees only one image at the real position of the source, so we are faced with a case of little relevance for gravitational lensing, at least as far as the production of images is concerned. Indeed, we are essentially almost observing the real source as we can also infer from the fact that the deflection angle $\delta \to 0$ for $\theta \to \infty$.

The analytical approach clearly provides interesting information on the effect produced by a point mass lens. But, as we shall soon see, it is not always possible to reach such conclusions so effortlessly, especially when the lens equation is not in such accessible form. To achieve our educational goals, we therefore need an alternative and simpler method of resolution. And this is where the graphical solution of eq. (3.17) comes into play, in particular through the use of Geogebra. In fact, besides giving the possibility to visualise the solutions, this method allows to conduct a deep qualitative analysis on the effects of gravitational lensing. This kind of analysis is in our opinion the most important and stimulating part of the learning process concerning this topic. However, although not in such a detailed way, it is also possible to quantitatively analyse the results, which are mainly numerical, and obtain all the fundamental information derived analytically. This is why we consider such an approach the simplest and most useful way to solve the lens equation, especially in the case of more complex equations, as we shall soon see.

In essence, thanks to Geogebra, it is possible to produce the graphic solution as a convenient diagram that provides the ability to follow and analyse variations in the gravitational lens effect using sliders to change the values θ_S and θ_E. In addition, by defining when the function $f(\theta) = \theta^2 - \theta_S\theta - \theta_E^2$ (derived from eq. (3.17)) intersects the θ-axis, operation that gives us the coordinates of all intersection points (namely the images positions), it is also possible to combine the diagram with a simulation of what the observer sees in the various configurations. These tools are in fact designed to be used together while teaching these concepts in order to facilitate students' understanding through observation. We are now going to discuss examples taken from these diagrams, in particular the special cases seen above which are also shown in figures 3.7 and 3.8.[21]

For the graphic solution, the two equations $f_1(\theta) = \theta - \theta_S$ and $f_2(\theta) = \theta_E^2/\theta$ are matched and, although the result is the same as that obtained analytically, in this case a simple but powerful visualisation is also produced. As we see represented in figures 3.7 and 3.8, the diagram of the graphical solution (above) is combined with the simulation of the resulting lensing effect (below). The files from which these images are taken are dynamic and once we set a value for the Einstein radius θ_E, moving the slider for the θ_S value, which, as already indicated, is always considered positive, we can follow the evolution of the lensing effect corresponding to different positions of the source. Specifically, we observe in fig. 3.7 the perfect source-lens-observer alignment, i.e. when $\theta_S = 0$. In this case, as expected, there are two solutions and they are on opposite sides of the lens, both at an angular distance $|\theta_E|$ from it, which is the radius of the Einstein ring

---

[21]We use here a plot θ vs. $f(\theta)$, but it is also possible to reproduce the same reasoning using $u \equiv \theta/\theta_E$ and plot u vs. $f(u)$.

that actually forms. Clearly, the separation between the two images is the ring diameter and the
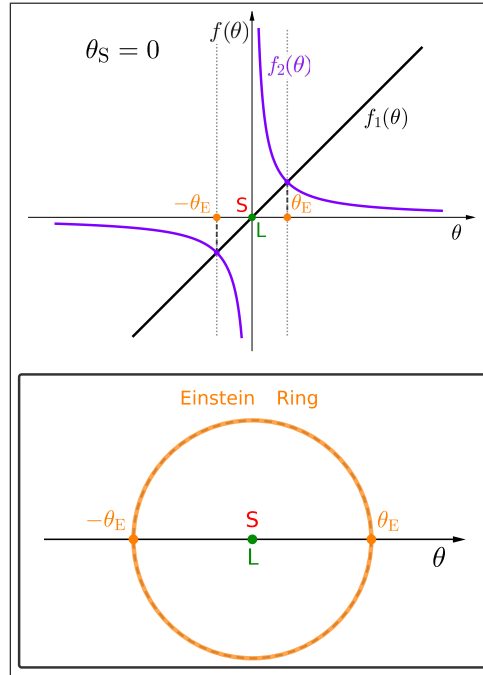
Figure 3.7: Graphical Geogebra solution of eq. (3.17) for the point mass lens in the special case of $\theta_S = 0$, namely with perfect source-lens-observer alignment. Due to full symmetry, the observer sees a ring of radius θ_E, the famous Einstein ring, which is shown in the bottom panel (the image in the panel is here enlarged for permitting a better view).

middle point the lens position.

In fig. 3.8 we then continue analysing what happens with $\theta_S > 0$, where we consider that the source moves further and further away, sideways, from the line joining the observer and the lens. We see indeed represented the last two analytically analysed special cases. In this situation, again two images of the source are visible, one is always positioned on the left side of the lens, internal to the Einstein ring, and the other on the right side (in our model the source side), but external to the ring. Moreover, the further the source moves laterally away from the lens, as seen in projection, the closer the internal image gets to the lens itself, eventually merging visually with it. Meanwhile, the external image moves away from the lens on the same side as the source and approaches the source's real position. This is when $\theta_S \gg \theta_E$ and we already saw why it is of little interest for us.

The aim of this approach is to demonstrate that, starting from the graph, we can also conduct a quantitative discussion, confirming many of the results obtained analytically. This is done also thanks to some features of Geogebra, observing the plots and their evolution, considering the algebraic section and by setting a random value for θ_E.[22] In particular, relying only on what Geogebra has to offer, we note that the value of $\bar{\theta}$ is always half the value of θ_S, as we expected from eq. (3.21). Moreover, we can monitor how the length of the segment connecting θ_1 to θ_2 varies, as well as the individual distances of the images from the centre of the lens. Another important observation to make concerns the relationship that exists between these quantities, considering also $u \equiv \theta/\theta_E$ (see footnote 21).

The advantage of this educational tool lies mainly in the fact that one can directly observe and analyse the simulation of the effect of gravitational lensing. At this point, exploiting this advantage, we can then decide on the type of approach best suited to our students. For example, we can

---

[22] It is also alternatively possible to choose a realistic value and simulate as much as possible a real gravitational lens example.
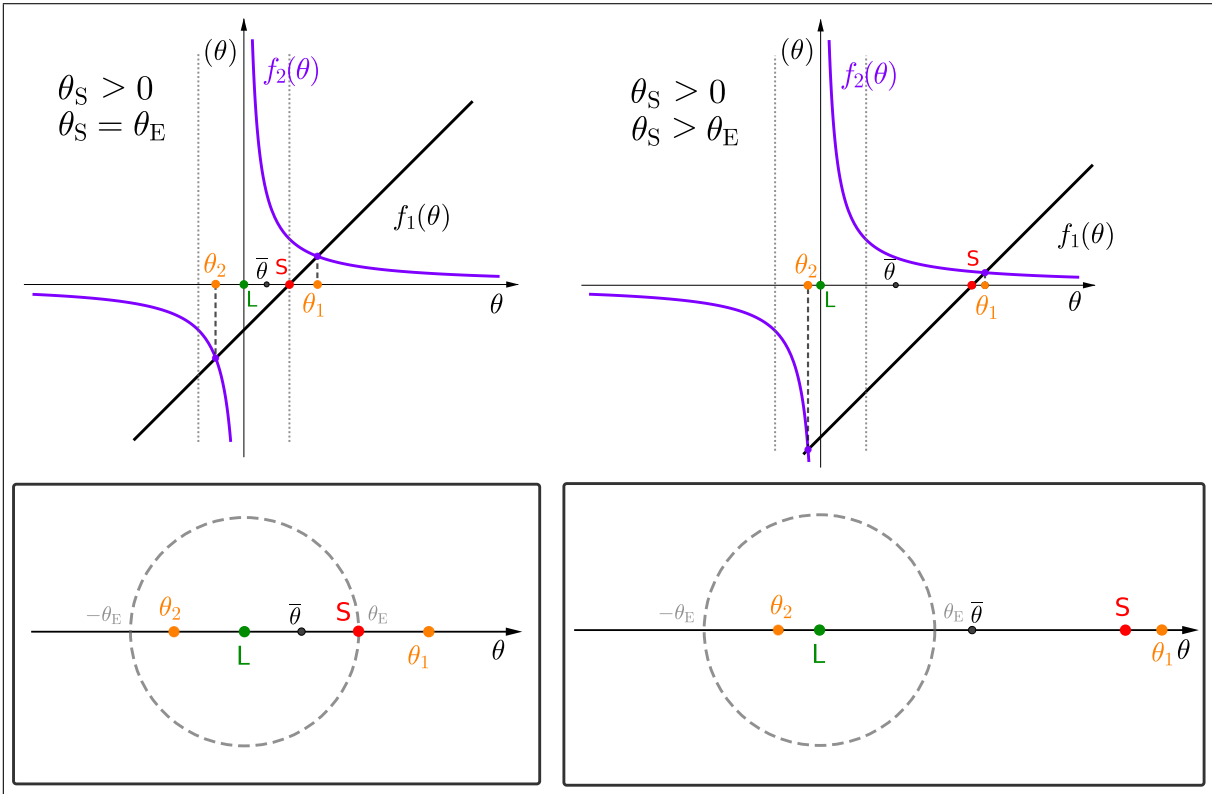
Figure 3.8: Graphical Geogebra solutions of eq. (3.17) for the point mass lens in case of $\theta_S > 0$ (in the left part is shown the special case $\theta_S = \theta_E$). The observer sees two images, one inside the Einstein ring (gray dotted lines above and dashed circle below) positioned at θ_2 and one outside at θ_1, as shown enlarged in the bottom panel. The further away the source is from the lens, as seen in projection, the closer the external image will be to the source itself and the other to the lens, the latter two arrive in extreme cases to merge visually so that they cannot be distinguished.

adopt a qualitative approach starting with the observation and discussion of the phenomenon, stimulating and guiding students to analyse what they see, ask questions and hypothesize the answers, based on the background knowledge they have developed. Then, eventually, we can proceed with the quantitative part and, if the students are at a proper mathematical level, also with the deepening of the equations that provide such results. Or, on the other hand, it is possible to approach the subject starting with the study of these equations and then continue with the analysis of the graphs obtained and the numerical results, investigating the various solutions. This latter approach is well suited to students of a slightly more advanced level, who are therefore already able to understand and make the connection between analytical and geometric results without problems.

For all these reasons and the fact that it is possible to visually reproduce the solution of the lens equation and the effects of gravitational lensing, we consider the graphic one the best approach, especially when the equation is in more complicated forms. Furthermore, this will be the approach we will adopt for all other lenses in this thesis.

The question that at this point naturally arises is "what about brightness?". In fact, since all elements are point-like, we have no clue on the brightness of the images. Therefore, to answer this question we have to calculate it using eq. (3.13) together with eq. (3.18). The magnification of the two images is then given by

$$\mu_{1,2} = \frac{\theta_{1,2}}{\theta_S} \frac{d\theta_{1,2}}{d\theta_S} = \frac{1}{2}\left(1 \pm \frac{\theta_S{}^2 + 2\theta_E{}^2}{\theta_S\sqrt{\theta_S{}^2 + 4\theta_E{}^2}}\right) = \frac{1}{4}\left(2 \pm \left(\frac{\Delta\theta}{\theta_S} + \frac{\theta_S}{\Delta\theta}\right)\right) , \qquad (3.22)$$

	$\boldsymbol{\theta_S = \theta_E}$	$\boldsymbol{\theta_S \gg \theta_E}$
$\boldsymbol{\mu_1}$	1.17	≈ 1
$\boldsymbol{\mu_2}$	-0.17	≈ 0
$\boldsymbol{\mu_{\text{tot}}}$	1.34	≈ 1

Table 3.2: Results from equations (3.22) and (3.23) for the magnification in the cases of interest. θ_E refers to the Einstein radius.

where in the last step we have also introduced eq. (3.19), expressing it with measurable quantities. According to section 3.2.4, the sign of μ determines the parity of the image, meaning its orientation with respect to the source, and for this lens model we see that $\mu_1 > 0$, positive parity, and $\mu_2 < 0$, negative parity. We can now calculate the total magnification which is

$$\mu_{\text{tot}} = |\mu_1| + |\mu_2| = \frac{\theta_S{}^2 + 2\theta_E{}^2}{\theta_S\sqrt{\theta_S{}^2 + 4\theta_E{}^2}} = \frac{1}{2}\left(\frac{\Delta\theta}{\theta_S} + \frac{\theta_S}{\Delta\theta}\right) \ . \tag{3.23}$$

Finally, we analyse the image brightness in the special cases named before. We already know that for $\theta_S = 0$ the magnification diverges and it is only a geometrical problem, so not real. In this case we have in fact a ring and it is very bright. The numerical value resulting in the other cases are instead collected in tab.3.2.

Referring to this table, we note that when $\theta_S = \theta_E$, the image I_1 is already at this point only slightly brighter than the source, whose magnification is by definition set as $\mu_S = 1$, and the image I_2 is quite dimmer. However, the total brightness of the images is ultimately higher.

Considering the case with $\theta_S \gg \theta_E$, where θ_E becomes negligible, we can take these results as a further confirmation that, even in terms of brightness, this situation is of little interest in the context of gravitational lensing.

Sometimes, however, it is very complex to achieve these results when the solution of the lens equation is not easy to calculate analytically. So we find ourselves struggling to untangle between functions and calculations that are absolutely elaborate and this is not useful for our educational purposes. So let's now explore an alternative solution for calculating the magnification with the help of Geogebra.

Unfortunately, with complicated equations even Geogebra is in difficulty and it cannot give us the solutions in the form of eq. (3.18), which we need to insert in eq. (3.13). Looking for an easier way to solve this problem, the idea arises by observing eq. (3.13).[23] In fact, we can say that

$$\mu = \left(\frac{\theta_S}{\theta}\frac{\mathrm{d}\theta_S}{\mathrm{d}\theta}\right)^{-1} , \tag{3.24}$$

which simplifies our calculations a lot because in the lens equation θ_S appears as a single term and we can easily make it explicit and replace it in this equation. Basically, it is solving eq. (3.24) with Geogebra that we reach our goal.

For the point mass lens, the first step consists of calculating $\mu_t{}^{-1} = \theta_S/\theta$ using $\theta_S = f(\theta) = \theta - \theta_E{}^2/\theta$, which is derived from eq. (3.17). Then, since calculating the derivative is very easy in this case, we can solve it by hand. Alternatively, we can use the Geogebra command "Derivative $(f(\theta))$" and obtain the first derivative $\mu_r{}^{-1} = f'(\theta) = \mathrm{d}\theta_S/\mathrm{d}\theta$. At this point, multiplying these outcomes, $\mu_t{}^{-1} \cdot \mu_r{}^{-1}$, and inverting the final result the searched magnification, $\mu(\theta)$, is reached. Naturally, Geogebra produces also the graph of this function, which allows to instantly visualise the trend of the magnification along the entire θ-axis, understanding in this way how the parity

---

[23]Inspired by the literature, see [17] and [76].

of the images changes at every image position, as shown in fig. 3.9 restricted to the areas of our interest. As expected, even for this solution the magnification diverges with full alignment. However, already moving slightly out of alignment, we can see that both images have very high magnification values, but they drop down very quickly as the source moves laterally with respect to the lens. The last step consists of inserting into $\mu(\theta)$ the numerical value of the position θ for
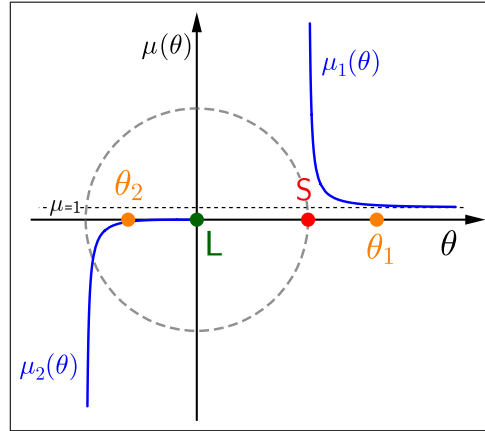
Figure 3.9: Magnification, plotted with Geogebra, for the point mass lens model. Specifically, this is the situation $\theta_S = \theta_E$, but we can follow the behaviour of the magnification along the θ-axis.

the images, taken from the simulation. In this way we obtain the numerical value of each image magnification when θ_S varies. We can also calculate easily the total magnification and analyse the results.

As expected, for every case, the outcomes are exactly the same obtained analytically and give us information about the brightness of the images. This method of obtaining the image magnification will therefore be applied to the next lenses we study.

Plummer Sphere Lens This case represents the lensing effects produced by galaxies or clusters of stars. The model for this lens, invented in 1911 [82], approximates a spherical halo. In fact the mass is distributed in an infinite sphere with a finite density core and it falls off as r^{-5} at large radii, as we can see from the first part of eq. (3.25). Actually it falls steeper than in a real galaxy, nevertheless this model is widely used in N-body simulations of stellar systems [97][16]. Typical of this lens is the fact that the total mass is reached at infinity and there is a scale radius a_P which roughly represents the radius of the galaxy halo. In fact, beyond this radius, as we consider ever greater values for r, the gravitational potential[24] approaches quite fast that of a point mass. Since, as said, we need to project the lens mass on the lens plane (see appendix F). We consider the mass density and mass radial profiles in three dimensions first and projected in two dimensions afterwards. Therefore, starting with the mass density radial profiles, which are shown in fig. 3.10, we have that

$$\sigma(r) = \frac{3\,a_P{}^2 M_{\text{tot}}}{4\pi\,(r^2 + a_P{}^2)^{\frac{5}{2}}} \quad \text{projected onto the lens plane becomes} \quad \Sigma(\rho) = \frac{a_P{}^2 M_{\text{tot}}}{\pi\,(\rho^2 + a_P{}^2)^2}\,, \tag{3.25}$$

where r in the mass density profile $\sigma(r)$ represents the distance from the lens centre in 3-space and ρ in the surface mass density profile $\Sigma(\rho)$ represents this distance in the lens plane instead. Moreover, M_{tot} is the total mass of the lens reached at infinity. Consequently, deriving the mass radial profiles, which are shown in fig. 3.11, we obtain that

$$M(r) = \frac{r^3 M_{\text{tot}}}{(r^2 + a_P{}^2)^{\frac{3}{2}}} \quad \text{projected onto the lens plane becomes} \quad M(\rho) = \frac{\rho^2 M_{\text{tot}}}{\rho^2 + a_P{}^2}\,. \tag{3.26}$$
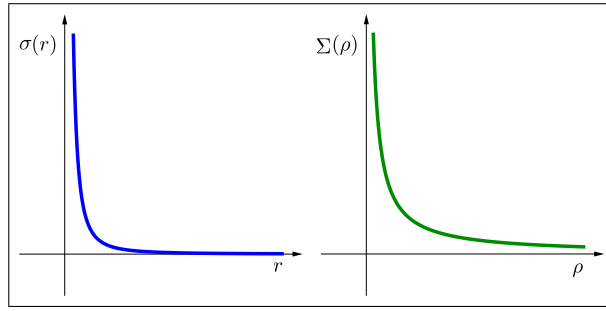
---

[24]$\Phi = -G\,M_{\text{tot}}/\sqrt{r^2 + a_P{}^2}$
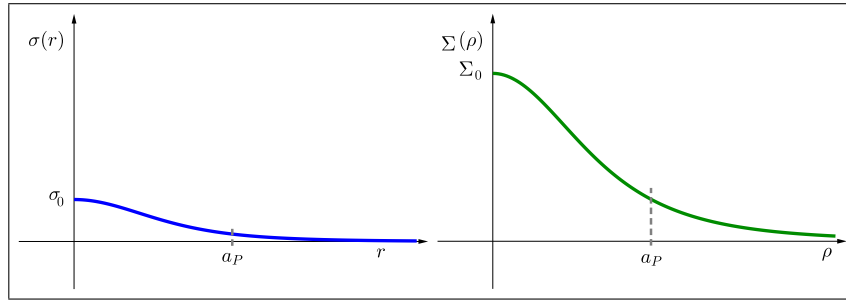
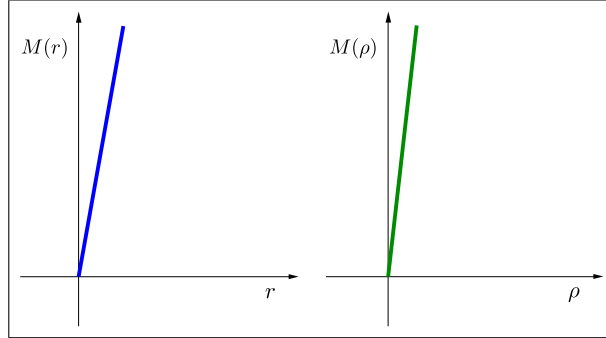Figure 3.10: Mass density radial profiles of the Plummer sphere, on the left in 3-space and on the right projected onto the lens plane. σ_0 and Σ_0 represent, respectively in the two cases, the value that the mass density has at the centre of the object under consideration.
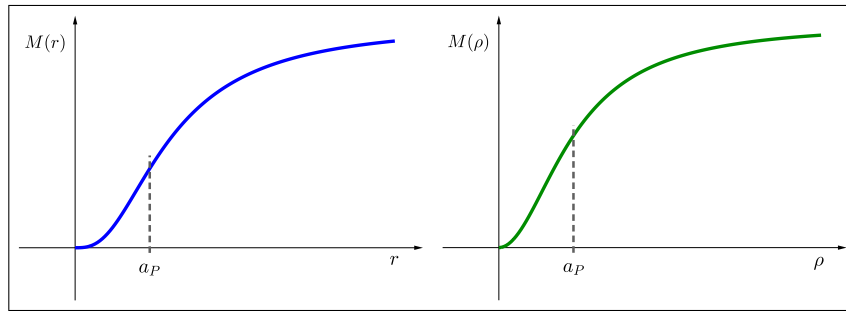
Figure 3.11: Mass radial profiles of the Plummer sphere, on the left in 3-space and on the right projected onto the lens plane.

Note that in the lens plane the mass enclosed within $r = a$ is $M(a) = \frac{1}{2}M_{\text{tot}}$. Now $M(|\rho|)$, expressed in the form $M(|\theta|)$,[25] is the searched projected mass that we have to substitute in the lens equation.

As said, teachers are free to approach the subject in the way they consider more convenient, but we prefer to start our discussion from the equations and end up analysing the graphical solution. Indeed, applying the same procedure as for the point mass lens and setting $a_{\text{P}} > 0$, we introduce now the projected mass from eq. (3.26) in equations (3.8), obtaining

$$\theta_{\text{E}}{}^2 = \frac{4G\,M_{\text{tot}}}{c^2}\,\frac{D_{\text{LS}}}{D_{\text{L}}D_{\text{S}}} - \theta_{\text{ap}}{}^2 = 2\,R_{\text{S}}\,\frac{D_{\text{LS}}}{D_{\text{L}}D_{\text{S}}} - \theta_{\text{ap}}{}^2\;. \tag{3.27}$$

R_{S} is the Schwarzschild radius belonging to M_{tot}. From this equation we straightforwardly see that the size of the Einstein ring depends now not only on the mass of the lens and the distances involved, but also on the size of the Plummer scale radius a_{P}. This leads to some restrictions on the existence of the ring. However, for simplicity, we consider only configurations where the Einstein ring exists. This is done, after having introduced the projected mass in eq. (3.7), expressing the lens equation in terms of the Einstein radius θ_{E} (or in alternative using directly eq. (3.9)). For the Plummer sphere model the resulting form of the lens equation is

$$\theta - \theta_S = \theta\,\frac{\theta_{\text{E}}{}^2 + \theta_{\text{ap}}{}^2}{\theta^2 + \theta_{\text{ap}}{}^2}\;. \tag{3.28}$$

Also in this case, solving eq. (3.28), number and position of produced images from a background point-like source are obtained. Clearly, the analytical solution consists in solving a cubic equation, which involves students in an interesting, but long and complex practice on this topic, something beyond our educational goal at the moment. Therefore, as we suggested before, we focus on the

---

[25]We have $\rho = \theta D_L$ and $a_{\text{P}} = \theta_{\text{ap}} D_L$.

Geogebra graphical solution of the lens equation and the discussion of its visual and numerical[26] results.

Basically, also for this lens model, we produce the Geogebra diagram of the graphic solution for various values of θ_S, combined with the simulation of the resulting gravitational lens effect. Now, with regard to the graphical solution, the two equations that must be matched are $f_1(\theta) = \theta - \theta_S$ and $f_2(\theta) = \theta \, \frac{\theta_E{}^2 + \theta_{ap}{}^2}{\theta^2 + \theta_{ap}{}^2}$. For the simulation instead, defining when the cubic eq. (3.28) intersects the θ-axis, we obtain directly the image points and their position, i.e. the coordinates of the intersection points. With these graphs, we can then observe and discuss the evolution of the gravitational lens effect when the source is considered moving laterally with respect to the lens, as seen in projection and investigate particular configurations, like the ones shown in figures 3.12 and 3.13. We again recommend, whenever possible, to use during the lectures the dynamic files from which our images are extracted. This is because they offer a better visualisation and are interactive. Also for this model, such diagrams and simulations are created following exactly the same procedure as for the point mass model.

Our first focus is again the perfect source-lens-observer alignment, $\theta_S = 0$, which is shown in fig. 3.12 (left). Observing this figure we see that, for the Plummer sphere model, we not only have
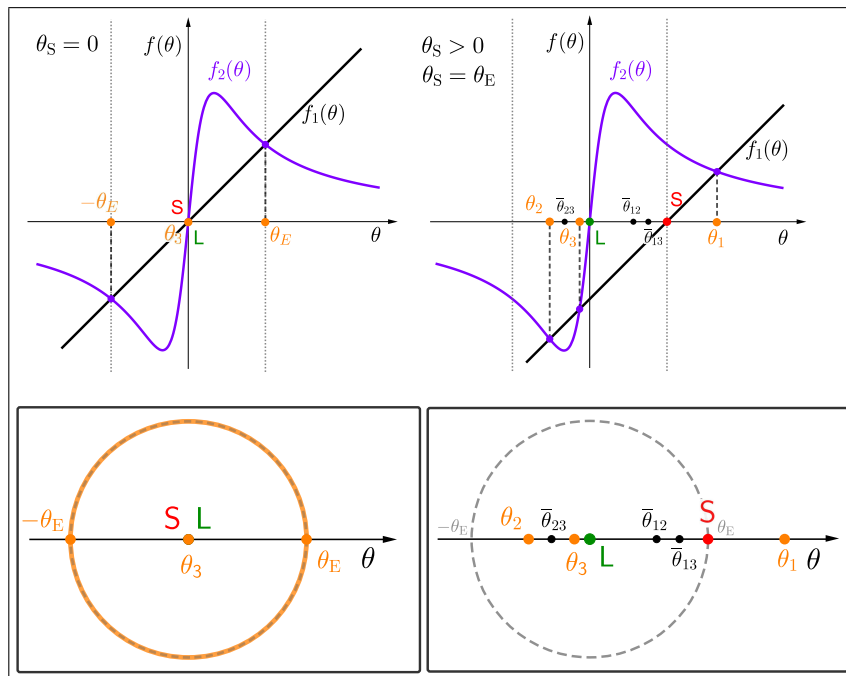
Figure 3.12: Graphical Geogebra solution of eq. (3.28) for the Plummer sphere lens. Left: The special case $\theta_S = 0$ where, due to full symmetry, the observer sees an Einstein ring of radius θ_E and a central point-like image, which are shown enlarged in the left bottom panel. Right: The case of $\theta_S > 0$ and in particular $\theta_S = \theta_E$. The observer sees at first three images, two inside the Einstein radius θ_E, positioned at θ_2 and θ_3, and one outside, positioned at θ_1, as shown enlarged in the right bottom panel.

two solutions, each on opposite sides of the lens at a distance $|\theta_E|$ from it, but also a central point-like image at $\theta_3 = 0 = \theta_L$, merged visually with the lens. We note that, also in this case, the angular separation between the two images equidistant from the lens corresponds to the Einstein ring diameter and its central point is the position of the lens and third image. Consequently, the third image is one Einstein radius away from each of the other two. And the midpoint of these distances is obviously half a radius. All these results can easily be verified also with the numerical

---

[26]From the algebraic section of Geogebra.

solutions of the algebraic part of Geogebra.

The analysis continues with $\theta_S > 0$ in figures 3.12 (right) and 3.13, where again the source is considered moving further away, sideways, from the line joining observer and lens. With the Plummer lens model, depending on how far away the source is from the lens, we will see respectively three, two or one image of the source. In this configuration, as soon as the system deviates from the perfect alignment (right side of fig. 3.12), three images of the source are visible, two are positioned on the left side of the lens, internal to the Einstein ring, and the other on the right side (the source side), but external to the ring. We can easily observe that $\theta_1 > 0$ and instead $\theta_2 < 0$ and $\theta_3 \leq 0$. In particular, in our case it is true that $|\theta_1| \geq |\theta_E|$, $|\theta_2| \leq |\theta_E|$ and $|\theta_3| \leq |\theta_2|$. In fact, the further the source moves laterally away from the lens, as seen in projection, the closer the internal-to-the-ring images get to each other, visually merging in a single image (the two superimposed) and then disappearing, as we can see in the plots in fig. 3.13. Meanwhile, also for this model the external image moves away from the lens, on the same side as the source, and approaches the source's real position. Reaching again in this manner the case of little interest for us, namely when $\theta_S \gg \theta_E$.

Observing and studying the evolution of the graph and the relative numerical results, it is possible to monitor now how the length of the segments connecting the images varies (for us these are angular distances), as well as the individual distances of the images from the centre of the lens. Moreover, it is possible to extrapolate possible relationships that exist between these quantities, checking their validity also for different configurations changing the values for θ_E, θ_S and θ_{ap}. Monitoring this system, we could actually identify some general features which are valid as long as we see at least two images. The first one is that the multiplication of the angular distances of each image from the lens always gives $|\theta_1| \cdot |\theta_2| \cdot |\theta_3| = \theta_{ap}^2 \theta_S$. The other two concern
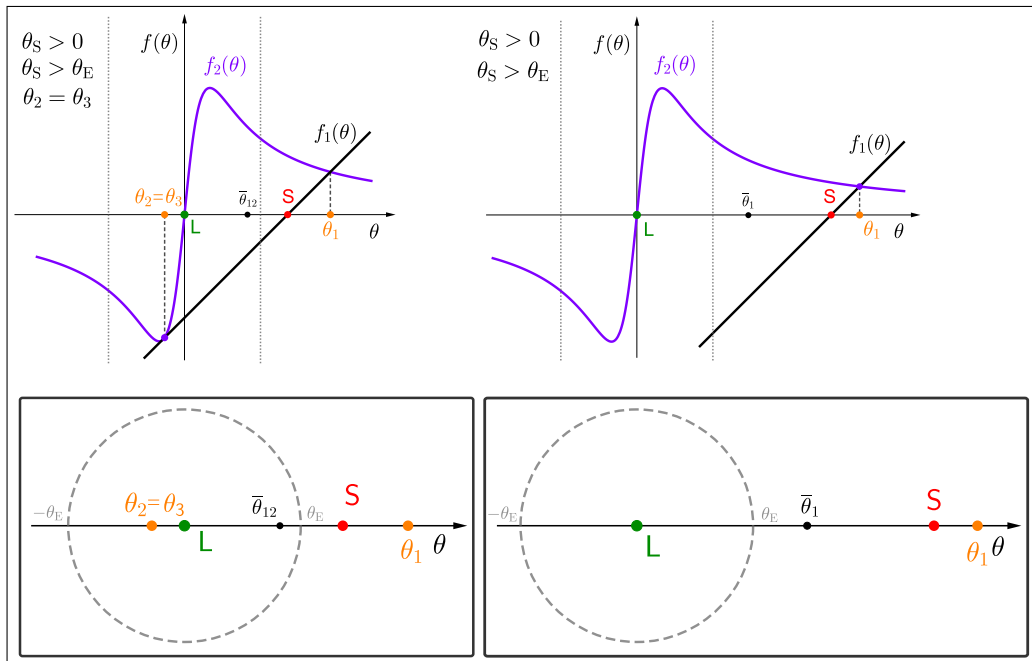
Figure 3.13: Graphical Geogebra solutions of eq. (3.28) for the Plummer sphere lens in case of $\theta_S > 0$. Now, the further away from the lens the source is, as seen in projection, the closer the external image will be to the real position of the source. The other two instead move towards each other, always remaining inside the ring radius, until they merge together into a single image (left panel), then disappear (right panel).

the actual position of the source, in fact $\theta_S = |\theta_1| - |\theta_2| - |\theta_3|$, and the Einstein ring with $\theta_E^2 = |\theta_1||\theta_2| - |\theta_2||\theta_3| + |\theta_1||\theta_3|$. We can also definitely infer the dependences for the midpoint,

$\overline{\theta}$, of the various image separations. In this regard we respectively obtain

$$\overline{\theta}_{12} = \theta_1 - \frac{\Delta\theta_{12}}{2} = \frac{1}{2}\left(\theta_S - \theta_3\right) = \frac{1}{2}\left(\theta_S + |\theta_3|\right)$$

$$\overline{\theta}_{13} = \theta_1 - \frac{\Delta\theta_{13}}{2} = \frac{1}{2}\left(\theta_S - \theta_2\right) = \frac{1}{2}\left(\theta_S + |\theta_2|\right) \tag{3.29}$$

$$\overline{\theta}_{23} = \theta_2 + \frac{\Delta\theta_{23}}{2} = \frac{1}{2}\left(\theta_S - \theta_1\right) = \frac{1}{2}\left(\theta_S - |\theta_1|\right).$$

All these characteristics, which clearly involve directly measurable quantities, give us information about the system under examination and the real position of the source, which as always with gravitational lensing is not directly visible.

In this context, leaving aside when $\theta_S \gg \theta_E$, we continue our investigation analysing the special cases we saw illustrated in figures 3.12 and 3.13. For the Plummer sphere model the case $\theta_S = \theta_E$ does not bring any interesting insights. Much more particular is the case $\theta_2 = \theta_3$, where images are reduced to two. In this case we get $|\theta_1| - \theta_S = 2 \cdot |\theta_2|$. These data, used in calculating the angular distance between the two images and the position of its midpoint, give

$$\Delta\theta_{12} = \theta_S + 3 \cdot |\theta_2| = \frac{1}{2}\left(3 \cdot |\theta_1| - \theta_S\right)$$

$$\overline{\theta}_{12} = \frac{1}{4}\left(\theta_S + |\theta_1|\right) = \frac{1}{2}\left(|\theta_1| - |\theta_2|\right). \tag{3.30}$$

Certainly, we are able to support all these findings with the numerical results in the algebraic section of Geogebra. From the case $\theta_2 = \theta_3$, a further lateral shifting of the source will make the second image disappear, leaving only the image on the right side of the lens that from now on will increasingly approach the true position of the lens.

We believe it is important to emphasise the fact that being able to see the typical relationships and features of the gravitational lens system from these types of graphs is not a trivial task and therefore such an activity requires some training. We may be trained enough in this type of analysis, however, students are generally not (with a few exceptions). Thus, we educators are asked to guide them in discovering these connections and results. In our opinion, which, as stated earlier, is supported by the literature in science education, the best way to achieve this goal is by actively stimulating students' capacity to discover them and not by simply revealing them. This type of exercise will not only help our students to extrapolate important information from graphs and diagrams, but will also stimulate their ability to observe, reason and investigate that could lead to the development of important competencies.

Finally, thanks to Geogebra, we can investigate the brightness of the images produced by the Plummer lens following the same reasoning as for the point mass lens. For this purpose we apply eq. (3.24) and solve it for $\theta_S = \theta - \theta\,\frac{\theta_E^2 + \theta_{ap}^2}{\theta^2 + \theta_{ap}^2}$ (derived from eq. (3.28)). In this way, we can draw the graph of how the magnification changes along the θ-axis, and with it the images parity, obtaining the desired information.

As is shown in fig. 3.14 and as expected, in case of $\theta_S = 0$ for the two images at a distance $|\theta_E|$ from the lens the magnification diverges. As we know from section 3.2.4, this effect of diverging is not real, in fact the observer sees a very bright ring. The brightness of the central image I_3, on the other hand, is very dim and therefore it should not be distinguishable from the central lens or entirely fused with it anyway. Moving out of alignment we observe that the two images I_1 and I_2 have at first high magnification that drops down very quickly as the source moves further to the side relative to the lens. As it is clear from the graph, the further the source moves laterally away from the lens, the more the brightness of I_1 tends to match that of the source. I_2 instead,
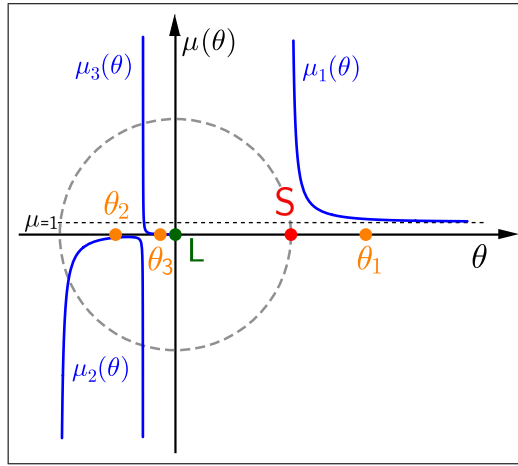
Figure 3.14: Magnification, plotted with Geogebra, for the Plummer sphere lens model. Specifically, this is the situation $\theta_S = \theta_E$, but we can follow the behaviour of the magnification along the θ-axis.

as it approaches I_3, becomes at first dimmer and dimmer and then, when the two images are close to each other, its brightness begins to increase very slowly. As for I_3, it remains very faint, although its magnification increases slightly but constantly. However, precisely when I_2 and I_3 merge together, the observer sees a very bright resulting image, in fact the magnification diverges again at this point. It is indeed confirmed from the plot that, just before this fusion, both images start to become very bright and we know that right after that they disappear.

Recalling section 3.2.4 on the topic of image parity, we observe that $\mu_1 > 0$ and $\mu_3 > 0$, hence I_1 and I_3 have positive parity despite being on different sides of the lens, and $\mu_2 < 0$, so I_2 has negative parity. Even if these details don't seem particularly relevant now, they will gain importance later on when we will treat extended sources in section 3.3.1.2.

At this stage, the procedure to be followed and the type of discussions that these observations bring should not only be straightforward and understood, but should also be part of our own knowledge. For this reason, in the analysis of other lenses we will only provide the results and highlight important features, leaving out the methodology.

Singular Isothermal Sphere (SIS) Lens The SIS lens is among the simplest models for describing galaxies and thus widely used [17]. In fact, it approximates again a spherical halo and is represented by an extended infinite sphere, whose mass behaves like an ideal gas. The sphere describes a self-gravitating system, a galaxy, with constant velocity distribution of its stars. This model is also considered a good approximation for explaining the flat rotation curves of spiral galaxies and therefore for investigating the hypothetical presence of dark matter [94]. Indeed, in such a system the velocity of the stars in circular orbits does not depend on the radius of the orbit. Typical for this model is that the total mass diverges when the radius goes to infinity and there is a singularity at zero radius. Since also in this case we need to project the lens mass on the lens plane, as we did for the Plummer sphere lens, we consider the mass density and mass radial profiles in three dimensions first and in two dimensions afterwards, which are shown in figures 3.15 and 3.16. Therefore we get that

$$\sigma(r) = \frac{\sigma_v^2}{2\pi G r^2} \quad \text{projected onto the lens plane becomes} \quad \Sigma(\rho) = \frac{\sigma_v^2}{2G\rho}, \qquad (3.31)$$

Figure 3.15: Mass density radial profiles of the singular isothermal sphere, on the left in 3-space and on the right projected onto the lens plane.

Figure 3.16: Mass radial profiles of the singular isothermal sphere, on the left in 3-space and on the right projected onto the lens plane.

where r and ρ are defined as in the Plummer-sphere case and σ_v is the velocity dispersion.[27] Thus, calculating the mass profile we obtain that

$$M(r) = \frac{2\,\sigma_v{}^2}{G} \cdot r \quad \text{projected onto the lens plane becomes} \quad M(\rho) = \frac{\pi\,\sigma_v{}^2}{G} \cdot \rho \,. \tag{3.32}$$

The projected mass $M(\rho)$, again in the form $M(|\theta|)$, should be then inserted in the lens equation in order to obtain information about number and position of the resulting images from a point-like source.

Proceeding exactly as we did for the previous lenses we calculate the Einstein radius θ_{E}

$$\theta_{\mathrm{E}} = \frac{4\,\pi\,\sigma_v{}^2}{c^2} \frac{D_{\mathrm{LS}}}{D_{\mathrm{S}}} \,. \tag{3.33}$$

And the lens equation is then

$$\theta - \theta_{\mathrm{S}} = \theta_{\mathrm{E}} \frac{|\theta|}{\theta} = \mathrm{sgn}(\theta) \cdot \theta_{\mathrm{E}} \,, \tag{3.34}$$

which should be treated cautiously because for $\theta > 0$, on the right side of this equation, it is $+\theta_{\mathrm{E}}$ and for $\theta < 0$ it is $-\theta_{\mathrm{E}}$.

By looking at eq. (3.34) we realise that we are dealing with a quite simple lens equation, which can therefore be approached analytically without difficulty, as done for the point mass model. However, as already mentioned, we focus on solving it graphically with Geogebra. In fact, in figures 3.17 and 3.18 we see the graphic solution obtained matching the equations $f_1(\theta) = \theta - \theta_{\mathrm{S}}$ and $f_2(\theta) = \theta_{\mathrm{E}} \frac{|\theta|}{\theta}$, together with the corresponding simulation. These diagrams, together with the algebraic part, allow us to infer all the useful information about this gravitational lens effect. Essentially, in case of source-lens-observer perfect alignment, $\theta_{\mathrm{S}} = 0$, two solution are present,

---

[27]The velocity dispersion σ_v is the statistical dispersion of velocities about the mean value $\overline{v}$ for a group of objects.
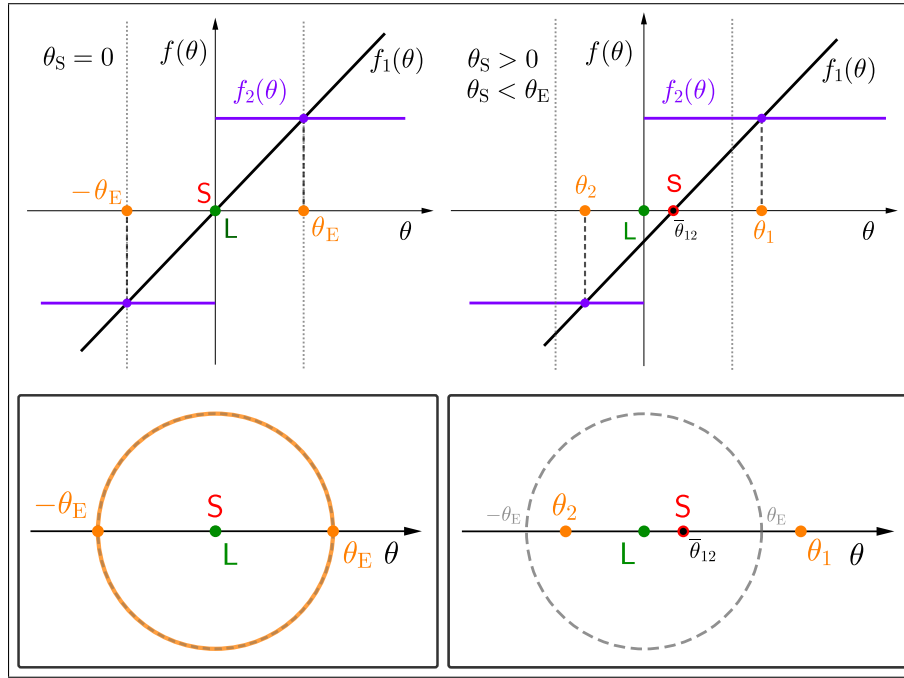
Figure 3.17: Graphical Geogebra solution for the SIS lens. In the special case of $\theta_S = 0$ the observer sees the Einstein ring of radius θ_E (left). In case of $\theta_S > 0$, the observer sees at first two images, one inside and one outside the Einstein radius θ_E (right). The further the source moves away from the lens, as seen in projection, the closer the internal image gets to the lens itself, until it disappears for $\theta_S > \theta_E$, and the further the external image moves away.

each on opposite sides of the lens and at a distance $|\theta_E|$ from it. Actually, due to full symmetry, this is when the observer sees the Einstein ring, as it is for the previously seen models. Once again, the source gradually moves sideways from the lens, so that $\theta_S > 0$. In this process, depending on whether the source is at a distance shorter or longer than the length of the Einstein radius, the observer will first see two and then only one image. This means that if $\theta_S < \theta_E$, we will observe two images, I_1 and I_2, with $|\theta_1| > |\theta_E|$ and $|\theta_2| < |\theta_E|$, where I_2 approaches the lens and I_1 moves away from it whereas if $\theta_S > \theta_E$, only I_1 will remain moving further and further away from the lens. As long as we have two images, characteristic of this lens is that $|\theta_1| \cdot |\theta_2| = \theta_E^2 - \theta_S^2$ and $|\theta_1| - |\theta_2| = 2\theta_S$. In addition, the distance $\Delta\theta_{12} = 2\,\theta_E$ between the two images always remains constant, namely the Einstein ring diameter, and the images remain equally distant also from the true position of the source. We can therefore deduce that the midpoint of this distance is always positioned where the source is located. Consequently

$$\theta_{1,2} = \theta_S \pm \frac{1}{2}\Delta\theta_{12} = \theta_S \pm \theta_E \ . \tag{3.35}$$

Moreover, from the moment on when we have only one image, its distance from the source still remains always equal to the Einstein radius θ_E, thus it will never approach its real position and we have $\theta_1 = \theta_S + \theta_E$. In table 3.3 we have summarised all the principal results obtained observing and investigating the diagrams and the numerical values, which, as said, we do not need to report and discuss again, and the case of little astrophysical importance $\theta_S \gg \theta_E$ is excluded.

The last outcome for this lens model concerns the magnification $\mu(\theta)$, whose behaviour for each image we can observe in fig. 3.19, which is produced with Geogebra following the usual procedure. As we noted for the previous models, also here the magnification diverges for the two images at a distance $|\theta_E|$ from the lens and produced with $\theta_S = 0$. This is when a bright Einstein ring is actually visible. And also here we see from the plot how the magnification for both images drops down quickly. The external image, I_1, tends indeed again to match the brightness of the
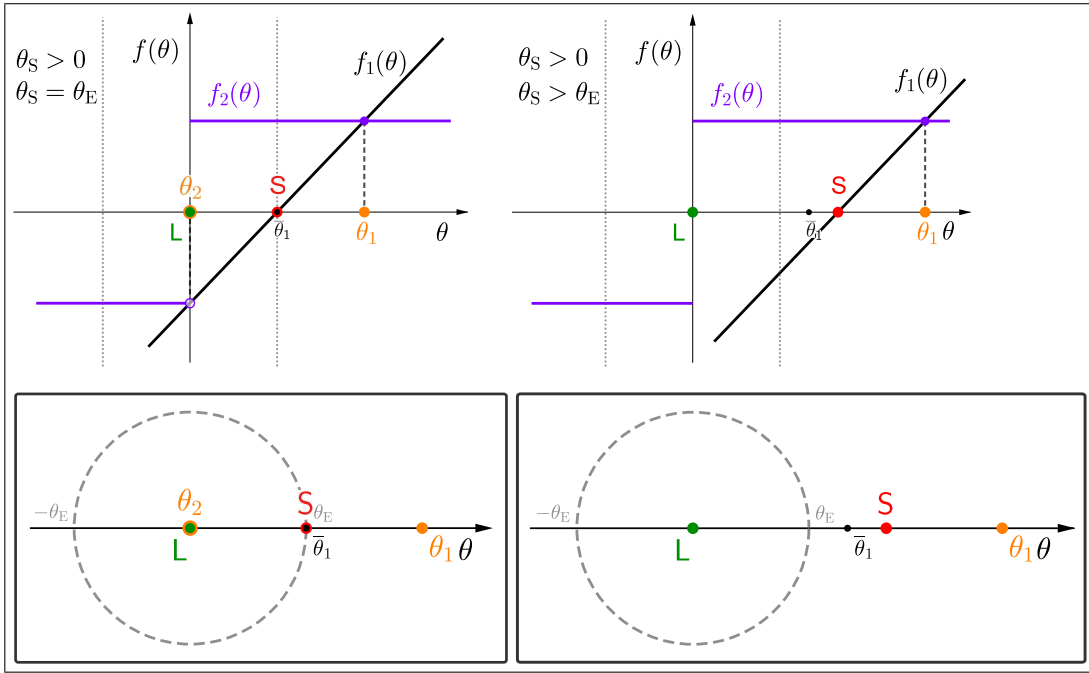
Figure 3.18: Graphical Geogebra solution for the SIS lens. In the special case of $\theta_S = \theta_E$ the observer should see two images for the last time. However, as we will understand analysing the magnification of this gravitational lens effect, the image that should be overlapped with the lens (drawn here as a circle) has actually zero brightness and thus is not visible, although formally it is a solution of the lens equation [22] (left). In case of $\theta_S > \theta_E$ the observer sees only the external image which moves away from the lens (right).

	$\boldsymbol{\theta_S = 0}$	$\boldsymbol{\theta_S < \theta_E}$	$\boldsymbol{\theta_S = \theta_E}$	$\boldsymbol{\theta_S > \theta_E}$
$\boldsymbol{\theta_{1,2}}$	$\pm\theta_E$	$\theta_S \pm \theta_E$	$\theta_E \pm \theta_E$	$\theta_S + \theta_E$
$\boldsymbol{\Delta\theta_{12}}$	$2\,\theta_E$	$2\,\theta_E$	$2\,\theta_E$	$\Delta\theta_1 = \theta_S + \theta_E > 2\,\theta_E$
$\boldsymbol{\overline{\theta}}$	0	θ_S	θ_E	$\overline{\theta_1} = \frac{1}{2}\Delta\theta_1 = \frac{1}{2}(\theta_S + \theta_E)$

Table 3.3: The main results of the SIS lens related to different source positions with respect to the lens, L, and Einstein radius, θ_E.
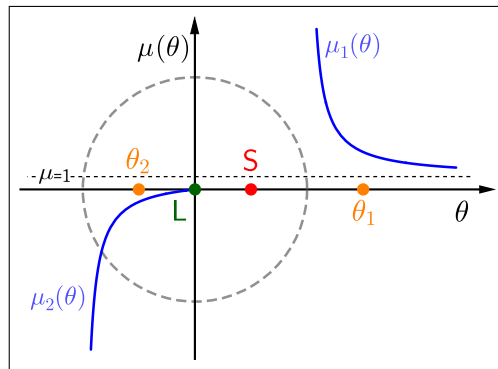
Figure 3.19: Magnification with Geogebra for the SIS lens model.

source for $\theta_S \to \infty$, while the brightness of the internal one, I_2, progressively decreases until it is zero, therefore not visible, for $\theta_S = \theta_E$. As a result, the image that should appear superimposed on the lens, which would probably be so faint that it would not be visible anyway, is not present at all. Consequently, I_1 has always positive parity, $\mu_1 > 0$, and I_2 negative or zero, $\mu_2 \leq 0$, which

defines the orientation of the images.

We would like to focus our attention for a moment on the fact that the SIS model, although very useful in approximating real galaxies, has the problem that the density at its centre is infinite. It is possible to get around this obstacle by introducing a central core of radius a_S with finite density. For this SIS with a core, which in the literature is often called Nonsingular Isothermal Sphere (NIS) [17], the mass density in 3-space is therefore given by

$$\sigma(r) = \frac{{\sigma_v}^2}{2\,\pi\,G\,\sqrt{r^2 + {a_\mathrm{S}}^2}}\;. \tag{3.36}$$

We are not going to enter into the details of this model, because, as already mentioned and as we will see in section 3.3.2.2, the results it provides are very similar to those of other analysed models.

Uniform Disk Lens   The lens model we now consider is a disk extended to infinity (zero thickness), which is seen face-on and is characterised by a uniform surface mass density $\Sigma(\rho) = \Sigma_0$, as shown in fig. 3.20. The fact that the entire mass of the disk, which of course diverges at infinity, is already considered on the lens plane not only simplifies our work, but also makes us straightforwardly understand that its mass profile is given by $M(\rho) = \Sigma_0 \pi \rho^2$. Here we only show the results for this general case, but it is also possible to truncate the uniform disk at a certain radius and then continue the model as if it were a point mass, thus simulating a finite object. Once more the mass $M(\rho)$, expressed in the form $M(|\theta|)$, should be then inserted in the lens
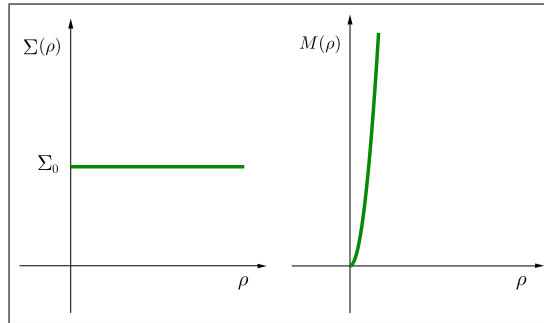
Figure 3.20: Mass density and mass radial profiles of the uniform disk. These are already on the lens plane, there is no need to project them. The plots have different scales.

equation in order to obtain information about number and position of the resulting images. Proceeding exactly as we did for the previous lenses, we calculate the Einstein radius θ_E using eq. (3.8) and $M(|\theta|) = \Sigma_0 \pi (\theta D_\mathrm{L})^2$. Nonetheless, for this lens we get a surprise, as we can see from

$$\frac{\theta_\mathrm{E}}{\theta_\mathrm{E}} = 1 = \frac{4G}{c^2}\,\Sigma_0 \pi\,\frac{D_\mathrm{L} D_\mathrm{LS}}{D_\mathrm{S}} = \frac{\Sigma_0}{\Sigma_\mathrm{c}} = k\;. \tag{3.37}$$

In fact, since the term θ_E cancels out, this means that for the uniform disk lens we never have an Einstein ring with the perfect source-lens-observer alignment. In fact, in eq. (3.37), which represents the case $\theta_\mathrm{S} = 0$, all the terms θ_E cancel out. Basically, excluding Σ_0, all other components of this equation have together the unit of measurement of a surface mass density. This permits us to define a new quantity which is comparable to Σ_0, namely the so-called critical surface mass density, Σ_c [85]. Now, Σ_c clearly depends on the distances involved, therefore, in this respect it is constant for a static configuration source-lens-observer. Moreover, comparing Σ_0 to Σ_c, we also define the parameter $k = \frac{\Sigma_0}{\Sigma_\mathrm{c}}$ which actually gives us the information about the images resulting from the gravitational lensing process for this lens model. In reality, already from

eq. (3.37) we note that $k = 1$ for perfect source-lens-observer alignment and we can suppose the existence of other conditions according to

$$k \lesseqqgtr 1 \qquad \text{if} \qquad \Sigma_0 \lesseqqgtr \Sigma_c \, . \tag{3.38}$$

In order to better understand the role played by k, let us now consider fixed the relative distance between source and lens, D_{LS}, instead the observer can hypothetically approach and move away from the lens (i.e. D_L can vary) with respect to the distance that defines $k = 1$, which we will call $D_{(k=1)}$. Specifically, being $\Sigma_c = \frac{c^2 D_S}{4G\pi \, D_L D_{LS}}$, it clearly depends on the distances involved and, in the specific case, on the position of the observer. Therefore, in the situation just described, we will have $\Sigma_c > \Sigma_0$ when $D_L < D_{(k=1)}$ and $\Sigma_c < \Sigma_0$ when $D_L > D_{(k=1)}$. At this point, calculating the lens equation and expressing it in terms of the parameter k we get

$$\theta - \theta_S = k \, \theta \, . \tag{3.39}$$

eq. (3.39) is very easy to solve, thus can be done also analytically, but we continue to emphasize the graphical solution that gives us in addition to the results also the powerful visualisation of the gravitational lens effect that we already know. This is shown in the Geogebra diagrams of fig. 3.2l, where the equations $f_1(\theta) = \theta - \theta_S$ and $f_2(\theta) = k \, \theta$ are matched and, as always, this is accompanied by pictures taken from the corresponding simulation. This lens model confronts
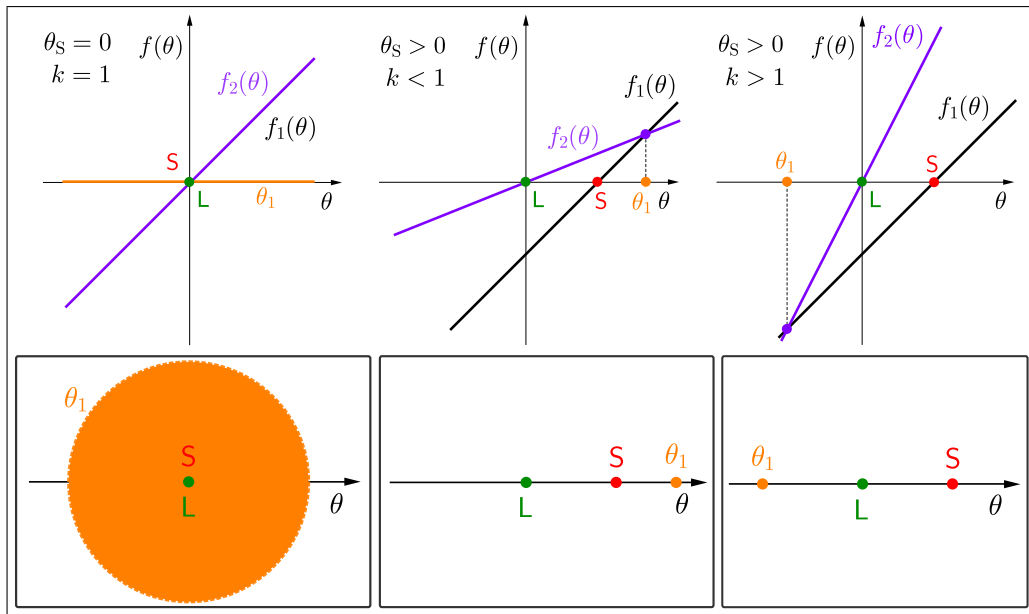
Figure 3.2l: Graphical Geogebra solution for the uniform disk lens. For $\theta_S = 0$ and $k = 1$ the observer sees a fully illuminated infinite disk (left – imagine that the disk goes to infinity). In case of $\theta_S > 0$, we distinguish for $k < 1$, where the observer sees one image on the same side with respect to the lens of the real source (centre), and $k > 1$, where the observer sees one image on the opposite side of the lens instead (right).

us with a very simple, but interesting, gravitational lens effect and we now present some special features and cases that can be observed and discussed with our students. All the peculiarities that we are going to list now, as well as those already faced, are easily verifiable with Geogebra's interactive graphs and the relative algebraic results.[28] As always we consider the best approach to guide students to the discovery and understanding of these results through observation, investigation and discussion.

---

[28]Although we do not show this part for all lens models, we can follow the same procedure as seen for the point mass lens and the Plummer sphere lens.

First of all, in the case of $\theta_S = 0$, as mentioned before, we do not see any Einstein ring. However this configuration corresponds to $k = 1$ and as we can observe in fig. 3.21 the lines produced by the two equations are perfectly superimposed, so a fully illuminated infinite disk is visible. In the figure it is obviously not possible to draw an infinite disk, but let us imagine that it goes to infinity. Interestingly, if $k = 1$ and $\theta_S > 0$, we have no image. In fact, from eq. (3.39), we understand that graphically we would get two parallel lines. Continuing instead to refer to fig. 3.21 and to focus on $\theta_S > 0$, we have images of the source only if $k \neq 1$ and never multiple images. In addition, as anticipated above, the possible situations depend on the distance of the observer from the lens and always Newton's shell theorem applies. In substance, if $k < 1$, i.e. the observer is closer to the lens than where he was with $k = 1$, the only produced image is visible on the same side with respect to the lens where the real source is. Similarly, we can consider the circumstance $k > 1$, i.e. when the observer is further away from the lens than he was with $k = 1$, and again always only one image is produced, but this time it will be visible on the other side with respect to the lens. In both cases, for a predetermined k, the value $|\theta_1|$ increases as θ_S increases, as well as the distance source-image, $\overline{S\theta_1}$. We can also notice that the ratio between the distance of the image from the lens, $\Delta\theta_1$, and θ_S is always constant for a fixed k.

On the other hand, if we analyse the results of the lensing effect produced by this model at equal θ_S, but for different values of k, we can understand other typical characteristics, which are collected in tab.3.4

$k < 1$		$k > 1$	
$k \to 0$	$\theta_1 \to \theta_S$	$k \to 1$	$|\theta_1| \to \infty$
$k \lesseqgtr 1/2$	$\theta_1 \lesseqgtr 2\,\theta_S$	$k \lesseqgtr 2$	$|\theta_1| \gtreqless \theta_S$
$k \to 1$	$\theta_1 \to \infty$	$k \to \infty$	$|\theta_1| \to 0$

Table 3.4: Features of the positions of the image produced by the uniform disk lens with θ_S fixed and k varying.

Finally, let's consider the magnification and parity of the produced images having a uniform disk as lens. The magnification also depends on the parameter k, in particular it is expressed by $\mu(k) = (1 - k)^{-2}$ and in fig. 3.22 we see some examples. From the figure we observe that the magnification is always positive, and so is the parity of the images, and remains constant with the variation of θ_S for each single configuration, that is for a fixed k. In particular, if $k \to 0$, then $\mu \to 1$ and the brightness of the image will then tend to that of the source. As k increases, with $k < 1$, the magnification will then continue to grow until it diverges for $k = 1$, where for $\theta_S = 0$ we have a fully illuminated disk. We can thus guess that its magnification is very high here. For $k > 1$, instead, the magnification will drop down, reaching the value of 1 for $k = 2$ and then tending to zero with $k \to \infty$.

In the context of strong gravitational lensing, the effects produced by this type of lens are not impressive, but they take on a more interesting role when seen in the context of weak lensing. However, we do not deal with this field of study. This is why after having introduced, explained and shown this model, we basically do not consider it anymore for our experimental part. However, it is up to the teachers to decide whether and how to deepen this model according to their teaching needs.

Kuzmin Disk Lens   Also this model is a disk, seen face-on and with the mass distributed on the lens plane, thus also in this case we do not need to project the mass. It is called Kuzmin disk and was invented in 1956 [57]. It consists of an axisymmetric infinitely thin disk and approximates the disk of spiral galaxies. For this reason it is used in N-body simulations of spiral galaxies, especially
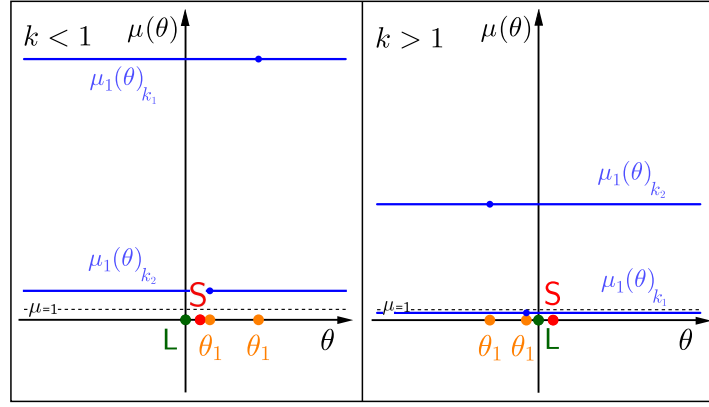
Figure 3.22: Magnification with Geogebra for the uniform disk lens model. Left: The case $k < 1$, where two different values are chosen for k with $k_1 > k_2$. Right: It is $k > 1$ and two other values for k are used, also here $k_1 > k_2$. The grey dashed line is $\mu_1(\theta) = 1$ and this corresponds to the real brightness of the source.

integrated with other components, e.g. embedded in a Plummer sphere halo [91]. Typical for this lens is the fact that the total mass is reached at infinity and there is a scale radius a_K outside of which the gravitational potential[29] in the lens plane approaches quite fast that of a point mass. The surface mass density is expressed for this model by

$$\Sigma(\rho) = \frac{a_\mathrm{K}\, M_\mathrm{tot}}{2\pi \left(\rho^2 + a_\mathrm{K}{}^2\right)^{\frac{3}{2}}}\;, \tag{3.40}$$

M_tot is also here the total mass of the lens reached at infinity. Thus, calculating the mass profile we obtain

$$M(\rho) = \frac{\left(\left(\rho^2 + a_\mathrm{K}{}^2\right)^{\frac{1}{2}} - a_\mathrm{K}\right) M_\mathrm{tot}}{\left(\rho^2 + a_\mathrm{K}{}^2\right)^{\frac{1}{2}}}\;. \tag{3.41}$$

In this case the mass quantity enclosed within $r = a_\mathrm{K}$ is $M(a_\mathrm{K}) = \left(1 - \frac{1}{\sqrt{2}}\right)M_\mathrm{tot}$. In fig. 3.23 the surface mass density and the mass profile of the Kuzmin disk are shown. As for the previous
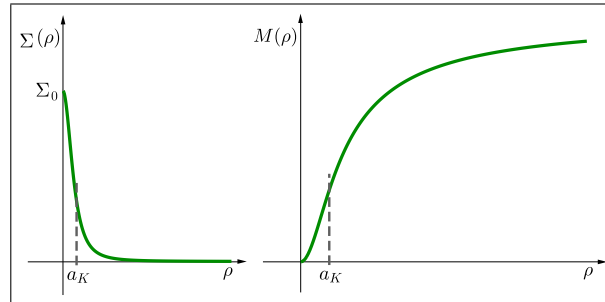
Figure 3.23: .Mass density and mass radial profiles of the Kuzmin disk. These are already on the lens plane, there is no need to project them. The plots have different scales.

models, the mass $M(\rho)$, in the form $M(|\theta|)$,[30] inserted in the lens equation gives information about number and position of the resulting images in the case of a point-like source.

---

[29]$\Phi = -G\,M_\mathrm{tot}/\sqrt{r^2 + (a_\mathrm{K} + |z|)^2}$, where the scale radius a_K is not and has not the same value of a_P for the Plummer sphere.

[30]We have $\rho = \theta D_L$ and $a_\mathrm{K} = \theta_{a_\mathrm{K}} D_L$.

We calculate now the Einstein radius θ_{E}. It is implicitly given by

$$\theta_{\mathrm{E}}{}^2 = \frac{4G\,M_{\mathrm{tot}}}{c^2}\,\frac{D_{\mathrm{LS}}}{D_{\mathrm{L}}D_{\mathrm{S}}}\,\frac{(\theta_{\mathrm{E}}{}^2 + \theta_{a_{\mathrm{K}}}{}^2)^{\frac{1}{2}} - \theta_{a_{\mathrm{K}}}}{(\theta_{\mathrm{E}}{}^2 + \theta_{a_{\mathrm{K}}}{}^2)^{\frac{1}{2}}} = 2\,R_{\mathrm{S}}\,\frac{D_{\mathrm{LS}}}{D_{\mathrm{L}}D_{\mathrm{S}}}\,\frac{(\theta_{\mathrm{E}}{}^2 + \theta_{a_{\mathrm{K}}}{}^2)^{\frac{1}{2}} - \theta_{a_{\mathrm{K}}}}{(\theta_{\mathrm{E}}{}^2 + \theta_{a_{\mathrm{K}}}{}^2)^{\frac{1}{2}}}\,. \tag{3.42}$$

And the lens equation is then

$$\theta - \theta_{\mathrm{S}} = \frac{\theta_{\mathrm{E}}{}^2}{\theta}\,\frac{(\theta_{\mathrm{E}}{}^2 + \theta_{a_{\mathrm{K}}}{}^2)^{\frac{1}{2}}}{(\theta^2 + \theta_{a_{\mathrm{K}}}{}^2)^{\frac{1}{2}}}\,\frac{(\theta^2 + \theta_{a_{\mathrm{K}}}{}^2)^{\frac{1}{2}} - \theta_{a_{\mathrm{K}}}}{(\theta_{\mathrm{E}}{}^2 + \theta_{a_{\mathrm{K}}}{}^2)^{\frac{1}{2}} - \theta_{a_{\mathrm{K}}}}\,. \tag{3.43}$$

eq. 3.43 clearly has a high degree of complexity and this makes it much more difficult to conduct our analysis. Nevertheless, thanks to Geogebra, we can still draw simulations of this gravitational lens effect. However, identifying the patterns that connect the various elements (analytically, but also graphically) with such convoluted equations is out of our possibilities and therefore we limit our discussion to a qualitative level. Emphasising once again the importance of the Geogebra graphics solution, it is precisely in cases like this that it is particularly effective and allows us to visualise and understand the effect produced by this lens model. A result that would otherwise be unlikely to be achieved.

For the Kuzmin disk lens the two equations considered for the graphical solution are $f_1(\theta) = \theta - \theta_{\mathrm{S}}$ and $f_2(\theta) = \frac{\theta_{\mathrm{E}}{}^2}{\theta}\,\frac{(\theta_{\mathrm{E}}{}^2 + \theta_{a_{\mathrm{K}}}{}^2)^{\frac{1}{2}}}{(\theta^2 + \theta_{a_{\mathrm{K}}}{}^2)^{\frac{1}{2}}}\,\frac{(\theta^2 + \theta_{a_{\mathrm{K}}}{}^2)^{\frac{1}{2}} - \theta_{a_{\mathrm{K}}}}{(\theta_{\mathrm{E}}{}^2 + \theta_{a_{\mathrm{K}}}{}^2)^{\frac{1}{2}} - \theta_{a_{\mathrm{K}}}}$. The first situation we see in fig. 3.24 (left) is again the perfect source-lens-observer alignment, $\theta_{\mathrm{S}} = 0$, where there are two solutions, each on opposite sides of the lens and distant $|\theta_{\mathrm{E}}|$ from it, and as we know, the observer actually sees an Einstein ring of radius θ_{E}. Also a central point-like image is present for this model, like the one we encountered for the Plummer sphere lens. Then we continue our analysis with $\theta_{\mathrm{S}} > 0$ in figures 3.24 (right) and 3.25, where again the source is considered moving further away, sideways, from the line joining observer and lens. Also with this model, depending on how far away the source is from the lens, the observer will see respectively three, two or one image of the source. Basically, as soon as the system deviates from the perfect alignment, three images of the source are visible, two are positioned on the left side of the lens, internal to the Einstein ring and the other on the right side (the source side), but external to the ring. In fact, as with the Plummer sphere lens, we have $\theta_1 > 0$, $\theta_2 < 0$ and $\theta_3 \leq 0$. In particular, it is also true that $|\theta_1| \geq |\theta_{\mathrm{E}}|$, $|\theta_2| \leq |\theta_{\mathrm{E}}|$ and $|\theta_3| \leq |\theta_2|$. Moreover, the further the source moves sideways away from the lens, the closer the internal images move towards each other, visually merging in a single image (the two superimposed) and then disappearing, as we can see in the plots in fig. 3.25. Meanwhile, also for this model the external image moves away from the lens on the same side as the source and approaches the source's real position, reaching again the case of little interest for us, namely when $\theta_{\mathrm{S}} \gg \theta_{\mathrm{E}}$.

Definitely, we can say that in general the resulting images for this lens and their behaviour are very similar to those of the Plummer sphere lens. What changes is actually their position. In fact the central image, I_3, for this model moves away from the lens very little and the source must move sideways much more than in the Plummer sphere example in order to see the images I_2 and I_3 superimposed.

We are ready to take into consideration now the behaviour of the magnification $\mu(\theta)$ for the images produced by the Kuzmin lens, which is displayed in fig. 3.26, created following the usual procedure. The magnification behaves basically like the one observed for the Plummer sphere model, therefore we will not go into detail about it. In short, in case of $\theta_{\mathrm{S}} = 0$, the magnification for the two images at a distance $|\theta_{\mathrm{E}}|$ from the lens diverges. The central image instead has a very, very low brightness, so it will certainly not be visible nor distinguishable from the lens. Then, coming out of the perfect alignment, where the magnification is high, for the two images I_1 and
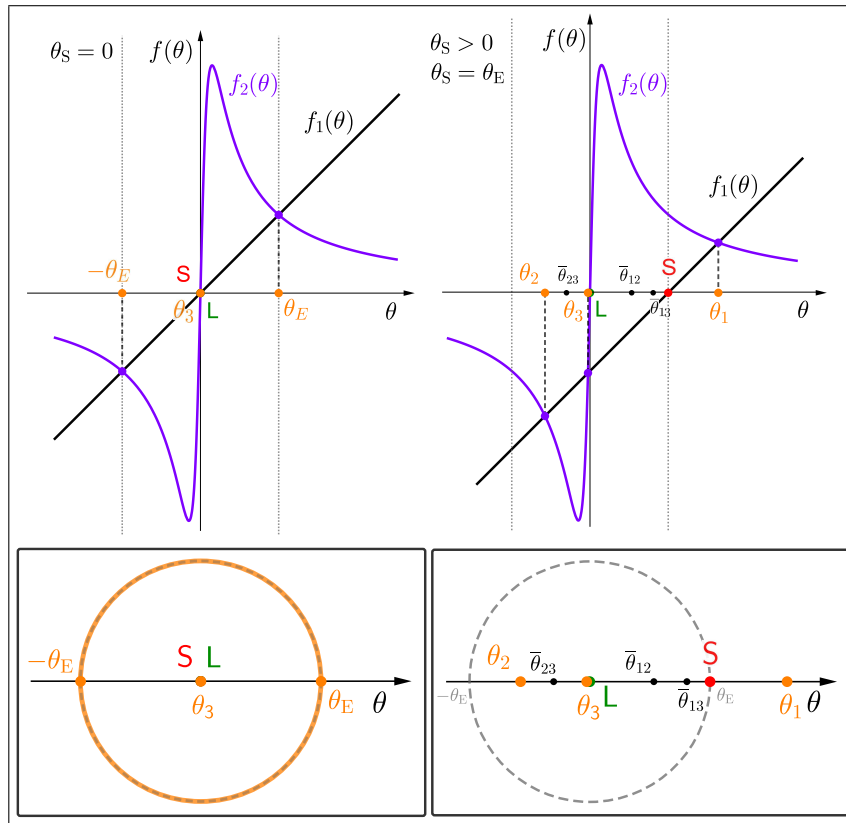
Figure 3.24: Graphical Geogebra solution of the lens equation for the Kuzmin disk lens. Left: The special case $\theta_S = 0$ where, due to full symmetry, the observer sees an Einstein ring of radius θ_E and a central point-like image, which are shown enlarged in the left bottom panel. Right: The case of $\theta_S > 0$ and in particular $\theta_S = \theta_E$. The observer sees at first three images, two inside the Einstein radius θ_E, positioned at θ_2 and θ_3, and one outside, positioned at θ_1, as shown enlarged in the right bottom panel.

I_2 it drops very rapidly. In addition, the more the source moves laterally with respect to the lens, the more the brightness of I_1 tends to coincide with that of the source itself. On the other hand, the brightness of I_2, as it approaches I_3, decreases and becomes barely visible. I_3 always remains very dim. Only just before the superposition of I_2 and I_3, the brightness of these two images suddenly increases and immediately after the merger they disappear. We furthermore observe from the plot that $\mu_1 > 0$ and $\mu_3 > 0$, hence I_1 and I_3 have positive parity despite being on different sides of the lens, and $\mu_2 < 0$, so I_2 has negative parity.

We can indeed confirm that the behaviour of the magnification is very similar to that seen for the Plummer sphere, but we must note that, in the case of the Kuzmin disk, the changes in brightness are more abrupt and extreme.

3.3.1.2 Different Extended Sources

At this point it is natural to wonder what happens with extended, i.e. non-point-like sources. First of all because in nature, no matter how small the sources are, they always have a finite size and secondly because this curiosity is a logical consequence of what we have seen so far. We also ask ourselves questions such as *what shapes will the produced images have if the source is a disk? And if it is a line?* From here we can use our imagination for many more shapes, although from an observational point of view and for simplicity we have limited ourselves to these simple figures.

In practice, in order to answer these questions using a simulation with Geogebra, we need to solve the lens equation of the model we want to study ideally for all the points of the source.
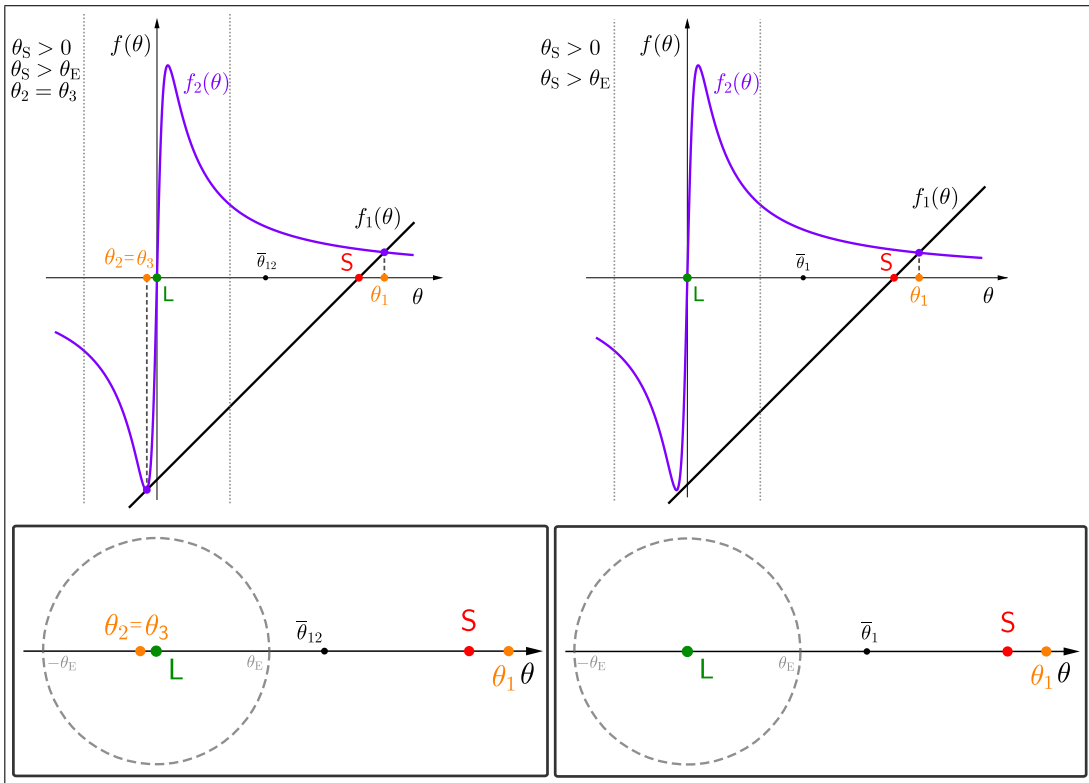
Figure 3.25: Graphical Geogebra solutions of the lens equation for the Kuzmin disk lens in case of $\theta_S > 0$. Now, the further away from the lens the source is, as seen in projection, the closer the external image will be to the source's real position. The other two images instead move towards each other, always remaining inside the ring radius, until they merge into a single image (left panel), then disappear (right panel).
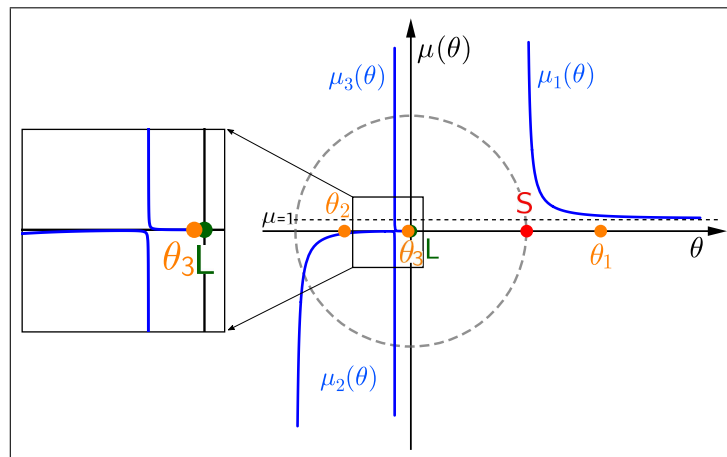
Figure 3.26: Magnification with Geogebra for the Kuzmin disk lens model. In the box, an enlargement to better see the behaviour of μ_2 and μ_3 close to the θ-axis.

Since this is impossible with our means, we limit ourselves to a sufficient number of points which are strategically placed so that the shape of the images is displayed. Thus, connecting with our imagination the image dots properly, we obtain for such sources the images produced by gravitational lensing of the mass distribution considered as the lens. Furthermore, we again produce interactive graphs, simulations of how the lensing effects vary when θ_S (represented as a slider) varies. Basically, all the chosen points are considered as single point-like sources. For these we solve the lens equation (3.7) to obtain the position of the point-like images produced along the

line passing through the point in question and the centre of the lens, as shown in fig. 3.27. This
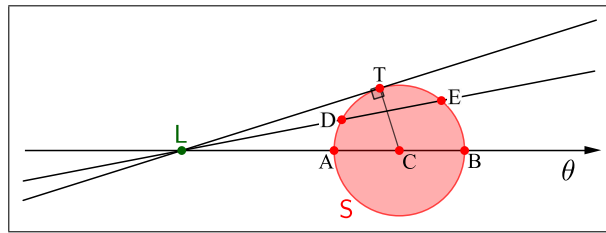
Figure 3.27: Some of the points selected for graphically solving the lens equation for extended sources. For the disk source S, the center C and a few other points along the periphery are shown. In addition, the visualisation lines passing through the selected points and the lens L are also displayed.

line will now be called the "visualisation line". In our case, the chosen source points are always the central point and various other points on the disk periphery of the disk or various other points along the line. Specifically, solving eq. (3.7) with Geogebra means finding where the corresponding function touches the θ-axis, as we have already done to create the simulations present in section 3.3.1.1. Then the θ-coordinate of the obtained points should be plotted along the visualization line they belong to so that the image is at the same distance from the lens. Fortunately, due to the axial symmetry of the chosen models, it is sufficient to find the images for only the upper half of the source and then derive the other half thanks to the reflection of the points with respect to the θ-axis.[31] For the simplest equations, such as those derived for the point mass or SIS model, this procedure is simple and totally feasible even for students at the end of secondary school. As we have seen in section 3.3.1.1, in such simple cases it is also easily possible to find the solution analytically, but we prefer to continue suggesting the Geogebra graphical solutions, an approach that further simplifies the procedure and also allows us to create the useful visualisations we already know. This method is no more complicated than the ones we have seen so far, since the functions and techniques for solving the problem are exactly the same. However, it is more time-consuming because we work with many point-like sources and the images must also be placed back on the corresponding visualisation line.[32] Remember that diagrams and simulations can be created using the preferred parameters, however all the material produced by us and used during the creation and testing of this project is available and directly usable. Let us now consider some examples taken from the simulations of the gravitational lensing effect with extended sources and analyse their fundamental characteristics. We limit ourselves to two cases of lenses with increasing difficulty, the point mass, which, as already mentioned, is among the simplest examples, and the Plummer sphere, which, as we know, has a higher degree of difficulty. However, we underline once again the idea that through the use of Geogebra it is possible even for non-advanced students to understand the most mathematically complicated cases.

Point Mass Lens   While we explore the results of gravitational lensing with extended sources, we will take a closer look at the disk because it has a special interest for us in the context of astrophysics. As far as the line as a source is concerned, we will present only the graphical results, which however, besides satisfying the curiosity about this kind of source, will be useful to understand geometrically the general idea of distortion for images produced by gravitational lensing plexiglass simulators, as we will see in section 3.3.2.3.

---

[31]In Geogebra this function is easily performed thanks to the command "Reflect Object in Line".

[32]For this purpose, once the angular distance θ of the image from the lens has been obtained, create the point at the same distance, but on the visualisation line with coordinates $(\theta \cos \alpha, \theta \sin \alpha)$, where α is the angle between the visualisation line and the θ-axis.

In fig. 3.28 we see on the left the case of perfect source-lens-observer alignment, $\theta_S = 0$,[33] for the point mass lens model with an extended **disk-shaped source** of radius θ_0. First we observe that the forming Einstein ring has a certain thickness and the image of the central point of the source corresponds to the *Einstein circle* in grey (from now on called in this way to distinguish it from the total Einstein ring and displayed as a dashed grey circle in the figure). Therefore, it is
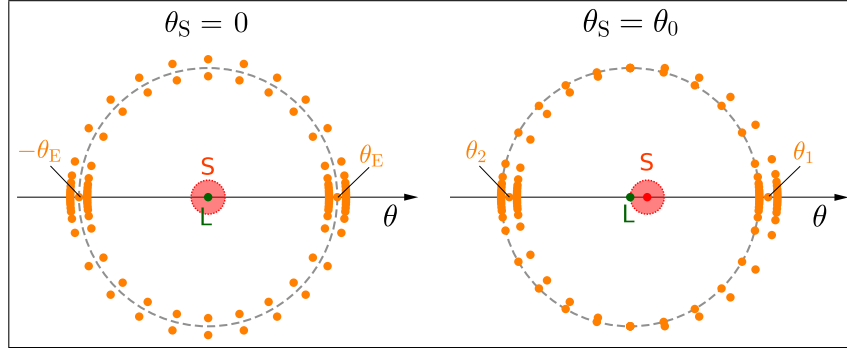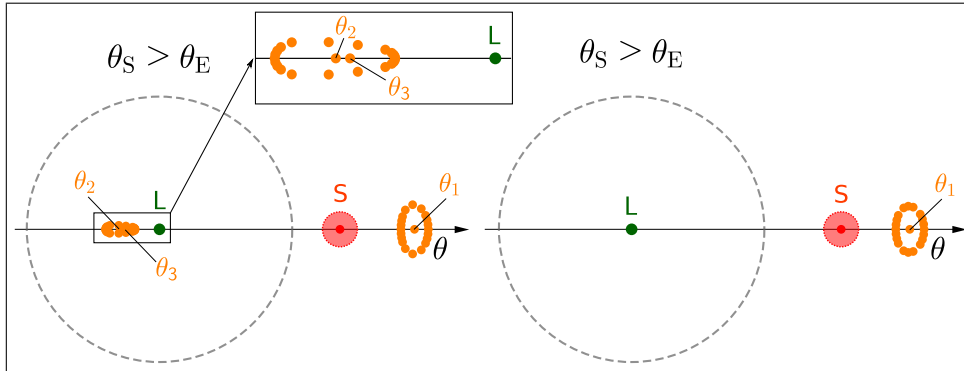

Figure 3.28: Simulation with Geogebra of the solution of the lens equation for the point mass lens in the case of an extended disk as source, S, of radius θ_0. Left: The case $\theta_S = 0$, where we observe the Einstein ring. Right: The lens L is positioned now at the edge of the source S and we observe two big arcs that touch each other on their extremities. The dots represent the produced images of specific points of the sources and give us an idea of the total images shape. The images of the source's central point are always indicated along the θ-axis with the usual notation adopted in section 3.3.1.1.

clear from these details that the larger the source disk, the thicker the Einstein ring. Due to the simplicity of the point mass model, these results can also easily be obtained analytically.

As far as magnification in general is concerned, considering eq. (3.13) and what has been said in section 3.2.4, we derived that for small sources its value is provided by the ratio between the area of the image and the area of the source. For its sign, therefore the parity of the image, we refer to what has been seen in the previous sections. Given that we are dealing with disks in this configuration, the procedure is quite simple. We deduce, in the specific case represented here, that if the source disk has area $A_S = \pi(\theta_0 D_S)^2$, where θ_0 is its angular radius, then for the magnification of the Einstein ring we will have

$$\mu_{\text{ring}} = \frac{A_I}{A_S} = \frac{(\theta_{\text{Eout}}{}^2 - \theta_{\text{Ein}}{}^2)}{\theta_0{}^2} \ . \tag{3.44}$$

Practically, this means that we compute the area of the bigger disk of angular radius θ_{Eout} minus the area of the smaller disk of angular radius θ_{Ein}. Now introducing eq. (3.18) and considering that for the points on the source edge $\theta_S = \theta_0$, we get

$$\mu_{\text{ring}} = \frac{\sqrt{\theta_0^2 + 4\theta_E{}^2}}{\theta_0} \ . \tag{3.45}$$

Moreover, following the same reasoning, the thickness of the Einstein ring can easily be obtained to be

$$\Delta\theta_E = \theta_{\text{Eout}} - \theta_{\text{Ein}} = \theta_0 \ , \tag{3.46}$$

which, as we note, corresponds to the radius of the source. All these results, obviously in numerical form, can also be easily obtained from the Geogebra graph, using the coordinates of the corresponding points, and in this way the same information as above is obtained. It is in fact

---

[33]We consider the centre of the source.

just a little bit of basic geometry.

In addition to all this, if we divide the source into coloured sectors, as in fig. 3.29, and keep the same colours for the respective images, it is immediately observed that the outer part of the Einstein ring, with respect to the Einstein circle, is oriented like the source, while the inner part is reversed both vertically and horizontally. In fact, from what we know about magnification and
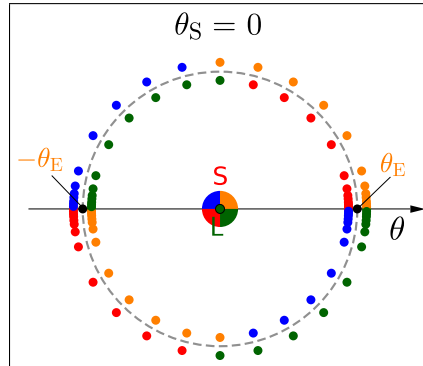
Figure 3.29: Simulation of the Einstein ring produced from an extended multicoloured disk source (S) for the point mass lens (L), represented by the green dot at the centre. We can observe if images are inverted with respect to the source and how.

parity and from the previous discussion about this model, we know that in order to understand if and how an image is subject to inversion, we also have to take into account whether it appears on the same side of the source or not and on which side, with respect to the lens, the source is located. What we therefore observe with this coloured Einstein ring is a consequence of the fact that half of the source is to the right of the lens and half to the left. Basically, considering only the source part on the right of the lens, we have as images the external part of the Einstein ring on the right, with positive parity, and the internal part of the Einstein ring on the left, with negative parity and thus inverted with respect to the horizontal axis. Vice-versa, for the other half source we will have as images the external part of Einstein ring on the left, with positive parity, and the internal part of Einstein ring on the right, with negative parity and thus inverted with respect to the horizontal axis. Putting all this information together we obtain the Einstein ring in fig. 3.29. These are all outcomes that we can deduce just by looking at and studying this figure.

Continuing our discussion, referring now to the right-hand side of fig. 3.28, we see that the lens L is now located on the edge of the source disk.[34] In this case the image is no longer a ring and we observe instead two large arcs joined by their extremities. It is interesting to note that the right arc (source side) has its internal profile on the Einstein circle and then extends outwards, while the left arc has its external profile on it and extends inwards.

If the source then continues to move sideways, as we see in fig. 3.30, the two arcs shrink and separate, forming two images of the source that appear as two deformed ellipses. These images respect the same cases and the same general rules seen in the previous section. In fact the image on the left of the lens, inside the Einstein circle, gets closer and closer to the lens itself and gets smaller and smaller according to what has been seen for the magnification. At the same time, the right-hand image moves further and further away from the lens and shrinks towards the actual size and position of the source.

In all these three last configurations, and certainly also in the intermediate ones, calculating the images' magnification analytically is complicated and exceeds our teaching objectives. However, once again Geogebra comes to our aid. In fact, if we join the image points of each distorted ellipse with segments thanks to the function "Polygon" (an example of such a polygon can be seen in fig. 3.48), Geogebra immediately gives us the area of such a polygon, which is a rough

---

[34]The lens is positioned at a distance θ_0 from the centre of the source.
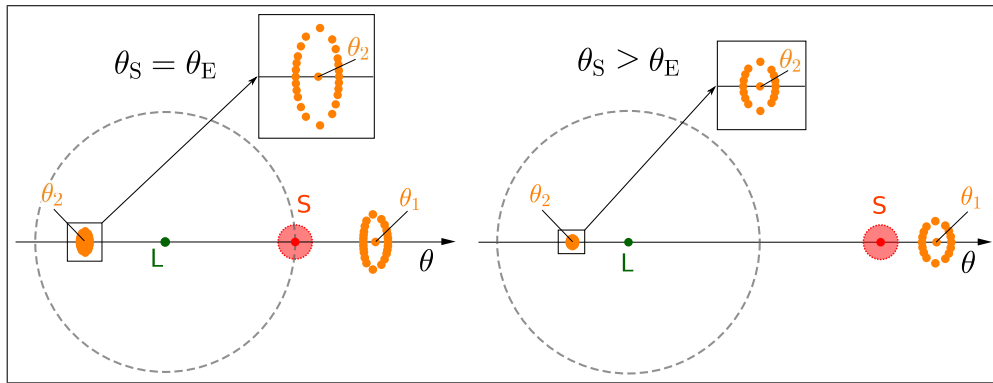
Figure 3.30: Simulation with Geogebra of the solution of the lens equation for the point mass lens in the case of an extended disk as source, S, of radius θ_0. As compared to fig. 3.29, the source S moves further sideways from the lens L. Left: The case $\theta_S = \theta_E$. Right: The case $\theta_S > \theta_E$. Note that the image I_2 centred at θ_2 becomes at a certain point so small that it is no longer possible to distinguish the various points, thus we show an enlargement of them in the small boxes. However, with the Geogebra files we can zoom the figures and observe them better. All images that form follow the rules seen in the previous section 3.3.1.1 and again we use the same notation.

estimate of the area of the total image. We can then divide this estimate by the value of the area of the source and obtain in good approximation the magnification of this image. As far as parity is concerned, keeping in mind what we have already seen and simply using a source divided into coloured sectors as done for the Einstein ring. If we appropriately change the colours of the image points in relation to their position with respect to the lens, we obtain all the necessary information about the possible inversion of the images. In the case of the point mass model we
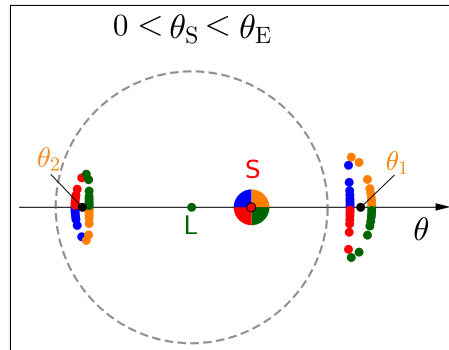
Figure 3.31: Simulation of two images produced from an extended multicoloured disk source (S) for the point mass lens (L) in the case $0 < \theta_S < \theta_E$. The centre of the source is indicated with a red dot. We clearly observe the the inversion with respect to the horizontal axis of the image I_2 centred at θ_2.

know that the image I_1, centred at θ_1, is oriented exactly like the source and I_2, centred at θ_2, is instead inverted with respect to the horizontal axis. All these facts are proved observing fig. 3.31.

The graphical solutions for the **line source** can be now observed and examined. The case of a line-shaped source divided in two equal pieces by the θ-axis is displayed in fig. 3.32. Starting from the first picture on the left, we immediately notice that with perfect alignment the produced images are a line, although longer than the source and superimposed on it, and an Einstein ring, which is the image of the central point of the line due to reasons of symmetry. In this situation and as shown in the other three pictures of fig. 3.32, when the source moves laterally relative to the lens, the observer sees as images a curve similar to the letter "c" to the left of the lens and a
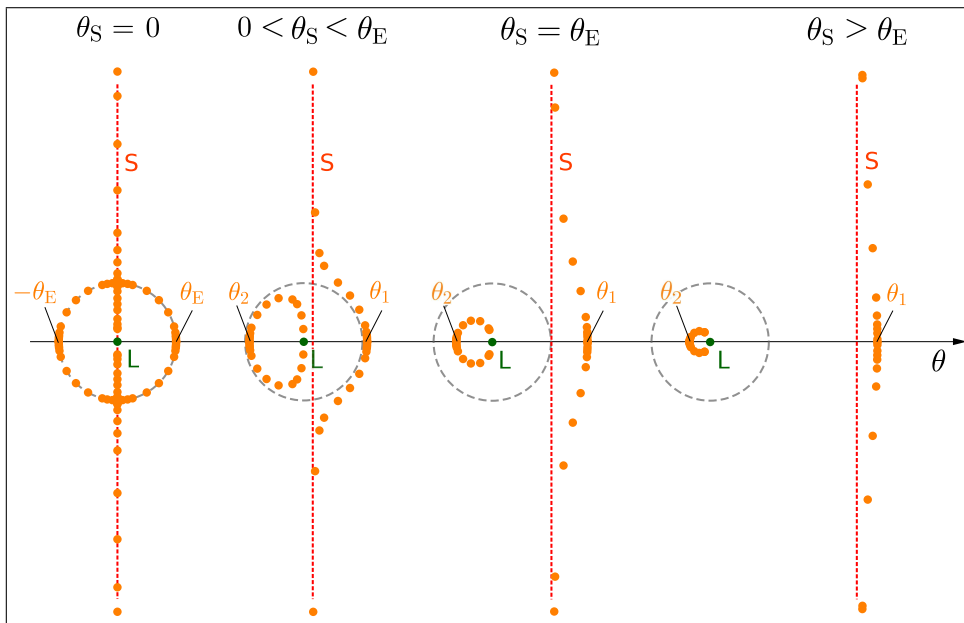
Figure 3.32: Simulation with Geogebra of the solution of the lens equation for the point mass lens in the case of a line as source, S. The sequence starts with the case $\theta_S = 0$, then, to the right, we see again the source S moving sideways away from the lens L. The dots represent the produced images of specific points of the sources and give us an idea of the total shape of the images (imagine to connect the dots with segments). The images of the source's central point are always indicated along the θ-axis with the usual notation adopted in section 3.3.1.1.

curved line to the right. The "c"-shaped image is positioned between the edge of the Einstein ring and the lens itself, almost closing its shape on it. The curved line instead is positioned outside the Einstein ring and in its central part follows the ring shape. As the source continues to move laterally, the "c" becomes smaller, always remaining near and to the left of the lens, while the curved line loses more and more of its deformation and approaches the source straight line.

Even if we do not treat this topic here, to get an idea of the magnification and parity of these images, we can just follow the procedures we have seen for the disk source, remembering that in this case we have to consider the length of the line source and of other curved or circular images.[35] The outcomes will naturally follow the rules seen so far and we can easily imagine what they will be.

Plummer Sphere Lens For the Plummer sphere lens model we only explore the results of gravitational lensing with an extended disk source, a type of source that, as we have just seen, is particularly interesting for our purposes, astrophysically speaking and in connection with the models we want to represent. As for the line source, we do not present this example because it is very similar to what we have just seen for the point mass lens. For the line source, in fact, the main differences, which are hardly noticeable anyway (apart from the last one), are three. Basically, with perfect alignment we have the addition of a central image superimposed on the lens, whereas in other configurations we see that what was previously a "c" shape is now a closed loop, which again narrows, but a little faster and then at some point disappears. This is in full agreement with the behaviour of this lens we have seen in section 3.3.1.1.

Focusing our attention on observing fig. 3.33, for the Plummer sphere lens model with the extended disk-shaped source of radius θ_0, we see on the left the case of perfect source-lens-observer alignment, $\theta_S = 0$. Also in this case the forming Einstein ring has a certain thickness and the

---

[35]It is possible to give a thickness, however small, to the source line and consequently to the images and obtain in this way their areas.

image of the central point of the source corresponds once more to the Einstein circle (dashed grey circle in the figure). In addition and as expected, there is also a central small image which is superimposed to the centre of the lens. However, as we understood analysing this model in the previous section, this central image should be dim and fused with the light from the lens. Basically, it follows from these details that also for this lens model the larger the source disk, the
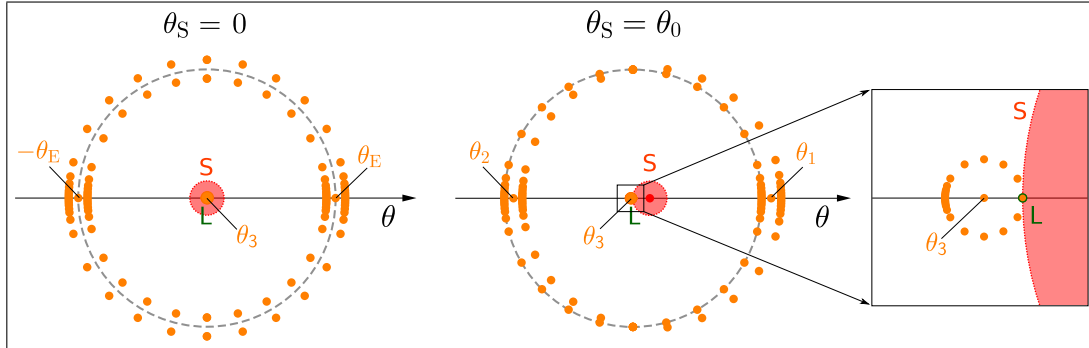
Figure 3.33: Simulation with Geogebra of the solution of the lens equation for the Plummer sphere lens in the case of an extended disk as source, S, of radius θ_0. Left: The case $\theta_S = 0$, where we observe the Einstein ring and the central image (orange disk positioned at the centre of the source), which covers the lens L, indicated but not visible at all. Right: The lens L is positioned now at the edge of the source S and we observe two big arcs touching at their extremities and the third image is slightly shifted to the left side of the lens, as can be seen enlarged in the box. Here we also note the position of the lens L. The dots represent the produced images of specific points of the source and give us an idea of the total shape of the images. The images of the source's central point are always indicated along the θ-axis with the usual notation adopted in section 3.3.1.1.

thicker the Einstein ring and the larger the central image.

Since the analytical approach is too complex for this example, we concentrate on the graphical one with Geogebra, showing again its great potential. At this point, following in principle the same reasoning as for the point mass lens, it is possible to deduce and numerically calculate from the graph the magnification of the Einstein ring and of I_3. In Geogebra, with the proper command "Area", we can easily obtain the area of the bigger disk of radius θ_{Eout} and of the smaller disk of radius θ_{Ein}. Subtracting the last from the first one and dividing the result by the source area $A_S = \pi(\theta_0 D_S)^2$, we obtain the magnification of the Einstein ring. Interestingly, at the same conditions for the point mass lens, thus for an equal amount of mass for both lenses, this ring is slightly brighter and this comes from the fact that it is a little thicker. We can indeed prove this calculating its thickness on the plot thanks to $\Delta\theta_E = \theta_{\text{Eout}} - \theta_{\text{Ein}}$. We discover that for the Plummer sphere lens $\Delta\theta_E > \theta_0$, albeit not by much. With regard to the central image I_3 instead, also being a disk at this stage, we simply calculate its area and divide it by the area of the source to obtain its magnification. As expected, also due to its small size and what has already been discussed for the magnification of the images produced by this gravitational lens model, this image will in any case be dim and probably completely fused with the light coming from the lens. As for the point mass model, also for this example, if we divide the source into coloured sectors (fig. 3.34), it is immediately observed that the outer part of the Einstein ring, with respect to the Einstein circle, is oriented like the source, while the inner part is reversed both vertically and horizontally. If we look at the central image, enlarged in the box, we see that it also appears reversed both vertically and horizontally. The reasons for this behaviour are exactly the same as explained for the point mass lens, namely that to understand if and how an image is subject to inversion, we also have to take into account whether it is on the same side of the source or not and on which side, with respect to the lens, the source is located. In this configuration we face
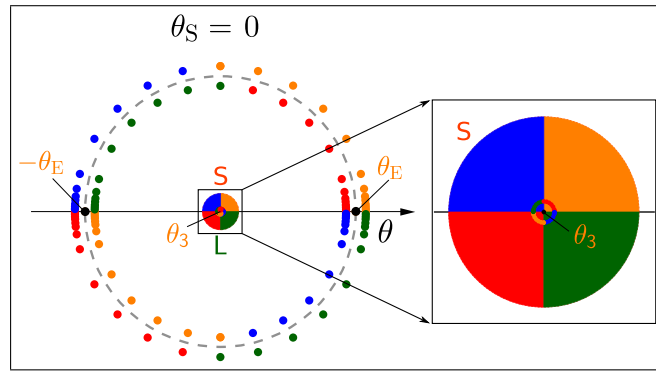
Figure 3.34: Simulation of the Einstein ring produced from an extended multicoloured disk source (S) for the Plummer sphere lens (L). The lens is indicated at the centre, where it is positioned, but it is not visible because covered by the the third image. In the box an enlargement of the central region is shown.

once more the fact that half of the source is to the right of the lens and half to the left. In light of these reasons, it is obvious that the central image is oriented in the same way as the inner part of the Einstein ring, because it is subject to the same conditions and undergoes the same process. Referring now to the right-hand side of fig. 3.33, we see again that the next configuration considers the lens L now located on the edge of the source disk. Also in this case there is no longer a ring, but we see instead two large arcs joined by their extremities and the additional central image is now shifted to the left side of the lens, as we note from the box in fig. 3.33 (right). The position of the arcs and the direction in which they extend are exactly the same as seen in the previous example of the point mass lens.

At first, if the source then continues to move sideways, as we see on the left of fig. 3.35, the two arcs shrink and separate, forming two images of the source that appear as two deformed ellipses. Moreover, the third image also starts to lose its circular shape and appears elongated. Obviously
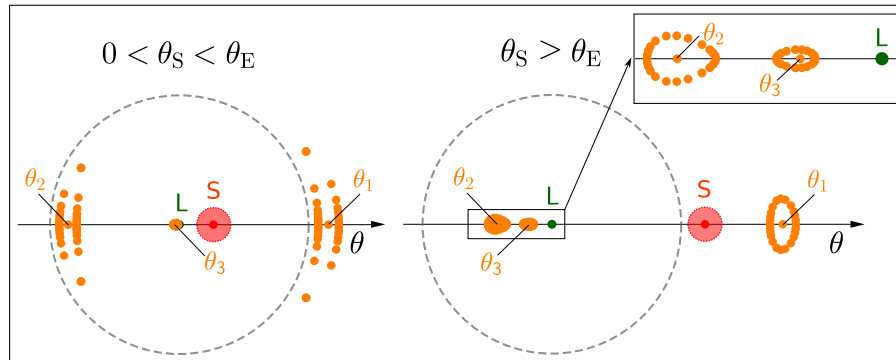
Figure 3.35: Simulation with Geogebra of the solution of the lens equation for the Plummer sphere lens in the case of an extended disk as source, S, of radius θ_0. With respect to fig. 3.33, the source S moves further sideways from the lens L. Left: The case $\theta_S < \theta_E$. Right: The case $\theta_S > \theta_E$ with the two images on the left still separated. These images become so small at a certain point that it is no longer possible to distinguish the various points, we show an enlargement of them in the box. However, with the Geogebra files we can zoom in on the figures.

following the same rules, what happens for point-like images as the source moves laterally away from the lens, also happens in general for extended images. In fact, observing the sequence of pictures in figures 3.35 and 3.36, we notice that as the source moves laterally away from the lens, the two images to the left of the lens and inside the Einstein ring move closer together. In this process they deform, becoming similar to each other, as can be seen in the box on the right-hand

side of fig. 3.35. The two images then merge into a single image that gradually becomes smaller as the various image points, one by one, merge and then disappear, as we saw when analysing the various cases with a point-like source in the previous section. At the end of this process of course the complete image will disappear. In fig. 3.36 we observe two pictures relating to this phase. On the left we see a moment in which, although we already have a single image on the left of the lens, the images of the central point at θ_2 and θ_3 have not yet merged and disappeared. On the right this phase is complete for each image on the left of the lens and they have all disappeared. At the same time, the image to the right of the lens moves away from the lens and will again

Figure 3.36: Simulation with Geogebra of the solution of the lens equation for the Plummer sphere lens in the case of an extended disk as source, S, of radius θ_0. With respect to fig. 3.35, the source S continues to move further sideways from the lens L. We observe the merging of the two images at θ_2 and θ_3 on the left and when they are already disappeared on the right. These are some of the cases that arise together with the corresponding images as θ_S increases. The two small images on the left are shown enlarged in the box.

tend to the actual size and position of the source.

At this point, using the same procedure as for the point mass model, Geogebra again helps us with regard to the magnification of the produced images. In fact, joining the image points for each distorted ellipse with segments thanks to the function "Polygon", Geogebra gives us the approximate area of every image. Then dividing them by the area of the source, we obtain a good approximation of their magnification. Once more, thanks to the source divided into coloured sectors, we can observe the inversion of images when present and obtain information about the parity. We can finally also better understand the meaning of the results that we have seen in section 3.3.1.1 about the parity of the produced images. In fact, what has been said about the Plummer sphere model is now observed, confirmed and comprehended in a deeper way. Specifically, the image I_1 positioned on the right side of the lens has $\mu_1 > 0$ and we see that it is oriented like the source. On the other hand, I_2 has $\mu_2 < 0$ and it is on the left side of the lens, thus it is inverted with respect to the horizontal axis, exactly as it is for the point mass lensed images. However, I_3, which has $\mu_3 > 0$ but it is on the left side of the lens, undergoes a double inversion and is flipped with respect to the horizontal and vertical axes. These outcomes are all visible in fig. 3.37, especially in the box.

From experience we can say that this graphical approach, combined together with the analytical one if possible, and these simulations capture the students' interest and involve them, at least in part, in a practical activity that keeps their focus and stimulates their curiosity. The feedback received regarding the effectiveness of teaching this subject through this approach and the response of satisfaction with the activities carried out has always been very positive. However, this increases considerably with the next educational tool we are now going to present. This is actually a teaching tool intended for more experimental activities to accompany what we have seen so far and designed
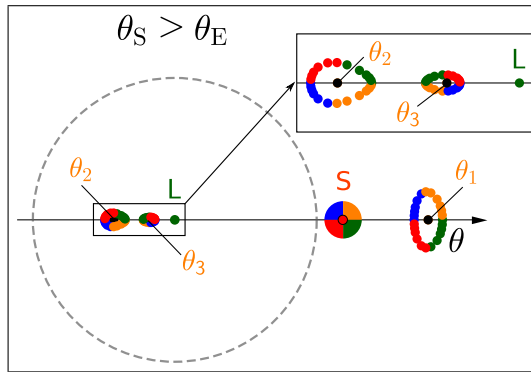
Figure 3.37: Simulation of three images produced from an extended multicoloured disk source (S) for the Plummer sphere lens (L) in the case $\theta_S > \theta_E$. The centre of the source is indicated with a red dot. In the box we clearly observe the inversion with respect to the horizontal axis of the image I_2 centred at θ_2 and the double inversion, horizontal and vertical, of the image I_3 centred at θ_3.

on the inspiration of research that has investigated the strong gravitational lensing effect before it was actually possible to detect it.

3.3.2   The Plexiglass "Gravitational" Lensing Experiment

Another tool designed to perform the task of visualising the gravitational lens effect produced by galaxies as lenses is the use of special plexiglass lenses that can recreate this effect. Also in this case, the idea is to represent different lens models and specifically the same five models seen for the Geogebra simulations (see appendix E). This is not only for practical reasons, in fact as said the equations involved are simpler, but also to offer continuity and consistency in the path of discovery of gravitational lensing. Of course, teachers are free to explore other models, indeed we strongly recommend it if they wish to do so. In fact, one of the goals of these projects that we have realised is to provide knowledge, tools, means and procedures so that it is also possible to create one's own personalised educational material.

This idea has been addressed before in the literature [85][105][27][58][48][1][44][45], but we are able to add new results. As far as we know, among the five plexiglass lenses studied, designed and built, we are the first to have produced the Plummer sphere and Kuzmin disk models. We stress once again the fact that the three models of lenses excluded from production for this educational tool have a high similarity with other considered models in terms of behaviour, resulting images and shape of the plexiglass lens. Therefore, the choice to produce the lenses defined by simpler functions was made, this for educational purposes, but also to facilitate their production by the university laboratory.

3.3.2.1   Shaping a Plexiglass Lens

We are certainly not the first to ask ourselves the question of how it is possible to visualise the gravitational lens effect. Refsdal wanted to answer the very same question in the 1960s, when still no gravitational lens had been detected. Thus, the idea of combining optics and general relativity with the aim of producing glass lenses capable of showing us the effects of gravitational lensing was apparently born. The modern answer to this question is clear, it is just enough searching through the stunning photos of the Hubble Space Telescope (HST) or other powerful telescopes and observing the gravitational lenses that nature offers us. However, it is now clear that we have some good alternatives that have proved to be useful educational tools in explaining this topic with the addition of an experimental part. We are of course talking about the simulations seen

with Geogebra and these special plexiglass lenses. Moreover, we can say that combining these three different ways of visualizing the gravitational lens effect provides the best result in teaching this topic.

Obviously, these plexiglass lenses must have a special profile to reproduce gravitational lensing in a physically correct way. In particular, as said in section 3.2.5, we can understand the shape of the lens solving the differential equation (3.15) after having introduced the desired mass distribution in place of $M(|y|)$.[36] Naturally, the plexiglass lens must be scaled down to practicable dimension for its use in the classroom, with the consequence that it will represent a much smaller amount of mass, but the effects, although on a different scale, will remain the same. This procedure will actually provide the function that describes the profile of the lens, moreover, thanks to the axial symmetry of our models, we only need this profile for positive values of the x and y variables, as can be seen in what follows for the five lens models we have chosen. In fact, as we know, by rotating the obtained profile with respect to an axis of symmetry, which in our case corresponds to the x-axis, we obtain the whole lens. Another detail to consider is that in a real gravitational lens event, the very central part is physically occupied by the lens and therefore the incident light in that area is naturally blocked. In our plexiglass lenses, the central part is free and the light rays can pass through. At the moment we do not have an effective way to avoid this effect. In fact, at least for us, a few too many rays of light is less annoying than the additional images produced by any objects which are blocking the light in the middle. Finally, the nature of the images of a background source that these plexiglass lenses should produce is the same we obtained analysing the lens equation solution for different mass models in the previous section 3.3.1.

Without entering now in technical details, with Geogebra it is easily possible to draw the lens profile just setting some of the parameters involved, for instance the size of the plexiglass lens. In particular, all our lenses have a 1 cm high flat base that allows them to be mounted on specific frames and this flat side receives perpendicularly the rays coming from the source. Furthermore, the produced lenses have a diameter of 15 cm and the refractive index for the plexiglass used is $n \simeq 1.5$. For technical reasons related to the manufacture of these lenses in the laboratory, which was a priority for us, the thickness had to remain as close as possible to 2 cm due to the initial size of the plexiglass plate used, thus limiting the choice of certain specifications, such as the amount of mass that the plexiglass simulator represents. However, at least as far as the theoretical part is concerned, it is possible to adopt different values.

As we believe that exploring the technical and practical details of creation of the lens does not meet our educational objectives, we only present the general solutions for each lens produced, which instead allow us to understand the analogy and the link between optical and gravitational lenses. Besides, being able to find out what shape the plexiglass lenses should be given in order to recreate the gravitational effects due to the different chosen mass distributions is a stimulating exercise. Again, there are different levels of difficulty regarding the mathematical part, so this kind of exercise can be adapted to students with different degrees of knowledge. In this respect, among the five lens models we discuss, we again consider point mass, SIS and uniform disk as the simplest to deal with, while the others require a slightly more advanced mathematical background. Let us now see what our plexiglass "gravitational" lenses look like.

Point Mass Lens   Knowing already that the point mass has the mass independent of the distance from its centre and is expressed by $M(|y|) = M_{\text{tot}}$, eq. (3.15) becomes

$$\frac{\mathrm{d}y}{\mathrm{d}x} = -\frac{(n-1)\,c^2}{4G\,M_{\text{tot}}} \cdot y \, . \tag{3.47}$$

At this point, solving it for a generic lens, namely without fixed parameters, we obtain

$$y = A \cdot e^{-\frac{(n-1)\,c^2}{4G\,M_{\text{tot}}} \cdot x} \, , \tag{3.48}$$

---

[36]In this case, since we want to calculate the lens profile, we need the mass expressed in terms of the y coordinate.

whose exponential function defines the shape of the lens as in the left side of fig. 3.38 and A is a constant. It is obvious that the lens must be cut at a certain distance from the y-axis and in the
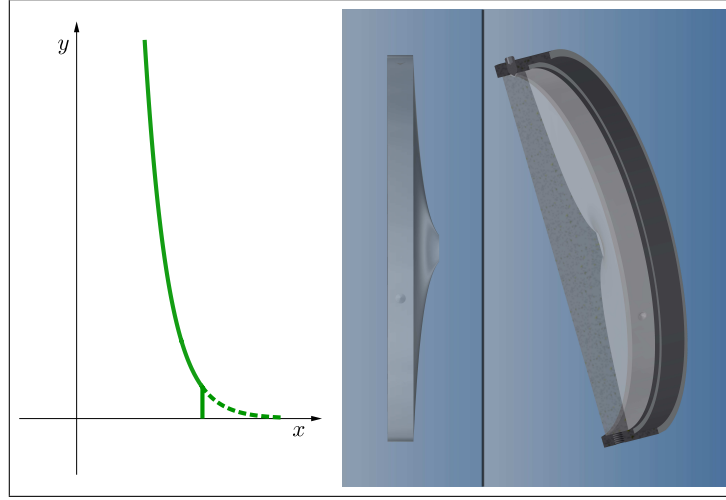
Figure 3.38: Point mass plexiglass lens profile with Geogebra (left) and Autodesk (right – Credit: T. Köhler).

right side of fig. 3.38 we see the particular shape of this lens, which has also the name "foot of a wineglass" lens (and it is not necessary to explain why). Even though the shape of a real wine glass foot is not an exponential function, it is still very similar and even the images it produces are in strong resemblance with the ones produced by this type of lens. It is however important to remember that we do not know what kind of mass distribution a real wine glass foot represents and not even if what it represents has physical meaning. Anyway, from a qualitative point of view, we can use the foot of a wine glass to have a rough, but accessible to everyone, simulation of this kind of gravitational lens.

Plummer Sphere Lens   For the Plummer sphere lens we insert the projected mass from eq. (3.26), namely $M(|y|) = |y|^2 \, M_{\text{tot}}/(|y|^2 + a_{\text{P}}{}^2)$, in eq. (3.15) obtaining

$$\frac{\mathrm{d}y}{\mathrm{d}x} = -\frac{(n-1)\,c^2}{4G\,M_{\text{tot}}}\,\frac{y^2 + a_{\text{P}}{}^2}{y} \; . \tag{3.49}$$

Solving it again for a generic lens, we get

$$y = \sqrt{A \cdot e^{-2\,\frac{(n-1)c^2}{4G\,M_{\text{tot}}}\cdot x} - a_{\text{P}}{}^2} \; , \tag{3.50}$$

whose profile is shown in the left side of fig. 3.39 and A is also in this case a constant. For this model we do not need to cut the lens, it naturally has the shape of a little hill, as we can see in the right side of fig. 3.39.

Singular Isothermal Sphere (SIS) Lens   For the SIS lens we once again insert the projected mass from eq. (3.32), $M(|y|) = \frac{\pi\,\sigma_v{}^2}{G} \cdot |y|$, in eq. (3.15), obtaining

$$\frac{\mathrm{d}y}{\mathrm{d}x} = -\frac{(n-1)\,c^2}{4}\,\frac{1}{\pi\sigma_v^2} \; . \tag{3.51}$$

Solving it for a generic lens, we have then

$$y = A - \frac{(n-1)\,c^2}{4\,\pi\sigma_v^2} \cdot x \; , \tag{3.52}$$
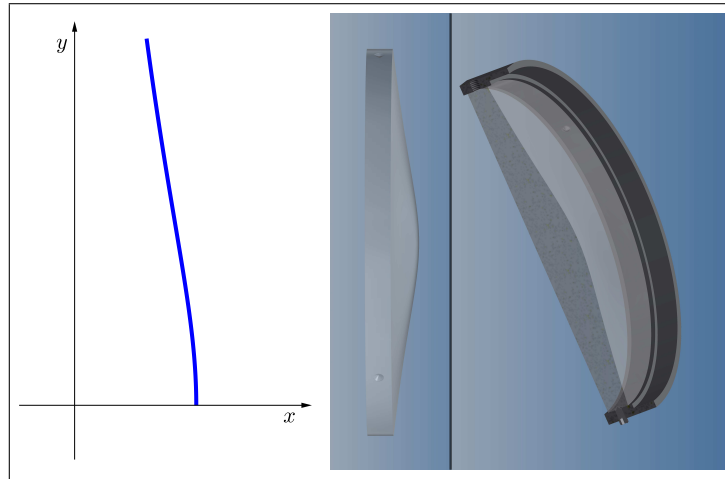
Figure 3.39: Plummer sphere plexiglass lens profile with Geogebra (left) and Autodesk (right – Credit: T. Köhler).
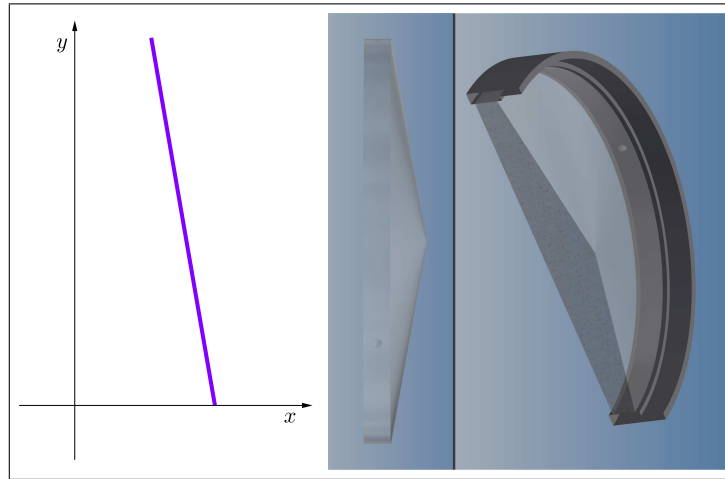
Figure 3.40: SIS plexiglass lens profile with Geogebra (left) and Autodesk (right – Credit: T. Köhler).

which is clearly a straight line and the corresponding lens profile is shown in the left side of fig. 3.40. A is again a constant. Rotating this line around a central axis, we get the entire lens shown in the right side of fig. 3.40, which is evidently a cone. After having studied and produced this lens model, we discovered that this kind of lens is part of a group of lenses with similar characteristics called axicons [72]. These lenses are actually very well known and used in various scientific researches and applications, including medicine, biology, astronomy, physics and wave optics. For example, these lenses are typically utilised in corneal surgery, optical coherence tomography, atomic traps, spherical aberration correction, acoustic testing, linear accelerator and many other fields [68].

We recall that the SIS is the simplest model representing a galaxy, and being a good approximation to explain the flat rotation curves observed at large radii of spiral galaxies, it is also considered in the search for evidence on the presence of dark matter and its abundance. In fact, since σ_v is an expression of the total mass of the galaxy, see previous chapter 2, by comparing the total mass with the luminous mass we can get an idea of the abundance of dark matter [17].

Uniform Disk Lens   Considering the projected mass of the uniform disk lens, $M(|y|) = \Sigma_0 \pi |y|^2$, eq. (3.15) becomes

$$\frac{\mathrm{d}y}{\mathrm{d}x} = -\frac{(n-1)\,c^2}{4G}\,\frac{1}{\Sigma_0 \pi \cdot y}\;. \tag{3.53}$$

For a generic lens, we solve it obtaining

$$y = \sqrt{A - 2\, \frac{(n-1)\, c^2}{4G\, \Sigma_0 \pi} \cdot x}\ , \tag{3.54}$$

which corresponds to a very wide half parabola. The lens profile is shown in the left side of fig. 3.41 and as usual A is a constant. We can then see this lens in the right side of fig. 3.41.
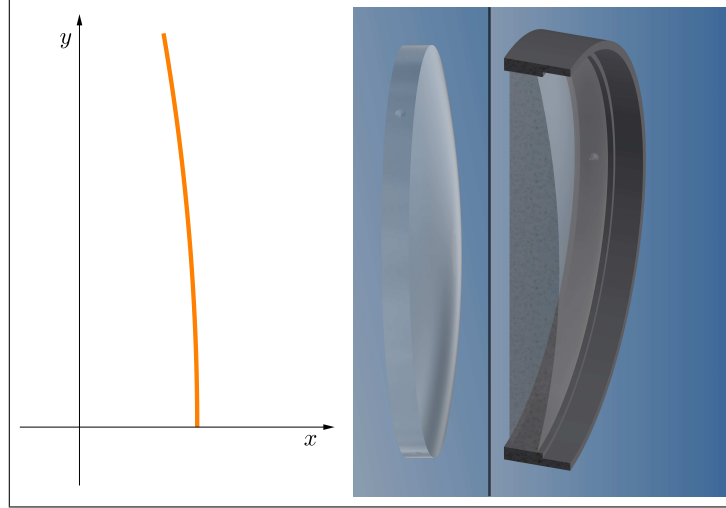
Figure 3.41: Uniform disk plexiglass lens profile with Geogebra (left) and Autodesk (right – Credit: T. Köhler).

Kuzmin Disk Lens   Last but not least, for the Kuzmin disk lens we insert the mass from eq. (3.41), $M(|y|) = \frac{\left((|y|^2 + a_K^2)^{\frac{1}{2}} - a_K \right) M_{\text{tot}}}{(|y|^2 + a_K^2)^{\frac{1}{2}}}$, in eq. 3.15 and we obtain

$$\frac{\mathrm{d}y}{\mathrm{d}x} = -\,\frac{(n-1)\, c^2}{4G\, M_{\text{tot}}}\ \frac{y\,(y^2 + a_K^2)^{\frac{1}{2}}}{(y^2 + a_K^2)^{\frac{1}{2}} - a_K}\ . \tag{3.55}$$

Solving it again for a generic lens, we have

$$y = \sqrt{A \cdot e^{-\frac{(n-1)\, c^2}{4G\, M_{\text{tot}}} \cdot x}\left(A \cdot e^{-\frac{(n-1)\, c^2}{4G\, M_{\text{tot}}} \cdot x} - 2a_K \right)}\ , \tag{3.56}$$

whose profile is shown in the left side of fig. 3.42 and A is once more a constant. As shown in the right side of fig. 3.42, also this lens has the shape of a little hill and we clearly see the similarity with the Plummer sphere lens. However, it is important to note that the central part is much steeper here, a fact that leads to a difference in position and size of the resulting images.

3.3.2.2   Lenses in Comparison

As already mentioned, of the eight examples of gravitational lenses considered, only five were analysed in depth (and used for this student project) and produced as simulator lenses in plexiglass (see fig. E.2). Behind this choice are several reasons, but mainly we have been careful not to complicate too much the level of the functions to be studied, even if we limit ourselves to graphical solutions and use Geogebra for visualisation. Furthermore, when building the plexiglass lenses, we had to find compromises to solve technical problems due to the manufacturing procedure and also in this case the functions used needed a certain simplicity. Therefore, in the
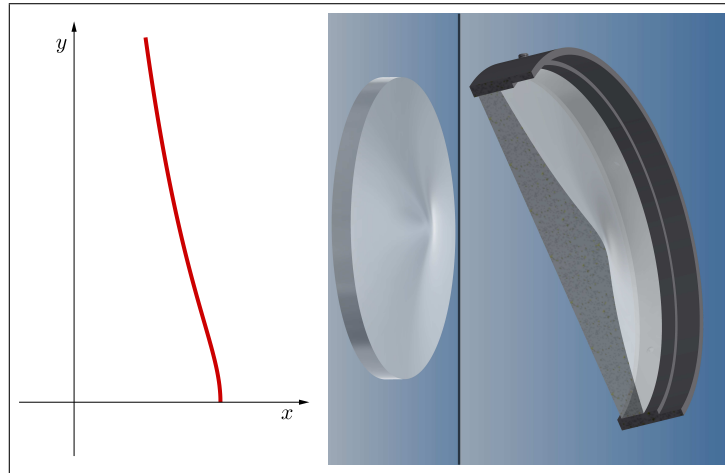
Figure 3.42: Kuzmin disk plexiglass lens profile with Geogebra (left) and Autodesk (right – Credit: T. Köhler).

light of these considerations, we compared all our models before deciding which ones to focus on. For the sake of completeness and in support of our choices, we now present this comparison without, however, touching on the mathematical part, but only considering the lenses' profile.[37] First of all, let us emphasize the fact that the three models we have not dealt with, i.e. the NIS, spiral galaxy and NFW lenses, are the most complicated from a mathematical point of view. Furthermore, as can be seen in fig. 3.43, where on the left we have the profile of our five lenses and on the right the profile of all eight models together, these three lenses have such similar profiles to one or another lens that they are hardly noticeable. To better understand the
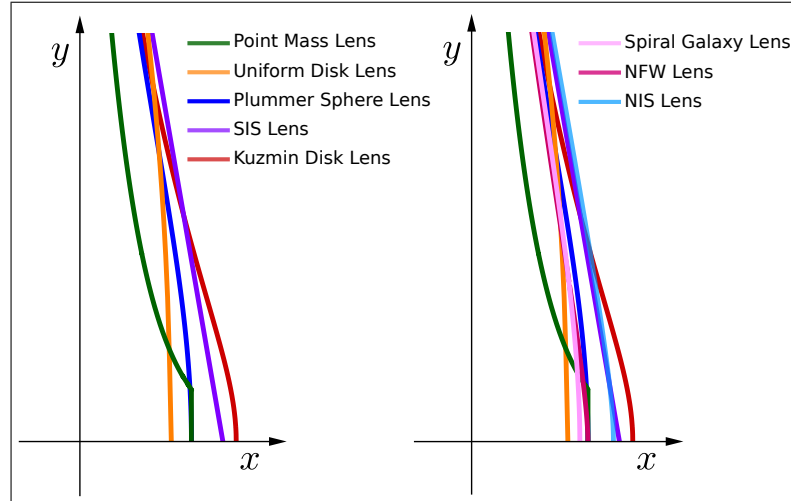
Figure 3.43: Comparison of the profile of the lens models we analysed (truncated before the outer edge for space reasons, see fig. E.1). Left: The five lenses we produced, which correspond to point mass, uniform disk, Plummer sphere, SIS and Kuzmin disk models (see the graph legend for the colours). Right: All eight models we studied, thus including spiral galaxy, NIS and NFW models.

resemblance, on the left-hand side of fig. 3.44 we isolate the profiles of the three extra models and then compare them with the two most similar models (on the right), namely the Plummer sphere and SIS lenses. In particular, we notice that the spiral galaxy and NFW models are very similar to each other and to the Plummer sphere lens. While the NIS lens is very similar to the SIS model, as expected as a variation of it, except for the central part due to the addition of the

---

[37]Although not visible in the pictures, all lens models are considered to have the same diameter and edge thickness.
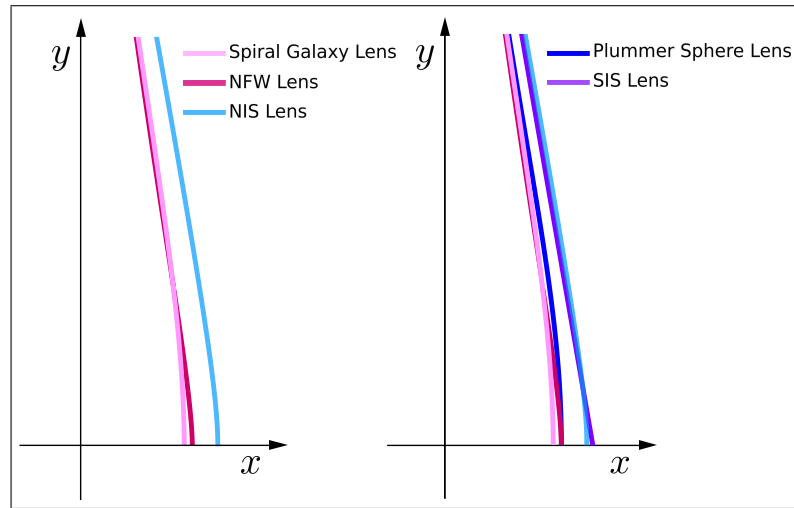
Figure 3.44: Comparison of the profile of the lens models we did not produce (truncated before the edge for space reasons). Left: The three lenses we excluded (spiral galaxy, NIS and NFW models). Right: Their comparison with the most similar models, namely the SIS and Plummer sphere lenses.

finite-density core.

In the interest of exhaustiveness and correctness, we also compare the graphical solution of the lens equation (3.7) for each lens model, including the three non-produced lenses. This is in order to understand the imaging behaviour of these lenses and to make sure we do not miss a significant example. In fig. 3.45, we represent the lens equation of each model seen in fig. 3.44, separated on the left the SIS and NIS models and on the right the Plummer sphere, spiral galaxy and NFW models. As we saw in section 3.3.1.1, where the straight line defined by $f_1(\theta) = \theta - \theta_S$ intersects the various other functions derived from eq. (3.7), we obtain the position of the images that are produced. In fig. 3.45 we see this line for different random values of θ_S, thus being able
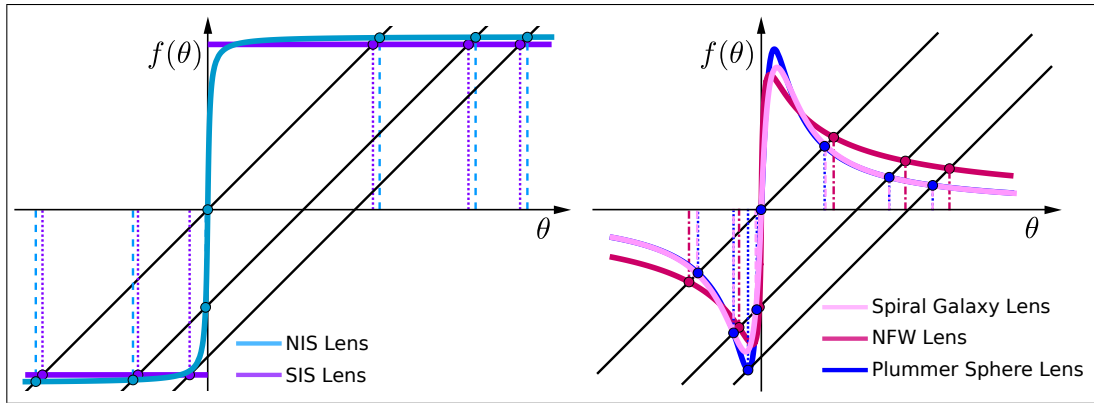
Figure 3.45: Comparison of the lens equations for the models seen in fig. 3.44. Left: SIS and NIS models. Right: Spiral galaxy and NFW models compared with Plummer sphere lens.

to study the evolution of the situation as the real source moves laterally away from the lens.[38]

Considering the SIS and NIS models (fig. 3.45 left), we see that there are no major discrepancies in the position of the images. The real difference is that to the left side of the lens, the NIS model produces two images, rather than just one as with the SIS model. Furthermore, these two images will disappear before the one produced by the SIS lens does. As mentioned above, this similarity is not surprising, as the NIS lens is a SIS lens with a variation in the central part.

Continuing the analysis of the remaining visual representation of the lens equations (fig. 3.45

---

[38]As always, the lens is positioned at the origin of the coordinate system.

right), we see that also for these models the difference in the position of the images is minimal, almost insignificant. In practice, only the moment when the two images to the left of the lens merge and then disappear occurs first for the NFW, then for the spiral galaxy and finally for the Plummer sphere model. Note how the functions representing the Plummer sphere and spiral galaxy models are almost identical, while the one for the NFW model is only slightly different.

At this point we can conclude that the decision to exclude the NIS, spiral galaxy and NFW lenses from production is fully justified from the point of view of the level of mathematical complexity, the lens profile and the behaviour of the produced images. In practice, we are not confronted with models having more peculiar characteristics or being extremely different from the others. Moreover, the treatment of these examples is much more complicated and can easily compromise our educational goals. Also the actual technical production of such plexiglass lenses is intricate, if not possible at all with the means at our disposal. In the end, these are the lines of reasoning and motivations that led us to consider only the five models of gravitational lenses presented in this work.

3.3.2.3 Experimenting

We are ready now for some suggestions on how to use the lenses in the classroom and what possibilities they can give us from an experimental point of view, alongside the theoretical explanation. Ultimately, the plexiglass lenses that reproduce gravitational lens effects are suitable for use mainly in two different configurations:

- It is in fact possible to shine light at the lens, preferably if the light rays from the source are collimated so that they arrive perpendicular to the flat surface of the lens as if from infinity. This is done to, at least partially, simulate the large distances involved in the process. The resulting effects are then observed on a screen behind a shield with a pinhole representing the observer.

- Alternatively, we can look at a source through the lens using simply our eyes or a (video)camera. The source can be anything (a point, a disk, a grid, a word, a picture, etc.), perhaps illuminated for a better view. In this case, the rays do not arrive perpendicularly to the lens. However, considering the modest distances kept during the experiment in class, this allows us to explore how they and gravitational lensing are related.
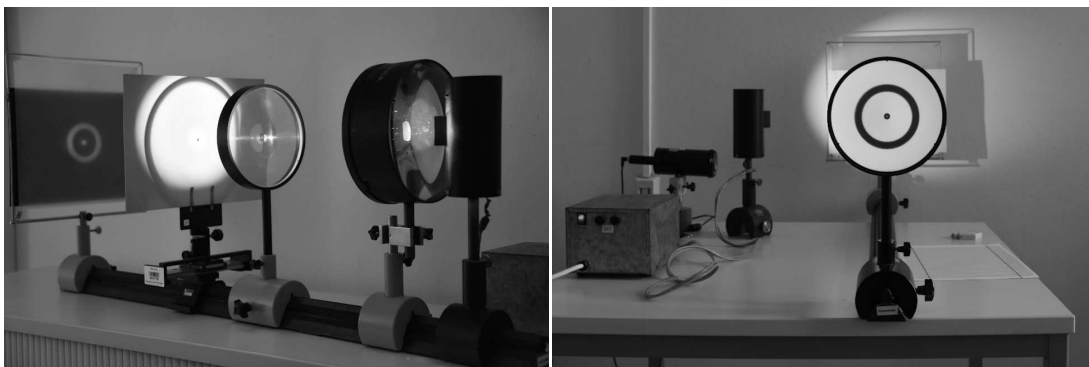
Figure 3.46: Experimental set-ups that can be used with the plexiglass lenses (here the Plummer sphere lens produces an Einstein ring). Left: Light is shined at the lens through a collimator. The last element, after the shield with a pinhole, is the screen where images form. Right: The observer looks at a source (a black disk), which is illuminated with a lamp, through the lens.

These two set-ups are shown in fig. 3.46 and both of them are effective for working with the gravitational lens simulators. However, we personally prefer the second one because it allows a

great variety of configurations. Basically, any figure, shape or photograph can be used as a source and we can easily produce pictures and videos. It also becomes a fun way to "play" with the lenses and engage students without making them lose their attention.

Let us now take a look at some of the most interesting tasks and observations that can be carried out with these plexiglass lenses. In addition, when exploring this topic in class, it is engaging to compare and discuss the results of two or more lens models, i.e. different mass distributions.

- **The Simplest Example of Extended Source** First of all, after the theoretical introduction of this topic, but before moving on to various examples of sources, it is advisable to observe through the chosen lenses a grid of horizontal and vertical lines, which is the geometrically simplest idea of an extended source (fig. 3.47). In this way, we can observe and learn what the resulting image looks like. In fact, this exercise aims to create an initial connection
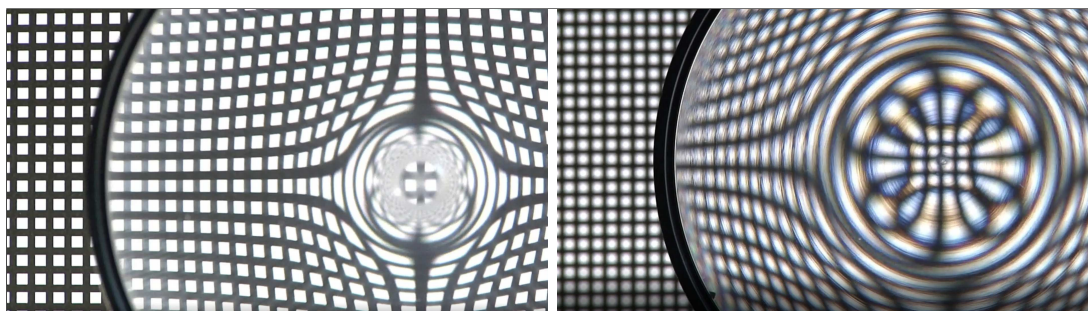
Figure 3.47: A grid seen through the point mass lens (left), where the very central part should not be visible at all (see comment in section 3.3.2.1), and the Plummer sphere lens (right), which is slightly blurred to allow all elements to be seen, otherwise this would not be possible. Credit: T. Schott

between theory and observation. By guiding our students with appropriate questions, they will be able to analyse and discuss how the grid lines are distorted and understand that the gravity of the gravitational lens is responsible for this phenomenon.[39]

- **A Small Disk as a Source** While continuing to encourage our students to observe and guide them in the discovery of the gravitational lensing phenomenon, we can now move on to using different types of sources, starting with a small circular disk. In this phase, we start by observing what happens when we have a perfect source-lens-observer alignment. We then continue by looking at what changes and how the disk is distorted when the alignment is broken. To break the alignment, depending on our convenience, we can move the source or lens or observer sideways, keeping the distances D_L, D_{LS} and D_S constant. In essence, we will notice not only that indeed the plexiglass lenses reproduce the same visual effects as we have already studied, but also the correspondence between the various cases. Keep in mind that accompanying this phase with Geogebra simulations can be a help to facilitate learning and understanding of what we are observing. In addition, whenever possible, we suggest combining images of real events of similar gravitational lensing, as shown in fig. 3.48.

- **Disks of Different Size as a Source** The same experiment and reasoning can be performed with disks of different sizes in order to observe how the images change. Above all it should be noted that the greater the radius of the source, the thicker the Einstein ring (in case of perfect alignment), as we have already seen with the simulations of extended sources and now we see in fig. 3.49. In this regard we recall what we have seen with the simulations of

---

[39]If there are difficulties in understanding how the lines are distorted, it is possible to use the Geogebra simulation with the line source and also observe through the chosen lens a separate set of vertical and/or horizontal lines and then return to the grid with a clearer idea.
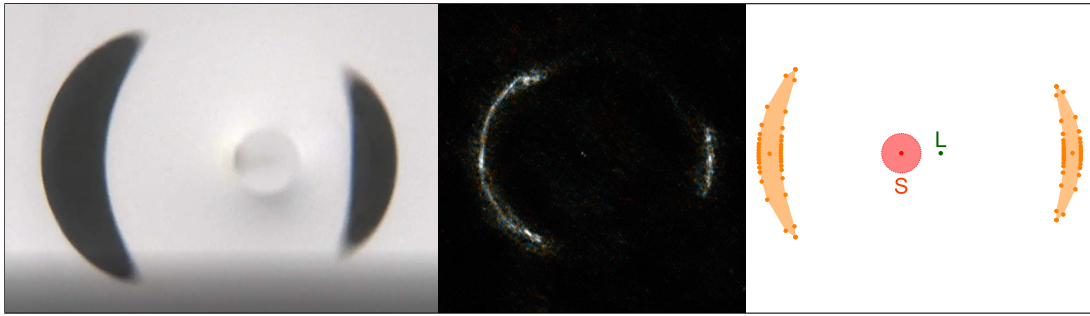
Figure 3.48: Example of arcs. In the centre the lensed galaxy SDP.81, on the left side the point mass lens in action with a disk source and on the right side a Geogebra simulation with a disk source. Credit for the central image: ALMA

.
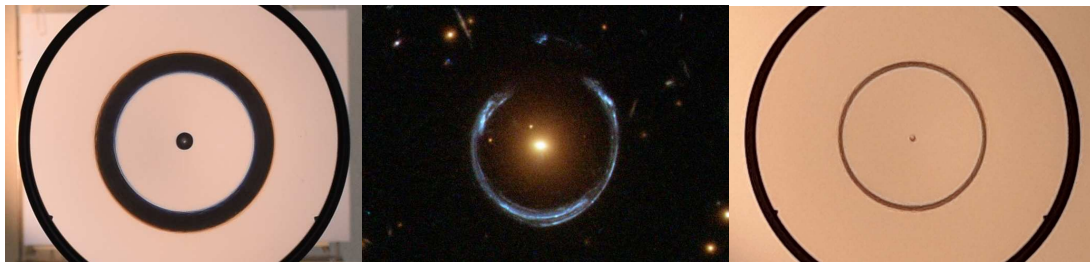
Figure 3.49: Example of Einstein rings. In the centre the lensed galaxy "Cosmic Horseshoe", the outer images are taken with the Plummer sphere lens in action (for which we see the lens frame: the big external ring) and, as a source, a disk of larger radius on the left side and a disk of smaller radius on the right side. Credit for the central image: ESA/Hubble NASA.

the gravitational lensing effect done with Geogebra: the images coming from a hypothetical point-like source, continue to be point-like (section 3.3.1.1), while in the case of extended sources, extended images are produced (section 3.3.1.2).

- **Dependences of the Einstein Ring** Another important point to explore is the strong dependence of the Einstein ring size on the amount of lens mass contained within the Einstein radius, as is clear from eq. (3.8). In case of non-perfect alignment, the amount of mass contained within the impact parameter plays the same role for the produced images, as follows from eq. (3.7). We can easily verify these characteristics by using lenses representing different amounts of mass.

  Moreover, as already expressed several times, the size of the Einstein ring also depends on the distances between source, lens and observer: D_L, D_{LS} and D_S. Experimentally we can verify this dependence, remembering however that with our simulators we are limited to very small distances. In particular, the easiest case to deal with is the perfect alignment, indeed, if we observe the chosen source directly through our lenses, we can verify and measure what happens to the Einstein ring as these distances vary, engaging our students in an interesting exercise.

  The difference in the angular size of the Einstein radius, θ_E, is actually only a few degrees, yet the results of the observations can easily be compared with the results analytically obtained from (3.8).[40]

---

[40]This type of exercise requires knowledge of principles of angle measurement and conversion between angles and lengths. These are topics that our students have already dealt with, however it is possible to find teaching material that covers this topic, for example the first part of [62] and [23].

- **The Parity of Images** If we also want to study the parity of the image, the simplest technique is to use a disk divided into coloured sectors, as seen in the sections 3.2.4 and 3.3.1.2. Thanks to this simple but effective expedient, we can observe and verify with the plexiglass lenses all that we have studied about image inversion. An example is shown in fig. 3.50. In this regard, it is also possible to use non-symmetrical shapes as a source, for
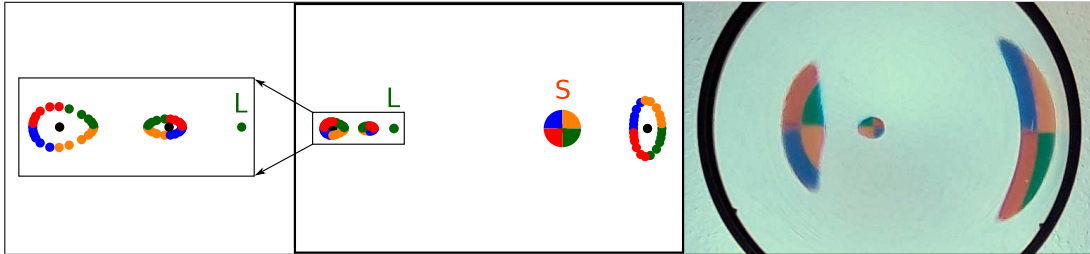
Figure 3.50: Comparison between Geogebra simulation and real plexiglass lens of the parity of images produced by the Plummer sphere model. Left: Simulation with three images produced from an extended multicoloured disk source as in fig. 3.37 (with enlargement for details in the box). Right: The Plummer sphere lens in action with an equal multicoloured disk source.

instance by looking at the word "GRAVITY" in fig. 3.52. However, for eyes unaccustomed to this type of observation it may be more difficult to observe the parity of images in this way.

- **Other Examples** However, the beauty of this instrument is that we can unleash our imagination with the most unusual shapes for sources, even pictures of real astronomical objects. Indeed, by taking an inverted-colour image of the Hubble Ultra Deep Field as a source and sliding one of our lenses in front of it, we observe a succession of highly distorted galaxies, arcs and Einstein rings. In fig. 3.51 we see one moment in time of this sequence compared with an example of a real gravitational lens event called "Cheshire Cat" because of its funny appearance. Here we see similar arcs and distorted images of galaxies in the background. But we should not forget that these distortions are due to the group of galaxies in the
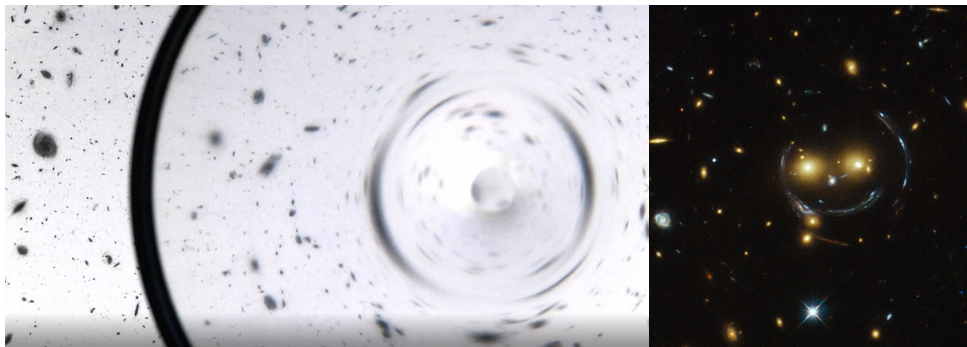
Figure 3.51: The Hubble Ultra Deep Field (Credit:ESA/Hubble NASA) seen through the point mass lens on the left. The lensed group of galaxies "Cheshire Cat" on the right. Credit for the right image: NASA/STScI.

foreground,[41] while our lenses represent always only a single galaxy and specifically in fig. 3.51 the point mass lens was used.

From our experience, we can say that the students are very curious and appreciate this experimental part, even going so far as to "play" with the lenses. This is something that we personally encourage if it is backed up by a good theoretical basis, also because it keeps

---

[41]They are actually two groups of galaxies merging.

their interest in the subject alive. And so it comes that the most varied pictures or scenes are observed through the lenses, of which we see some examples in fig. 3.52. Nevertheless, we

Figure 3.52: Playing with the lenses. Above: Our faculty building through the Plummer sphere lens (left), a portrait of Einstein through the point mass lens (right). Bottom: The word "GRAVITY" through the point mass lens, inspired by [37]. This last picture shows how images seen through the lenses can also be inverted.

always try to analyse with our students, at least qualitatively, the images we produce, even those produced for fun. After all, we can see how the lines are bent and distorted, which images previously analysed we find again, where the various elements of the original figure are reproduced and how the images are inverted (when this is clearly visible). Ultimately, especially if properly guided, students are able to perform these kinds of observations and understand the connections with what has been studied and seen in theory.

To see a practical example of how the teaching material of this project can be used, see appendix G and [47].

Finally, we would like to say a few words and make a few suggestions regarding the possible future of this type of research, including a technical point of view.

In our case, some constraints have arisen due to the limited means at our disposal, both in terms of tools, technology and money. Therefore, it would be interesting to investigate and test the possibility of using other equipments (for instance 3D printers [104]) for the creation of such lenses in a simpler and affordable way, in order to make them more accessible to schools and teachers and to spread their use in the classroom (without having to break the home wine glass service). All this without neglecting the quality of the manufacturing process and the precision in respecting the functions that define the shape of the lenses. It can indeed happen that, as a result of the polishing process, the lens is not uniformly polished over its entire surface and this can lead to big changes in the behaviour of the lens. In this respect, there are companies that are specialised in this area, but the costs unfortunately become prohibitive. A further field of investigation, if the necessary means are available, would be to design and create the same lens model in several specimens where each one represents a different amount of mass, in order to show the differences in the effects produced by more or less massive gravitational lenses. Or, alternatively, several models representing the same amount of mass, thus focusing on the different mass distribution. Also, exploring the possibility of creating lenses that represent several celestial objects or clusters in a single specimen would be a very useful and interesting field. As far as the experimental part is concerned, if a professional optical laboratory is available, one could test

the lenses with quality lasers and then perform measurements on the images produced with the aim of creating, if feasible, data sets for the development of numerical exercises and subsequent comparison with data from real gravitational lens events.

The future is obviously not limited to these points and there are many more possibilities to explore, as can be seen from [98]. However, based on our experience, the first themes to be considered or continued to be developed among the various ones could be precisely these.

3.4   Conclusions

We conclude this chapter by expressing our satisfaction with this project as well. In fact, we have managed to create teaching tools that reproduce in the classroom, even if using simplified models, some of the effects of strong gravitational lensing that we see in the universe. Innovative is the fact that we are the first to have analysed lenses representing the Plummer sphere and Kuzmin disk models in this educational context and produced them in plexiglass. Furthermore, all our simulations are produced with an accessible software, familiar to many teachers, without having to use complicated programming languages.

Not only these tools allow us to recreate such phenomena visually, but also to analyse and deeply understand the mechanism that produces them. These instruments are accompanied by a series of theoretical exercises that lead first of all to a deeper understanding of gravitational lensing, but at the same time can be directly introduced to support physics, mathematics and astronomy lessons. In fact, we are faced with the possibility to apply to a fascinating astrophysical phenomenon, as well as a real example, some notions that are normally taught at the end of secondary school. We have already seen the benefits that this technique brings, both in terms of fascination, motivation and inspiration for students, encouraging their learning, and in terms of developing important skills that will be useful later in life and in the world of work.

From personal experience, thanks to the presentation and use of the project material on many occasions, from conferences to teacher training and also directly in the classroom, and from the feedback from teachers who have tested this project with their students, we can say that it has been a great success. In fact, not only are all the physical and mathematical concepts involved absolutely understandable and practicable for students even in their final years of secondary school, but also the level of interest has been very high on every occasion. As a matter of fact, the topic stimulates, after a few teaching hours of introduction for the basic knowledge, a strong curiosity and the will to know and understand more about this phenomenon. This then showed its positive effects, as the basic principles of the phenomenon of gravitational lensing proved to be effectively understood. The students appreciated mainly the possibility to recreate this effect in the classroom and to use the simulator lenses with their own hands. Moreover, the idea of the optical illusion created by this phenomenon made them wonder if they can really trust what their eyes see and this stimulated the deepening of the topic. The combination of an experimental part with a subject that is often only treated theoretically is considered by the teachers to be a strong point, together with the interactivity of the simulations.

Finally, simulations with Geogebra and plexiglass lenses have proven to be powerful educational tools in teaching the phenomenon of light deflection due to weak gravitational fields (in particular strong gravitational lensing), especially when they are used in combination. In addition, all this allows, but does not oblige, the practice of mathematical concepts such as the solution of equations of various degrees, differential and integral calculus applied to elementary functions and trigonometry. Consequently, these tools permit to integrate theory and experimentation very well, touching on various important concepts such as the deflection angle, Snell's law, trigonometry and Newton's shell theorem.

Chapter 4

Conclusions

Very rarely cosmology topics are included in physics and astronomy lessons in secondary schools or in the first years of university. The main reason for this is surely the complexity of these subjects and the teachers' lack of time to go into them in depth and adequately elementarise them for the students. The growing disaffection for science among students of all ages is also a well-known fact. This is of course a problem and even more worrying since economic development is strongly suppressed in a country where scientific education doesn't occupy a prominent role [40][80][28][43]. In this respect the issue is not the absence of science knowledge, but lies more importantly in how science knowledge is transferred to learners [74].
The combination of these challenges is the driving force behind this PhD project.

By implementing the two student projects described in this work, we are providing concrete support for the teaching of physics and astronomy by introducing fascinating examples of cosmology. And we are contributing to making the learning of these subjects more attractive and exciting for students thanks to new experimental tools and innovative technological aspects. As it is clear at this point, underlying the produced material and the obtained results is a combined research and design work where the aim is to expand old knowledge, develop new knowledge and produce new processes, tools, artefacts and resources.
In the introduction (chapter 1) all the inspiring motivations and objectives behind the conception and creation of this PhD project are explored. Where also the various stages of development of the whole work are described, with particular attention to the definition of the target audience and the choice of the most suitable themes, means and approaches. The project on the dark matter problem and that on gravitational lensing are dealt with in detail in the two central chapters. In particular, in addition to the theoretical foundations, they consist of exercises and activities applied to practical, real examples. This is because, as shown by educational research in physics and astronomy, by making students active, learning and development of important skills are stimulated [49][84][113][75][31][99].
When teachers use the educational material exposed in this thesis in their lessons, they get students to work as astronomers for a few hours. So besides learning new knowledge, applying it and developing important skills, they experience a glimpse of how science is done. An experience that can be stimulating for students and open up new horizons.

In chapter 2 we saw that the practical aim of the project on the dark matter problem is to retrace the path that led to the formulation of the hypothesis of the presence of this non-visible matter, starting from the dynamics of spiral galaxies. By introducing the concepts of spider diagram and rotation curve, we focus students on understanding the difference and relating radial and rotational velocities. Then, by putting Kepler's laws and Newton's laws of motion and gravitation into practice, the mass of the galaxy is obtained. This mass has to

be compared with the one obtained by considering the brightness of the galaxy in order to study whether it corresponds or not. All this is done by training computer skills, visualising graphically and interpreting data. Other supporting topics are important for this project, indeed students need to familiarise themselves with Newton's shell theorem and the theory of parallel projections. In addition, plane trigonometry and the Cavalieri approach to integration are also taken into account during the assignment. Another important aspect that will engage students' minds is to work with different gravitationally bound rotating systems, understanding their differences and similarities and extracting useful information. This is what happens when applying the concepts seen to the Solar System and spiral galaxies. Finally, a very stimulating point for students is also the fact that the problem of dark matter is still an unsolved mystery.

With the project on gravitational lensing, discussed in chapter 3, students learn about the phenomenon of light deflection due to weak gravitational fields, in particular strong gravitational lensing is studied. Students will doubt that what they see in the universe is actually the reality of things. This is because they will understand that gravitational lensing is the phenomenon that leads to the formation of multiple, distorted images of distant light sources. Starting from the geometry of the gravitational lens system, the concepts of deflection angle and lens equation are introduced. With these concepts, students learn for different models of mass distributions acting as lenses, how many images are produced and where they are positioned. Furthermore, for extended sources, it is understood how the related images are distorted. It is also possible, as mentioned in section 3.2.3, to calculate by means of gravitational lensing the mass of a galaxy acting as a lens. Comparing then the result with the mass-to-luminosity ratio and with the outcomes obtained thanks to the rotation curves (chapter 2), we obtain two independent methods suggesting the possible presence of dark matter. The brightness of the images in comparison with that of the source can also be analysed and discussed, i.e. their magnification. To carry out these tasks, the solution of equations of various degrees, differential calculus applied to elementary functions and trigonometry will be practised. Using Geogebra, however, students are particularly encouraged to use a graphical approach, practising computer skills and even creating interactive simulations of the gravitational lensing effect. In practice, they create a powerful visualisation of the phenomenon they are examining, while much of the information they obtain can also be demonstrated using other equally feasible methods, for instance by ray-tracing diagrams as done in [85]. At this point, by combining the notions of general relativity learned so far with geometric optics, we find out what shape plexiglass lenses should have in order to reproduce the gravitational lensing effects obtained from the simulations. Lenses that we have designed and produced so that students can continue the project by experimenting with gravitational lensing in the classroom. Snell's law and the concept of refraction are additional topics to support this part. Integral calculus with elementary functions can also be introduced. Newton's shell theorem, on the other hand, remains a topic to be kept in mind throughout the project. The basic aim of this project is to visualise light on curved paths under the influence of gravity, which is achieved by means of the above-mentioned simulations and special plexiglass lenses. In practice, these instruments represent the experimental part of this topic. The experimental part is more technological in the case of the simulations and more hands-on in the case of the lenses.

These projects are the result of careful research work. They underwent a meticulous process of creation, evaluation and revision. In this process, mainly teachers (in-service and future) were involved, but also students, for completeness. This made it possible to evaluate many important aspects, such as feasibility and effectiveness of teaching, knowledge and level of learning of concepts, autonomy of students, acquisition of competences and also degree of inspiration and involvement. All this with the purpose of highlighting project and product needs, necessary changes and promoting possible modifications and improvements during their development. In

this respect, the collaboration of the teachers was fundamental because it allowed us to test the material from two points of view: that of the teacher and that of the student. Feedback, advice and suggestions from both sides were always very helpful. This has led to a progressive improvement of the resources produced. When the high level of quality we aimed for was achieved, dissemination began. First in teacher training, then at conferences and in dedicated journals and finally to the introduction of specific seminars in university courses for future teachers.

This does not mean that the work is finished, there is always room for improvement. On the contrary, we welcome constructive criticism and new suggestions. And we also sincerely hope to inspire future ideas and developments in this area.

We can now present the results of the final summative evaluation stating, thanks to the feedback received, that this work has been very successful in answering the research questions posed and the challenges presented. Colleagues, teachers and students involved during the implementation of this project consider the resources and tools produced innovative and of high quality. Using this material in the training of teachers, who will then introduce it in their lessons with students, brings concrete benefits in the effectiveness of teaching these subjects on all levels considered. This is achieved by fruitfully combining theory and experimentation, by actively involving and interesting, by transmitting knowledge and stimulating new competences. With the final aim of giving students not only the possibility and the ability to understand, but hopefully also planting in them the seed of curiosity and the desire to know. This is why these resources represent a significant contribution to the field of physics, mathematics and astronomy education. We know very well that not all students will become scientists, but encouraging and passing on not only knowledge, but also a distinctive way of thinking and new capabilities plays an important role in improving the quality of life of the individual and the long-term growth of society [80]. As we have seen on several occasions, effective teaching of science subjects (although we focus on physics, mathematics and astronomy) promotes the development of special skills (such as problem solving, logical reasoning, creativity, critical and scientific thinking, research and questioning, decision making, adaptability and many others) that can help students to take advantage of the scientific knowledge they have acquired, improving all aspects of their lives [32][43].

In conclusion, this is essentially the message that should resonate in the minds of teachers and why they should pay close attention to how they teach, the topics they choose to include, the resources they use and find ever better and inspiring ways. This message also reflects the great importance of research and projects such as those developed and discussed in this thesis. These define a particular field, characterised by constant give and take in terms of knowledge, satisfaction and fulfilment. A field of research that not only makes one grow and improve, but also fuels the fire of passion that drives and pushes to contribute more and better.

Appendices

Appendix A

Newton Shell Theorem: Gravitational Force Analysis

In spite of the fact that the gravitational force approach for the Newton shell theorem is more complicated, it remains the most widely used method to explain it. This is reason enough to consider it and to give an example suitable for secondary-school students. Unfortunately, using the same methodology we have seen for the energy analysis is not advisable in this case because without integration it becomes too difficult to solve for the students. However, we can fortunately adopt an alternative procedure.

The starting point is again the spherically symmetric hollow shell of mass M and radius R and a test point-mass m at a distance ρ from the centre of the sphere. As we can see in figure A.1, the shell is cut in two sectors (the green rings) by two cones which have both vertex in B and axis through C [63][86]. Moreover, thanks to the symmetry of the problem, everything in the upper half of the sphere is mirrored in the lower half, permitting us to confine our work to one part only.

The force of attraction that the closest ring (ring 1) of height Δs and mass $M_1 = \Sigma \cdot 2\pi \cdot R\,\Delta s$ exerts on the point-mass in B is given by

$$F_1 = G\,\frac{m \cdot M_1}{b^2}\,\cos\alpha = G\,\frac{m \cdot \Sigma \cdot 2\pi \cdot R\,\Delta s}{b^2}\,\cos\alpha\;. \tag{A.1}$$

This becomes for the farthest ring (ring 2):

$$F_2 = G\,\frac{m \cdot M_2}{b'^2}\,\cos\alpha = G\,\frac{m \cdot \Sigma \cdot 2\pi \cdot R\,\Delta s'}{b'^2}\,\cos\alpha\;. \tag{A.2}$$

In particular, the factor $\cos\alpha$ defines which components of the force has to be considered. Indeed, because of the symmetry of the ring, it is clear that only the components parallel to the line connecting B and C, in direction of C, contribute to the force attracting the point-mass. All the perpendicular components compensate each other. Therefore, for both rings the force acts on this line and in the same direction. At this point, it is possible and useful to express the ratio of the forces obtaining

$$\frac{F_2}{F_1} = \frac{\Delta s'}{\Delta s}\left(\frac{b}{b'}\right)^2\;. \tag{A.3}$$

Considering now the geometry of the system from figure A.1, we can rearrange eq.(A.3) in a more suitable form. In fact, from the triangles $\triangle CS_1P_1$ and $\triangle S_1BP_1$ and the Pythagoras' theorem, we easily calculate

$$R^2 = s_1^2 + \left[b^2 - (\rho - s_1)^2\right]\;. \tag{A.4}$$

Using the same method, from the triangle $\triangle CBP_2$ we obtain

$$R^2 = (s_1 - \Delta s)^2 + \left[a^2 - (\rho - s_1 + \Delta s)^2\right]\;. \tag{A.5}$$
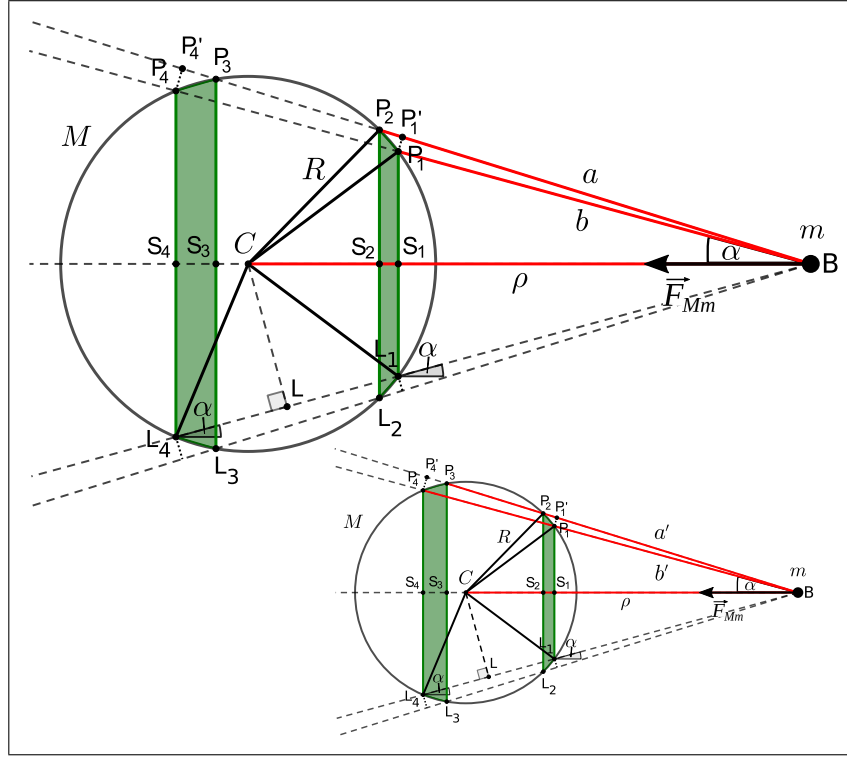
Figure A.1: 2D-representation of the system composed of a spherically symmetric hollow shell of total mass M and radius R, cut into sectors by the two cones with vertex in B, and a test point-like body of mass m at distance ρ from the centre of the sphere. The lower, smaller version of the diagram is only to highlight a' and b'. It is also useful to define some lengths: $\overline{P_1'P_2} = \Delta b$ and $\overline{P_3P_4'} = \Delta b'$, $\overline{S_1S_2} = \Delta s$ and $\overline{S_3S_4} = \Delta s'$ and $\overline{CS_1} = s_1$, $\overline{L_1L} = \overline{LL_4} = \frac{1}{2}(b' - b) = \frac{1}{2}l$ and $\overline{L_2L_3} = l - \Delta l$.

Then equalling these last two equations and substituting $a = b + \Delta b$ the result is

$$(2b + \Delta b)\,\Delta b = 2\rho\,\Delta s \tag{A.6}$$

and considering the limit $\lim_{\Delta b \to 0}(2b + \Delta b)$ it becomes

$$\Delta s = \frac{b}{\rho}\,\Delta b \ . \tag{A.7}$$

The same procedure is now applied to ring 2 and the triangles $\triangle CBP_4$ and $\triangle CBP_3$ resulting in

$$\Delta s' = \frac{b'}{\rho}\,\Delta b' \ . \tag{A.8}$$

Introducing these results in eq.(A.3), the ratio of the forces is thus expressed by

$$\frac{F_2}{F_1} = \frac{\Delta b'}{\Delta b}\frac{b}{b'} \ . \tag{A.9}$$

Knowing that $a = b + \Delta b$ and $a' = b' + \Delta b'$, the intersecting secants theorem[1] then leads to

$$b'\Delta b - b\Delta b' = 0 \qquad \text{and} \qquad \frac{\Delta b'}{\Delta b} = \frac{b'}{b} \tag{A.10}$$

---

[1] $a\,a' = b\,b' = \text{const}$, one of the cases when treating the problem of two intersecting lines and a circle, for a detailed explanation see [25] or search in any elementary plane-geometry textbook.

and from eq.(A.9) consequently to the equality

$$F_1 = F_2 \ . \tag{A.11}$$

This result is not unexpected, as the procedure works because the force is proportional to the inverse of the square of the distance and the area is proportional to the square of the distance [29]. This means that, even if the surfaces of the rings are not the same, they exert the same attracting force on the point-mass. It is thus enough to calculate only one of the two forces.

Thereafter, in order to simplify the calculation, it is useful to express $\cos \alpha$ in terms of b and b'. Basically, looking at the triangle $\triangle CLB$ and at the geometry (in particular the symmetry) of the system in figure A.1, it is clear that $\overline{BL} = \rho \cdot \cos \alpha = b + \frac{l}{2} = b' - \frac{l}{2}$. Consequently, this directly gives

$$\cos \alpha = \frac{b + b'}{2\rho} \ . \tag{A.12}$$

Furthermore, from the figure and thanks to eq.(A.10) we can define

$$\overline{L_1 L_4} - \overline{L_2 L_3} = \Delta l = \Delta b + \Delta b' = \left(\frac{b'}{b} + 1\right) \Delta b \ . \tag{A.13}$$

Inserting equations (A.7), (A.12) and (A.13) in eq.(A.1), we obtain the force in the form

$$F_1 = F_2 = G \, \frac{m \cdot \Sigma \cdot \pi \cdot R}{\rho^2} \, \left(\frac{b'}{b} + 1\right) \Delta b = G \, \frac{m \cdot \Sigma \cdot \pi \cdot R}{\rho^2} \, \Delta l \ . \tag{A.14}$$

Since $F_1 = F_2$, in order to calculate the total gravitational force F exerted by the shell, we need first to expand the two sectors so that they cover the entire sphere and then it is enough to calculate the force for one of them and double it. The two sectors can cover the entire sphere only at their maximum extension, namely when the larger cone is tangent to the sphere and the smaller one reduced to a line through C, which means solving $\sum\limits_{l=0}^{2R} \Delta l$. The result is

$$F = 2F_1 = 2 \cdot G \, \frac{m \cdot \Sigma \cdot \pi \cdot R}{\rho^2} \, \sum_{l=0}^{2R} \Delta l = G \, \frac{m \cdot \Sigma \cdot \pi \cdot 4 \cdot R^2}{\rho^2} = G \, \frac{m \cdot M}{\rho^2} \ . \tag{A.15}$$

Also from the force analysis, this theorem proves that for $\rho \geq R$ the gravitational force depends only on the distance ρ, once again as if all the mass of the sphere were concentrated at its centre. The same derivation can be performed for $\rho < R$, the geometry of the system is shown in figure A.2. The result in this case is that $F_2 = -F_1$, therefore $F = 0$, namely the interior of the shell is force free and additional calculations are not needed.

   At this point, if we consider the sphere full of mass and apply the same procedure like for the energy analysis, for $\rho \geq R$ we include the total mass of the sphere M_{tot} solving the summation $\sum\limits_{\alpha=1}^{n} M_\alpha$. Therefore, the gravitational force depends exclusively on the distance ρ as if all the mass of the sphere were concentrated at its centre. Then again, for $\rho < R$ this remains true only for the shells internal to the radius ρ and the force is instead zero for the shells external to it.

   With the purpose of making the exercise more challenging, an advanced approach with infinitesimal calculus can be introduced. Even if we can apply the infinitesimal calculus to the just-seen procedure, it is far more simple to adopt the method of dividing the shell in many infinitesimal rings as we did for the energy analysis.

Therefore, we consider once more figure 2.3 and the force exerted from an infinitesimal ring on the point-mass is then expressed by

$$\mathrm{d}F = G \, \frac{m \cdot \mathrm{d}M}{\rho_i^2} \, \cos \alpha = G \, \frac{m \cdot \Sigma \cdot 2\pi R^2 \cdot \sin \theta_i \, \mathrm{d}\theta_i}{\rho_i^2} \, \cos \alpha \ . \tag{A.16}$$
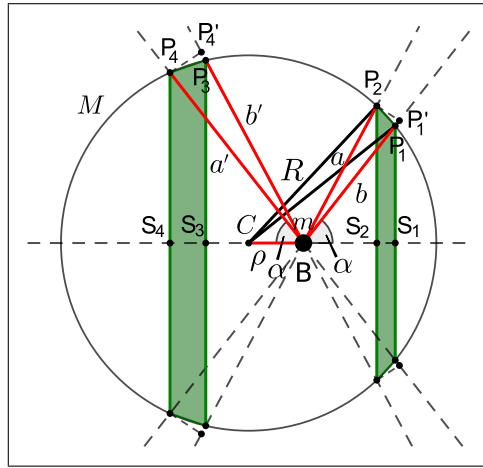
Figure A.2: 2D-representation of the system composed of a spherical symmetric hollow shell of total mass M and radius R, cut into sectors by the two double cones with vertex in B, and a point-mass m positioned inside the sphere and at distance ρ from its centre.

Introducing now eq.(B.3) and the cosines law for $\cos\alpha$ in eq.(A.16), we obtain

$$\mathrm{d}F = G\,\frac{m\cdot\Sigma\cdot\pi R}{\rho^2}\,\frac{\rho^2 - R^2 + \rho_i^2}{\rho_i^2}\,\mathrm{d}\rho_i\,. \tag{A.17}$$

According to figure 2.4, we perform a simple integration on the interval between the smallest and the biggest value of ρ_i and we get

$$F(\rho) = \begin{cases} G\,\frac{m\cdot\Sigma\cdot\pi R}{\rho^2}\int_{\rho-R}^{\rho+R}\frac{\rho^2 - R^2 + \rho_i^2}{\rho_i^2}\,\mathrm{d}\rho_i = G\,\frac{m\cdot\Sigma\cdot 4\pi R^2}{\rho^2} & \text{if } \rho \geq R \\[2ex] G\,\frac{m\cdot\Sigma\cdot\pi R}{\rho^2}\int_{R-\rho}^{\rho+R}\frac{\rho^2 - R^2 + \rho_i^2}{\rho_i^2}\,\mathrm{d}\rho_i = 0 & \text{if } \rho < R\,, \end{cases} \tag{A.18}$$

where $\Sigma\cdot 4\pi R^2 = M$.

Finally, a last case is worthy to be named, this is the famous Poisson equation derived from Gauss law of gravity, which expresses the relation between mass density and gravitational potential. Solving the Poisson integral for a spherical distribution of mass, we achieve the same result seen so far in an elegant and formal derivation. This method, given its difficulty, is mainly suitable for undergraduate university students. We do not discuss this approach here because it is covered in any physics course and many books (for example [42][103]), normally in its corresponding form for electrostatics, hence it is not of interest for our educational purposes. In fact, the objective of projects like this is to provide alternatives, simplified as much as possible and with different levels of difficulty, to traditional methods of resolution.

Appendix B

Advanced Treatment of Some Explored Concepts

We suggest here how to treat some of the topics seen in the previous sections with a more advanced approach suitable for students with a deeper mathematical background.

- From section **Newton Shell Theorem** 2.2.2:

  For more advanced students, it is possible to render the gravitational potential energy approach more challenging introducing infinitesimal calculus which involves very basic differentials and definite integrals. This is very similar to and inspired by Feynman's simple approach in [30]. The chain of reasoning remains the same, but the rings' thickness is considered infinitesimal $\Delta\rho_i \to 0$ and eq.(2.1) is now expressed in the form

$$\mathrm{d}U = -G\,\frac{m \cdot \mathrm{d}M}{\rho_i} = -G\,\frac{m \cdot \Sigma \cdot 2\pi R^2 \cdot \sin\theta_i\,\mathrm{d}\theta_i}{\rho_i}\ . \tag{B.1}$$

Simply calculating the first derivative on both sides of the equation seen in the law of cosines we obtain $\rho_i\,\mathrm{d}\rho_i = \rho R\,\sin\theta_i\,\mathrm{d}\theta_i$, which is then introduced in eq.(B.1). This result, once introduced in eq.(B.1), leads to

$$\mathrm{d}U = -G\,\frac{m \cdot \Sigma \cdot 2\pi R}{\rho}\,\mathrm{d}\rho_i\ . \tag{B.2}$$

The next step consists of calculating a simple definite integral on the interval between the smallest and the biggest value of ρ_i. As it is for the simpler approach we just saw, also here the limits of integration play a fundamental role to define when the point-mass is inside or outside the spherical shell and the diagram of figure 2.4 remains valid. Hence, solving the equation

$$U(\rho) = \begin{cases} -G\,\frac{m \cdot \Sigma \cdot 2\pi R}{\rho} \displaystyle\int_{\rho-R}^{\rho+R} \mathrm{d}\rho_i & \text{if } \rho \geq R \\[3mm] -G\,\frac{m \cdot \Sigma \cdot 2\pi R}{\rho} \displaystyle\int_{R-\rho}^{\rho+R} \mathrm{d}\rho_i & \text{if } \rho < R\ . \end{cases} \tag{B.3}$$

we achieve again eq.(2.4) with all the discussed results that it entails. Easily this reasoning can also be extended and applied to the sphere full of mass.

- From section **The Rotation Curve of a Spiral Galaxy** 2.3.3:

    The Bulge – At a more challenging level, the problem of calculating the mass of the total sphere can be performed using directly integration

    $$M_{\mathrm{B}}(r) = \int_0^r \rho^2 \sigma_{\mathrm{B}}(\rho) \, \mathrm{d}\rho \int_0^\pi \sin\theta \, \mathrm{d}\theta \int_0^{2\pi} \mathrm{d}\phi = 4\pi \int_0^r \rho^2 \sigma_{\mathrm{B}}(\rho) \, \mathrm{d}\rho \, . \tag{B.4}$$

    This integral, after introducing $\sigma_{\mathrm{B}}(\rho)$,[1] is very easy to solve and gives

    $$M_{\mathrm{B}}(r) = 4\pi a \int_0^r \rho^{(k+2)} \, \mathrm{d}\rho = \frac{4\pi a}{k+3} \, r^{(k+3)} \, . \tag{B.5}$$

    This result corresponds to eq. (2.25). From now on, we can proceed as we did in section 2.3.3.1 achieving the same results. In fact, deducing that $k = 0$ (which means $\sigma_{\mathrm{B}}(r) = a = \sigma_{\mathrm{B}}$) we then derive equations (2.28) and (2.30).

    The Halo – The advanced solution of the problem of calculating the mass of the halo follows in a straightforward manner the reasoning for the bulge and the interval of integration is in this case between R_{B} and r. Therefore, the mass for the halo alone at a radius r is calculated as

    $$\begin{aligned}
    M_{\mathrm{H}}(r) &= 4\pi \int_{R_{\mathrm{B}}}^r \rho^2 \sigma_{\mathrm{H}}(\rho) \, \mathrm{d}\rho \\
    &= 4\pi d \int_{R_{\mathrm{B}}}^r \rho^{(k+2)} \, \mathrm{d}\rho \\
    &= \frac{4\pi d}{k+3} \left(r^{(k+3)} - R_{\mathrm{B}}^{(k+3)} \right) \, .
    \end{aligned} \tag{B.6}$$

    Where $\sigma_{\mathrm{H}}(\rho) = d \cdot \rho^k$, as it is explained in section 2.3.3.2. Clearly, this result corresponds to eq. (2.34) and leads us to the same solution as in section 2.3.3.2. We deduce, in fact, that $k = -2$ obtaining equations (2.35) and (2.37).

---

[1] $\sigma_{\mathrm{B}}(\rho) = a \cdot \rho^k$, as explained in section 2.3.3.1.

Appendix C

Spiral Galaxy in the Section with Keplerian Decline

In this appendix we analyse the rotation curve and the spider diagram of a spiral galaxy in the hypothetical Keplerian decline area, starting therefore from a radius about ten times bigger than the visible radius of the galaxy disk. As we already know, the situation represented in this case resembles the one we have seen in the solar system, but for clarity the explanation is given here.

Rotation Curve

Considering figure 2.17, where the radius is $r \geq R_H$, we see that the rotation velocity follows the Keplerian decline. The information we can extract from the curve is

$$v_K^2(r) = G\frac{M_G(R_H)}{r} = G\frac{M_B(R_B) \cdot R_H}{R_B \cdot r} = v_H^2(R_H)\,\frac{R_H}{r} = v_B^2(R_B)\,\frac{R_H}{r}\,, \qquad (C.1)$$

where $M_G(R_H)$ is the total mass of the galaxy at radius R_H, expressed by eq.(2.38), and it is a constant. In this case, according to Newton's shell theorem, the mass of the entire galaxy would act gravitationally on a test mass orbiting at $r \geq R_H$ as if it were all concentrated in one point at the centre of the system. Therefore, from R_H on we are facing a planet-like rotation with most of the mass concentrated in the centre, exactly like for the Solar System. This means that the further away we could measure the orbital velocity the more this would decrease proportionally to $r^{-1/2}$. As shown in figure C.1, the first available measurement would be at the edge of the galaxy and thus the rotation curve appears exactly as in figure 2.17.

Spider Diagram

The spider diagram drawn from this region of the rotation curve, namely for $r \geq R_H$, should appear similar to the one for the Solar System, considering of course that it regards only radii bigger than the maximum radius of the galaxy. From the definition of the spider diagram and the fact that the rotation velocity is expressed by eq.(C.1) and the radial velocity by eq.(2.15), as we did in section 2.3.4 we derive

$$v_r - v_{\text{sys}} = v(r) \cdot \cos\theta \cdot \sin i = v_B(R_B) \sqrt{\frac{R_H}{r}} \cdot \cos\theta \cdot \sin i \stackrel{!}{=} B\,. \qquad (C.2)$$

Once more we group all constants and according to the definition of A in eq.(2.43), we obtain then

$$r^{-1/2}\,\cos\theta = \frac{B \cdot \sqrt{R_H}}{\sin i \cdot v_B(R_B)} = A \cdot \sqrt{R_H}\,. \qquad (C.3)$$
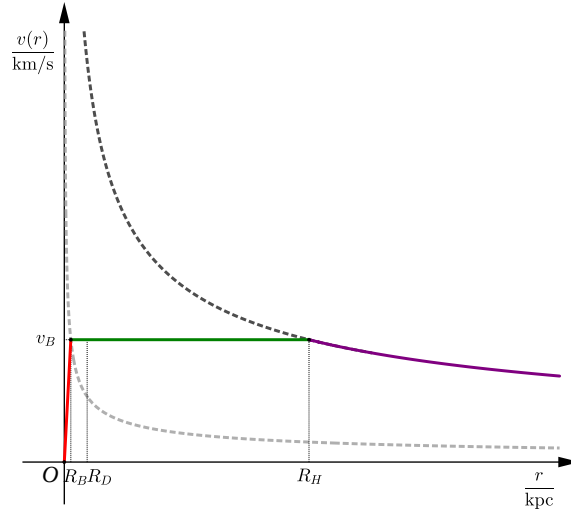
Figure C.1: Representation of the entire Keplerian decline rotation curve (dashed dark gray line). We could eventually measure and draw only the purple line because of the limit of measurements at the border of the galaxy. It is also shown as the Keplerian decline would be in absence of a halo (dashed light gray line).

After few steps, we present this result in Cartesian coordinates as

$$\frac{r\cos\theta}{r^{3/2}} = \frac{x}{(\sqrt{x^2+y^2})^{3/2}} = A \cdot \sqrt{R_\mathrm{H}} \; . \tag{C.4}$$

The solution of this equation, which represents the iso-velocity contours in the galaxy plane, is

$$y^2 = \left(\frac{1}{A \cdot \sqrt{R_\mathrm{H}}}\right)^{4/3} x^{4/3} - x^2 \; . \tag{C.5}$$

This corresponds to eq.(2.18), but for the spiral galaxy case instead. The result is very similar to the Solar System spider diagram in figures 2.14 and 2.16, however we consider only the radii bigger than the edge of the galaxy, as shown in figure C.2 (we have here already set $y' = y\cos i$ for the spider diagram lines and the circles of the different areas and $i = 60°$). Comparing eq.(C.3) with equations (2.43) and (2.46), we see that free parameters are still only r and θ, A is also here present and we have now as an extra constant the radius of the halo, R_H.

The complete version of the spider diagram in figure 2.21 for a spiral galaxy inclined of $i = 60°$, namely including the Keplerian decline part, is shown in figure C.3.
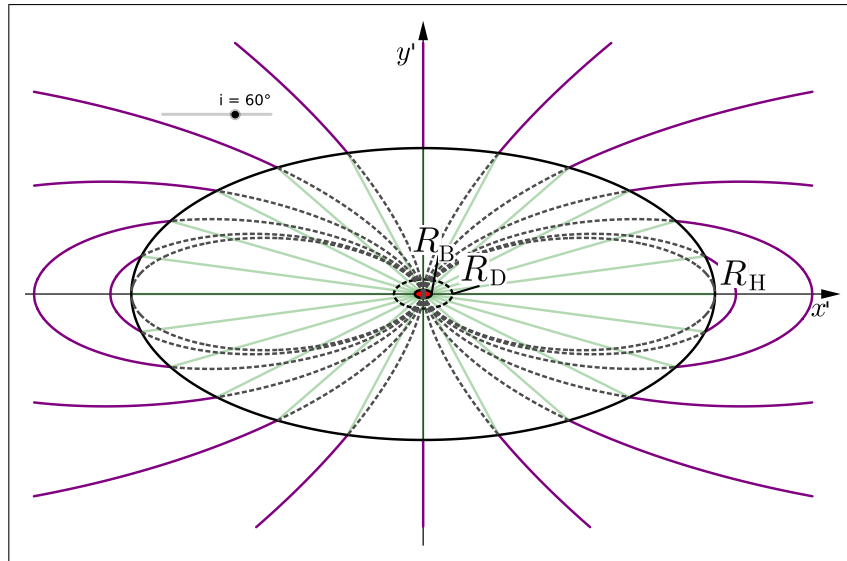
Figure C.2: Representation of the entire Keplerian decline spider diagram (dashed dark gray line) for a spiral galaxy. Also here we could eventually measure and draw only the lines in purple. In absence of the halo, we would not have the lines in green and the Keplerian decline lines should be set anew according to the dashed light gray line of figure C.1.
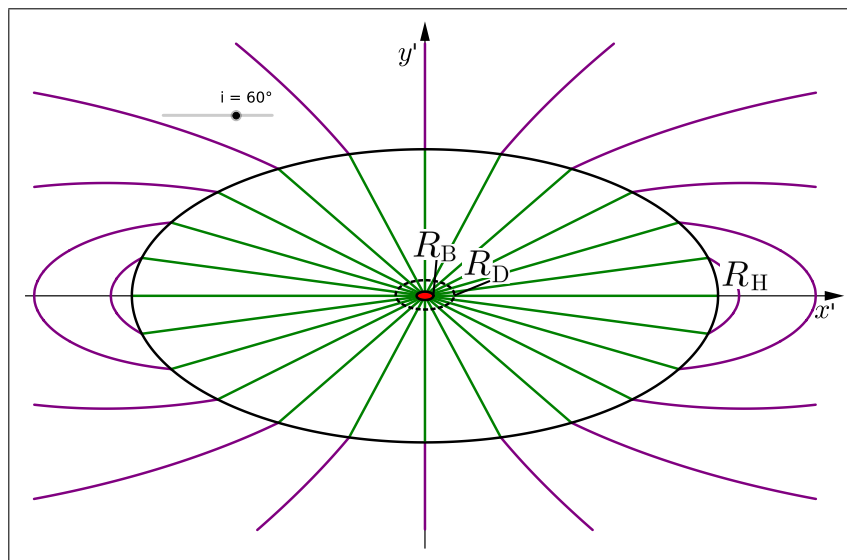
Figure C.3: Spider diagram of a spiral galaxy with all sections represented: bulge – red, halo – green and Keplerian decline – purple.

Appendix D

The Mass-to-Luminosity Ratio

Knowing the amount of visible mass inside a specific radius, it is possible to determine how much is this in comparison with the quantity of dark matter at the same radius. This comes from inferring the ratio between total mass (which includes dark matter), deduced from the rotation curve, and visible mass inside that radius if this last information is known. In case this information should not be directly available, we can achieve the same result calculating the mass-to-luminosity ratio $\frac{M}{L}$ for the observed galaxy. The mass-to-luminosity ratio is an indicator of how efficient is some quantity of visible, luminous mass in producing photons. In an ideal case, using solar units of measurement, one solar mass should produce one solar luminosity $\frac{M_\odot}{L_\odot} = 1$, but for many reasons this is not the reality for all stars. In fact not only the presence of dark matter affects this ratio, but for the visible mass also the properties of different stellar populations [94].

It is indeed known from observations that for spiral galaxies the average mass-to-luminosity ratio for the visible mass, in solar units, is $\frac{M_{\text{vis}}}{L} = 3\frac{M_\odot}{L_\odot}$ [94]. Considering instead the total mass of the observed galaxy at any point outside the visible radius $r \geq R_{\text{D}}$, the ratio $\frac{M_{\text{G}}(r)}{L}$ is given by the quantity of total mass derived from the rotation curve, expressed by eq.(2.38), divided the total luminosity of the galaxy, calculated from the absolute magnitude. This is actually possible because the intrinsic luminosity of celestial objects is expressed by the absolute magnitude M, the apparent brightness is instead expressed by the apparent magnitude m.[1]

The magnitude scale (the same for apparent and absolute one) is an inverse logarithmic scale and expresses a measure of the brightness of a celestial object as seen from Earth. It is an inverse measure because the brighter an object is, the smaller the numerical value of its magnitude is. This scale has its modern roots on Pogson's ratio [83]. Basically, the measured-on-Earth intensities from two objects I_1 and I_2, in units of energy flux density ($[I] = \frac{\text{W}}{\text{m}^2}$),[2] correspond to two apparent magnitudes m_1 and m_2. These intensities and magnitudes are related by

$$\frac{I_1}{I_2} = 100^{\frac{\text{m}_2 - \text{m}_1}{5}} \ . \tag{D.1}$$

Given that the intensity is expressed by $I = \frac{L}{4\pi d^2}$, where L is luminosity ($[L] = \text{W}$), it is clear that the intensity of light received from a celestial object depends on its distance d (inverse-square law). Now, if we consider two galaxies or stars at the same distance from the observer, the intensity ratio (or the magnitude difference) is an expression of their luminosity ratio $\frac{L_1}{L_2}$ only. This leads us to the concept of absolute magnitude, which corresponds to the apparent brightness of a celestial object if it would be at the standard distance of $d_0 = 10\text{pc}$. In this way, the absolute magnitude is independent of the different-distance problem and an indication of the intrinsic luminosity of the object.

---

[1] M and m are not in italics, they should not be confused with mass symbols.

[2] It is common use among astronomers to express it in $\frac{\text{erg}}{\text{s} \cdot \text{m}^2}$, nevertheless we will not use these last units of measurement. They are not well known among teachers and students, who as a rule use the International System of Units.

Therefore, from eq.(D.1) and using the absolute magnitude for avoiding the different-distance problem, we derive

$$\mathrm{M}_2 - \mathrm{M}_1 = 2.5 \log \frac{L_1}{L_2} \; . \tag{D.2}$$

Introducing now the known values from the literature for the observed galaxy (index 1) and for the Sun (index 2), we easily solve it for the galaxy luminosity

$$L_{\mathrm{G}} = L_{\odot} 10^{\frac{2}{5}(\mathrm{M}_{\odot} - \mathrm{M}_{\mathrm{G}})} \; . \tag{D.3}$$

Finally, since the total luminosity remains the same for the visible and for the total mass of the galaxy, we are allowed to compare the respective mass-to-luminosity ratios. In this way we obtain a rough estimate of the ratio of visible mass to total mass at a certain radius $r \leq R_{\mathrm{D}}$, expressed as $\frac{M_{\mathrm{vis}}}{M_{\mathrm{G}}(r)}$, which gives also the estimate of dark matter at the same radius.

The Mass-to-Luminosity Ratio for NGC3198

According to the previous section, if we do not have the total luminosity of the considered galaxy L_{G}, we can easily calculate it using its absolute magnitude M, the one of the Sun and the Sun's total luminosity as in eq.(D.3). Indeed, from the absolute magnitudes M_V in table 2.3 and knowing that for the Sun it is $L_{\odot V} = 4.83$ and $1 L_{\odot} = 3.9 \cdot 10^{26}$ W, we have

$$L_{\mathrm{GV}} = L_{\odot \mathrm{V}} \, 10^{\frac{2}{5}(4.83 + 19.80)} = 7.11 \cdot 10^9 \, L_{\odot} = 2.77 \cdot 10^{36} \text{ W} \; .$$

As we can see, it is very similar to the value from the literature in table 2.3. Now, adopting this value for the luminosity of the galaxy and the values in table D.1 for the mass, we derive the ratio $\frac{M}{L}$ at different radii of interest in the form $\frac{M_{\mathrm{G}}(r)}{L} = n \frac{M_{\odot}}{L_{\odot}}$. Here n assumes different values depending on what radius it is calculated at. The results significant for us are listed in table D.1. The last step consists of comparing the results for this ratio with the mean value of $\frac{M}{L}$ for the visible mass in a spiral galaxy, that is $\frac{M_{\mathrm{vis}}}{L} = 3 \frac{M_{\odot}}{L_{\odot}}$. This comparison gives us an estimate of the quantity of visible mass in relation to the total dynamical mass of the galaxy, considering the fact that for the entire visible mass of the galaxy we can set $L_{\mathrm{vis}} = L_{\mathrm{GV}} = L$ constant. Therefore, we derive

$$M_{\mathrm{vis}} = \frac{3}{n} \, M_{\mathrm{G}}(r) \; , \tag{D.4}$$

calculated for each value of n and $M_{\mathrm{G}}(r)$. Then with $M_{\mathrm{dark}} = (1 - 3/n) \, M_{\mathrm{G}}(r)$, we easily obtain the same ratio for the non-visible matter. All these last results are also collected in table D.1. It is indeed from the last three columns of table D.1 that we have the searched evidence of the

NGC3198	$\sigma_{\mathrm{H}}(r)$ in kg/kpc^3	$\sigma_{\mathrm{H}}(r)$ in $M_{\odot}$/kpc^3	$M_{\mathrm{G}}(r)$ in kg	$M_{\mathrm{G}}(r)$ in $M_{\odot}$	n	$M_{\mathrm{vis}}/M_{\mathrm{G}}(r)$	$M_{\mathrm{dark}}(r)/M_{\mathrm{G}}(r)$	$M_{\mathrm{dark}}(r)/M_{\mathrm{vis}}$
R_{B}	$5.18 \cdot 10^{37}$	$2.60 \cdot 10^7$	$4.16 \cdot 10^{40}$	$2.09 \cdot 10^{10}$	–	–	–	–
R_{D}	$4.23 \cdot 10^{36}$	$2.12 \cdot 10^6$	$14.56 \cdot 10^{40}$	$7.32 \cdot 10^{10}$	10.30	0.29	0.71	2.45
R_{30}	$9.20 \cdot 10^{35}$	$4.62 \cdot 10^5$	$31.20 \cdot 10^{40}$	$15.68 \cdot 10^{10}$	22.05	0.14	0.86	6.14
R_{max}	$3.31 \cdot 10^{35}$	$1.66 \cdot 10^5$	$52.02 \cdot 10^{40}$	$2.61 \cdot 10^{11}$	36.71	0.08	0.92	11.50
R_{H}	$4.23 \cdot 10^{34}$	$2.12 \cdot 10^4$	$145.64 \cdot 10^{40}$	$7.32 \cdot 10^{11}$	102.95	0.03	0.97	32.33

Table D.1: Results for mass density, mass, M/L ratio and amount of visible and dark matter at different radii of the spiral galaxy NGC3198. $R_{30} = 30$ kpc is a value fro the radius used later for comparing these results to the ones from the literature, $R_{\mathrm{max}} = 50$ kpc is the maximum radius reached for measurements, $R_{\mathrm{H}} = 140$ kpc is the hypothetical maximum radius of the halo.

presence of a huge amount of mass that we cannot see, the famous dark matter.
Despite the fact that this is not our primary objective, we try to assess the accuracy of our results by comparing them with some values taken from the literature, which are summarised in table

NGC3198	Luminosity $10^9\ L_\odot$	Halo Mass Density $M_\odot/\text{pc}^3$	Visible Mass $10^9\ M_\odot$	Total Mass $10^{10}\ M_\odot$
Begeman [6]	$L_B = 9$ $L_V = 7.3$	–	$M_{Gvis}(R_{max}) = (5+34)$ gas+stars	–
van Albada [110]	$L_B = 8.6$ $L_V = 7$	$\sigma_H(R_8) = 0.0042$	$M_{Gvis}(R_{max}) = 5$ gas	–
Bosma [11]	$L_B = 7.95$	–	$M_{Gvis}(R_{max}) = 5$ gas	–
Kostov [55]	$L_V = 7$	–		$M_G(R_D) = 7.2$ (or 6.5_{trunc})
Daod [18]	–	$\sigma_H(R_B) = 0.0187$ $\sigma_H(R_{30}) = 0.00278$	$M_{Gvis}(R_D) = 17$	
	Total Mass $10^{10}\ M_\odot$	Mass-to Light Ratio $M_\odot/L_\odot$	Mass-to Light Ratio $M_\odot/L_\odot$	Mass Quantities Ratio
Begeman [6]	$M_G(R_{30}) = 15$	$M/L = 3.8$ visible disk	–	–
van Albada [110]	$M_G(R_{30}) = 15$	$M/L = 3.6_B$ (or 4.4_V) visible disk	$M/L = 18_{R_{30}}$ (or $25_{R_{50}}$)	$M_{dark}(R_{30})/M_{vis} = 3.9$
Bosma [11]	$M_G(R_{26}) = 9.2$	–	–	–
Kostov [55]	$M_G(R_{30}) = 15$ (or 11_{trunc})	$M/L = 9.3$ total disk	$M/L = 21$ total galaxy	–
Daod [18]	$M_G(R_{30}) = 5.26$	–	–	$M_{vis}/M_G(R_{30}) = 0.324$

Table D.2: Data about the spiral galaxy NGC3198 taken from the literature and used as comparison for assessing the accuracy of our results.

D.2. Almost all the literature cited in this table states that at R_{30} the quantity of dark matter should be at least four times that of visible mass. And all of them conclude that the spiral galaxy NGC3198 can be essentially described by two components: the visible disk and the spherical halo of dark matter. We achieve the same conclusion about the components of the galaxy, however, using our simplified model and neglecting any kind of deviation from this model and uncertainty, the amount of dark matter we derive is six times more than the visible mass. Thus, in comparison, our result is overestimating the amount of dark matter. Since the calculated luminosity L_{GV} and the total mass $M_G(R_{30})$ are in very good agreement with [6], [110] and [55], we conclude that the assumed values for the distance of the galaxy, the Hubble constant H_0 and the mean mass-to-luminosity ratio $\frac{M}{L}$ chosen for the visible mass play an important role for the final result and may cause this overestimation.

Finally we can be satisfied with the results obtained for the galaxy NGC3198. They are mostly in good agreement with what is reported in the literature and allow us to understand the process that leads to the formulation of the concept of dark matter.

Appendix E

The Produced Lenses

For the sake of completeness, we now show the graph with the full profile (from the centre to the outer edge) of the lenses we have produced in plexiglass and the photo of these lenses.

The Schwarzschild radius,[1] R_{S}, is given in the caption for each lens model whose total mass does not diverge. This suggests that these three lenses (point mass, Plummer sphere and Kuzmin disk) are representative of the gravitational lens effect that would be caused by objects whose total mass is in the range of 10% to 25% of the mass of the Earth.[2] As we have already mentioned in section 3.3.2.1, for the production of such lenses, technical feasibility was more important than the representation of real astronomical objects.
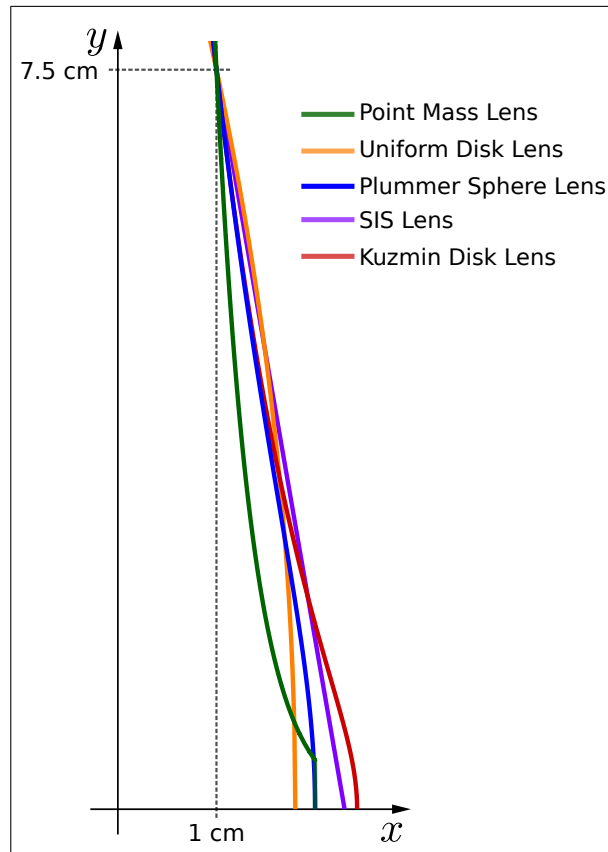
Figure E.1: Comparison of the entire profile of the five lenses we produced, which correspond to point mass ($R_{\mathrm{S}} = 0.09\,\mathrm{cm}$), uniform disk, Plummer sphere ($R_{\mathrm{S}} = 0.25\,\mathrm{cm}$), SIS and Kuzmin disk ($R_{\mathrm{S}} = 0.25\,\mathrm{cm}$) models (see the graph legend for the colours).

---

[1] R_{S} is defined in section 3.2.

[2] The Schwarzschild radius of the Earth is approximately 0.9 cm.

Figure E.2: The five lenses we produced. From left to right: point mass ($R_{\mathrm{S}} = 0.09$ cm), uniform disk, Plummer sphere ($R_{\mathrm{S}} = 0.25$ cm), SIS and Kuzmin disk ($R_{\mathrm{S}} = 0.25$ cm) models.

Appendix F

Projecting the Lens Mass onto a Plane

In this appendix we will see the procedure to obtain the mass of a sphere projected onto a plane as a function of the radius. This procedure, as we have seen in our simplified approach, is used in cases where the lens models we consider are not disks, but actually spheres. We start with the simple example of a homogeneous sphere of finite dimension, whose mass is uniformly distributed. We then move on to an example taken from our lens models, namely the Singular Isothermal Sphere – SIS seen in section 3.3.1.1.

Homogeneous Sphere Example

The sphere whose mass we want to project onto a plane, represented in figure F.1, has the following characteristics:

- constant mass density $\sigma(r) = \sigma_0$,

- $0 \leq r \leq R$ with R the radius of the entire sphere,

- the volume element in spherical coordinates is defined by $\mathrm{d}V = r^2 \sin\theta \, \mathrm{d}\theta \, \mathrm{d}\phi \, \mathrm{d}r$.
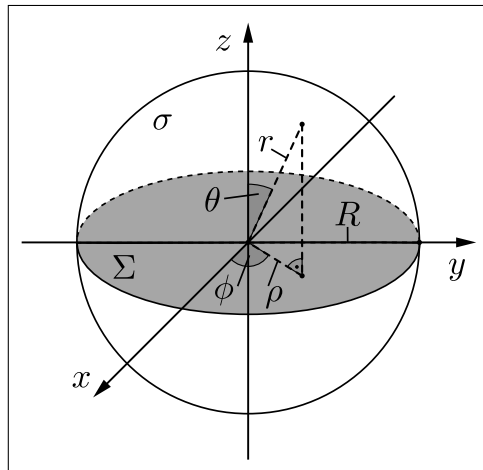
Figure F.1: The finite homogeneous sphere. The disk in grey represents the plane onto which we want to project the entire mass of the sphere. We define r as the radial distance from the centre (and ρ its projection), R as the maximum radius of the sphere, θ as the polar angle and ϕ as the azimuth angle.

We can easily calculate the total mass of this sphere by means of

$$M(R) = \int_V \sigma_0 \, \mathrm{d}V = \sigma_0 \int_0^\pi \sin\theta \, \mathrm{d}\theta \int_0^{2\pi} \mathrm{d}\phi \int_0^R r^2 \, \mathrm{d}r = 4\pi\,\sigma_0\,\frac{1}{3}\,R^3 \; . \tag{F.1}$$

If, on the other hand, we want to consider a generic intermediate radius r, the mass contained within it is given by $M(r) = 4\pi\,\sigma_0\,\frac{1}{3}\,r^3$. Switching now to Cartesian coordinates with $r^2 = x^2 + y^2 + z^2$, we can introduce the projection on the xy-plane of the radius r in 3-space. This, as can be seen from the figure, is represented by $\rho = r\,\sin\theta$, obtaining $r^2 = \rho^2 + z^2$.

At this point we can project the mass density onto the xy-plane and calculate thus the surface mass density

$$\Sigma(\rho) = \sigma_0 \int_{-(R^2-\rho^2)^{\frac{1}{2}}}^{(R^2-\rho^2)^{\frac{1}{2}}} \mathrm{d}z = 2\,\sigma_0 \sqrt{R^2 - \rho^2}\ . \tag{F.2}$$

The limits of integration are defined as shown in figure F.2, namely by the z-coordinates of pairs of points of the sphere mirrored with respect to the xy-plane and expressed in terms of R and ρ. In fact, from the figure we deduce that $z_\mathrm{P} = \sqrt{R^2 - \rho^2}$ and $z_\mathrm{P'} = -\sqrt{R^2 - \rho^2}$. When ρ varies,
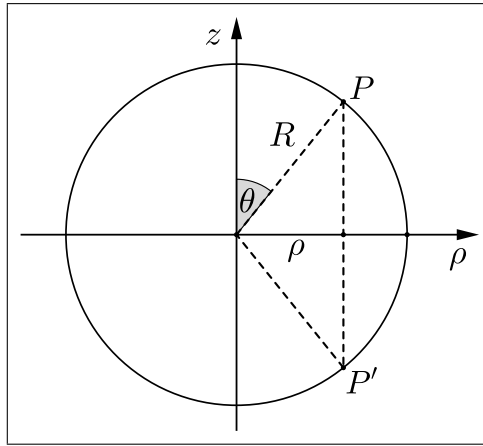
Figure F.2: The sphere observed in the ρz-plane in order to define the limits of integration along the z-axis.

considering that $0 \le \rho \le R$, we can thus describe these coordinates for each pair of points. Thanks to $\Sigma(\rho)$ and considering the surface element $\mathrm{d}S = \rho\,\mathrm{d}\phi\,\mathrm{d}\rho$ of the xy-plane, we derive the projected mass

$$M(\rho) = \int_S \Sigma\,\mathrm{d}S = \int_0^{2\pi} \mathrm{d}\phi \int_0^\rho \rho\,\Sigma(\rho)\,\mathrm{d}\rho = 4\,\pi\,\sigma_0\,\frac{1}{3}\left(R^3 - (R^2 - \rho^2)^{3/2}\right)\ . \tag{F.3}$$

Figures F.3 and F.4 show mass density and mass radial profiles of the finite homogeneous sphere
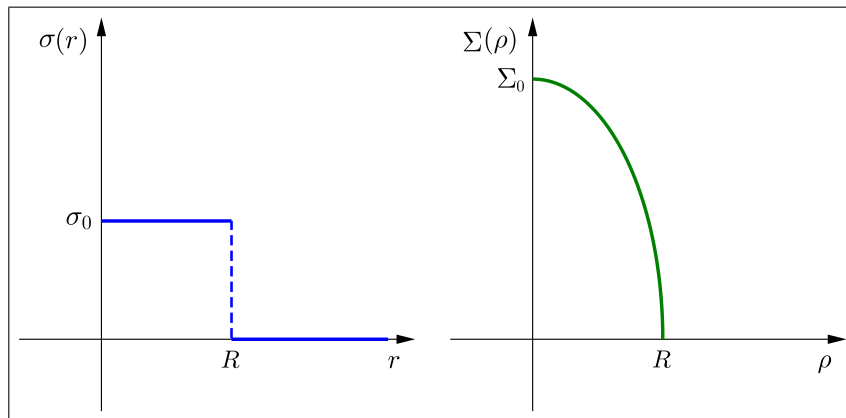
Figure F.3: Mass density radial profiles of the finite homogeneous sphere, on the left in 3-space and on the right projected onto the xy-plane.

of radius R before and after the projection onto a plane.

If we consider the total projected mass, therefore for the case $\rho = R$, we obviously obtain $M(R) = 4\pi\sigma_0\frac{1}{3}R^3$. Indeed, as expected, the total mass does not change, but its distribution is of course different.
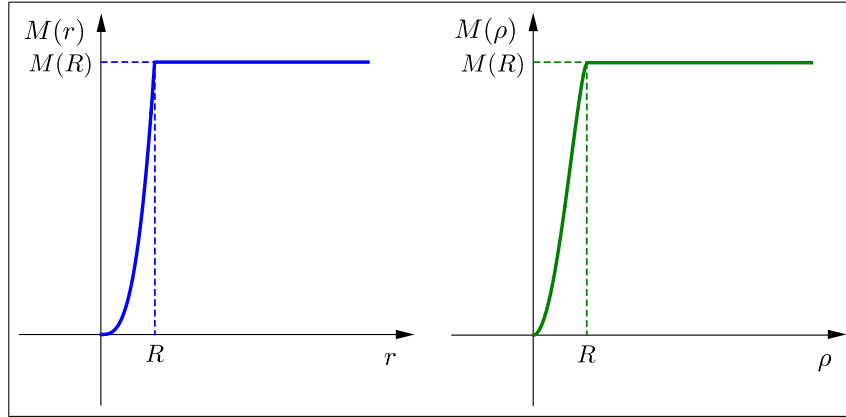
Figure F.4: Mass radial profiles of the finite homogeneous sphere, on the left in 3-space and on the right projected onto the xy-plane.

SIS Example

Now we apply the reasoning we just saw to the SIS model considering that for this sphere we have $0 \leq r < \infty$ and $\sigma(r) = \frac{\sigma_v{}^2}{2\pi G\, r^2}$. Hence, for a general radius r, from eq.(F.1) we get

$$M(r) = \int_0^\pi \sin\theta\, d\theta \int_0^{2\pi} d\phi \int_0^r r^2\,\sigma(r)\, dr = \frac{2\,\sigma_v{}^2}{G}\, r \;. \tag{F.4}$$

At this point applying eq.(F.2) with proper limits of integration[1] and using $r^2 = \rho^2 + z^2$, we can calculate the surface mass density

$$\Sigma(\rho) = \int_{-\infty}^{\infty} \sigma(\rho, z)\, dz = \frac{\sigma_v{}^2}{2\pi G} \int_{-\infty}^{\infty} \frac{1}{\rho^2 + z^2}\, dz = \frac{\sigma_v{}^2}{2\,G}\,\frac{1}{\rho} \;. \tag{F.5}$$

Finally, we are able to derive the projected mass thanks to eq.(F.3), obtaining

$$M(\rho) = \int_0^{2\pi} d\phi \int_0^\rho \rho\,\Sigma(\rho)\, d\rho = \frac{\pi\,\sigma_v{}^2}{G}\,\rho \;. \tag{F.6}$$

In fact, we reach exactly equations (3.31) and (3.32) used in the case of the SIS lens, the representations of which are in figures 3.15 and 3.16.

---

[1]Remember that the sphere is infinite.

Appendix G

Example of a Problem Sheet about Gravitational Lensing

Example of a problem sheet on how to calculate the shape of the profile to be given to a plexiglass lens, so that it simulates the gravitational lens effects typical of the simplified models we have analysed. This type of exercise guides students in the discovery of what we have seen in section 3.3.2.1. Prerequisite is to provide the students with the background information as seen in section 3.2 and the characteristics of the model we want to analyse (as in section 3.3.1.1). The extra step the teacher has to consider is to adapt the background content to the level of the audience.

In these exercises only point mass, SIS and uniform disk models are considered, as we know that these are the easiest to solve. It is also recommended that these exercises, when applied to the Plummer sphere and Kuzmin disk models, should only be done by advanced students.

For further exercises we suggest considering the proceedings of the Jena 2019 Heraeus Summer School "Astronomy from 4 Perspectives" [64]. Where there are practical examples on how to use the teaching tools and material we have developed on gravitational lensing.

Understanding the Shape of the Plexiglass Lens Simulating Gravitational Lens Effects

After the introduction of the phenomenon of the gravitational lens effect, we now want to derive the shape of a plexiglass lens that is able to bend light like a gravitational lens. To accomplish this task, as we have seen, we need to combine optics and general relativity.

For simplicity the surface where the light rays are incident is considered flat. The rays enter perpendicularly to this surface. Instead, the shape of the other surface is currently unknown to us and this is what we want to discover.

The goal of these exercises is to derive the profile of the plexiglass lens using the given deflection angle $\delta(y) = \frac{4G}{c^2} \frac{M(|y|)}{y}$ and Snell's law $n \cdot \sin \alpha = n_1 \cdot \sin \beta$.[1] We apply the procedure to several examples of mass distribution corresponding to the gravitational lenses we want to represent.

Exercise 1: General Differential Equation

We begin by deriving the general differential equation that will allow us to calculate the plexiglass lens profile. This differential equation is the same for all gravitational lens models we want to simulate.

---

[1] In our examples $n_1 = 1$ is the refraction index of air and $n = 1.5$ of the plexiglass. Thus α is the angle of incidence and β of refraction with respect to the normal to the lens surface in P (see figure G.1).
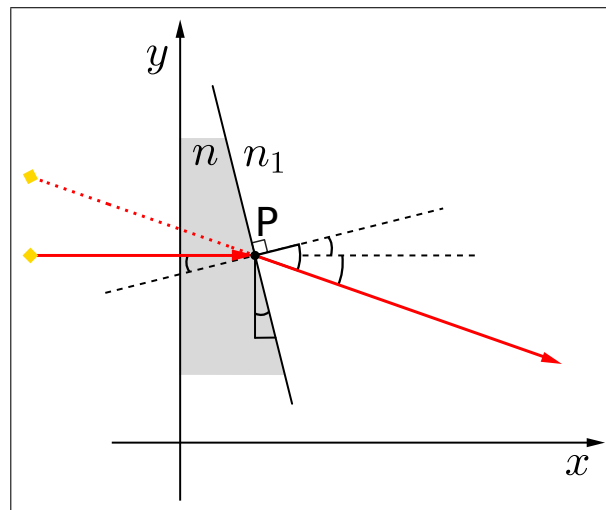
Figure G.1: Deflection of a light ray passing from one medium to another with different index of refraction.

a) First of all, let's analyse the geometry of the system. Label the various components of the diagram in figure G.1 according to the provided information.

b) Now consider Snell's law and apply it to the system shown in the diagram. Rearrange the terms and express n in terms of δ and α.

   (Hint: $\sin(\alpha \pm \beta) = \sin\alpha\cos\beta \pm \sin\beta\cos\alpha$ trigonometric angle sum and difference identities.)

c) Consider the tangent line to the lens surface in P. Calculate the slope of the tangent $\frac{\mathrm{d}y}{\mathrm{d}x}$ in terms of α.

d) Now combine the results of parts b) and c) and introduce the expression giving the deflection angle δ. Formulate a general differential equation in the form $\frac{\mathrm{d}y}{\mathrm{d}x}$.
   This differential equation allows us to calculate the lens profile once we have chosen the mass distribution we wish to investigate as a gravitational lens.

   (The resulting differential equation is $\frac{\mathrm{d}y}{\mathrm{d}x} = -\frac{(n-1)\,c^2}{4\,G\,M(|y|)} \cdot y$.)

Exercise 2: Point Mass Lens

(*As an alternative, this exercise can be done by the teacher as an initial example and then have the students do the rest following the same procedure.*)

Now that we have the general differential equation, we introduce into it the expression for the desired mass distribution. By solving this equation we obtain a function that describes the profile of the plexiglass lens.
At this point, we continue by dealing with the case of the point mass lens.

a) What is the characteristic of this lens model that primarily interests us?

b) Enter this characteristic of the mass distribution into the differential equation obtained from Exercise 1. Collect all constants into a single constant called k. How is k defined in this case? What units of measurement are characteristic of k? Discuss the result.

c) Once the final differential equation for this case has been formulated, think about the catalogue of functions you know. Is there any known function that satisfies this equation? Discuss the result.

   (*Alternatively, we can provide students with a list of known functions.*)

d) **(Advanced – instead of part c))** Solve the differential equation for y.

e) Taking into account the result of part c) (or d)), draw a sketch of the lens profile (Geogebra software can be used).
   Imagine and describe what the shape of the lens looks like in 3 dimensions. Discuss the result.

   (Hint: The 3-dimensional lens shape is a rotational solid that is obtained by rotating the lens profile about the axis of rotation (x-axis).)

f) After describing the shape of the lens (cone, paraboloid of rotation, etc.), draw a sketch of the plane cross-section containing the centre of symmetry.

Exercise 3: SIS Lens

We have already discussed what the characteristics of this gravitational lens model are. We also know that the mass distribution to be considered is given by the projection of the mass in 3-space onto a plane. In this case, as seen, it is $M(|y|) = \frac{\pi \sigma_v{}^2}{G} \cdot |y|$.

a) Enter $M(|y|)$ into the differential equation obtained from Exercise 1. Collect all constants into a single constant called k. Answer the same questions of Exercise 2 part b). Is k in this case defined as for the point mass model?

b) Apply parts c) (or d)), e) and f) of Exercise 2 to this case and answer the same questions.

Exercise 4: Uniform Disk Lens

Perform all parts of Exercise 3 applied to the seen uniform disc model, whose mass we know to be given by $M(|y|) = \Sigma_0 \pi |y|^2$.

Bibliography

[1] Adler, R. J., Barber, W. C., and Redar, M. E. Gravitational lenses and plastic simulators. *American Journal of Physics 63*, 6 (1995), 536–541.

[2] Arecchi, V., Messadi, T., and RJ, K. *Field Guide to Illumination*. SPIE Press, Bellingham, WA, 2007. Excerpt at URL: spie.org/publications/fg11_p02_solid_angle?SSO=1.

[3] Azarian, M. K. Al-Kashi's Fundamental Theorem. *International Journal of Pure and Applied Mathematics* (2004), 409–504.

[4] Bartelmann, M. Gravitational lensing. *Classical and Quantum Gravity 27*, 23 (2010), 233001.

[5] Bartelmann, M. Introduction to Gravitational Lensing. *Proceedings of the Jena 2019 Heraeus Summer School "Astronomy from 4 Perspectives": Thinking Gravitational Lensing for Teaching (Lotze, K.-H. and Simionato, S., editors)* (2021).

[6] Begeman, K. HI rotation curves of spiral galaxies. I-NGC 3198. *Astronomy and Astrophysics 223* (1989), 47–60.

[7] Bertone, G. *Particle dark matter: observations, models and searches*. Cambridge University Press, 2010.

[8] Bertone, G., and Hooper, D. History of dark matter. *Reviews of Modern Physics, APS 90*, 4 (2018), 045002.

[9] Bertone, G., Hooper, D., and Silk, J. Particle dark matter: Evidence, candidates and constraints. *Physics Reports, Elsevier 405*, 5-6 (2005), 279–390.

[10] Binney, J., and Tremaine, S. *Galactic dynamics*, second edition ed. Princeton University Press, 2008.

[11] Bosma, A. 21-cm line studies of spiral galaxies. I-Observations of the galaxies NGC 5033, 3198, 5055, 2841, and 7331. *The Astronomical Journal 86* (1981), 1791–1824.

[12] Bosma, A. 21-cm line studies of spiral galaxies. II. The distribution and kinematics of neutral hydrogen in spiral galaxies of various morphological types. *The Astronomical Journal 86* (1981), 1825–1846.

[13] Bottema, R. The stellar kinematics of the spiral galaxies NGC 3198 and NGC 3938. *Astronomy and Astrophysics 197* (1988), 105–122.

[14] Bransford, J., Brown, A., and Cocking, R. *How people learn: Brain, mind, experience, and school*. National Academy Press, 2000, 2000.

[15] Brosche, P., and Schwarz, O. The galactic surface density derived from K giants. *Astronomische Nachrichten: Astronomical Notes 328*, 2 (2007), 178–185.

[16] Casertano, S., and Hut, P. Core radius and density measurements in N-body experiments Connections with theoretical and observational definitions. *The Astrophysical Journal 298* (1985), 80–94.

[17] Congdon, A. B., and Keeton, C. R. *Principles of Gravitational Lensing.* Springer, 2018.

[18] Daod, N. A., and Zeki, M. K. Density and Mass Distribution of Spiral Galaxy NGC 3198. *The Astrophysical Journal 870*, 2 (2019), 107.

[19] De Swart, J., Bertone, G., and van Dongen, J. How dark matter came to matter. *Nature Astronomy 1*, 3 (2017), 0059.

[20] Delic, H., and Bećirović, S. Socratic Method as an Approach to Teaching. *European Researcher 111* (11 2016), 511–517.

[21] Dodelson, S. The real problem with MOND. *International Journal of Modern Physics, World Scientific 20*, 14 (2011), 2749–2753.

[22] Dodelson, S. *Gravitational lensing.* Cambridge University Press, 2017.

[23] D'Ambrosio, A. Come misurare le dimensioni di oggetti con uno smartphone? La Fucina delle Scienze, 2014. URL: http://www.lafucinadellescienze.it/wordpress/archives/6069.

[24] Einstein, A. Lens-like action of a star by the deviation of light in the gravitational field. *Science 84*, 2188 (1936), 506–507.

[25] Euclid of Alexandria. *Elements.* 300 BC.

[26] Event Horizon Telescope Collaboration. First M87 Event Horizon Telescope Results. I.Shadow of the Supermassive Black Hole. *Astrophysical Journal Letters 875*, 1 (2019), L1.

[27] Falbo-Kenkel, M., and Lohre, J. Simple gravitational lens demonstrations. *The Physics Teacher 34*, 9 (1996), 555–557.

[28] Falco, A. M. D. Crisi delle lauree scientifiche. *La Rivista – Bollettino dell'Ateneo dell'Università degli Studi di Catania* (2007).

[29] Feynman, R. *The character of physical law.* MIT press, 1965.

[30] Feynman, R. P., Leighton, R. B., and Sands, M. *The Feynman lectures on physics, Vol. I: The new millennium edition: mainly mechanics, radiation, and heat,* vol. 1, chapter 13. Basic books, 2011.

[31] Ford, J., Stang, J., and Anderson, C. Simulating gravity: Dark matter and gravitational lensing in the classroom. *The Physics Teacher 53*, 9 (2015), 557–560.

[32] Ford, M., and Forman, E. Redefining disciplinary learning in classroom contexts. *Review of research in education, JSTOR 30* (2006), 1–32.

[33] Gentile, G., Józsa, G., Serra, P., Heald, G., de Blok, W., Fraternali, F., Patterson, M., Walterbos, R., and Oosterloo, T. HALOGAS: Extraplanar gas in NGC 3198. *Astronomy & Astrophysics 554* (2013), A125.

[34] Ginsburg, D., Groose, B., Taylor, J., and Vernescu, B. History of the integral from the 17th century. *The history of the calculus and the development of computer algebra systems* (2015).

[35] Girard, A. *Invention nouvelle en l'algèbre.* Imprimé chez Muré frères, 1884.

[36] Gose, M. When Socratic dialogue is flagging: Questions and strategies for engaging students. *College Teaching 57*, 1 (2009), 45–50.

[37] Gott, J. R. Gravitational Lenses: Cosmic mirages produced by gravitational bending of light may solve some of the most pressing problems in cosmology today. *American Scientist 71*, 2 (1983), 150–157.

[38] Governo Italiano. Indicazioni nazionali riguardanti gli obiettivi specifici di apprendimento concernenti le attivita' e gli insegnamenti compresi nei piani degli studi previsti per i percorsi liceali di cui all'articolo 10, comma 3, del decreto del Presidente della Repubblica 15 marzo 2010, n. 89, in relazione all'articolo 2, commi 1 e 3, del medesimo regolamento. Decreto 7 ottobre 2010, n. 211, Ministero della Pubblica Istruzione, 2010. GU Serie Generale n.291 del 14-12-2010 - Suppl. Ordinario n. 275.

[39] Gradshteyn, I. S., and Ryzhik, I. M. *Table of integrals, series, and products.* Academic Press, 2014.

[40] Grauwe, A. D. *Without capacity, there is no development.* UNESCO, International institute for educational planning (IIEP), 2009.

[41] Greve, J.-P. D. Astronomy Education: Research Paving the Road to Enthusiasm for Studying Science. *IAU Symposium, Cambridge Univ Press* (12 2011).

[42] Halliday, D., Resnick, R., and Krane, K. S. *Physics, Volume 1 and 2.* John Wiley and Sons, 2001.

[43] Hampden-Thompson, G., and Bennett, J. Science Teaching and Learning Activities and Students' Engagement in Science. *International Journal of Science Education 35*, 8 (2013), 1325–1343.

[44] Higbie, J. Gravitational lens. *American Journal of Physics 49*, 7 (1981), 652–655.

[45] Higbie, J. Galactic lens. *American Journal of Physics 51*, 9 (1983), 860–861.

[46] Hohmann, S. Die Entwicklung der Sterne – Eine elementarisierte Betrachtung. PhD Thesis, University of Siegen, 2019.

[47] Huwe, P., and Field, S. Modern gravitational lens cosmology for introductory physics and astronomy students. *The Physics Teacher 53*, 5 (2015), 266–270.

[48] Icke, V. Construction of a gravitational lens. *American Journal of Physics 48*, 10 (1980), 883–886.

[49] Jarosievitz, B. Physics Teaching Activities and Resources used Innovatively In Higher Education. *Informatica 38*, 3 (2017), 22–26.

[50] Jones, M. H., Lambourne, R. J., and Serjeant, S. *An Introduction to Galaxies and Cosmology.* Cambridge University Press, 2015.

[51] Jungnickel, C., McCormmach, R., et al. *Cavendish: The experimental life.* Bucknell University Press, 1999.

[52] Kaenders, R., and Schmidt, R. Mit GeoGebra mehr Mathematik verstehen. *Wiesbaden: Vieweg+ Teubner* (2011).

[53] Karukes, E., Salucci, P., and Gentile, G. The dark matter distribution in the spiral NGC 3198 out to 0.22 Rvir. *Astronomy & Astrophysics 578* (2015), A13.

[54] Kittel, C., Knight, W. D., and Ruderman, M. A. *Berkeley Physics Course - Vol 1: Mechanics.* McGraw-Hill New York, 1965.

[55] Kostov, V. Mass distribution of spiral galaxies in a thin disk model with velocity curve extrapolation. *arXiv preprint astro-ph/0604395* (2006).

[56] Kravitz, B. Lecture on solid angle, 2009. URL: https://silo.tips/download/lecture-on-solid-angle.

[57] Kuzmin, G. Model of the steady galaxy allowing of the triaxial distribution of velocities. *Astron. Zh 33* (1956), 27.

[58] Liebes Jr, S. Gravitational lens simulator. *American Journal of Physics 37* (1969), 103–104.

[59] Lincoln, D. Dark matter. *The Physics Teacher, AAPT 51*, 3 (2013), 134–138.

[60] Lindblad, B. On the state of motion in the galactic system. *Monthly Notices of the Royal Astronomical Society 87* (1927), 553–564.

[61] Lotze, K.-H. Ein schwarzes Loch im Zentrum der Galaxie M87. *Astronomie und Raumfahrt 36* (1999), 8–13.

[62] Lotze, K.-H. Die Bestimmung großer kosmischer Entfernungen. *Astronomie + Raumfahrt 49*, 5 (2012), 10–16.

[63] Lotze, K.-H., and Schwarz, O. Chap 4 of Handbuch der experimentellen Physik. Sekundarstufe II (Kuhn W.). *Aulis Verlag in Friedrich Verlag GmbH, Band 1: Mechanik* (2006), 105–137.

[64] Lotze, K.-H., and Simionato, S. (Editors) Proceedings of the Jena 2019 Heraeus Summer School "Astronomy from 4 Perspectives". In *Thinking Gravitational Lensing for Teaching* (2021).

[65] Lotze, K.-H., and Simionato, S. *Gravitational Lensing as Focal Point for Teaching General Relativity.* Chapter from the book: (Blair, D. and Kersting, M., editors) Teaching Einsteinian Physics in Schools. Routledge, Taylor & Francis Group, 2021.

[66] Lotze, K.-H., and Simionato, S. Henry Cavendish and the Effect of Gravity on Propagation of Light: A Postscript. *The European Physical Journal H 46*, 24 (2021).

[67] Lovas, S., and Kielkopf, J. F. Distribution of dark and luminous mass in galaxies. *The Astronomical Journal 147*, 6 (2014), 135.

[68] Mallik, P. The Axicon. College of Optical Sciences - University of Arizona, 2005. URL: http://wp.optics.arizona.edu/wp-content/uploads/2016/03/axicon_Proteep.pdf.

[69] Mangrum, J. R. Sharing practice through Socratic seminars. *Phi Delta Kappan 91*, 7 (2010), 40–43.

[70] McDermott, L. C. Research on conceptual understanding in mechanics. *Physics Today, AAPT 37* (1984), 24–32.

[71] McDermott, L. C., Rosenquist, M. L., and Van Zee, E. H. Student difficulties in connecting graphs and physics: Examples from kinematics. *American Journal of Physics, AAPT 55*, 6 (1987), 503–513.

[72] McLeod, J. H. The axicon: a new type of optical element. *JOSA 44*, 8 (1954), 592–597.

[73] Meneghetti, M. Introduction to Gravitational Lensing - Lecture scripts. *URL: http://www.ita.uni-heidelberg.de/~massimo/sub/Lectures/gl_all.pdf* (2016).

[74] Michaels, S., Shouse, A., and Schweingruber, H. *Ready, Set, Science!: Putting research to work in k-8 science classrooms.* The National Academies Press, Washington, 2007.

[75] Mynbayeva, A., Sadvakassova, Z., and Akshalova, B. Pedagogy of the twenty-first century: Innovative Teaching methods. In *New Pedagogical Challenges in the 21st Century-Contributions of Research in Education.* IntechOpen, 2017.

[76] Narayan, R., and Bartelmann, M. Lectures on gravitational lensing. *Formation of Structure in the Universe (A. Dekel & J.P. Ostriker, editor)* (1999), 360.

[77] Newton, I. *Opticks: : Or, a Treatise of the Reflexions, Refractions, Inflexions and Colours of Light.* London, 1721.

[78] Nobre, C. N., Meireles, M. R. G., Vieira Jr, N., De Resende, M. N., Da Costa, L. E., and Da Rocha, R. C. The Use of Geogebra Software as a Calculus Teaching and Learning Tool. *Informatics in Education 15*, 2 (2016), 253–267.

[79] Oort, J. H., et al. Observational evidence confirming Lindblad's hypothesis of a rotation of the galactic system. *Bulletin of the Astronomical Institutes of the Netherlands 3* (1927), 275.

[80] Osborne, J., Simon, S., and Collins, S. Attitudes towards science: a review of the literature and its implications. *International Journal of Science Education 25*, 9 (2003), 1049–1079.

[81] Paczynski, B. Gravitational microlensing by the galactic halo. *The Astrophysical Journal 304* (1986), 1–5.

[82] Plummer, H. C. On the problem of distribution in globular star clusters. *Monthly Notices of the Royal Astronomical Society 71* (1911), 460–470.

[83] Pogson, N. Magnitudes of Thirty-six of the Minor Planets for the first day of each month of the year 1857. *Monthly Notices of the Royal Astronomical Society 17* (1856), 12–15.

[84] Prince, M. J., and Felder, R. M. Inductive teaching and learning methods: Definitions, comparisons, and research bases. *Journal of Engineering Education 95*, 2 (2006), 123–138.

[85] Refsdal, S., and Surdej, J. Gravitational lenses. *Reports on Progress in Physics 56*, 2 (1994), 117–185.

[86] Richter, G. Die Keplerschen Gesetze und Newtons Gravitationsgesetz. *Die Sterne 54* (1978), 218–236.

[87] Ritchie, S., and Norton, S. Teaching and learning science and mathematics through technology practice. *International handbook of research and development in technology education* (2009), 419–430.

[88] Rubin, V. C. Dark matter in spiral galaxies. *Scientific American 248*, 6 (1983), 96–109.

[89] Rubin, V. C., and Ford Jr, W. K. Rotation of the Andromeda nebula from a spectroscopic survey of emission regions. *The Astrophysical Journal 159* (1970), 379.

[90] Rubin, V. C., Ford Jr, W. K., and Thonnard, N. Extended rotation curves of high-luminosity spiral galaxies. IV-Systematic dynamical properties, SA through SC. *The Astrophysical Journal 225* (1978), L107–L111.

[91] Salo, H. N-body code for simulation of planar disk-disk encounters - Application to tidally triggered bar formation. *Astronomy and Astrophysics 243* (1991), 118–138.

[92] Sauer, T., and Schütz, T. Exploring gravitational lensing. *European Journal of Physics 40*, 3 (2019), 035301.

[93] Schmid, C. Newton's superb theorem: An elementary geometric proof. *American Journal of Physics 79*, 5 (2011), 536–539.

[94] Schneider, P. *Extragalactic astronomy and cosmology: an introduction.* Springer, 2015.

[95] Schneider, P., Ehlers, J., and Falco, E. *Gravitational Lenses.* Springer, 1999.

[96] Schneider, P., Kochanek, C., and Wambsganss, J. *Gravitational lensing: strong, weak and micro.* Springer, 2006.

[97] Sellwood, J. Relaxation in N-body simulations of spherical systems. *Monthly Notices of the Royal Astronomical Society 453*, 3 (2015), 2919–2926.

[98] Selmke, M. An optical n-body gravitational lens analogy. *American Journal of Physics 89*, 1 (2021), 11–20.

[99] Simionato, S. Development of Astronomy Educational Resources: the Case of "Universe Awareness". Master Thesis, University of Padua, 2013.

[100] Simionato, S. Three Redshifts: Doppler, Cosmological, and Gravitational. *The Physics Teacher 59*, 5 (2021), 333–336.

[101] Simionato, S., and Lotze, K.-H. Distance Determination of the Spiral Galaxy NGC3198 with Cepheids, using Real Data from the Missions OGLE-IV and Gaia-DR1. *In preparation* (2021).

[102] Soldner, J. Ueber die Ablenkung eines Lichtstrals von seiner geradlinigen Bewegung, durch die Attraktion eines Weltkörpers, an welchem er nahe vorbei geht. *Astronomisches Jahrbuch für das Jahr 1804* (1801), 161–172.

[103] Sparke, L. S., and Gallagher III, J. S. *Galaxies in the universe: an introduction.* Chap. 3. Cambridge University Press, 2007.

[104] Su, J., Wang, W., Wang, X., and Song, F. Simulation of the gravitational lensing effect of galactic dark matter halos using 3D printing technology. *The Physics Teacher 57*, 9 (2019), 590–593.

[105] Surdej, J., Delacroix, C., Coleman, P., Dominik, M., Habraken, S., Hanot, C., Le Coroller, H., Mawet, D., Quintana, H., Sadibekova, T., et al. The optimal gravitational lens telescope. *The Astronomical Journal 139*, 5 (2010), 1935.

[106] Takači, D., Stankov, G., and Milanovic, I. Efficiency of learning environment using GeoGebra when calculus contents are learned in collaborative groups. *Computers & Education 82* (2015), 421–431.

[107] Thean, A., Mundell, C., Pedlar, A., and Nicholson, R. A neutral hydrogen study of the Seyfert galaxy NGC 5033. *Monthly Notices of the Royal Astronomical Society 290*, 1 (1997), 15–24.

[108] ThILLM. Lehrplan für den Erwerb der allgemeinen Hochschulreife. Physik, Mathematik, Astronomie, Thüringer Institut für Lehrerfortbildung, Lehrplanentwicklung und Medien, 2020. URL: https://www.schulportal-thueringen.de/web/guest/lehrplaene/gymnasium.

[109] Thorpe, E. *The Scientific Papers of the Honourable Henry Cavendish, F.R.S., Volume II: Chemical and Dynamical.* Cambridge University Press, 1921.

[110] van Albada, T. S., Bahcall, J. N., Begeman, K., and Sancisi, R. Distribution of dark matter in the spiral galaxy NGC 3198. *The Astrophysical Journal 295* (1985), 305–313.

[111] Vièta, F. Opera Mathematica. 1579. Reprinted Leiden, Netherlands, 1646.

[112] Voelker, S. Schuelerprojekte mit astronomischen Originaldaten fuer den Einsatz im Astronomieunterricht der Oberstufe. PhD Thesis, Friedrich-Schiller University of Jena, 2015.

[113] Wallace, C. S., and Prather, E. E. Teaching physics with Hubble's law and dark matter. *American Journal of Physics 80*, 5 (2012), 382–390.

[114] Walter, F., Brinks, E., De Blok, W., Bigiel, F., Kennicutt Jr, R. C., Thornley, M. D., and Leroy, A. THINGS: The HI nearby galaxy survey. *The Astronomical Journal 136*, 6 (2008), 2563.

[115] Wambsganss, J. Gravitational lensing in astronomy. *Living Reviews in Relativity 1*, 1 (1998), 1–74.

[116] Weisstein, E. W. Solid Angle. From MathWorld–A Wolfram Web Resource, Wolfram Research, Inc. URL: mathworld.wolfram.com/SolidAngle.html.

[117] White, S. Simulations of the Dark Matter Distribution. Max Planck Institute for Astrophysics, DM Workshop Fermilab May 2007. `https://wwwmpa.mpa-garching.mpg.de/~swhite/talk/fermilab.pdf`.

[118] Will, C. M. Henry Cavendish, Johann von Soldner, and the deflection of light. *American Journal of Physics 56*, 5 (1988), 413–415.

[119] Zwicky, F. The redshift of extragalactic nebulae. *Helv. Phys. Acta 6*, 110 (1933), 138.

[120] Zwicky, F. Nebulae as gravitational lenses. *Physical Review 51*, 4 (1937), 290.

Miscellanea

List of Figures

List of Tables

List of Publications

[1] Simionato, S., Master Thesis: "Development of Astronomy Educational Resources: the Case of Universe Awareness". http://tesi.cab.unipd.it/62553/ (2013)

[2] Simionato, S. (author and editor), and Russo, P. (editor), "100 Educational Activities about Light and Photonics". OER E-Book for the 2015 International Years of Light. https://www.unawe.org/resources/guides/100light/ (2015)

[3] Lotze, K.-H., and Simionato, S., "Albert Einstein's Handwritten Curriculum Vitae", Proceedings of the WE-Heraeus Summer School "Astronomy from 4 Perspectives" Jena 2015: Gravitational Wave Astronomy (Editors Lotze K.-H. and Voelker S.) (2016).

[4] Simionato, S., "Was ist und wie entsteht Rotverschiebung?", MNU Journal 70, 04 (2017), pp. 234-240

[5] Simionato, S., "The Glass "Gravitational" Lens Experiment", PhyDid B – Didaktik Der Physik, Beiträge zur DPG-Frühjahrstagung Bonn 2020 (2020), pp. 47-54
http://www.phydid.de/index.php/phydid-b/article/view/1039

[6] Simionato, S., "Three Redshifts: Doppler, Cosmological, and Gravitational", The Physics Teacher 59, 5 (2021), 333–336

[7] Lotze, K.-H., and Simionato, S., "Gravitational Lensing as Focal Point for Teaching General Relativity", chapter of the book Teaching Einsteinian Physics in Schools (Editors Blair D. and Kersting M.), Routledge – Taylor and Francis Group (2021)

[8] Simionato, S., "The Optical Gravitational Lensing Experiment", Proceedings of the WE-Heraeus Summer School "Astronomy from 4 Perspectives" Jena 2019: Thinking Gravitational Lensing for Teaching (Editors Lotze K.-H. and Simionato S.) (2021)

[9] Lotze, K.-H., and Simionato, S., "Henry Cavendish and the Effect of Gravity on Propagation of Light: A Postscript", The European Physical Journal H 46, 24 (2021)

[10] Simionato, S., "Experimente mit gläsernen "Gravitations"-Linsen", Astronomie + Raumfahrt, accepted for publication (2021)

[11] Simionato, S., and Lotze, K.-H. "Distance Determination of the Spiral Galaxy NGC3198 with Cepheids, using Real Data from the Missions OGLE-IV and Gaia-DR1", in preparation (2021)

[12] Simionato, S., "Quasar in Classroom: an Historical Approach", in preparation (2021)

[13] Lotze, K.-H., and Simionato, S., "Henry Cavendish on Gravitational Deflection of Light", Annalen der Physik, Wiley Online Library, in preparation (2021)

Flyers:

[14] Simionato, S., "Die Laterna Magica: ein didaktisches Instrument für den Astronomieunterricht im 18. Und 19. Jahrhundert", flyer distributed during the Jena Astronomie-Lehrerfortbildung 2019 (2019)

[15] Lotze, K.-H., and Simionato, S., "John Michell and Henry Cavendish on the Effect of Gravity on Propagation of Light", flyer distributed during the WE-Heraeus Summer School "Astronomy from 4 Perspectives" Jena 2019 : Thinking Gravitational Lensing for Teaching (2019)
Also in the corresponding Proceedings (2021)

List of Lectures and Workshops in Conferences

WE-Heraeus Summer School "Astronomy from 4 Perspectives":

- Simionato, S., "Big Bang Nucleosynthesis and the Deuterium Bottleneck", Heidelberg, 2013

- Simionato, S., "Disprove the Doppler Origin for the Measured Redshift of the First Discovered Quasar" (Part of the section AGNs: elementary approach for educational purposes – The Discovery of the first Quasars), Padova, 2014

- Simionato, S., "Hand-On Gravitational Waves", Jena, 2015

- Simionato, S., "Introduction to Gravitational Waves Part I", Jena, 2015

- Simionato, S., "Introduction to Gravitational Waves Part II", Jena, 2015

- Simionato, S., Rotation Curves of Spiral Galaxies and their Implication for Dark Matter Part I", Heidelberg, 2017

- Simionato, S., Rotation Curves of Spiral Galaxies and their Implication for Dark Matter Part II", Heidelberg, 2017

- Simionato, S., "The Optical Gravitational Lensing Experiment", Jena, 2019

- Simionato, S., "Galaxies Distance Determination with Cepheids", Firenze (online) 2021

Astronomie Lehrerfortbildung Jena:

- Simionato, S., "Students as Astronomer: Bringing Quasars into Classroom", Jena, 2015

- Simionato, S., "Dark Matter and Gravitational Lensing: How We Can Use Astronomy in Teaching Physics", Jena, 2016

- Simionato, S., "Experimental Gravitational Lensing Cosmology", Jena, 2017

Bad Honnef Physikzentrum:

- Simionato, S., "Pulsare und Gravitationswellen als Laboratorien extremer Physik Part I" at DFG Lehrerfortbildung with the same name, Bad Honnef, 2017

- Simionato, S., "Pulsare und Gravitationswellen als Laboratorien extremer Physik Part II" at DFG Lehrerfortbildung with the same name, Bad Honnef, 2017

- Simionato, S., "Combining General Relativity and Optics to Visualise Light on Curved Paths" at Heraeus Seminar General Relativity as a Challenge for Physics Education, Bad Honnef, 2019

Tag Der Physik Jena:

- Simionato, S., Lotze, K.-H., "Licht auf Krummern Wegen", Jena, 2019

Circolo Astrofili Mestre:

- Simionato, S., "La Scoperta dei Quasar", Marghera (Mestre-Venezia), 2014

- Lotze, K.-H., and Simionato, S., "Luce su Traiettorie Curve – Light on Curved Paths", Marghera (Mestre-Venezia), 2018

MINT Festival Jena:

- Simionato, S., "Das Glas-"Gravitations"-Linsenexperiment", Jena (online) 2021

Ehrenwörtliche Erklärung

Ich erkläre hiermit ehrenwörtlich, dass ich die vorliegende Arbeit selbständig, ohne unzulässige Hilfe Dritter und ohne Benutzung anderer als der angegebenen Hilfsmittel und Literatur angefertigt habe. Die aus anderen Quellen direkt oder indirekt übernommenen Daten und Konzepte sind unter Angabe der Quelle gekennzeichnet.

Weitere Personen waren an der inhaltlich-materiellen Erstellung der vorliegenden Arbeit nicht beteiligt. Insbesondere habe ich hierfür nicht die entgeltliche Hilfe von Vermittlungs- bzw. Beratungsdiensten (Promotionsberater oder andere Personen) in Anspruch genommen. Niemand hat von mir unmittelbar oder mittelbar geldwerte Leistungen für Arbeiten erhalten, die im Zusammenhang mit dem Inhalt der vorgelegten Dissertation stehen.

Die Arbeit wurde bisher weder im In- noch im Ausland in gleicher oder ähnlicher Form einer anderen Prüfungsbehörde vorgelegt.

Die geltende Promotionsordnung der Physikalisch-Astronomischen Fakultät ist mir bekannt.

Ich versichere ehrenwörtlich, dass ich nach bestem Wissen die reine Wahrheit gesagt und nichts verschwiegen habe.

Jena, den 13.10.2021   Silvia Simionato